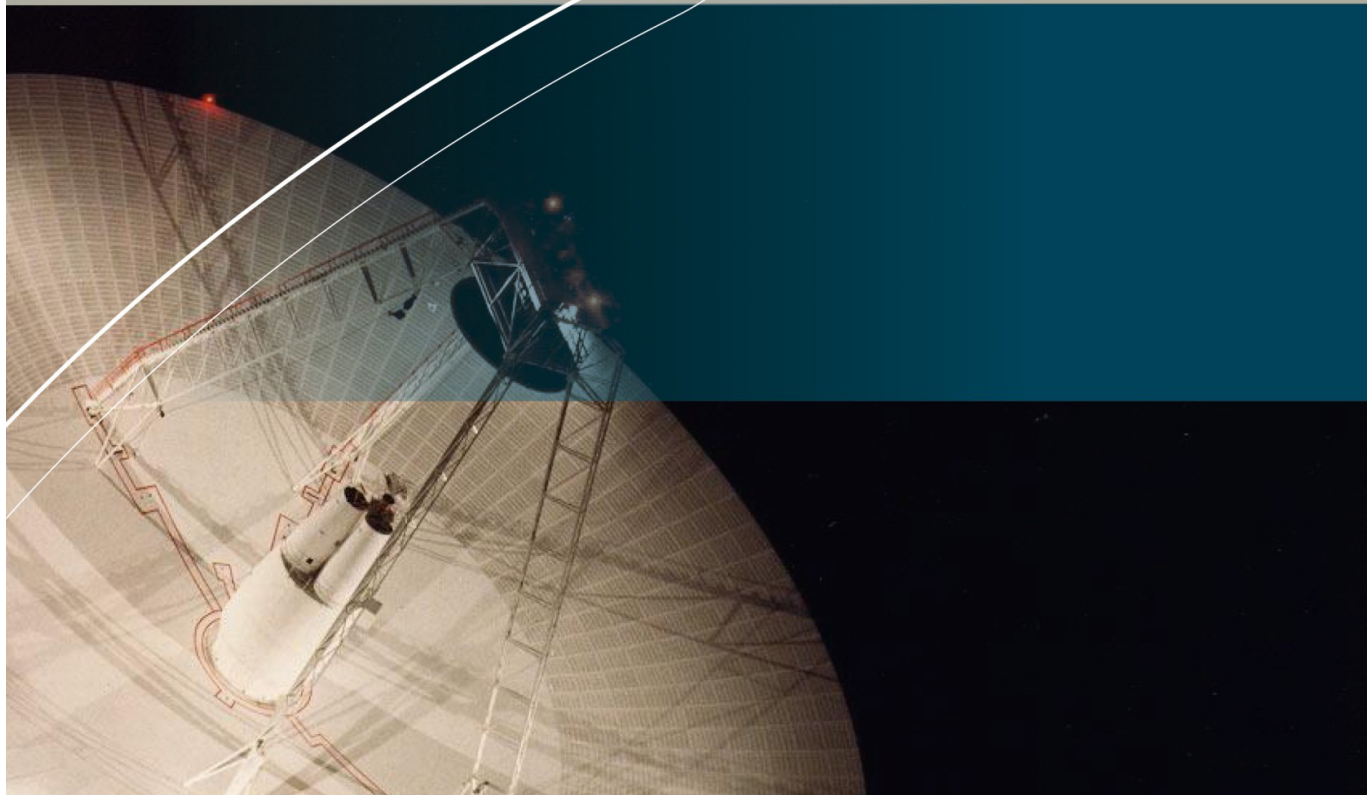




GRASP



Technical Description

www.ticra.com



TICRA
Pioneering Antennas

TICRA is an antenna engineering company with world leading expertise in software tools and consultancy services within design, analysis and measurement techniques for antennas. Based in the centre of Copenhagen, Denmark, TICRA employs highly skilled professionals with over 240 man-years of expertise in their fields.

GRASP, Technical Description

Editor: Knud Pontoppidan, TICRA, Denmark.

© 2005-2008

TICRA Engineering Consultants, Copenhagen, Denmark.

It is permitted to copy this book or part of it on condition that a full reference to the source is shown.

TABLE OF CONTENTS

1. INTRODUCTION	1
1.1 Object oriented approach	1
1.2 Graphics	2
1.3 Reflector surfaces	4
1.4 Reflector rim definitions	5
1.5 Support struts	5
1.6 Feed types	6
1.7 Reflector materials	6
1.8 Analysis methods	7
1.9 Report overview	7
2. ANTENNA SYSTEM DEFINITION	11
2.1 Coordinate systems	11
2.2 Scatterers	14
2.2.1 Reflectors	14
2.2.1.1 Reflector surfaces	15
2.2.1.1.1 Ellipsoid	16
2.2.1.1.2 Hyperboloid	17
2.2.1.1.3 Paraboloid	17
2.2.1.1.4 Conic mirror surface	18
2.2.1.1.5 Pyramidal surface	19
2.2.1.1.6 Surface expressed as a second order polynomial	20
2.2.1.1.7 Surface given in a regular grid	21
2.2.1.1.8 Tabulated rotationally symmetric surface	24

2.2.1.1.9	Surface expressed by cubic spline functions	25
2.2.1.1.10	Surface expressed by Zernike modes	28
2.2.1.1.11	Surface expressed by random values in a regular grid	33
2.2.1.1.12	Surface given by irregularly spaced points	37
2.2.1.1.13	Mesh surface with ribs	42
2.2.1.1.14	Mesh surface for unfurlable truss antenna	45
2.2.1.2	Reflector rims	48
2.2.1.2.1	Circular or elliptical rim	48
2.2.1.2.2	Rectangular rim	48
2.2.1.2.3	Triangular rim	49
2.2.1.2.4	Superelliptical rim	49
2.2.1.2.5	Tabulated rim	50
2.2.1.3	Reflector with hole	52
2.2.1.4	Reflector with panels in a polar grid	54
2.2.1.4.1	Specification of panels	55
2.2.1.4.2	Inter-panel gaps	56
2.2.1.4.3	Panel misalignments	56
2.2.1.5	Reflectors with individually defined panels	57
2.2.1.5.1	Panels	57
2.2.1.5.2	Hinges	57
2.2.1.6	Reflector with serrated edge	58
2.2.1.7	Reflector with distortions	61
2.2.2	Flat plates	62
2.2.3	Scatterer material properties	62
2.2.3.1	Definition of reflection and transmission coefficients	64
2.2.3.2	Material defined by the reflected and transmitted power	68
2.2.3.2.1	Perfect conductivity	69
2.2.3.2.2	Perfect absorption	69
2.2.3.3	Finite conductivity	69
2.2.3.4	Ideal grid	70

2.2.3.5	Strip grid	72
2.2.3.6	Wire grid	75
2.2.3.7	Mesh grid	76
2.2.3.8	Dielectric layer	79
2.2.3.9	Tabulated reflection and transmission coefficients	81
2.2.3.10	Cascading several layers	84
2.2.4	Struts	87
2.3	Feed systems	88
2.3.1	Feed element types	89
2.3.1.1	Tabulated pattern	92
2.3.1.1.1	Number of modes included	93
2.3.1.1.2	Cut adjustment	95
2.3.1.1.3	Time factor	95
2.3.1.1.4	Phase reference	95
2.3.1.1.5	Normalisation	96
2.3.1.2	Feed defined by spherical wave expansion	97
2.3.1.2.1	Number of modes included	97
2.3.1.2.2	Phase reference	98
2.3.1.2.3	Normalisation	98
2.3.1.3	Gaussian beam	98
2.3.1.3.1	The source model	98
2.3.1.3.2	Comparison to an accurate feed model	101
2.3.1.3.3	Near-field properties of the complex point source	103
2.3.1.3.4	Gaussian beams	104
2.3.1.3.5	Definitions of a complex point source in GRASP	107
2.3.1.3.6	Forced far-field calculations	108
2.3.1.4	Simple tapered pattern	109
2.3.1.4.1	Feed model	109
2.3.1.4.2	Polarisation	110
2.3.1.4.3	Normalisation	110
2.3.1.4.4	Cross polarisation	110
2.3.1.5	Elliptical pattern	110

2.3.1.5.1	Feed model	111
2.3.1.5.2	Polarisation	112
2.3.1.5.3	Normalisation	112
2.3.1.5.4	Comparison between simple tapered pattern and elliptical pattern	112
2.3.1.6	Radiation from simple apertures	113
2.3.1.6.1	Determination of the far field	114
2.3.1.6.2	Rectangular horn	116
2.3.1.6.3	Conical horn	120
2.3.1.6.4	Fundamental mode waveguide	121
2.3.1.6.5	Potter horn	121
2.3.1.6.6	Hexagonal horn	122
2.3.1.7	Microstrip feed	126
2.3.1.8	Axial-mode monofilar helix feed	128
2.3.1.9	Bifilar equi-angular spiral feed	134
2.3.1.10	Halfwave dipole	140
2.3.1.11	Hertzian dipole	141
2.3.1.12	Cardioid pattern	142
2.3.1.13	Hybrid mode conical horn	143
2.3.2	Electromagnetic source generated by a planar tabulated field	146
2.3.3	Plane wave illumination	150
2.3.4	Arrays of radiating elements	150
3.	ANALYSIS METHODS	153
3.1	Physical Optics	153
3.1.1	Induced surface currents	154
3.1.2	Surface integral	157
3.1.2.1	Polar grid	160
3.1.2.2	Rectangular and parallelogram grid	166
3.1.2.3	Triangular grid	168
3.1.3	Convergence of the physical optics integral	171

3.1.3.1	General convergence properties	171
3.1.3.2	Automatic convergence procedure	174
3.1.4	Spillover calculation	178
3.2	Physical Theory of Diffraction	179
3.3	Reflector with gaps	182
3.3.1	The PTD-gap contribution	183
3.3.2	Integration Grids	185
3.3.3	Numerical Example	186
3.4	Strut calculations	189
3.4.1	Typical strut contributions	189
3.4.2	Computational approach for circular struts	190
3.4.2.1	Simple PO	191
3.4.2.2	Canonical solution	193
3.4.2.2.1	Plane wave incidence	193
3.4.2.2.2	Spherical wave incidence	194
3.4.2.3	Comparison between methods	196
3.4.3	Computational approach for polygonal struts	202
3.4.3.1	PO	202
3.4.3.2	PTD	203
3.4.3.2.1	On the propagation through the wedge	204
3.4.3.3	Examples	206
3.4.3.3.1	The square cylinder	207
3.4.3.3.2	Square to circular cylinder	210
3.5	Physical Optics for scatterers with material properties	213
3.6	Ray-optical methods	218
3.6.1	Geometrical Optics	220
3.6.2	Geometrical Theory of Diffraction	225

3.6.2.1	Caustic corrections	227
3.6.2.2	GTD for scatterers with material properties	231
3.7	Special techniques involving the direction of the incident field	238
3.8	Examples illustrating PO and GTD	241
3.8.1	Single offset reflector geometry	241
3.8.2	Calculation of main beam and near-in sidelobes	242
3.8.3	Wide-angle pattern prediction by PO and GTD	244
3.8.4	The significance of an accurate feed model in PO calculations	246
3.8.5	Near-field predictions	247
3.8.6	Guidelines on selecting PO or GTD	248
3.9	Gaussian beam analysis	250
3.10	Spherical wave expansion	252
3.10.1	Theoretical number of modes	254
3.10.2	Spherical expansion expressed in the <i>ab</i> -modes	255
3.10.3	Spherical expansion expressed in the <i>Q</i> -modes	258
3.10.4	Field determination	259
4.	OUTPUT CAPABILITIES	261
4.1	Definition and normalisation of field components	261
4.1.1	Field units	261
4.1.2	Definition of far field	263
4.1.3	Feed normalisation	264

4.1.4	Polarisation	267
4.1.4.1	Far fields	267
4.1.4.2	Near fields	273
4.1.4.2.1	Near-field points on a sphere	273
4.1.4.2.2	Near-field points on a circular cylinder	274
4.1.4.2.3	Near-field points on a plane	275
4.1.4.2.4	Example illustrating near-field normalisation	276
4.1.4.3	Redefinition of the polarisation components	278
4.2	Output points	280
4.2.1	One-dimensional cuts	281
4.2.2	Two-dimensional grids	283
4.2.2.1	Spherical grids	283
4.2.2.2	Cylindrical grid	287
4.2.2.3	Planar grid	288
4.2.3	Irregularly spaced output points	290
4.2.4	Surface points and aperture fields	290
4.2.4.1	One-dimensional surface cuts	291
4.2.4.2	Two-dimensional surface grids	292
4.2.4.3	Aperture fields	292
4.3	Interpolation techniques	293
4.3.1	Cubic interpolation	293
4.3.2	Whittaker interpolation	296
4.4	Beam analyses	298
4.4.1	Peak gain, peak direction and beamwidth	299
4.4.2	Efficiency calculation	301
4.4.3	Beam contour area calculation	304
4.4.4	Pattern envelope calculation	306

5. APPLICATIONAL EXAMPLES	309
5.1 Single reflector with three struts	309
5.1.1 Geometry	309
5.1.2 Nominal pattern analysis	312
5.1.3 Strut scattering of spherical wave	313
5.1.4 Strut scattering of plane wave	315
5.1.5 Total pattern	316
5.2 Dual reflector with blockage	317
5.2.1 Geometry	317
5.2.2 Pattern analysis	318
5.2.3 Blockage considerations	320
5.2.4 A closer look at the hole in the reflector	322
5.3 A single shaped reflector with circular polarisation	324
5.3.1 Shaped reflector geometry	324
5.3.2 Coverage requirements	325
5.3.3 Co-polar pattern analysis	326
5.3.4 Cross polar pattern analysis	327
5.4 Dual gridded reflector	330
5.4.1 Dual gridded reflector geometry	330
5.4.2 Analysis procedure	333
5.4.2.1 Rear feed reflected in the front reflector	336
5.4.2.2 Rear feed through front reflector, scattered in the rear	336
5.4.2.3 Transmission of the rear reflector field through the front reflector	338
5.4.2.4 Total field	340

5.4.3	A closer look at the scattering between the rear and the front reflector	342
5.5	Feed array	344
5.6	Compact antenna test range with serrated edges	346
5.6.1	Side-fed offset Cassegrain CATR	347
5.6.2	Analysis	348
5.7	Beam waveguide	350
6.	USEFUL GEOMETRICAL RELATIONS FOR REFLECTOR ANTENNAS	355
6.1	Paraboloids	355
6.2	Hyperboloids	358
6.3	Ellipsoids	361
6.4	Caustic considerations	363
6.5	Basic reflector antenna designs	365
6.5.1	Single reflector design	366
6.5.1.1	Default parameters	367
6.5.1.1.1	Coordinate systems	367
6.5.1.1.2	Feed parameters	367
6.5.1.1.3	Output parameters	367
6.5.1.1.4	Computational approach	367
6.5.2	Dual reflector design	368
6.5.2.1	Default parameters	371
6.5.2.1.1	Coordinate systems	371
6.5.2.1.2	Feed parameters	371
6.5.2.1.3	Output parameters	372
6.5.2.1.4	Computational approach	372
6.5.2.2	Equivalent single reflector paraboloid	372
6.5.2.3	Compensated dual reflector systems	375
7.	REFERENCES	379

8. SUBJECT INDEX

379

1. INTRODUCTION

This report provides a technical description of the GRASP software package for general reflector antenna analysis.

GRASP is a set of tools for analysing general reflector antennas and antenna farms. GRASP provides a graphical interface in the form of a pre- and post- processor. The pre-processor assists the user in setting up the geometry of the problem to be analysed and provides a means for visualising the system. The post-processor contains several plotting facilities for calculated patterns. Plots can be in the form of pattern cuts or, plots can be in the form of contour plots in various projections. An Earth map facility is available for viewing satellite antenna coverage graphically.

GRASP is a general tool which can calculate the electromagnetic radiation from systems consisting of multiple reflectors with several feeds and feed arrays. It is possible to analyse the interaction between various antenna systems which is a requirement often encountered on satellites where several antennas may be mounted in the vicinity of each other. The scattering due to a feed or a reflector of one system in a reflector of another system can thus be calculated.

The time factor is $e^{j\omega t}$ throughout this document and the notation for logarithms is $\log(x)$ for the logarithm of base 10 and $\ln(x)$ for the logarithm of base e .

1.1 Object oriented approach

GRASP is developed using the Fortran 90 language and makes extensive use of object-oriented programming techniques. All reflector surfaces and feed systems are described in terms of objects belonging to different classes. For example the paraboloid-class for a parabolic reflector and the Gaussian-feed-class for a feed radiating a Gaussian beam. This object- oriented approach greatly facilitates the analysis of composite systems.

A further advantage is that it becomes easier to analyse secondary, but important, characteristics of an antenna system. For example in previous versions of GRASP there was a clear distinction between the main and the subreflector of a dual-reflector system. This was apparent in the sequence in which the pattern computations were performed, i.e. first the feed scattering in the subreflector and then the reflection of that field in the main reflector. If there was a reason to analyse the scattering of the main reflector field in the subreflector, one had to perform successive runs with the program and redefine the input so that the subreflector became the main reflector, and vice versa. In GRASP it is possible to perform all these calculations in the same run, and in a much more practical manner than previously.

The Fortran 90 language has a further advantage in its dynamic memory allocation capability. This is a must when considering systems consisting of an arbitrary number of reflectors and feeds.

1.2 Graphics

Due to the great flexibility GRASP allows the user when creating complex antenna structures, a method for visualising the system is indispensable. This is provided in the pre-processor which can plot the system geometry from any view angle. GRASP also contains a feature by which a file containing 3D-data for the system geometry can be generated. The file is in a format that can be used as input to a CAD program. Furthermore, it is possible to convert the file into graphics formats which can be routed to a printer or imported into documents. An example of the graphics output from GRASP is presented in Figure 1.2-1.

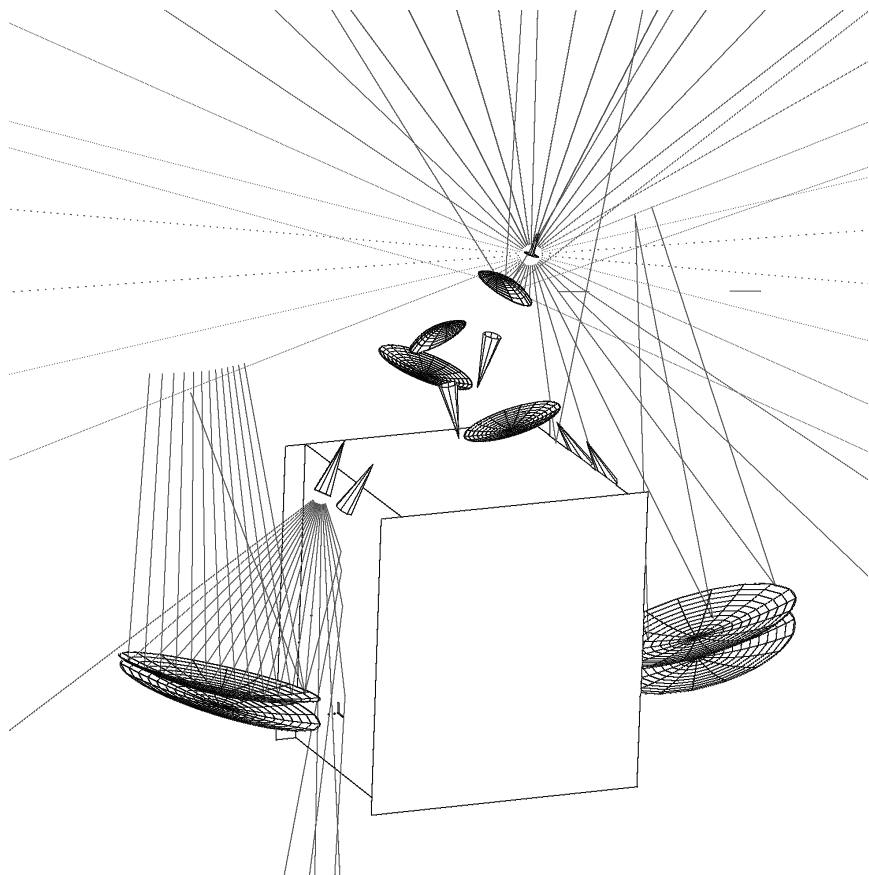


Figure 1.2-1 Realistic satellite structure with rays.

Alternatively, the geometry may be shown in OpenGL. An example on this representation is shown in Figure 1.2-2.

The two figures show a complex antenna farm on a spacecraft platform. All structures are made from reflector objects in GRASP, which allows one to analyse all relevant interactions and scatterings. Dual-gridded systems with one feed for the front reflector and another feed (in the opposite polarisation) for the rear reflector are mounted on the side walls. Two shaped dual reflector systems are located on the Earth deck and a TT&C (Telemetry, Tracking and Command) antenna is mounted on top of one of the subreflectors. The latter antenna radiates an omni-directional beam which can easily be distorted due to the presence of reflectors in its vicinity.

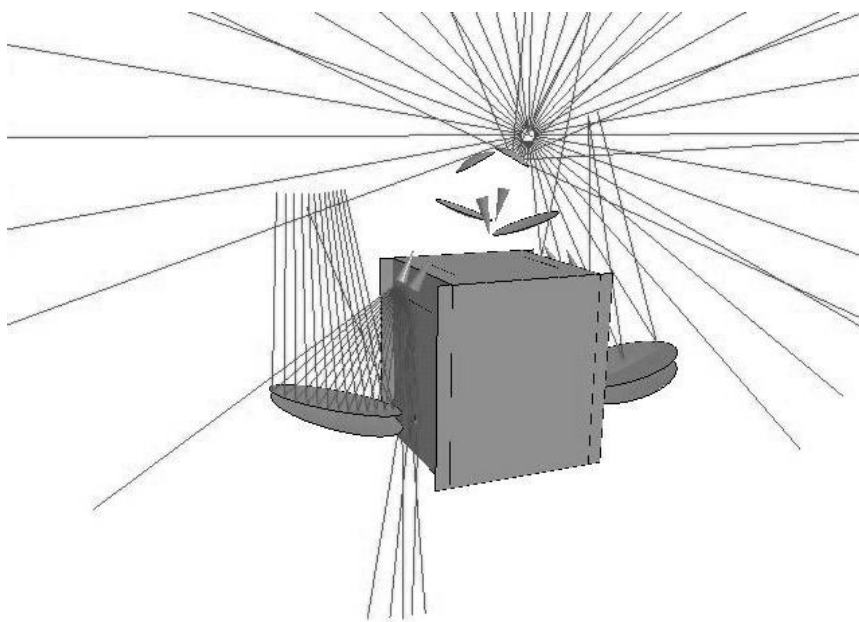


Figure 1.2-2 OpenGL drawing of the same satellite structure as in Figure 1.2-1.

The plot also demonstrates the ray plotting feature of GRASP. Rays can be emitted from any feed and traced through all reflectors, providing an easy way of identifying potential problems of interaction very early in the design period.

1.3 Reflector surfaces

The reflector shape can be selected among a number of types, including

- paraboloid, hyperboloid, ellipsoid
- general second-order expression in x and y
- numerically defined in a regular xy -grid
- numerically defined in an irregular grid, for instance measured surface points with corresponding values of x , y and z
- rotationally symmetric reflector with the cross-section defined numerically

- expansion in Zernike modes
- random z -values, specified by a correlation distance and an amplitude
- Flat plates

In addition it is possible to superimpose distortions on reflectors. The distortions may be specified as any of the above types.

1.4 Reflector rim definitions

The shape of the reflector rim is determined as the intersection between the surface and a cylinder with its cross section defined in the xy -plane of the reflector coordinate system. In this way the surface shape and the rim shape can be defined independently of each other. The following rim shapes are available:

- circular or elliptical rim
- superelliptical rim
- rectangular rim
- triangular rim
- numerically defined in the xy -coordinate space.
- triangle or parallelogram (for flat plates)
- serrated reflector rim

The serrated edge option is useful to determine the quiet-zone performance of a compact range.

1.5 Support struts

Accurate strut analysis methods are incorporated in GRASP. These techniques are valid for both thin and thick circular struts. The struts will cause direct blockage of the reflector field and also distortions of the reflector illumination. Both of these effects may be calculated since the struts belong to the scattering class of objects just as reflectors do.

1.6 Feed types

One of the attractive features of the general program is the availability of numerous different feed models. Some of the most important ones are

- smooth pyramidal or conical horns
- simple model for corrugated horn
- feed represented by a Gaussian beam
- tabulated feed pattern (measured or predicted)
- feed described by a spherical wave expansion
- Potter horn
- microstrip feed
- helix
- dipoles

Some of the feed models mentioned above include the near-field effects from the source such as the Gaussian beam model and the spherical wave expansion. Other feed models, such as the radiating apertures, are only valid in the far-field. However, for all feed models in GRASP the near-field is automatically calculated by an internal spherical wave expansion of the far-field.

1.7 Reflector materials

While it is often assumed in antenna analysis that the reflectors are perfectly conducting, this is never the case in practice and when high accuracy is needed it may be necessary to account for the electrical properties of the materials used. GRASP provides models for different types of surface materials such as

- finite conductivity
- ideal metal grid, strip grid or wire grid
- mesh
- dielectric layer

- tabulated reflection and transmission coefficients

A realistic reflector may be composed by several layers of the above surface materials. For example a painted reflector can be modelled by a thin dielectric layer on a perfect conductor, and a polarisation sensitive (gridded) reflector as a grid on top of a thin dielectric support shell. Dielectric material may also be used to model the influence of a radome on the radiation pattern.

1.8 Analysis methods

GRASP is based on well-established analysis techniques such as Physical Optics (PO) supplemented with the Physical Theory of Diffraction (PTD), Geometrical Optics (GO) and Uniform Geometrical Theory of Diffraction (GTD). The ray-based analysis methods (GO and GTD) can only be applied to one single reflector at a time to limit the complexity of the associated ray-tracing problem. PO and PTD can be applied to any number of reflector analyses in arbitrary order. This makes GRASP very flexible because the induced currents obtained by a PO analysis on one reflector can be used as a source illuminating a second reflector.

The scattering effects from supporting struts are determined by means of PO. For thick struts the conventional PO approach is used and for thin struts a special technique is developed which makes it possible to calculate the surface currents on both the illuminated and the shadow side of the strut. Two important effects from struts are typical for reflector antennas: 1) they may block the field from the main reflector travelling towards the far field and 2) they may shadow the field from the feed illuminating the reflector. Both of these effects may be calculated in GRASP.

1.9 Report overview

It is the purpose of this technical description of GRASP to present the capabilities of the program and to explain the basic principles of the analysis methods. The description is aimed at

the practical antenna engineer. It is written in general physical terms, and experience with GRASP or previous versions of GRASP is not a prerequisite. The precise information for the actual usage of GRASP must be found in the GRASP Reference Manual or in the GRASP Help facility.

Chapter 2 describes the components of an antenna system such as coordinate systems, reflectors, struts and feeds and feed arrays. This chapter also explains the various options for different reflector materials.

The analysis methods used in GRASP are described in Chapter 3:

Physical Optics (PO)

Physical Theory of Diffraction (PTD)

Special techniques for strut calculations

Geometrical Optics (GO)

Geometrical Theory of Diffraction (GTD)

The chapter also includes a number of examples where the different methods are compared and their relative merits are identified.

Chapter 4 describes the output capabilities. It contains important information on the normalisation and polarisation definitions used in GRASP. The different options for the location of the field points, both in one and two dimensions, are presented. Chapter 4 also contains interpolation techniques and some special beam analyses available in the Post-processor.

Chapter 5 is devoted to typical examples illustrating the various facilities in GRASP. The first example is a single reflector antenna with three struts and the different types of strut contributions are presented. The second example concerns a rotationally symmetric dual reflector antenna typical for large Earth station antennas. The subreflector will generate unavoidable blockage effects and the techniques to compute these effects are demonstrated.

The third example in Chapter 5 treats a shaped reflector antenna. The antenna operates in circular polarisation and one particular purpose of this example is to demonstrate the importance of PTD for an accurate assessment of the cross-polar field component.

The fourth example is a realistic, dual gridded, shaped reflector antenna operating in two orthogonal linear polarisations to generate a contoured beam. The example illustrates the use of non-perfectly conducting materials and it shows how to handle reflectors where both reflected and transmitted fields play an important role for the antenna performance.

The fifth example is a multi-feed system. Shaping the surface of a reflector is one way of generating a contoured beam tailored to a specific coverage – another method is to let an array of feeds illuminate a parabolic reflector. The results are compared to the dual gridded antenna in the previous example.

The next example in Chapter 5 is a compact antenna test range with serrations on the reflector edges. It illustrates the calculation of near-field points in the quiet zone and the use of the serrated edge option.

The final example in Chapter 5 illustrates the efficient way of analysing a sequence of scatterers. The example is the beam waveguide for the ESA Deep Space Antenna located in Perth, Australia.

Chapter 6 presents some useful geometrical relations for basic reflector antenna systems. It also describes the background for the antenna design features available in GRASP, and for the dual reflector systems the equivalent single reflector concept is introduced. Finally, the so-called compensated dual reflector systems are described.

2. ANTENNA SYSTEM DEFINITION

This chapter describes the various elements needed to define a complete antenna system. They are divided into two main groups: feed systems and scatterers. The feed system is the actively radiating element and it may consist of a single feed or an array of feeds. The scatterers are passive structures which could be antenna reflectors or disturbing elements such as a neighbouring solar panel or support struts.

In GRASP dimensions are given in SI-units or Imperial units. Frequencies are given in GHz or MHz and the conductivity in Siemens/m (S/m).

2.1 Coordinate systems

All structural elements in GRASP are specified in a coordinate system. This coordinate system therefore defines the position and orientation of the element. The number of coordinate systems is unlimited.

Coordinate systems can be specified relative to any other coordinate system or to the “global coordinate system”. The global coordinate system is an inherent coordinate system with origin at (0,0,0) and unit vectors (1,0,0), (0,1,0) and (0,0,1). At least one coordinate system must be defined relative to the global coordinate system.

The origin of a new coordinate system is given by the x -, y - and z -value in the reference coordinate system. The orientation of the new coordinate system is defined by two orthogonal vectors along any two of the three coordinate vectors. An alternative option is to specify the three angles θ , ϕ and ψ in a spherical coordinate system. The latter option is illustrated in Figure 2.1-1.

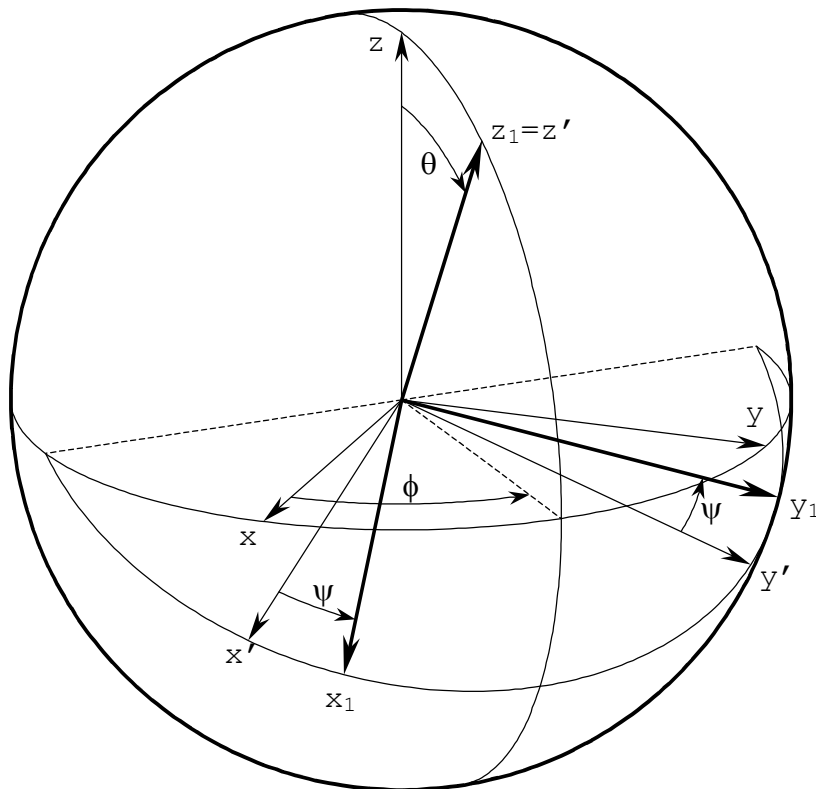


Figure 2.1-1 The orientation of the new coordinate system $x_1y_1z_1$ relative to xyz specified by the angles θ , ϕ and ψ .

The new coordinate system is $x_1y_1z_1$ specified in the reference coordinate system xyz . First, the z -axis is tilted the angle θ by rotating the xyz -coordinate system around the line in the xy -plane orthogonal to the line making the angle ϕ with the x -axis (the dotted line in Figure 2.1-1). This process generates the coordinate system $x'y'z'$. The $x_1y_1z_1$ -coordinate system is then obtained by rotating the angle ψ around the z' -axis. The orientation definition described here is particularly useful for specifying the direction of a feed. The first two coordinates, θ and ϕ , then describe the pointing of the feed and the ψ -value controls the polarisation direction.

The unit vectors of the rotated coordinate systems are given by

$$\begin{aligned}\hat{x}_1 &= \hat{\theta} \cos(\phi - \psi) - \hat{\phi} \sin(\phi - \psi) \\ \hat{y}_1 &= \hat{\theta} \sin(\phi - \psi) + \hat{\phi} \cos(\phi - \psi), \\ \hat{z}_1 &= \hat{r}\end{aligned}\quad (2.1-1)$$

where

$$\begin{aligned}\hat{\theta} &= \hat{x} \cos \theta \cos \phi + \hat{y} \cos \theta \sin \phi - \hat{z} \sin \theta \\ \hat{\phi} &= -\hat{x} \sin \phi + \hat{y} \cos \phi \\ \hat{r} &= \hat{x} \sin \theta \cos \phi + \hat{y} \sin \theta \sin \phi + \hat{z} \cos \theta\end{aligned}\quad (2.1-2)$$

Another way to describe the orientation of one coordinate system with respect to another is by the Euler angles α , β and γ . These angles are here defined as follows (other definitions exist). The original system, xyz , in Figure 2.1-1, is first rotated the angle α around the z -axis. Next, the system is rotated around the new y -axis the angle β so the z -axis reaches the final z_1 -axis. Finally, the system is rotated around the new z -axis the angle γ so the x -axis reaches its final position x_1 . All rotations are around the positive axes (right hand rule). The relations between the two definitions are

$$\alpha, \beta, \gamma = \phi, \theta, -\phi + \psi . \quad (2.1-3)$$

When the Euler angles (α, β, γ) are given then (θ, ϕ, ψ) may be found from

$$(\theta, \phi, \psi) = (\beta, \alpha, \alpha + \gamma) . \quad (2.1-4)$$

If a coordinate system 2 is obtained by rotating coordinate system 1 as specified by θ , ϕ and ψ (or α , β and γ) defined above, then the opposite rotation, namely to rotate system 2 back to system 1, is obtained by rotating the three Euler angles backwards in the opposite directions

$$\alpha', \beta', \gamma' = -\gamma, -\beta, -\alpha = \pi - \gamma, \beta, \pi - \alpha . \quad (2.1-5)$$

The corresponding GRASP angles are

$$\theta', \phi', \psi' = -\theta, \phi - \psi, -\psi = \theta, \pi + \phi - \psi, -\psi . \quad (2.1-6)$$

The last expressions in (2.1-5) and (2.1-6) are converted to a positive polar angle θ (or β).

2.2 Scatterers

Scatterers include reflectors, flat plates and struts. Reflectors are normally used to collimate the field from the feed and redirect it to a desired direction. Flat plates are used to model other parts of the structure like solar panels and a spacecraft body.

Reflectors and flat plates can have surface material properties other than perfectly conducting. These possibilities are described in Section 2.2.3. Struts are always assumed perfectly conducting and the cross section is either circular or polygonal.

2.2.1 Reflectors

A reflector is defined by means of a reflector surface and a reflector rim. Both of these two items are specified in the same coordinate system as illustrated in Figure 2.2-1.

A number of different reflector surfaces and reflector rim shapes are available in GRASP as described in the following subsections.

Reflectors may have a centre hole and a serrated edge and it may be subject to thermal distortions. These options are described in Sections 2.2.1.3 to 2.2.1.7.

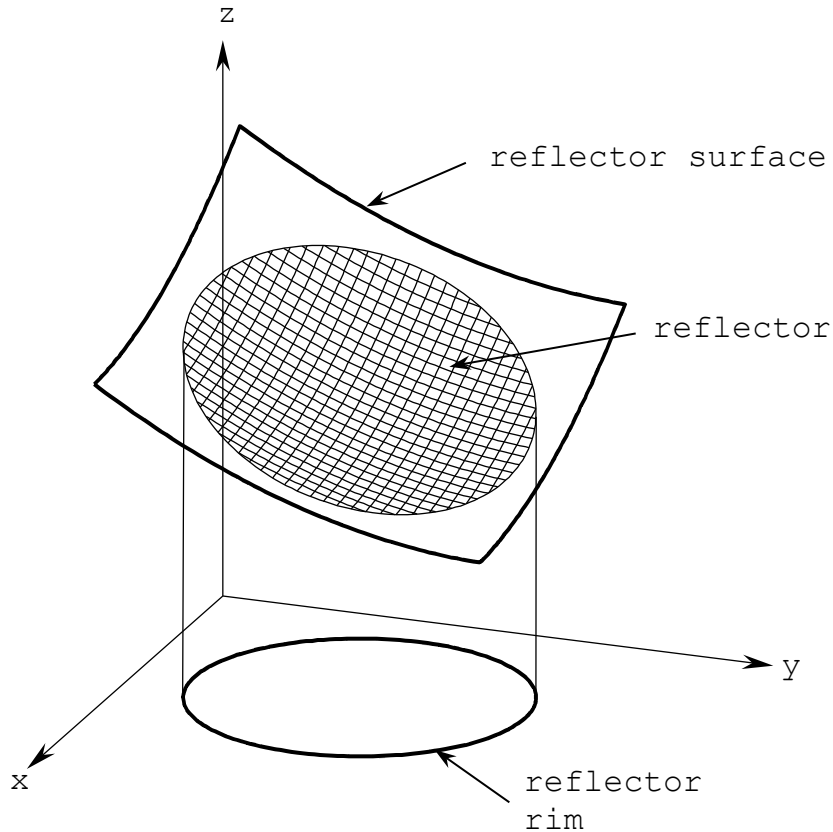


Figure 2.2-1 A reflector is defined by a reflector surface cut by a cylinder with the reflector rim as the cross section.

2.2.1.1 Reflector surfaces

Internally in GRASP the surface is represented by

$$z = F(x, y) \quad (2.2-1)$$

The surface shape must therefore be a well-defined function of the independent variables x and y within the region determined by the rim of the reflector.

The positive normal to the reflector surface is selected as the one which is directed to the same side of the surface as the positive z -axis. This distinction is necessary when dealing with

reflectors with several layers surface materials, see Section 2.2.3.10. The various surface options available are described in the following subsections.

2.2.1.1.1 Ellipsoid

The rotationally symmetric ellipsoid is the classical subreflector for a Gregorian reflector antenna design. The ellipsoid is illustrated in Figure 2.2-2. The major axis is $2a$ and the distance between the two foci F_1 and F_2 is $2c$, $a > c > 0$. A ray coming from a feed in F_2 will, after reflection in the surface, appear as coming from F_1 .

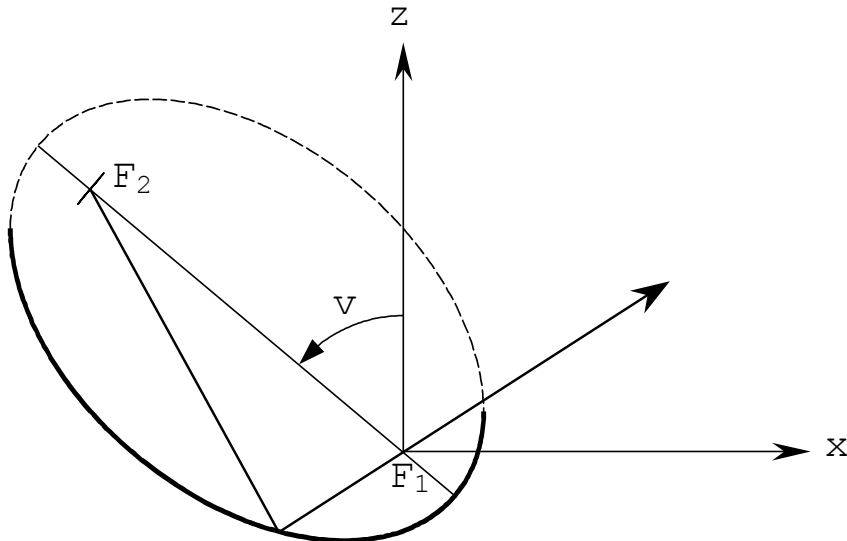


Figure 2.2-2 Ellipsoidal reflector.

F_1 is the origin of the coordinate system. It is possible to tilt the axis of the ellipsoid the angle v from the z -axis towards the negative x -axis. The available area of the reflector is indicated by the thick line in Figure 2.2-2. The option of tilting the reflector axis is very useful when designing offset (non-rotational) antenna systems, see Section 6.5.

2.2.1.1.2 Hyperboloid

The rotationally symmetric hyperboloid is the classical subreflector for a Cassegrain reflector antenna design. The hyperboloid is illustrated in Figure 2.2-3. The distance between the vertices is $|2a|$ and the distance between the two foci F_1 and F_2 is $2c$, $|a| < c$. A ray coming from a feed in F_2 will, after reflection in the subreflector, appear as coming from F_1 . F_1 is the origin of the coordinate system. The sign of a determines which part of the hyperboloid that will be used. The convex part is obtained when a is positive and the concave part for the negative sign of a .

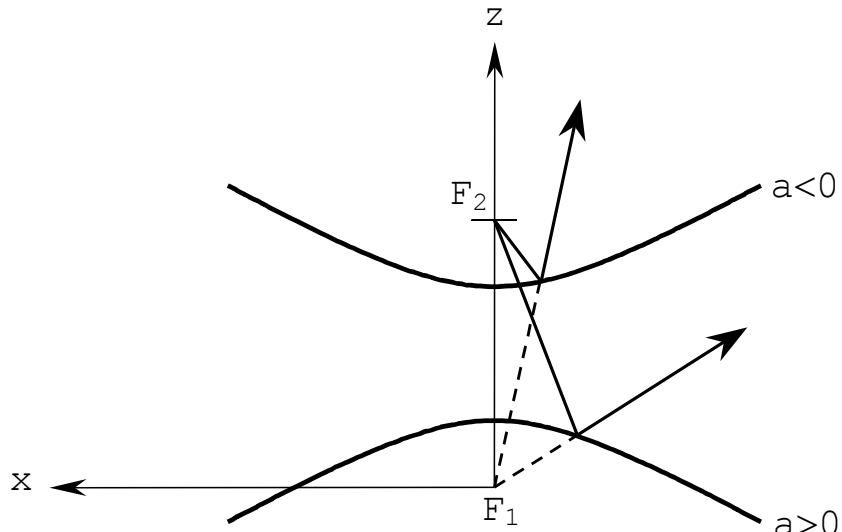


Figure 2.2-3 Hyperboloid of revolution. Both convex and concave part is shown.

The hyperboloids are given by

$$z = c - \frac{a}{b} b^2 + x^2 + y^2^{\frac{1}{2}} ; b = \sqrt{c^2 - a^2} . \quad (2.2-2)$$

2.2.1.1.3 Paraboloid

The surface of the paraboloid is given by

$$z - z_0 = \frac{(x - x_0)^2 + (y - y_0)^2}{4f} \quad (2.2-3)$$

The focal length, f , can be selected negative in which case the surface will appear convex when seen from the positive z -axis. The vertex may be translated to an arbitrary position given by x_0, y_0, z_0 .

2.2.1.1.4 *Conic mirror surface*

This type of surface is able to represent both ellipsoids, hyperboloids and paraboloids in a general way. It turns out to be a very practical alternative when describing reflector surfaces for beam waveguides and quasi-optical systems.

The basic principle in this surface definition is illustrated in Figure 2.2-4. A point, P , and a normal vector, \hat{n} , is selected. Two line segments each making the same angle, θ_i , with the normal and of lengths r_1 and r_2 are inserted from the point P . The other ends of the line segments define the two points F_1 and F_2 .

A conic section through P is now defined using F_1 and F_2 as focal points and the final surface is obtained by rotating the conic section around the line connecting F_1 and F_2 . If r_1 and r_2 are both positive, as in Figure 2.2-4, the resulting surface becomes a concave ellipsoid when seen from the positive side of the normal. If r_1 and r_2 are both negative F_1 and F_2 are located on the opposite side of the surface relative to the direction of the normal and the surface becomes a convex ellipsoid. If r_1 and r_2 are of opposite signs the surface becomes a hyperboloid, and it is convex if $r_1 + r_2 > 0$ and concave if $r_1 + r_2 < 0$. If either r_1 or r_2 is infinite, the surface becomes a paraboloid.

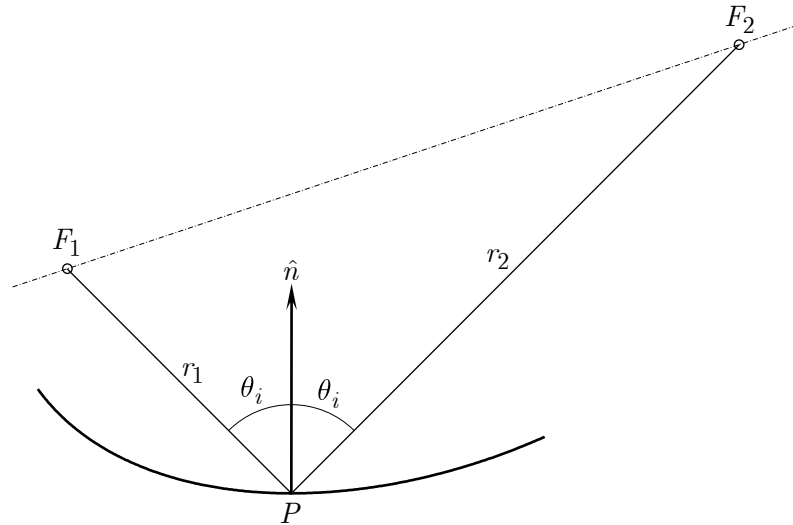


Figure 2.2-4 Definition of the conic mirror surface

2.2.1.1.5 Pyramidal surface

This surface may be useful for modelling various types of shields in a reflector antenna environment. The surface is defined as a regular pyramid with N sides and with vertex O , as shown in Figure 2.2-5 for $N = 4$. The shape is controlled by the angle, θ_c , from the z -axis to the edges, $0 < \theta_c < \pi$.

It is also possible to introduce a rounding of the edges of the pyramid. In Figure 2.2-5 an arbitrary plane orthogonal to the axis is shown with a line from the axis point, O' , to one the corner points, P . Two lines lying in the same plane and making an angle, θ_r , with the line $O'P$ intersect the pyramid at the points P_1 and P_2 . The rounding of the edge OP is now obtained by replacing the sector OP_1PP_2 by a circular cone with apex at O and with an opening angle such that cone is tangent to the pyramid along the lines OP_1 and OP_2 .

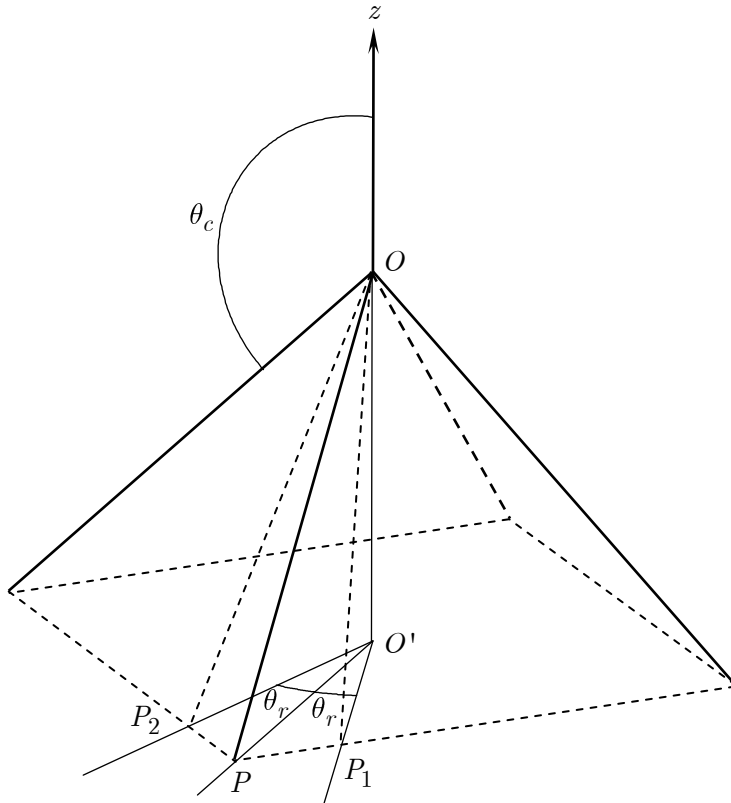


Figure 2.2-5 Pyramidal surface with four sides.

2.2.1.1.6 *Surface expressed as a second order polynomial*

The surface function $z = F(x, y)$ is here implicitly given by the expression

$$\begin{aligned} Ax^2 + Bxy + Cy^2 + Dx + Ey + F = \\ Gz^2 + Hz + Ixz + Jyz \end{aligned} \tag{2.2-4}$$

The surface may be rotated around the x , y - and z -axes in arbitrary order and it may further be translated along the three coordinate axes.

If $G \neq 0$, the expression will give two solutions for z and the user must specify which one he wants. Also the user must make sure that the function is defined (it provides real roots for z) within the actual antenna aperture area defined by the rim of the reflector.

The expression (2.2-4) is perfectly capable of generating all kinds of quadric surfaces like the common reflector surfaces: paraboloids, hyperboloids and ellipsoids. These particular surfaces are, however, easier described by the surface modules described above. This is also the case for the following simple geometrical shapes:

a flat plate, $z = ax + by + c$,

a circular cone, $z^2 = a x^2 + y^2$,

a circular cylinder, $z^2 = r^2 - y^2$,

a spherical reflector, $z^2 = r^2 - x^2 - y^2$,

The general expression is useful to generate more complex shapes as:

a shaped reflector with two foci, $z = \frac{x^2}{4f_x} + \frac{y^2}{4f_y}$,

2.2.1.1.7 *Surface given in a regular grid*

In this model the z -values of the surface are given at the nodes of a regular grid in x and y . A cubic interpolation procedure, described in Section 4.3.1, yields a smooth surface between the values at the nodes.

In the following the optimum density of the input points will be discussed. Concentrating on the x -variation we have

$$z = f(x) \quad (2.2-5)$$

where the function values are given at an equidistant spacing h . The first and second order derivatives become

$$\frac{dz}{dx} \cong \frac{1}{2h} [f(x+h) - f(x-h)] \quad (2.2-6)$$

$$\frac{d^2z}{dx^2} \cong \frac{1}{h^2} [f(x+h) + f(x-h) - 2f(x)] \quad (2.2-7)$$

It is well known that the above approximate expressions for the derivatives are only accurate if h is sufficiently small. To substantiate this, it is now assumed that the surface has a wavy structure given by

$$z = a \sin k_s x, \quad k_s = 2\pi/\lambda_s \quad (2.2-8)$$

where λ_s is the period of the surface variations. The derivatives become

$$\frac{dz}{dx} = ak_s \cos k_s x \quad (2.2-9)$$

$$\frac{d^2z}{dx^2} = -ak_s^2 \sin k_s x \quad . \quad (2.2-10)$$

Using the approximate formulas (2.2-6) and (2.2-7) for tabulated input gives

$$\frac{dz}{dx} = ak_s \cos k_s x \quad \left(1 - \frac{1}{6} h k_s^2\right) \quad (2.2-11)$$

$$\frac{d^2z}{dx^2} = -ak_s^2 \sin k_s x \quad \left(1 - \frac{1}{12} h k_s^2\right) \quad (2.2-12)$$

The second order derivative is especially critical for GO calculations. If it is required that the error term in (2.2-12) is less than one per cent one finds

$$hk_s < 0.35 \quad (2.2-13)$$

or

$$p = v/c \quad , \quad (2.2-14)$$

which means that the surface shall be sampled with at least 18 points per period of the surface variation.

The next problem to consider is the accuracy of the input points. The tabulated surface option is useful if the surface has been measured or if it is the result of another program, for example shaping or thermal analysis software. In both cases the accuracy of the input numbers is finite. Assume that the input is given with n significant digits. The maximum relative round-off error is then

$$\varepsilon = 5 \cdot 10^{-n} . \quad (2.2-15)$$

Again the second order derivative is the most critical and one finds from (2.2-7) under worst case combinations

$$\frac{d^2z}{dx^2} \cong \frac{1}{h^2} [f(x+h) + f(x-h) - 2f(x) + 4\varepsilon f'(x)] \quad (2.2-16)$$

and the expression (2.2-12) for a sinusoidal variation is changed to

$$\frac{d^2z}{dx^2} \cong -ak_s^2 \sin k_s x \left[1 - \frac{1}{12} h k_s^2 - \frac{4\varepsilon}{h k_s^2} \right] \quad (2.2-17)$$

where the third term represents the round-off error. Requiring this term to be less than one per cent gives

$$h k_s > 20\sqrt{\varepsilon} \quad (2.2-18)$$

or

$$h / \lambda_s > 7 \cdot 10^{-n/2} . \quad (2.2-19)$$

If the input values are given with six significant figures ($n = 6$) the expressions (2.2-14) and (2.2-19) show that input spacing in the interval

$$0.007 < h / \lambda_s < 0.055 \quad (2.2-20)$$

will ensure that discretization errors as well as round-off errors are less than one per cent.

In many cases the surface shape is very smooth such that we can assume that the period of the surface variation is $\lambda_s = 2D$,

where D is the diameter of the reflector. The above criteria then lead to the following rules

$$h \leq 0.11 D \quad (2.2-21)$$

and

$$h > 14 \cdot 10^{-n/2} D \quad (2.2-22)$$

which cannot be met unless there are at least five significant digits ($n = 5$) in the input values.

It should be noted that the above analysis is related to GO/GTD calculations where the second order derivatives play an important role. If the antenna is analysed only by PO the spacing of the input data is much less critical. First of all the round-off errors can be neglected. For the discretization errors the rule given by (2.2-21) still applies for the modelling of a smooth reflector. If the problem is to model more rapid but small surface distortions, the experience has shown that five points per period of the distortions are sufficient.

2.2.1.1.8 *Tabulated rotationally symmetric surface*

The surface shape is given by

$$z = F(\rho), \quad \rho = \sqrt{x^2 + y^2} \quad (2.2-23)$$

where $F(\rho)$ is given at discrete points - not necessarily equidistant - along a radius. The comments in the previous section concerning the spacing and accuracy of the input points also apply to this type of input.

The surface may have a tip at the centre. The surface shape is obtained by cubic interpolation between the input points, as described in Section 4.3.1. The first three input points define a parabola which will define the shape of the tip at the centre. It is possible to force the surface to be smooth across the centre point. This is simply done by duplicating the first input point to the other side of the rotation axis. If the first input point is

directly on the axis it is the second input point that is duplicated.

2.2.1.1.9 *Surface expressed by cubic spline functions*

When the surface is expressed by cubic spline functions the surface shape is given by

$$z = \sum_{i=1}^{NX} \sum_{j=1}^{NY} c_{ij} B_{ij}(x, y) , \quad \begin{array}{l} x_{\min} \leq x \leq x_{\max} \\ y_{\min} \leq y \leq y_{\max} \end{array} \quad (2.2-24)$$

where B_{ij} are so-called bi-cubic B-splines and c_{ij} are so-called spline coefficients. The splines are normalised such that if all the coefficients in (2.2-24) have the same value, $c_{ij} = q$, then the function will be constant, $z = q$. Each spline function is only non-zero over a part of the reflector which makes the expansion an efficient choice in reflector shaping. Examples of bi-cubic B-splines are shown in Figure 2.2-6 and Figure 2.2-7.

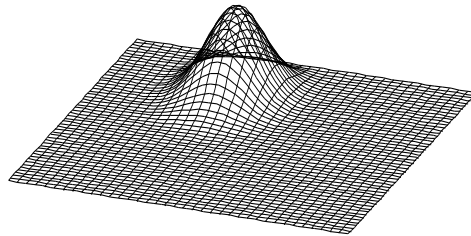


Figure 2.2-6 Example of a single bi-cubic B-spline function.

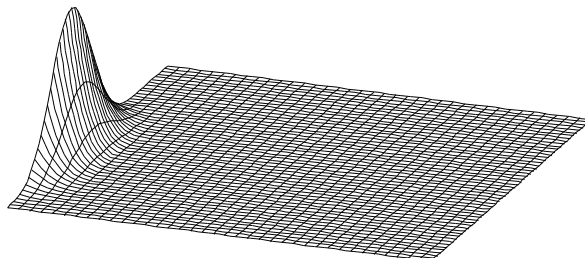


Figure 2.2-7 Example of a bi-cubic B-spline close to one of the edges.

The bi-cubic B-spline is defined by

$$B_{ij}(x, y) = B_i(x) \cdot B_j(y) \quad (2.2-25)$$

where B_i is a cubic B-spline.

The cubic B-spline is associated with a so-called knot-sequence, which is a sequence of M points t_1, t_2, \dots, t_M , $-\infty < t_1 < t_2 < \dots < t_M < \infty$. It is a third-order polynomial in each of the $M-1$ knot-intervals. Further, the polynomial pieces are joined in such a way that the cubic B-spline has continuous first and second order derivatives with respect to x .

The cubic B-spline has further the following three properties:
i) The B-spline No. k , $B_k(x)$, is uniquely defined from the location of the five knots $t_{k-2}, t_{k-1}, t_k, t_{k+1}, t_{k+2}$; ii) $B_k(x)$ is identical zero for $x \leq t_{k-2}$ and for $x \geq t_{k+2}$; iii) $B_k(x)$ is positive for $t_{k-2} < x < t_{k+2}$.

More precisely, the cubic B-spline is defined as (Boor, 1978)

$$B_k(x) = \frac{1}{t_{k+2} - t_{k-2}} \sum_{m=k-2}^{k+2} \frac{(x - t_m)^3}{\omega_k(t_m)} , \quad t_1 \leq x \leq t_M \quad (2.2-26)$$

with

$$(x - t_m)_+^3 = \begin{cases} 0, & x < t_m \\ (x - t_m)_+^3, & x \geq t_m \end{cases} \quad (2.2-27)$$

and

$$\omega_k(x) = \prod_{l=k-2}^{k+2} (x - t_l) \quad (2.2-28)$$

The interpolated function is a summation of the cubic B-splines and between any 2 knots four B-splines will contribute according to property (ii) above. In order to have four B-splines also at the ends of the x - and y -intervals additional knots are introduced here.

In GRASP, it has been chosen to place the M knots t_1 through t_M equidistantly within $t_1 = x_{\min}$ and $t_M = x_{\max}$. The additional end-knots are chosen as $t_{-2} = t_{-1} = t_0 = t_1$ at x_{\min} and $t_{M+3} = t_{M+2} = t_{M+1} = t_M$ at x_{\max} . A B-spline function with equispaced knots is shown in Figure 2.2-8. The B-spline functions near $x = x_{\max}$ are shown in Figure 2.2-9.

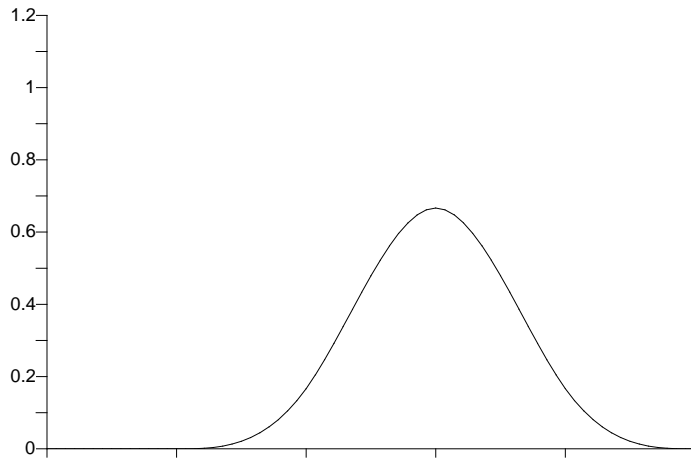


Figure 2.2-8 Example of B-spline function based on equispaced knots (the marks on the x -axis).

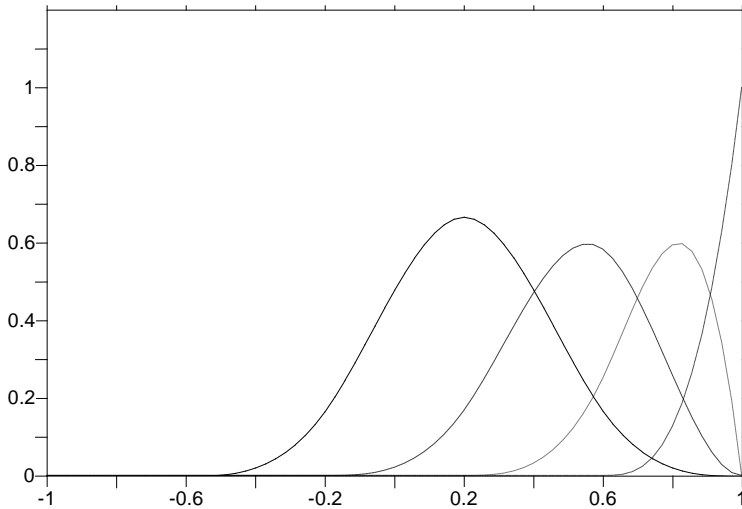


Figure 2.2-9 End-B-splines, when the three extra knots are placed at the end-knot at $t_M = x_{\max} = 1$. The other knots are equispaced with spacing 0.4.

A spline function associated with the M knots t_1 through t_M has $M+2$ independent unknowns. Thus, when a spline surface with NX coefficients in x is requested in GRASP, the associated knot sequence has $M = NX-2$ knots (excluding the 6 additional end-knots). This in turn means that the spline consists of $NX-3$ polynomial pieces between the equispaced knots. The same applies for the specification along y .

2.2.1.1.10 Surface expressed by Zernike modes

Zernike polynomial expansion is an efficient means to describe a moderately shaped reflector surface. The Zernike polynomials are used in optics for the investigation of aberrations (see e.g. Born and Wolf, 1983). They are used in TICRA's shaping software package POS (Physical Optics Shaping) (Sørensen et al. (1999)). The applicability of the Zernike modes for reflector surface distortion analyses is described by Pontoppidan (1986). For large contoured beam antennas where a highly shaped surface is needed, the Zernike polynomials may result in unnecessarily large surface variations. It is instead

recommended to describe the surface by cubic splines as shown in Section 2.2.1.1.9.

The Zernike polynomials are in general complex valued functions. In the present context we are interested in the real part only and each mode may then be written

$$Z_n^m(x, y) = a_n^m R_n^m(\rho) \cos(m\phi - \phi_n^m) \quad (2.2-29)$$

where a_n^m is the amplitude and ϕ_n^m is a reference direction. The radial function $R_n^m(\rho)$ is a polynomial in ρ containing the powers $\rho^m, \rho^{m+2}, \dots, \rho^n$. The Zernike polynomials are orthogonal over the unit circle:

$$\iint_{x^2+y^2 \leq 1} Z_n^m Z_{n'}^{m'} dx dy = \begin{cases} \frac{\pi}{n+1} \delta_{nn'} & , m = m' = 0 \\ \frac{\pi}{2(n+1)} \delta_{nn'} & , m = m' \neq 0 \\ 0 & , m \neq m' \end{cases} \quad (2.2-30)$$

The orthogonality relation in (2.2-30) implies that

$$\int_0^1 R_n^m(\rho) R_{n'}^{m'}(\rho) \rho d\rho = \frac{1}{2(n+1)} \delta_{nn'} \quad , \quad (2.2-31)$$

where δ_{ij} is the Kronecker symbol. A useful relation between $R_n^m(\rho)$ and the Bessel function is given by

$$\int_0^1 R_n^m(\rho) J_m(\nu\rho) \rho d\rho = -1^{\frac{n-m}{2}} \frac{J_{n+1}(\nu)}{\nu} \quad (2.2-32)$$

The polynomials $R_n^m(\rho)$ are listed in Table 2.2-1 for $m \leq 8$ and $n \leq 8$ (from Born and Wolf, 1983). The functions are normalised such that $R_n^m(1) = 1$.

The Zernike polynomials are characterised by the fact that they are not only polynomials for the radial dependence $R_n^m(\rho)$ but they are also polynomials in x and y . Inserting $x = \rho \cos \phi$ and $y = \rho \sin \phi$ in the polynomials in Table 2.2-1 one finds for the lowest order modes:

$$Z_0^0 = 1$$

$$Z_2^0 = 2\rho^2 - 1 = 2(x^2 + y^2) - 1$$

$$Z_4^0 = 6\rho^4 - 6\rho^2 + 1 = 6(x^2 + y^2)^2 - 6(x^2 + y^2) + 1 \quad (2.2-33)$$

$$Z_1^1 = \rho \cos \phi = x$$

$$Z_3^1 = (3\rho^3 - 2\rho) \cos \phi = 3x^3 + 3y^2x - 2x$$

$$Z_2^2 = \rho^2 \cos 2\phi = x^2 - y^2$$

The modes $m = n = 1$ and $m = 0, n = 2$ represent a tilt and an axial defocusing, respectively. The modes for which $m + n = 4$ are the primary aberrations in optical systems:

$m = 0, n = 4$: spherical aberration

$m = 1, n = 3$: coma

$m = 2, n = 2$: astigmatism

The radial dependence of $R_n^m \rho$ for the first six modes in n is depicted graphically in Figure 2.2-10 for $0 \leq m \leq 5$. Three-dimensional plots of some of the Zernike polynomials are shown in Figure 2.2-11.

$\begin{array}{c} n \\ \diagdown \\ m \end{array}$	0	1	2	3	4	5	6	7	8
0	1	$2\rho^2 - 1$		$\frac{6\rho^4}{6\rho^2 + 1}$		$\frac{20\rho^6}{30\rho^4 + 12\rho^2 - 1}$			$\frac{70\rho^8}{140\rho^6 + 90\rho^4 - 20\rho^2 + 1}$
1		ρ		$\frac{3\rho^3}{2\rho}$		$\frac{10\rho^5}{12\rho^3 + 3\rho}$		$\frac{35\rho^7}{60\rho^5 + 30\rho^3 - 4\rho}$	
2		ρ^2		$\frac{4\rho^4}{3\rho^2}$		$\frac{15\rho^6}{20\rho^4 + 6\rho^2}$			$\frac{56\rho^8}{105\rho^6 + 60\rho^4 - 10\rho^2}$
3			ρ^3		$5\rho^5 - 4\rho^3$			$\frac{21\rho^7}{30\rho^5 + 10\rho^3}$	
4				ρ^4		$6\rho^6 - 5\rho^4$			$28\rho^8 - 42\rho^6 + 15\rho^4$
5					ρ^5			$7\rho^7 - 6\rho^5$	
6						ρ^6			$8\rho^8 - 7\rho^6$
7							ρ^7		
8									ρ^8

Table 2.2-1 Table of the radial polynomials $R_n^m(\rho)$ for $m \leq 8$ and $n \leq 8$. From Born and Wolf (1983).

Per default the input to GRASP takes place by specifying the amplitudes a_n^m and the reference directions ϕ_n^m . However, earlier versions of the TICRA shaping program used a slightly different formulation in which (2.2-29) is written in terms of odd and even modes by using the trigonometric addition formulas:

$$\begin{aligned}
 a_n^m R_n^m \rho \cos m\phi - \phi_n^m &= a_n^m R_n^m \rho \\
 \cos m\phi \cos(m\phi_n^m) + \sin m\phi \sin(m\phi_n^m) &= \\
 a_n^m \cos(m\phi_n^m) R_n^m \rho \cos m\phi & \\
 + a_n^m \sin(m\phi_n^m) R_n^m \rho \sin m\phi &
 \end{aligned} \tag{2.2-34}$$

It is therefore also possible to input Zernike mode coefficients given on this form to GRASP.

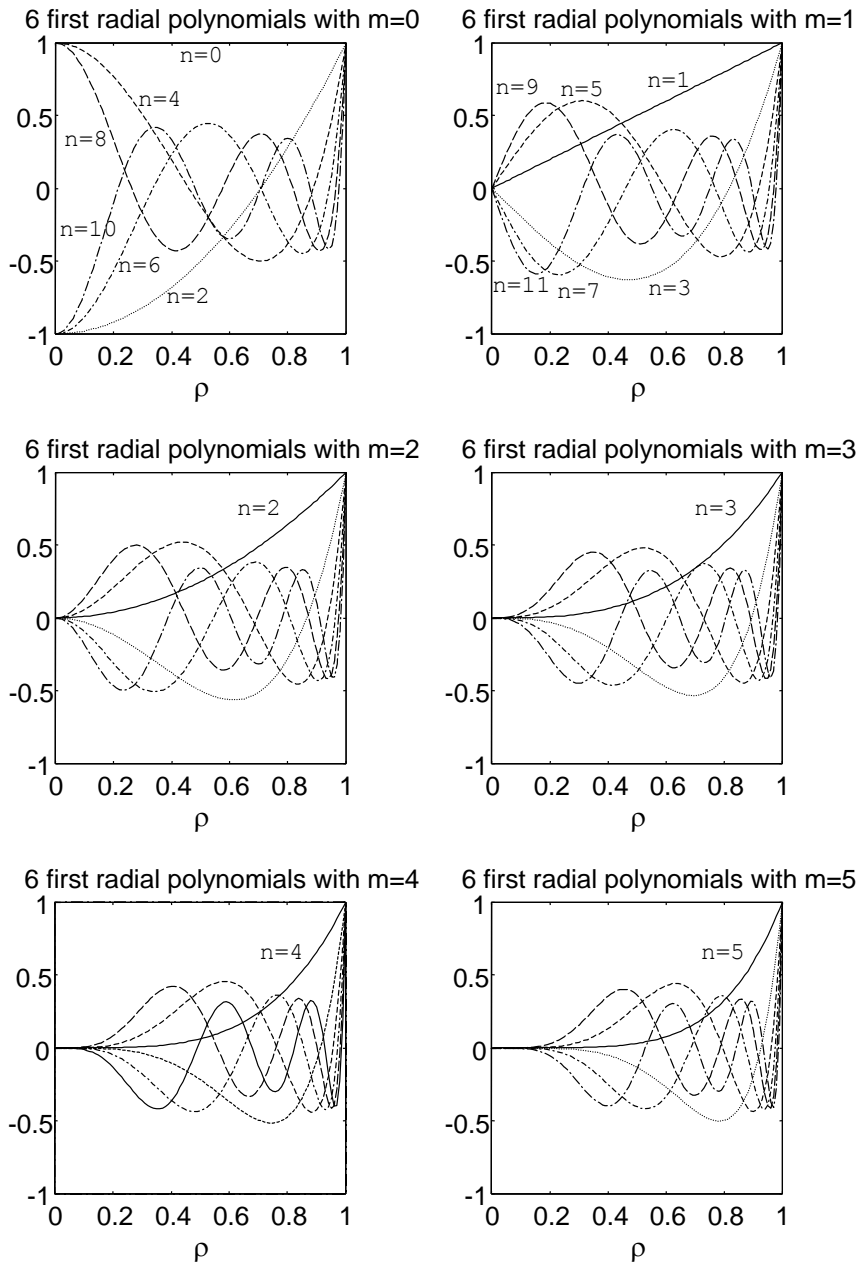


Figure 2.2-10 Graphical representation of $R_n^m(\rho)$.

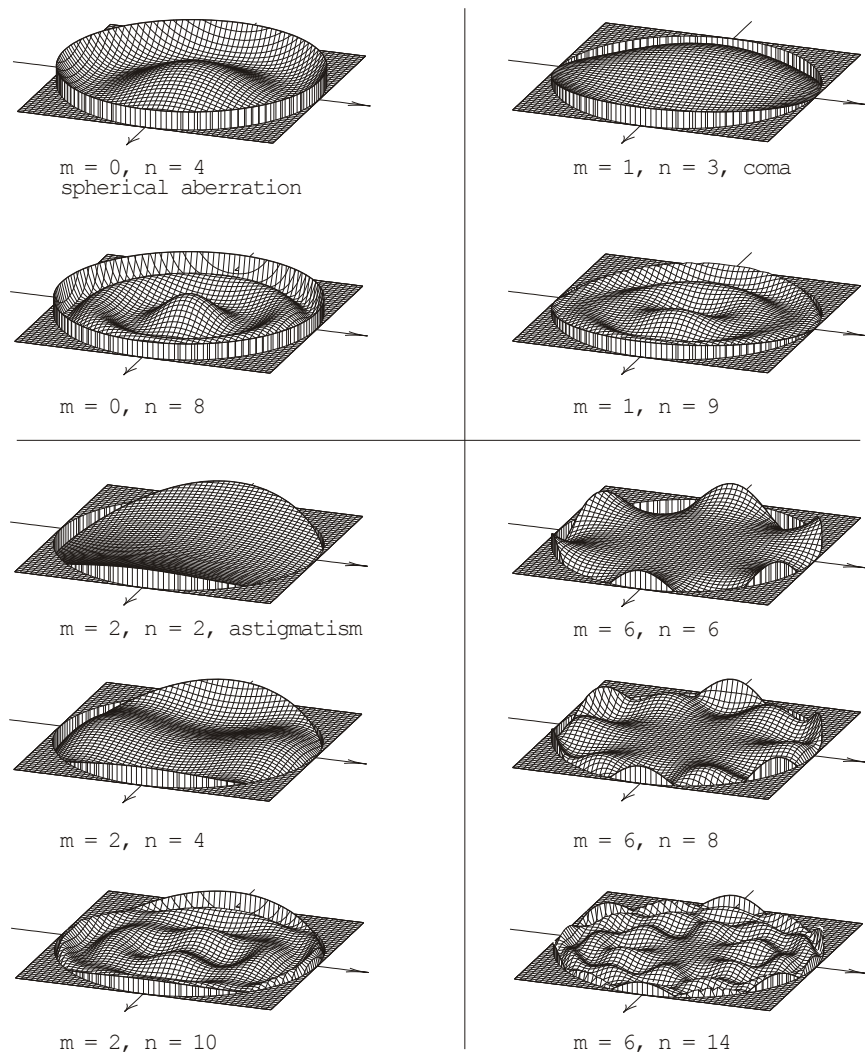


Figure 2.2-11 Samples of Zernike modes for surface representation.

2.2.1.1.11 *Surface expressed by random values in a regular grid*

This surface option is primarily used to model reflector distortions. It is possible to model slowly varying errors which are typical for thermal distortions as well as rapidly varying errors which are more typical for manufacturing tolerances or a finite measurement accuracy. The following example illustrates this further.

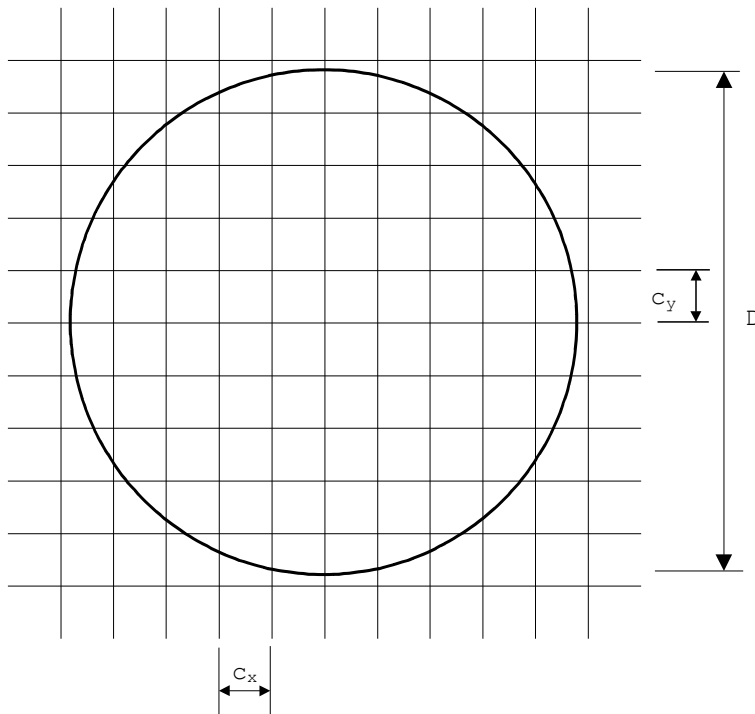


Figure 2.2-12 Grid for reflector distortions definition.

A rectangular grid covering the reflector aperture is introduced, as shown in Figure 2.2-12 for a circular aperture. The surface values at the nodes of the grid are selected as random numbers uniformly distributed in a given interval (the peak-to-peak value) and with a mean value equal to zero. A cubic interpolation function, see Section 4.3.1, yields a smooth surface between the random values at the nodes. The spacing between the nodes, c_x and c_y , relative to the reflector diameter, D , determines the roughness of the surface. This is illustrated in Figure 2.2-13 which shows typical surface distortions for $c_x/D = c_y/D = 0.4, 0.2, 0.1$ and 0.05 . The correlation distance is $2c_x$ in the x -direction and $2c_y$ in the y -direction, meaning that within an elliptical area of diameter $2c_x$ by $2c_y$ the surface distortions are correlated, whereas they are completely uncorrelated for larger distances.

The rms-value of the distortions is the selected peak-to-peak value times 0.24.

Random errors on the reflector surface will scatter the field from the forward direction into the side lobe region thus reducing the peak gain and increasing the side lobes. Slowly varying distortions will affect the antenna pattern near the main beam and the first side lobes and these errors are therefore important for antennas with stringent side lobe requirements.

For rapid surface variations the field is scattered into a wider angular region but at a lower amplitude. However, the value of c_x or c_y should not be selected smaller than one half electrical wavelength for the scattered fields to remain in the visible region of space.

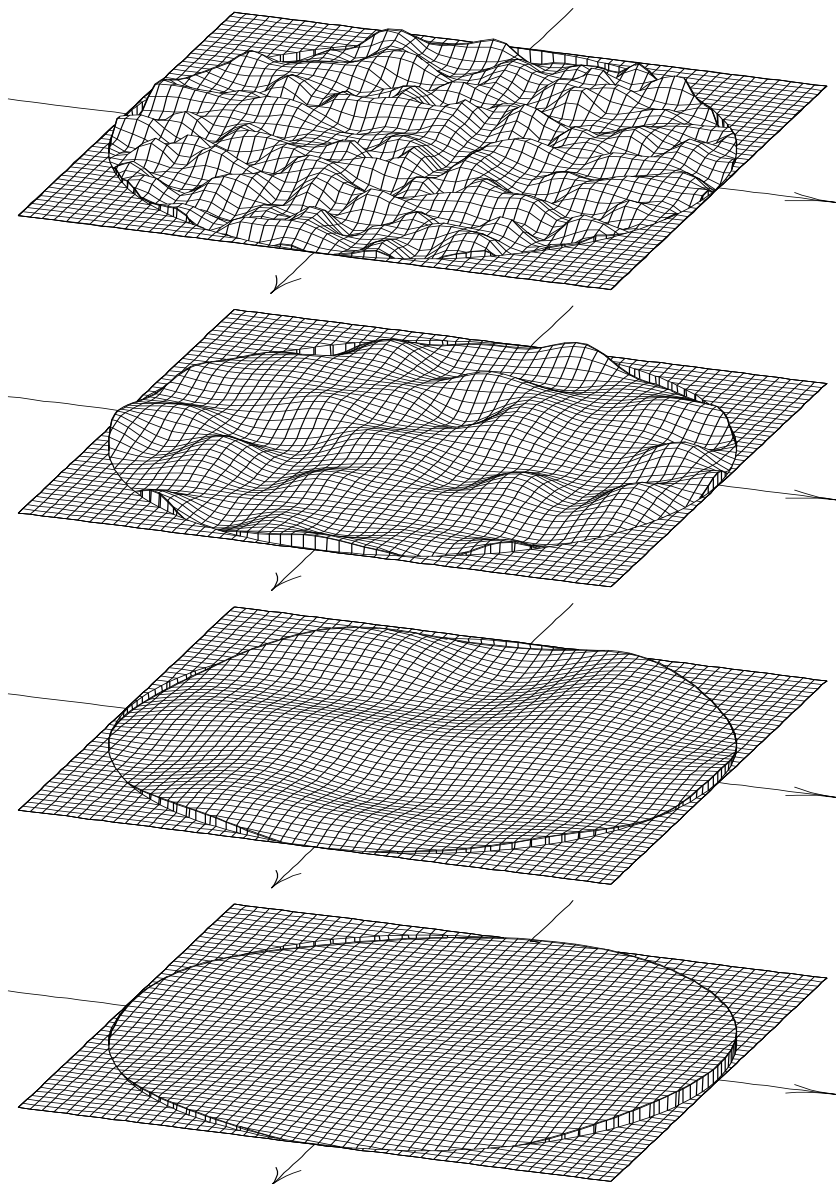


Figure 2.2-13 Typical random surface shapes for different values of $c_x/D = c_y/D$.
Top: $c_x/D = c_y/D = 0.05$
Below top: $c_x/D = c_y/D = 0.1$
Above bottom: $c_x/D = c_y/D = 0.2$
Bottom: $c_x/D = c_y/D = 0.4$.

2.2.1.1.12 Surface given by irregularly spaced points

The result of a thermal analysis will often generate a number of surface points which are not arranged in a regular grid with constant spacing in x and y . The surface can also be given as a result of a photogrammetric measurement. In both cases the points are more or less irregularly spaced and special interpolation is needed. Two interpolation methods are available in GRASP, the one is based on quintic pseudo splines and the other on triangulation as described briefly in the following.

The quintic pseudo splines is a global approach developed by Bergmann et al. (1994). The pseudo spline solution was originally introduced to solve the problem of minimising a functional description of the energy associated with a thin plate flexed to occupy previously defined positions. The requirement of continuous second order derivatives results in the expression:

$$z(x, y) = \sum_{i=1}^N a_i r_i(x, y)^5 + b_1 x^2 + b_2 xy + b_3 y^2 + b_4 x + b_5 y + b_6 \quad (2.2-35)$$

where N is the number of data points x_i, y_i, z_i and

$$r_i(x, y) = \sqrt{(x - x_i)^2 + (y - y_i)^2} . \quad (2.2-36)$$

The coefficients a_i are found by point matching at the input points and requiring in addition

$$\begin{aligned} \sum_{i=1}^N a_i x_i^2 &= 0, & \sum_{i=1}^N a_i x_i y_i &= 0, & \sum_{i=1}^N a_i y_i^2 &= 0, \\ \sum_{i=1}^N a_i x_i &= 0, & \sum_{i=1}^N a_i y_i &= 0, & \sum_{i=1}^N a_i &= 0, \end{aligned} . \quad (2.2-37)$$

Expressions (2.2-37) result from forcing the second order derivatives to remain finite (Bergmann et al. (1994)).

The $N + 6$ coefficients are found directly by the LAPACK symmetric matrix operation routines calculating the inverse

matrix. Note that the surface must be given in at least six points (due to the six b -coefficients) to solve the linear system of equations. The coefficients are used directly in GRASP not only for the surface function value itself but also for the first and second order derivatives without going to an intermediate regular grid.

The quintic pseudo splines is a global approach meaning that a change in one of the input points will affect the shape over the entire surface. The matrix inversion involved in the quintic pseudo splines means that if the number of input points is very large the computer time may become a problem. In that case the triangulation method described in the following may be preferable.

In the triangulation approach all the input points are connected by straight lines in such a way as to form a mesh of triangles as uniform as possible. The first and second order derivatives at each corner are then found using all input points weighted with the inverse distance to the corner point. In each triangle a fifth order polynomial is fitted to the input data subject to the requirement that the surface value and the first and second order derivatives become smooth from one triangle to the neighbouring triangles. It is alternatively also possible to require that the surface is planar within each triangle.

The quintic pseudo splines and the triangulation method will be illustrated by a simple example. Assume that a spherical offset reflector of diameter $D = 1$ m is manufactured. The reflector is supplied with 176 target points as shown in Figure 2.2-14.

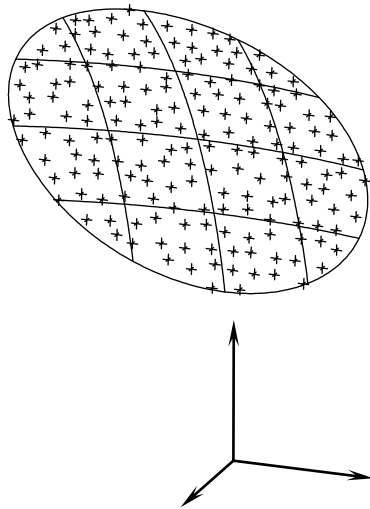


Figure 2.2-14 Spherical reflector supplied with 176 target points.

The position of each target point is now measured and in this example it is assumed that the reflector shape is exactly spherical and that the measurement accuracy is infinite. It is therefore possible to compare the reflector surface modelled as a sphere as described in Section 2.2.1.1.6 with the quintic pseudo splines and the triangulation. The results are shown in Figure 2.2-15 and Figure 2.2-16, respectively. It is clearly visible that the quintic pseudo splines give a more accurate and smooth representation of the surface shape.

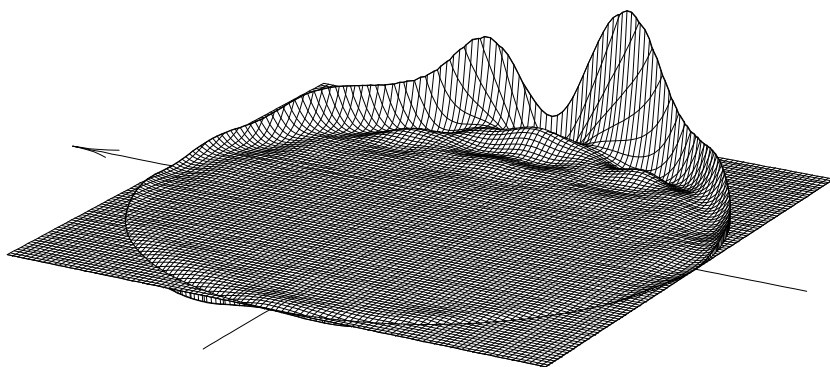


Figure 2.2-15 Accuracy of the quintic pseudo splines when using the irregular points in Figure 2.2-14 as input. The z -values are scaled by a factor 3,000.

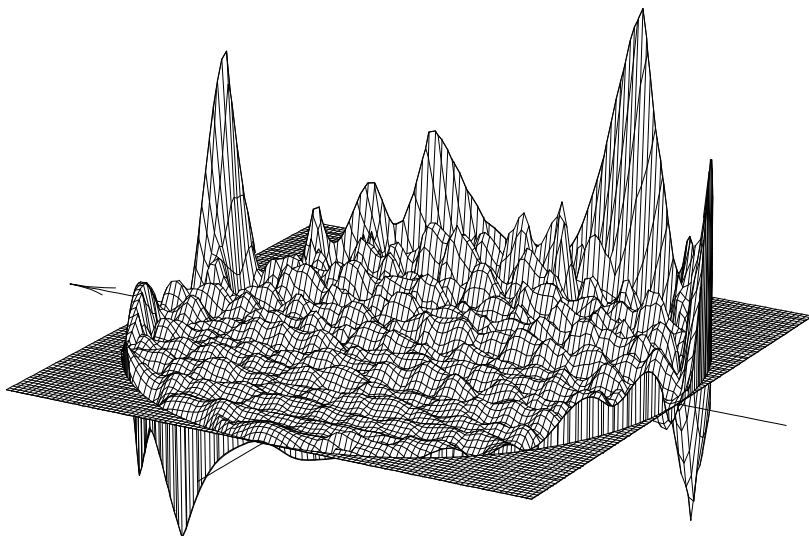


Figure 2.2-16 Accuracy of the triangulation method when using the irregular points in Figure 2.2-14 as input. The z -values are scaled by a factor 3,000.

The triangulation for the input points in Figure 2.2-14 are shown in Figure 2.2-17. The figure shows that there is an area between the outer triangles and the reflector rim where no triangles exist. In this area it is therefore necessary to calculate the surface by extrapolation from the nearest triangle and, especially if the rim points are located nearly on a straight line, this can give rise to very oblong triangles and extrapolation errors. It may be better to remove these triangles. In GRASP this is done by requiring that if the altitude is smaller than a certain fraction of the base the triangle is removed. An example is shown in Figure 2.2-18 where this fraction is selected to 0.2.

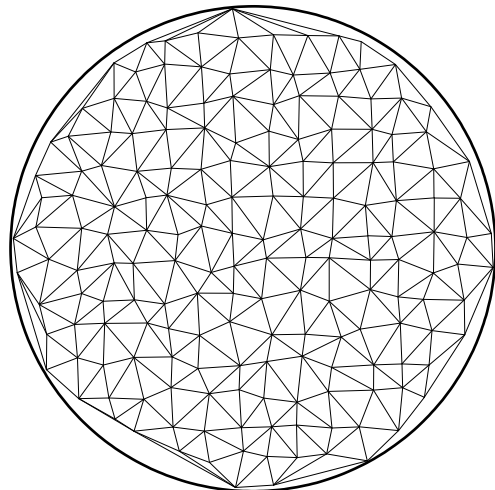


Figure 2.2-17 Triangulation for the input points shown in Figure 2.2-14

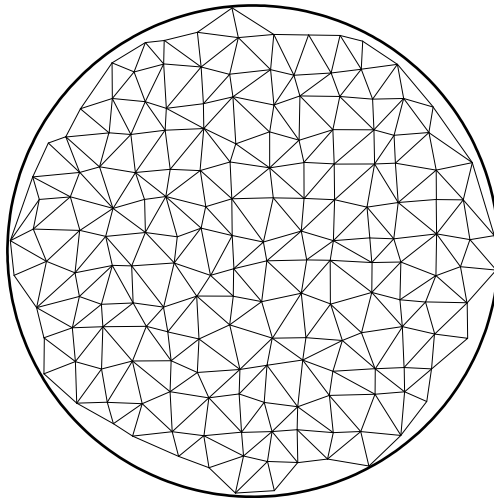


Figure 2.2-18 Triangulation for the input points shown in Figure 2.2-14. Oblong triangles along the edge are removed.

In general the quintic pseudo splines are to be preferred. If the reflector has been measured by an automatic measurement procedure the number of input data may be very large and often much larger than what is actually necessary to describe the surface variation. Instead of using the triangulation method it may then be better to reduce the number of input points and use the quintic pseudo splines.

2.2.1.1.13 *Mesh surface with ribs*

This surface option is used to model an unfurlable rib reflector where the surface material is a tricot mesh. A tricot mesh behaves as a membrane with no bending stiffness and only in-plane tensions. The mesh is attached continuously along the supporting ribs which are part of a parent paraboloid. The mesh surface shape in the area between the ribs is determined as illustrated in Figure 2.2-19.

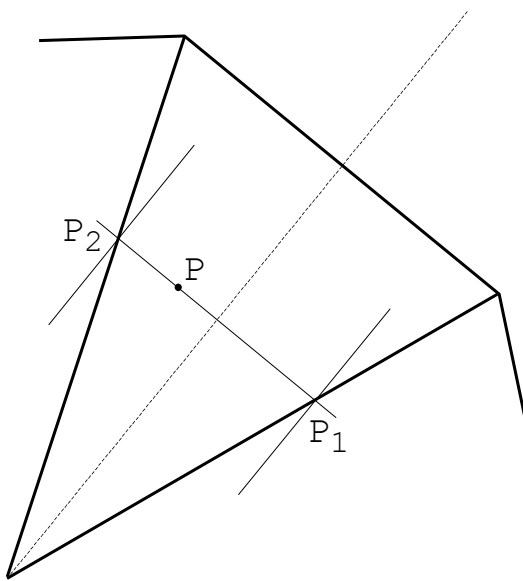


Figure 2.2-19 Gore section of radial rib surface.

A line through a point P orthogonal to the centre line of the gore cuts the ribs in the points P_1 and P_2 . The circle of curvature to the ribs is introduced at P_1 and P_2 . Next, these two circles are rotated around the rib normal such that they become parallel to the centre plane of the gore. Finally, the rib surface along the line from P_1 to P_2 is approximated as the surface of a membrane between these two parallel circular discs.

The surface deviations from the parent paraboloid are illustrated in Figure 2.2-20.

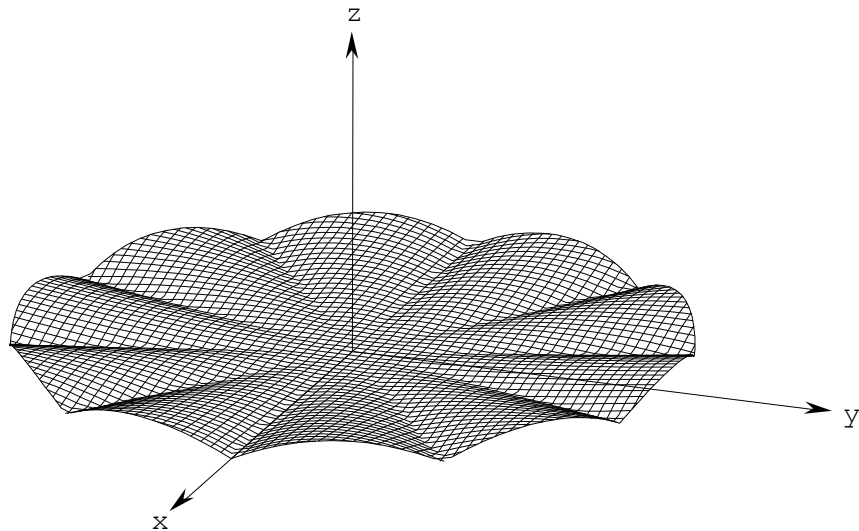


Figure 2.2-20 Surface deviations from paraboloid for radial rib antenna.

The gores sections in Figure 2.2-20 give rise to increased side lobes, the so-called gore lobes. The gore lobes do not affect the pattern near the main beam and the first side lobes, but they appear at an angle given approximately by

$$\sin \theta_g = \frac{N_g}{\pi} \frac{D/\lambda}{ } \quad (2.2-38)$$

where

N_g = number of ribs (or gores)

D = reflector diameter

λ = wavelength

with an amplitude which depends on N_g and D/λ . The gore lobes are approximately rotationally symmetric around the main beam axis.

NOTE: The surface can only be used in a PO calculation and not with GTD, since the second order derivatives of the surface are undefined at the ribs.

2.2.1.1.14 Mesh surface for unfurlable truss antenna

The reflector aperture of an unfurlable truss (3D-scissors) antenna is sketched in Figure 2.2-21. The nodes are located in a triangular lattice. Since a mesh has a very small bending stiffness, it behaves like a membrane; it can carry no compression. Furthermore the tension must be reasonably uniform and isotropic in order to assure good electrical conductivity (and, hence, rf reflectivity) of the mesh.

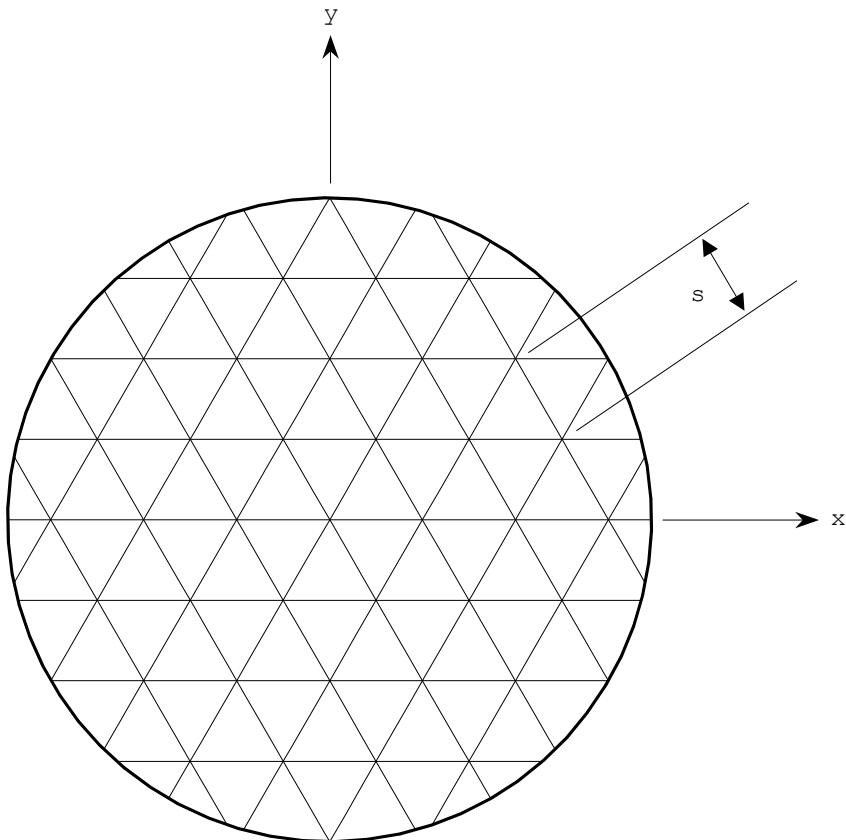


Figure 2.2-21 Truss (3D-scissors) concept.

A bi-axially tensioned membrane with no lateral loading must have zero mean curvature. Thus, if the curvature in one direction is positive, the curvature in the other direction must be negative, and the surface shape will satisfy the Laplace equation, $\Delta\phi = 0$.

A computer program for solving two-dimensional Laplacian problems with general boundary conditions has been applied to the problem. Figure 2.2-22 shows an elementary triangular facet with vertices Q_1 , Q_2 and Q_3 . These three points define a plane, $\phi = 0$. The mesh is attached to small circular plates at each lattice node, and the boundary condition is therefore $\phi = 0$ along these. The neighbour points P_1 , P_2 and P_3 will be out of the plane $\phi = 0$ and if the height at P_1 is ϕ_1 the normal derivative along the side $Q_1 Q_2$ will be

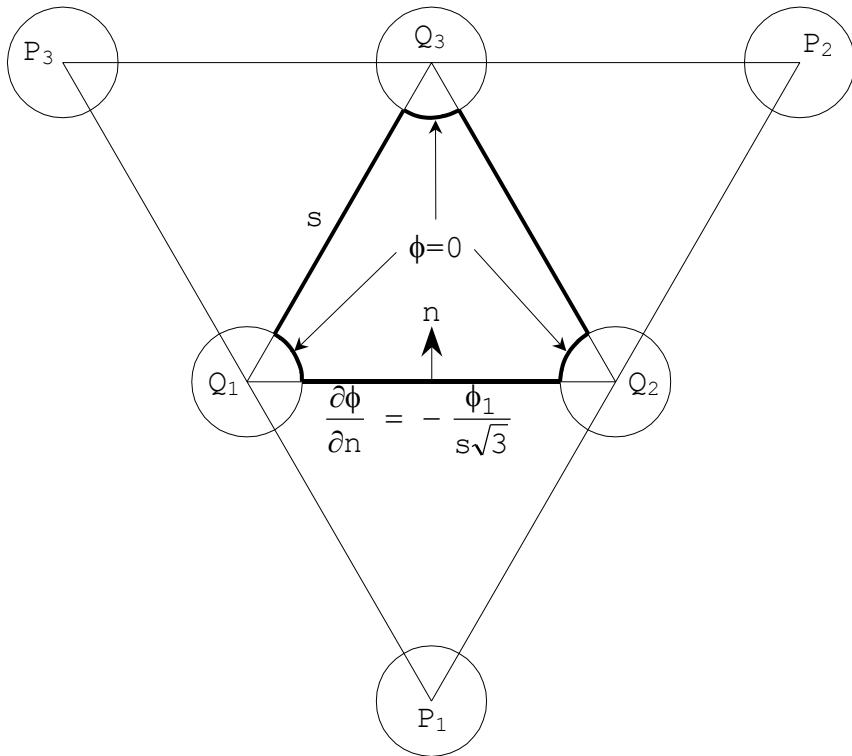


Figure 2.2-22 Triangular facet with neighbours.

$$-\frac{\phi_1}{s\sqrt{3}} \quad (2.2-39)$$

where s is the side length of the triangular element, and similarly for the two other sides. In this way the boundary value problem is specified and the mesh surface can be determined. For the solution implemented in GRASP the radius of the small circular plates is fixed to $s/20$. This solution is included

in the software and in this way a very fast description of the complicated surface is achieved. An example of the surface deviation from the parent paraboloid is illustrated in Figure 2.2-23.

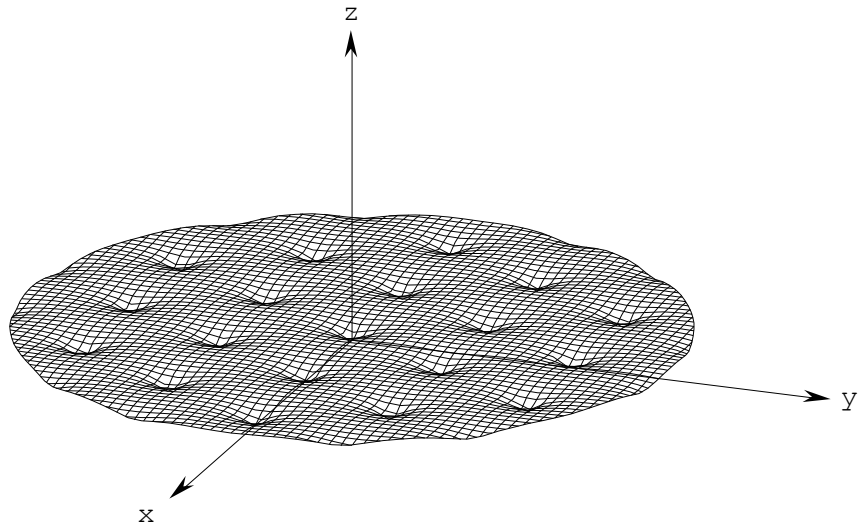


Figure 2.2-23 Surface deviations from paraboloid for truss (3D-scissors) antenna.

The two-dimensional periodic structure of the surface in Figure 2.2-23 gives rise to grating lobes at

$$\sin \theta_g = \frac{2\lambda}{s} \quad (2.2-40)$$

in the $\phi = 0^\circ + p \cdot 60^\circ$ planes and at

$$\sin \theta_g = \frac{2\lambda}{\sqrt{3}s} \quad (2.2-41)$$

in the $\phi = 30^\circ + p \cdot 60^\circ$ planes. The grating lobes closest to the main beam are given by the last expression and it is reasonable in a design procedure to require that the grating lobes fall outside the region of interest for the particular application. Introducing the reflector diameter D yields

$$\frac{s}{D} = \frac{2}{\sqrt{3} D / \lambda \sin \theta_g} \quad (2.2-42)$$

which gives the node distance relative to the diameter s/D as a function of the grating lobe position θ_g and D/λ .

NOTE: The surface can only be used in a PO calculation and not with GTD, since the second order derivatives of the surface are undefined at the rim of the attachment buttons .

2.2.1.2 *Reflector rims*

The rim of a reflector is defined as the intersection between the reflector surface (including possible distortions) and a cylinder in the z -axis direction with a cross section given in the xy -plane. Note, that both the reflector and the rim are defined in the same coordinate system, the reflector coordinate system.

The various built-in reflector rim options are described in the following sections.

2.2.1.2.1 *Circular or elliptical rim*

This rim shape is given by

$$\left(\frac{x - x_c}{a}\right)^2 + \left(\frac{y - y_c}{b}\right)^2 = 1 \quad (2.2-43)$$

where the centre x_c, y_c and the half axes a and b are given by input. It is possible to rotate the ellipse an arbitrary angle.

2.2.1.2.2 *Rectangular rim*

A rectangular reflector rim is given by the centre, the side lengths and a possible rotation.

The sides of the rim are numbered from 1 to 4 in the positive direction of rotation in the xy -plane. The numbering is important when PTD or GTD is employed in the field analysis.

When the rectangular rim class is applied in PO calculations the PO integration grid is automatically selected to conform with the rectangular boundary, as described in Section 3.1.2.2.

2.2.1.2.3 *Triangular rim*

A triangular rim may be useful for modelling special reflector shapes such as the details of a serrated reflector for a compact range in which case a triangular rim shall be modelled for each tooth of the serrations. The triangular rim is specified by the position of the three corners when projected into the xy -plane.

The sides of the triangular rim are numbered from 1 to 3. This has importance for the application of PTD and GTD. When applying PO the integration grid will automatically fit to the triangular boundary as described in Section 3.1.2.3.

2.2.1.2.4 *Superelliptical rim*

This type of rim is included to allow the modelling of a rectangular reflector with rounded corners. The general expression is

$$\left| \frac{x - x_c}{a} \right|^m + \left| \frac{y - y_c}{b} \right|^m = 1 \quad (2.2-44)$$

where the centre x_c, y_c , the half axes a and b and the exponent m are input parameters. It is possible to rotate the superellipse an arbitrary angle.

An example for $a = 2$, $b = 1$ and $m = 5$ is shown in Figure 2.2-24. It is reasonable to define the rectangularity of the superellipse by

$$r = \frac{OP}{OR} \quad (2.2-45)$$

where the points O , P and R are indicated in the figure. This rectangularity depends on m as

$$r = (0.5)^{1/m} \quad . \quad (2.2-46)$$

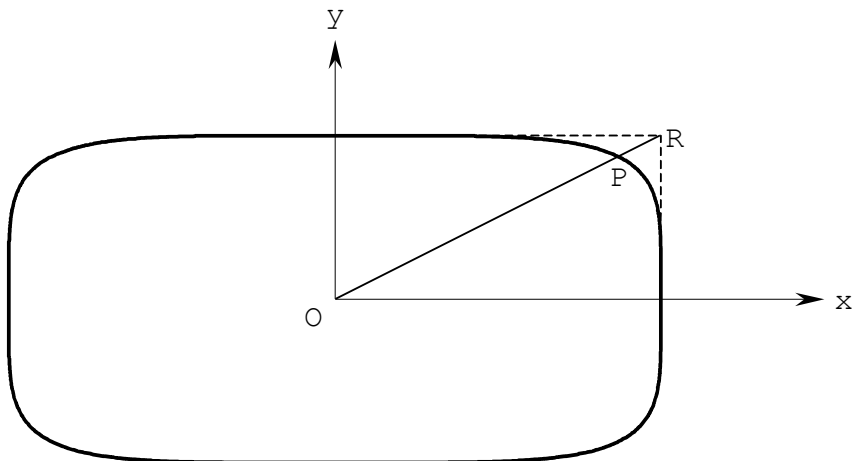


Figure 2.2-24 Superelliptical aperture
 $a = 2, b = 1, m = 5.$

2.2.1.2.5 Tabulated rim

The edge may be defined by a number of points given in the xy -plane of the reflector coordinate system. The points may be specified in rectangular xy -coordinates or in polar $\rho\phi$ -coordinates. In the first case the points are converted to a polar representation internally in the program. It is therefore necessary in both cases to specify an internal point, θ in Figure 2.2-25, as the origin for polar representation. In the case of xy input the origin can be automatically calculated as the gravity point:

$$x_o = \frac{1}{n} \sum_{i=1}^n x_i, \quad y_o = \frac{1}{n} \sum_{i=1}^n y_i \quad . \quad (2.2-47)$$

The points may be input in arbitrary order and there are no requirements to the spacing of the input points. The polar origin must be selected such that ρ becomes a single-valued function of ϕ .

The input points defining the rim may be of two kinds, ordinary points and corner points, as illustrated in Figure 2.2-25. The part of the rim between two corner points is denoted a section. If a section contains no ordinary points the rim will be a straight line between the two corner points. If a section contains only one ordinary point the rim will be a circular arc through the three points. If a section contains more than one ordinary point the rim will be represented by a spline passing through all the ordinary points and the two end points.

The rim sections are numbered consecutively in the positive direction of rotation in the xy -plane. This numbering is useful when PTD or GTD is employed in the field analysis.

If no corner points are defined the spline interpolation makes use of a 2π periodic cubic spline routine operating directly on the input points.

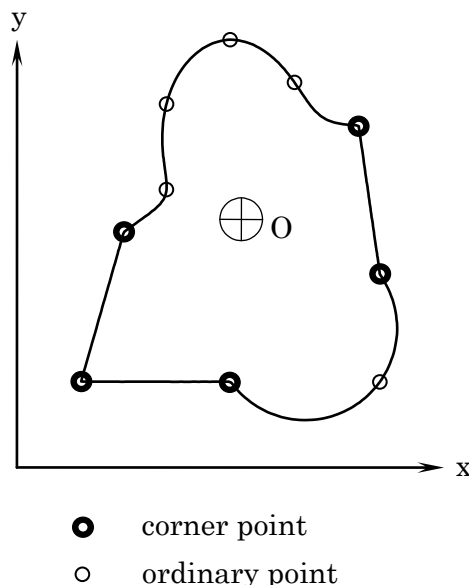


Figure 2.2-25 Example of tabulated rim curve containing ordinary as well as corner points.

The possibility to specify some of the input points as corner points may be very useful for defining irregularities to a reflector rim. An example is illustrated in Figure 2.2-26 where a small part has been removed from the circular reflector aperture.

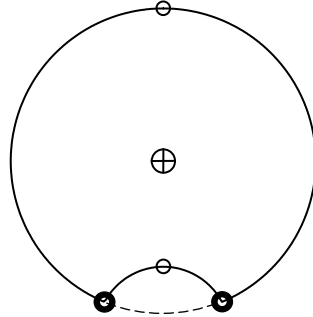


Figure 2.2-26 Circular reflector rim with circular cut-out.
The total rim is defined by four points, two ordinary points and two corner points.

2.2.1.3 Reflector with hole

It is possible to model a reflector with a circular hole. The centre of the hole is the point x_c, y_c defined for the elliptical and superelliptical rims and the origin O in Figure 2.2-25 for the tabulated rim. The reflector surface currents are set to zero inside the hole in subsequent PO calculations. The feature can be used to model central blockage from e.g. a feed horn or a subreflector, and provides an accurate estimate of the blockage in the forward direction. Note that the option is only significant for PO analysis, not GO or GTD. Also, it does not apply to reflectors with a rectangular or a triangular rim.

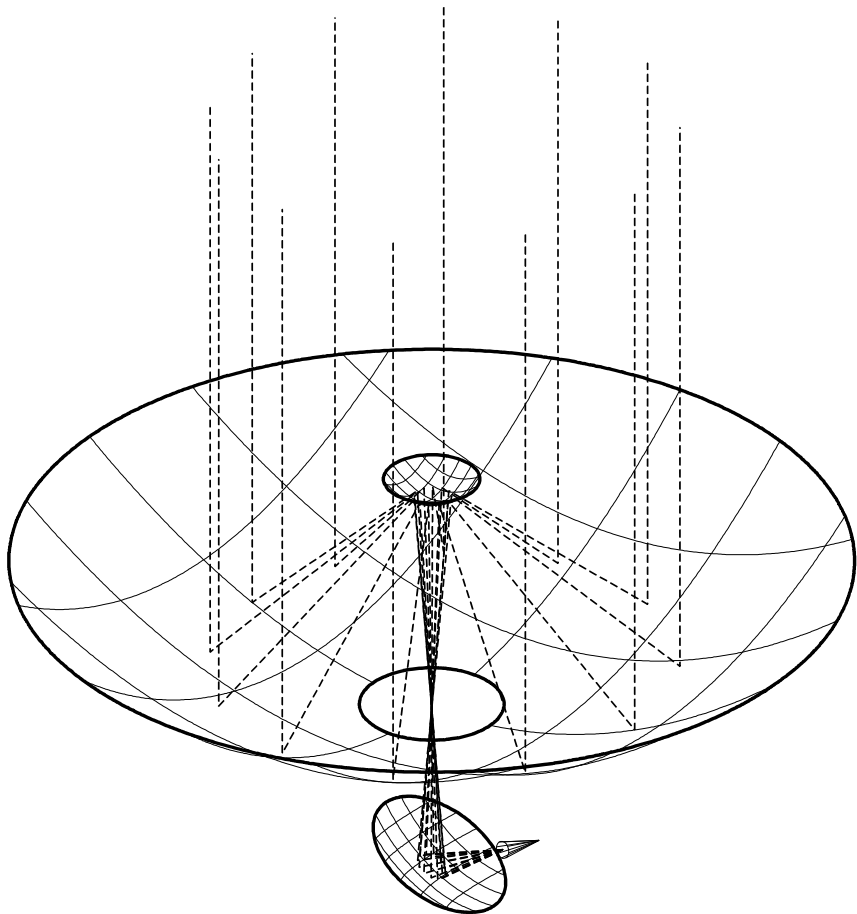


Figure 2.2-27 Rotationally symmetric dual reflector antenna illuminated from the back through a hole in the main reflector.

Figure 2.2-27 shows an example where this option is used to illuminate a rotationally symmetric antenna system by means of a very simple beam waveguide. Note, that the ray tracing procedure recognises the existence of the hole such that the rays are allowed to pass through it.

Another and more general way to treat a hole in a reflector is exemplified in Figure 2.2-28 by a rectangular reflector with a small elliptical hole. First, the rectangular reflector is defined without the hole. Next, the hole is defined as another reflector using the same surface but with the rim of the hole. The influence of the hole is now obtained by subtracting the field from

the hole from the normal reflector field without the hole. The procedure is general in the sense that the hole can be located anywhere and all the reflector rim options are available.

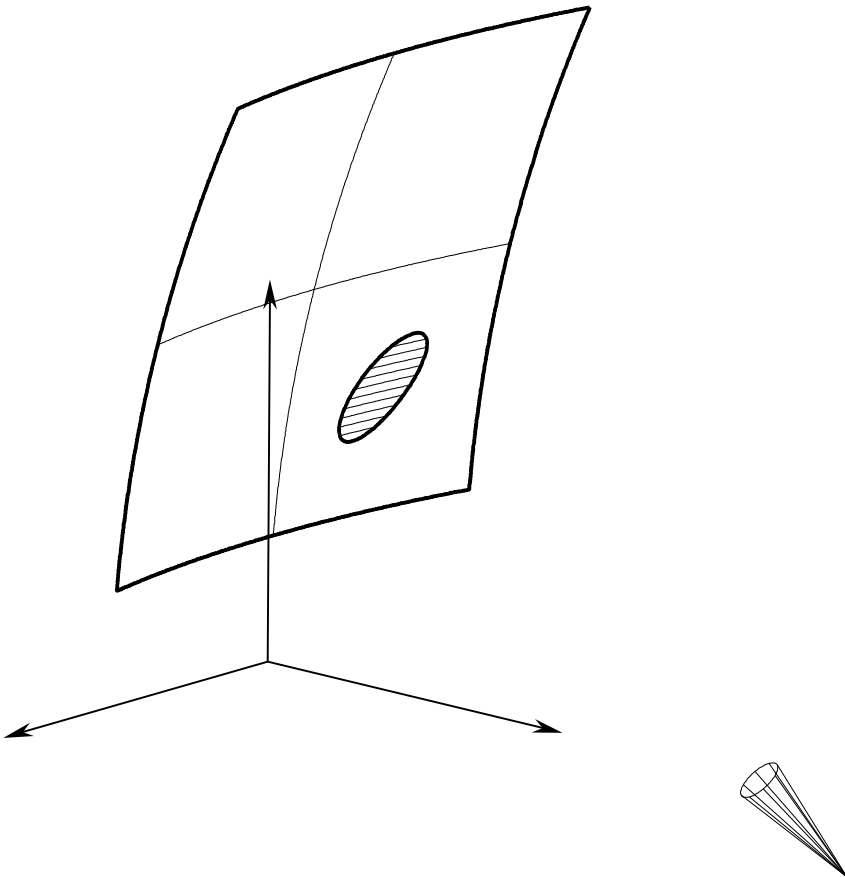


Figure 2.2-28 The hole in the reflector is generated by another reflector with the rim of the hole.

2.2.1.4 Reflector with panels in a polar grid

The “Panels in Polar Grid” reflector is a scatterer which is formed by a number of panels arranged in a polar grid. The panels may be arranged with a gap between neighbouring panels. This is described in Section 2.2.1.4.2 below. In the initial configuration, all panels are part of the same general curved surface. However, it is possible to specify misalign-

ments to each of the panels individually, as described in Section 2.2.1.4.3 below.

2.2.1.4.1 Specification of panels

The panels of the Panels in Polar Grid reflector are defined by means of a reflector surface and a polar grid. Both of these two items are specified in the same coordinate system as illustrated in Figure 2.2-29.

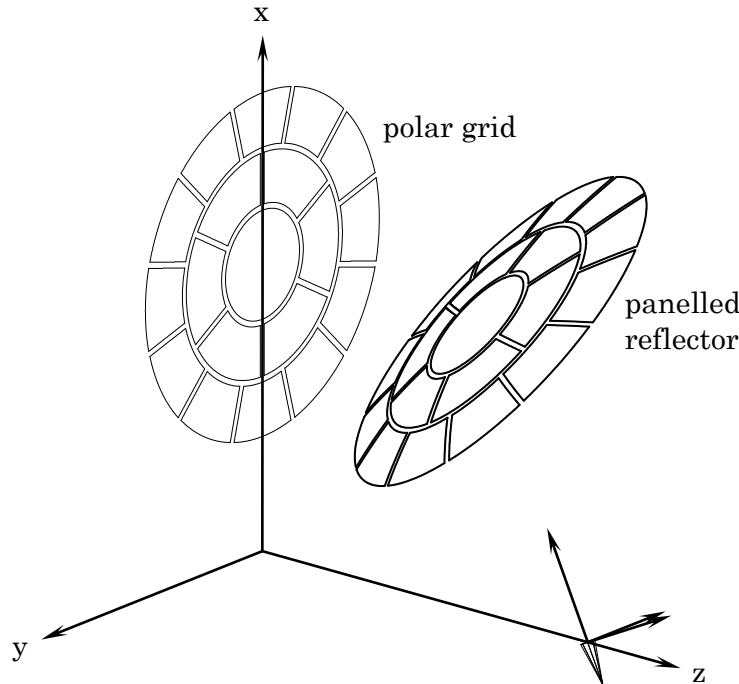


Figure 2.2-29 Reflector with panels defined by a polar grid.

The reflector surface is any of the surfaces described in Section 2.2.1.1, and thus of the form

$$z = F(x, y) .$$

The polar grid is defined in the xy -plane of the coordinate system. The polar grid contains an arbitrary number of rings of

arbitrary width. Each ring is defined by the outer radius of the ring, the angular position of one of the radial gaps, and the number of panels in the ring. All panels belonging to the same ring of the polar grid have identical size and shape in the xy -plane. The available area of the reflector is the projection of the polar grid on the reflector surface.

2.2.1.4.2 *Inter-panel gaps*

A single gap width can be specified for all circular gaps. Similarly, a single gap width can be specified for all radial gaps. Both gap widths are given tangentially to the reflector surface. The centre lines of the gaps are coinciding with the polar grid.

Internally in the program the gap widths need to be specified in the xy -plane of the reflector coordinate system and the gap width must not vary along a gap. However, a uniform gap width in the tangential plane to the reflector does not necessarily correspond to a uniform gap width projected onto the xy -plane, and vice versa.

Therefore, for each gap a number of test points along the gap are projected onto the xy -plane and the average value of the projected gap width is calculated. This value is then used for the present gap in the computations. As a consequence the tangential gap widths may vary slightly over the surface.

2.2.1.4.3 *Panel misalignments*

It is possible to change the position of one or several of the panels to model misalignments of the panels. For each panel, three or more control points may be given. For each of these control points, a misalignment vector is specified defined as the vector from the position of the control point on the ideally positioned panel to the actual position of the control point on the misaligned panel. Each panel is assumed to be stiff and is displaced from the ideal position to fit the specified misalignments.

If a panel has more than three adjustment points it may not be possible to fit the stiff panel to the misaligned control points. In this case, the panel is displaced such that the distances from the specified, misaligned control points to the control points of the modelled panel are minimised in a least square sense.

2.2.1.5 *Reflectors with individually defined panels*

The “Individually Defined Panels” is a scatterer built of panels defined individually and arranged arbitrarily. The panels may be connected by hinges to simulate a non-perfect deployment of an unfurlable reflector.

2.2.1.5.1 *Panels*

Each panel of the scatterer is defined by means of a panel surface and a panel rim similarly to the definition of reflectors, c.f. Section 2.2.1. All surface and rim definitions are given in the same coordinate system, but otherwise the panels may be defined arbitrarily.

2.2.1.5.2 *Hinges*

Hinges may be defined to model non-perfect alignment or unfurling of panels connected by hinges.

Each hinge is specified by a coordinate system. The z -axis of the coordinate system defines the hinge rotation axis. Otherwise the definition of the coordinate system may be chosen arbitrarily.

Each panel may be associated with one of the hinges, such that the entire panel is misaligned by a rotation around the hinge axis. When the rotation angle equals zero, the panel is perfectly aligned or unfurled in the sense that the panel definition (given by the specification in surface and rim) is left unchanged. When the rotation angle differs from zero, the panel is rotated this angle around the z -axis of the hinge coordinate system.

A hinge coordinate system, such as Hinge_1 in Figure 2.2-30, may be defined relatively to another hinge coordinate system, the Base-hinge in the figure. When the rotation angle of the base-hinge differs from 0, hinge_1 will be rotated. Consequently, all panels referring to the base-hinge as well as to the hinge_1 will be rotated.

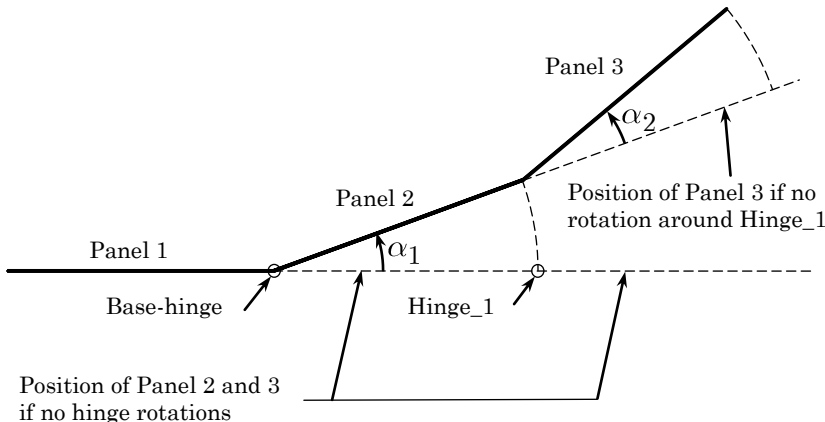


Figure 2.2-30 Position of panels when the rotation around the Base-hinge is α_1 , the rotation around Hinge_1 is α_2 and Hinge_1 is defined relatively to the Base-hinge.

2.2.1.6 Reflector with serrated edge

It is possible in GRASP to simulate serrations on a reflector edge. This is particularly useful for the analysis of compact ranges. The serrations are defined by means of two rim specifications, one for the tip and one for the foot of the serrations, as illustrated in Figure 2.2-31 for a circular reflector. The two rim shapes do not need to be of the same type, one could for example have an elliptical outer rim and a rectangular inner rim.

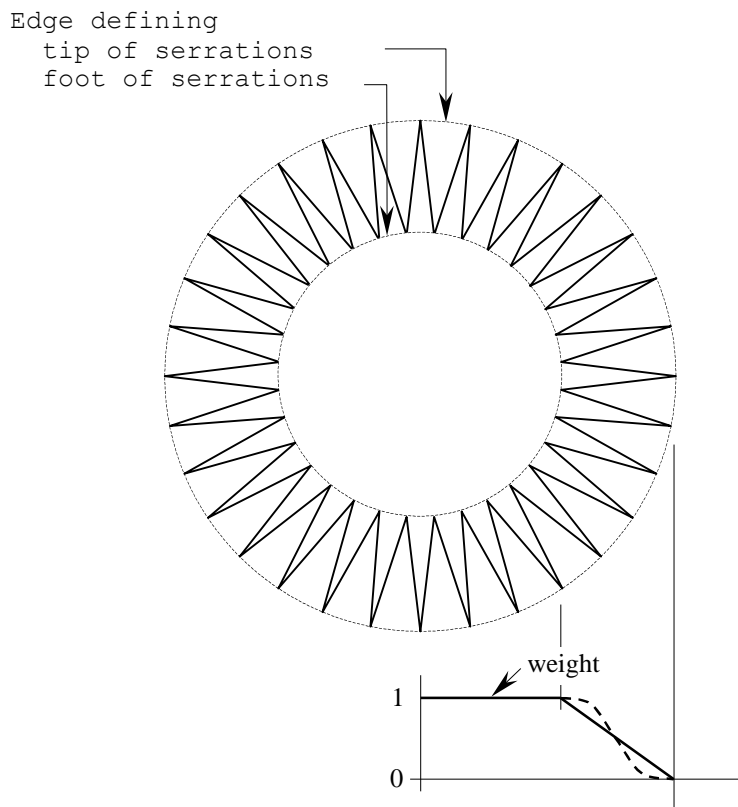


Figure 2.2-31 Reflector with serrated edge.

The electrical influence of the serrations is simulated by modifying the PO surface currents that would exist for an un serrated reflector. This modification is carried out by multiplying the surface currents by a weight factor which is unity for a point inside the inner rim and which gradually decreases from one to zero when the point moves from the inner to the outer edge. For triangular serrations the rate of decrease is selected linear and for cosine-shaped serrations a cosine rate of decrease is available. It must be noted that the number of serrations or the actual position of the individual elements is not taken into account.

The above described technique for the analysis of serra tion effects is extremely simple but yet it has proven to provide very good results for practical applications. The method has been tested against results obtained by Beeckman (1986, Figures 6

and 8) for the flat serrated square illustrated in Figure 2.2-32. The solid inner square has a side length of 45λ and the length of the serrations is 9λ such that the outer rim is a square with side length 63λ .

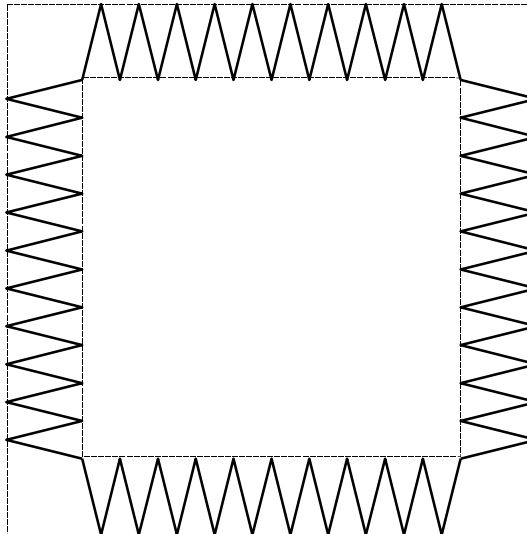


Figure 2.2-32 Square serrated plate

Inner square: $45 \times 45 \lambda$

Outer square: $63 \times 63 \lambda$

Serration length: 9λ .

The reflector in Figure 2.2-32 is assumed to be illuminated by a plane wave from the front direction and the scattered field is calculated in a cut across the quiet zone located 128λ in front of the reflector. The full line curve in Figure 2.2-33 is the result obtained with GRASP using the simple approach described above. The dotted curve shows Beeckman's result which is based on a quasi-analytical method which is limited to rectangular reflectors. Beeckman's approach gives slightly different results depending on whether the pattern cut goes through the tip or the foot of the serrations but these differences are too small to have any practical effect. The pattern in Figure 2.2-33 is a cut half way between these two extremes and it is seen to agree very well with the GRASP result.

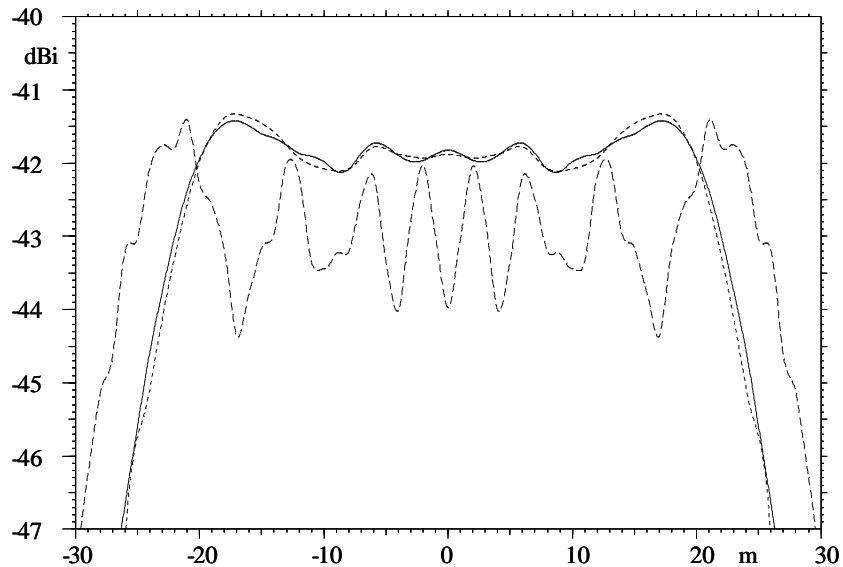


Figure 2.2-33 Plane pattern cut through the quiet zone
128 λ in front of the reflector in Figure 2.2-32.
full line: GRASP result
dotted line: Beeckman's result
dashed line: pattern without serrations.

Figure 2.2-33 also shows the GRASP calculated pattern if the serrations are removed, i.e. the plate is a square 63λ by 63λ . The result clearly indicates the importance of the serrations for reducing the ripples in the quiet zone for a compact range reflector. An example of a more realistic compact range reflector antenna system is described in Section 5.5.

2.2.1.7 Reflector with distortions

Distortions can be generated by a superposition of any two surface objects. Typical distortion surfaces are random, Zernike and irregularly spaced points.

2.2.2 Flat plates

The reflectors described in Section 2.2.1 are very general in the sense that many different types of surface shapes can be combined with many different types of rim shapes. For practical applications, for example to model a spacecraft body, it is convenient to have available some simple structures that can be defined by simple means. To this end the flat triangles, rectangles and parallelograms are introduced as illustrated in Figure 2.2-34.

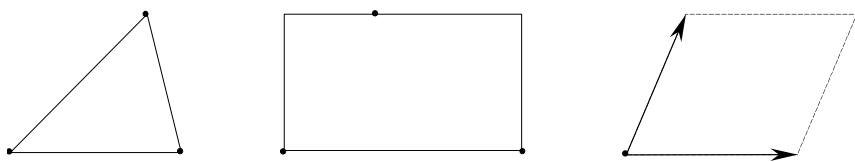


Figure 2.2-34 Flat plate structures in GRASP.

The structures are defined relative to a coordinate system specified by the user. The triangle is given by the xyz -coordinates of the three vertices. The rectangle is given by the two corners on the same side and one point on the opposite side. The parallelogram is defined by the position of one corner and the two side vectors from that corner.

It is currently only possible to use PO and PTD, but not GO and GTD, on flat plates, and while it is allowed to specify other material parameters than perfectly conducting, it will only have effect for PO computations. However, it is also possible to model the plate as a flat reflector and then these restrictions are removed.

2.2.3 Scatterer material properties

For the investigation of reflector antenna systems it is normally assumed that the reflectors are perfectly conducting. This is also the default option in GRASP. However, for many modern antennas this assumption is not valid. Reflector antennas may be supplied with special surface materials in order to improve their performance. Strip grids are used to control the polarisa-

tion characteristics and frequency selective surfaces (FSS) are used to separate frequency bands. Such antennas can also be analysed by GRASP and the general approach is to use PO assuming that the material properties locally can be approximated by those of an infinite plane.

However, dual curved reflectors may give rise to problems. Such reflectors are not unfurlable and this means that a planar surface material cannot be bent into the shape of the reflector without wrinkling. Consequently, the parameters of the surface must inevitably vary across the reflector with a possible impact on the resonance frequency and the polarisation performance.

The practical realisation of surface materials can be carried out in different ways. One approach is to laser etch a thin conducting layer into the desired pattern. This is the most general technique and can be used for both strip grids and FSS. Another approach is to cut narrow strips from a planar sheet of the material and then arranging them on the surface side by side.

It may be difficult to model the precise layout of a particular design and in most cases one will have to accept the approximations assuming the same material parameters and the same orientation all over the reflector surface.

The principles of Physical Optics (PO) still apply, i.e. the local surface currents on the reflector are determined as if a plane wave of the same direction, amplitude and phase was illuminating an infinite plane being the tangent plane to the surface at that point. When the reflector material is not perfectly conducting it is convenient to introduce both electric and magnetic surface currents as described in Section 3.5.

The reflection and transmission properties for plane wave incidence are sufficient to describe the behaviour of a reflector material. The definition of the reflection and transmission coefficients is described in Section 2.2.3.1. In the subsequent sections the following material types are presented:

- Material defined by reflected and transmitted power, including perfect conductivity and perfect absorption
- Finite conductivity
- Ideal grid
- Strip grid
- Wire grid
- Mesh surface
- Dielectric layer
- Tabulated reflection and transmission coefficients

Several surface types may appear at the same time and this is described in Section 2.2.3.10.

2.2.3.1 *Definition of reflection and transmission coefficients*

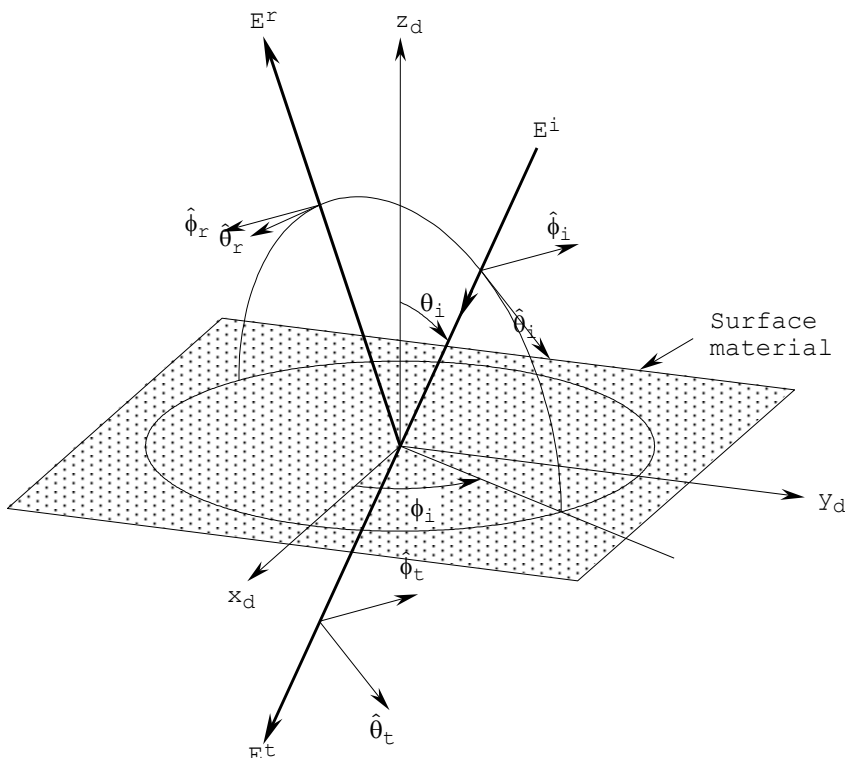


Figure 2.2-35 Unit vectors for the definition of reflection and transmission coefficients. Incidence from the front side.

A planar sample of a general reflector material is illustrated in Figure 2.2-35. A material definition coordinate system, $x_d y_d z_d$, is introduced with the z_d -axis normal to the surface. The direction of an incident plane wave is given by the spherical coordinates θ_i, ϕ_i , where θ_i is measured from the positive z_d -axis and ϕ_i from the positive x_d -axis. The angle θ_i is limited to the range $0 \leq \theta_i < 90^\circ$.

The incident plane wave can be decomposed as

$$\bar{E}^i = E_\theta^i \hat{\theta}_i + E_\phi^i \hat{\phi}_i \quad (2.2-48)$$

and is partly reflected and partly transmitted through the surface where the unit vectors of incidence, $\hat{\theta}_i$ and $\hat{\phi}_i$ are the usual polar vectors shown in Figure 2.2-35 and defined explicitly by

$$\begin{aligned} \hat{\theta}_i &= \hat{x}_d \cos \theta_i \cos \phi_i + \hat{y}_d \cos \theta_i \sin \phi_i - \hat{z}_d \sin \theta_i \\ \hat{\phi}_i &= -\hat{x}_d \sin \phi_i + \hat{y}_d \cos \phi_i \end{aligned} \quad . \quad (2.2-49)$$

The reflected field is given by

$$\bar{E}^r = E_\theta^r \hat{\theta}_r + E_\phi^r \hat{\phi}_r \quad (2.2-50)$$

where

$$\begin{Bmatrix} E_\theta^r \\ E_\phi^r \end{Bmatrix} = \begin{Bmatrix} R_{\theta\theta} & R_{\theta\phi} \\ R_{\phi\theta} & R_{\phi\phi} \end{Bmatrix} \begin{Bmatrix} E_\theta^i \\ E_\phi^i \end{Bmatrix} \quad (2.2-51)$$

and the unit vectors of reflection, $\hat{\theta}_r$ and $\hat{\phi}_r$ are the negative mirror images of $\hat{\theta}_i$ and $\hat{\phi}_i$, respectively, so that

$$\begin{aligned} \hat{\theta}_r &= 2 \hat{\theta}_i \cdot \hat{z} \hat{z} - \hat{\theta}_i \\ \hat{\phi}_r &= -\hat{\phi}_i \end{aligned} \quad . \quad (2.2-52)$$

Similarly, the transmitted field is given by

$$\bar{E}^t = E_\theta^t \hat{\theta}_t + E_\phi^t \hat{\phi}_t \quad (2.2-53)$$

where

$$\begin{Bmatrix} E_\theta^t \\ E_\phi^t \end{Bmatrix} = \begin{Bmatrix} T_{\theta\theta} & T_{\theta\phi} \\ T_{\phi\theta} & T_{\phi\phi} \end{Bmatrix} \begin{Bmatrix} E_\theta^i \\ E_\phi^i \end{Bmatrix}, \quad (2.2-54)$$

and the unit vectors of transmission $\hat{\theta}_t$ and $\hat{\phi}_t$ are defined by

$$\hat{\theta}_t = \hat{\theta}_i, \quad \hat{\phi}_t = \hat{\phi}_i. \quad (2.2-55)$$

Until now only the coefficients for incidence on the front side of the reflector have been considered. However, the reflector may not be identical from the two sides. Assume for example, that the reflector is perfectly conducting and covered by a dielectric layer of white paint for thermal protection. The paint will affect the reflection from the front side but it will have no influence at all on fields coming in from the back side. It is therefore necessary to define reflection and transmission coefficients also for incidence from the back side.

Incidence from the rear is illustrated in Figure 2.2-36. The angle θ_i is measured from the negative z_d -axis to the incident ray so that we still have $0 \leq \theta_i < 90^\circ$. The angle ϕ_i is as before measured from the positive x_d -axis towards the positive y_d -axis, as indicated in Figure 2.2-36. The unit vectors $\hat{\theta}_i$ and $\hat{\phi}_i$ of incidence are now defined by

$$\begin{aligned} \hat{\theta}_i &= -\hat{x}_d \cos \theta_i \cos \phi_i - \hat{y}_d \cos \theta_i \sin \phi_i - \hat{z}_d \sin \theta_i \\ \hat{\phi}_i &= -\hat{x}_d \sin \phi_i + \hat{y}_d \cos \phi_i. \end{aligned} \quad (2.2-56)$$

The relations (2.2-50) through (2.2-55) are also valid when the incident field illuminates the back side.

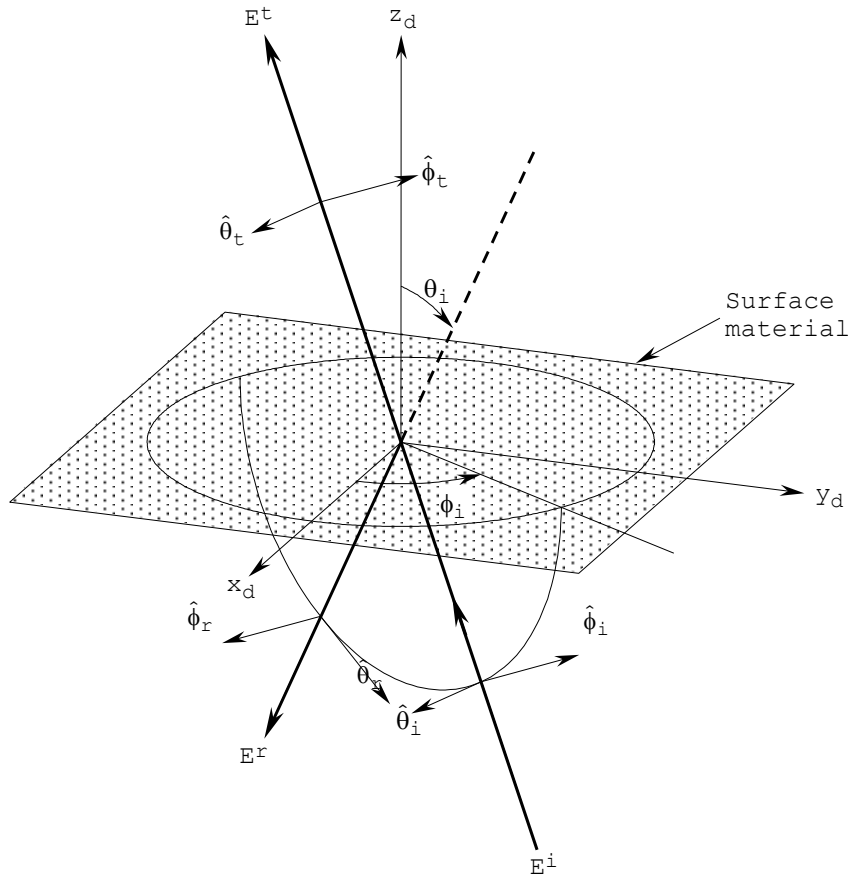


Figure 2.2-36 Unit vectors for the definition of reflection and transmission coefficients for incidence from the back side.

Realistic reflector materials will have a certain thickness and it is important to specify the position of the reference plane to which the reflection and transmission coefficients apply. In the formulation described above the $x_d y_d$ -plane of the definition coordinate system is the reference plane both for reflection and transmission and for incidence both from the front and from the back side. For each of the specific materials described in the following sections the position and orientation of the definition coordinate system is given relative to the physical geometry.

To specify a material for a given reflector one must note that the reflector surface defined in Section 2.2.1.1 is a mathematical surface. The material is applied to the surface by specifying how the material definition coordinate system is located on the reflector surface. This is done by

- 1) the distance, s , from the reflector surface to the $x_d y_d$ -plane, measured along the surface normal. s may be both positive and negative.
- 2) the direction of the x_d -axis of the definition coordinate system on the surface.

The z_d -axis of the definition coordinate system always coalesce with the positive direction of the surface normal.

Some software packages for prediction of reflection and transmission coefficients may use different reference planes for reflection and transmission, for instance the front side for the reflection coefficients and the rear side for the transmission coefficients. In that case, a correction must be applied, and this is in the transmission case

$$e^{jk\delta \cos \theta_i} \quad (2.2-57)$$

where δ is the thickness of the material and θ_i is the angle of incidence.

2.2.3.2 *Material defined by the reflected and transmitted power*

This type of reflector material is included in order to be able to model the properties of more complicated structures in a very simple way. It can be used to model a frequency selective surface, a power splitter or any other material for which the reflection and transmission are known or can be estimated by other means.

The material is assumed to be infinitely thin and the relative reflected and transmitted power is R_{power} and T_{power} , respectively, and they are independent of the angle of incidence. The

sum of the two cannot exceed unity, but it can be less than unity to represent losses in the material. It is possible to specify different values for different frequency bands.

The reflection and transmission coefficients of the material are now given by

$$\begin{aligned} R_{\theta\theta} &= R_{\phi\phi} = \sqrt{R_{power}} \\ T_{\theta\theta} &= T_{\phi\phi} = \sqrt{T_{power}} \\ R_{\theta\phi} &= R_{\phi\theta} = T_{\theta\phi} = T_{\phi\theta} = 0 \end{aligned} \quad . \quad (2.2-58)$$

2.2.3.2.1 *Perfect conductivity*

A perfect conductor is simulated by specifying

$$R_{power} = 1, \quad T_{power} = 0 \quad . \quad (2.2-59)$$

It has previously been mentioned that the default option in GRASP is a perfectly conducting reflector. However, the perfectly conducting material is necessary if one wants to combine it with other materials, for example a perfectly conducting reflector covered with paint.

2.2.3.2.2 *Perfect absorption*

It is possible to model the effects of an absorber by

$$R_{power} = 0, \quad T_{power} = 0 \quad . \quad (2.2-60)$$

An application example with a perfect absorber is presented in Section 3.6.2.2.

2.2.3.3 *Finite conductivity*

Real reflectors are made of metals or composite materials like CFRP for which the conductivity is not infinite. At high frequencies the losses associated with the finite conductivity may be important. The reference plane is the front surface of the material sample. The following reflection coefficients from Stratton (1941) are sufficiently accurate:

$$\begin{aligned}
R_{\theta\theta} &= (1 - x / \cos \theta_i) e^{-j2x / \cos \theta_i} \\
R_{\phi\phi} &= (1 - x \cos \theta_i) e^{-j2x \cos \theta_i} \\
R_{\theta\phi} = R_{\phi\theta} &= T_{\theta\theta} = T_{\phi\phi} = T_{\theta\phi} = T_{\phi\theta} = 0 \\
x &= \sqrt{\frac{2\omega\mu\varepsilon_0}{\mu_0\sigma}}
\end{aligned} \tag{2.2-61}$$

where ω is the angular frequency, μ and μ_0 are the permeabilities of the reflector and free space, respectively, ε_0 is the permittivity of free space and σ is the conductivity of the reflector material. For most reflectors $\mu = \mu_0$ which gives

$$x = 1.06 \cdot 10^{-5} \sqrt{\nu / \sigma} \tag{2.2-62}$$

where ν is the frequency in Hertz and σ is the conductivity in Siemens/m (S/m).

2.2.3.4 *Ideal grid*

The ideal grid is an idealisation of strip grids or wire grids presented in the following sections. It can be thought of as an infinitely thin sheet of closely spaced perfectly conducting parallel wires. The performance of the grid can be understood in the following way: Assume that a plane wave is coming from a given direction. The grid is projected on a plane orthogonal to the direction of incidence. All field components parallel to this projected grid will be perfectly reflected whereas all other components will be transmitted through the surface with no loss. The ideal grid is very useful to model the initial designs of gridded reflectors before the actual dimensions of the real grid have been decided.

The $x_d y_d$ -plane of the definition coordinate system is the plane of the grid and the x_d -axis is the grid wire direction. The reflection and transmission coefficients for the front side are:

$$\begin{aligned}
 R_{\theta\theta} &= \frac{\cos^2 \theta_i \cos^2 \phi_i}{1 - \sin^2 \theta_i \cos^2 \phi_i} \\
 R_{\theta\phi} = R_{\phi\theta} &= -\frac{\cos \theta_i \cos \phi_i \sin \phi_i}{1 - \sin^2 \theta_i \cos^2 \phi_i} \\
 R_{\phi\phi} &= \frac{\sin^2 \phi_i}{1 - \sin^2 \theta_i \cos^2 \phi_i} \\
 T_{\theta\theta} &= 1 - R_{\theta\theta} \\
 T_{\phi\phi} &= 1 - R_{\phi\phi} \\
 T_{\theta\phi} = T_{\phi\theta} &= -R_{\theta\phi}
 \end{aligned} \tag{2.2-63}$$

The same expressions apply for the back side except for a sign change in the off-diagonal elements. They can be derived from the formulas for the strip grid in Section 2.2.3.5 but they can also be derived directly from the properties for plane wave incidence, as described above.

To use the ideal grid on a reflector surface one must specify the displacement of the reference plane along the surface normal. In addition the local direction of the grid on the surface shall be defined. This is done in GRASP by means of a so-called reference coordinate system, $x_c y_c z_c$, as illustrated in Figure 2.2-37. A line in the $x_c y_c$ -plane making the angle α with the x_c -axis is defined. A plane through this line and the z_c -axis is introduced. Planes parallel to this plane will cut the reflector surface in curved lines and the tangent to these curves is the local direction of the x_d -axis of the material definition coordinate system. This procedure implies that all the wires of the grid will appear as straight lines when the surface is seen in the direction of the z_c -axis.

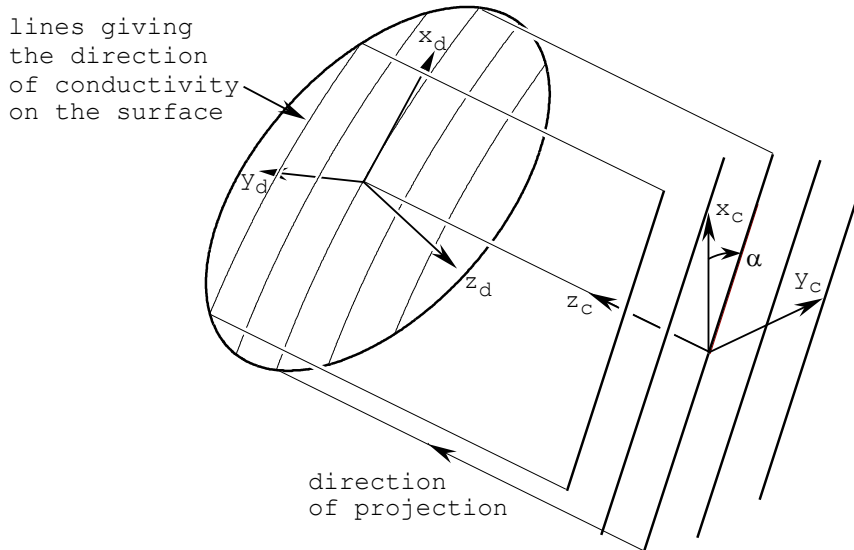


Figure 2.2-37 The reference coordinate system, $x_c y_c z_c$, specifying the local orientation of the material definition coordinate system, $x_d y_d z_d$, on the reflector surface.

The above described definition of the local orientation of the reflector material is very useful for practical applications and it is also used for the strip grid, the wire grid, the mesh surface and for tabulated input as described in Sections 2.2.3.5, 2.2.3.6, 2.2.3.7 and 2.2.3.9, respectively.

2.2.3.5 Strip grid

A strip grid consists of parallel strips. Each strip has a width w and the spacing of the strips is s (the distance from the centre of one strip to the centre of the next). The reference plane is the plane of the strips.

The reflection and transmission coefficients are given by Nakamura and Ando (1988). The coordinate systems used by Nakamura and Ando are different from the definition used in GRASP but the coefficients can be transformed by simple vector algebra. For a plane wave at normal incidence, $\theta_i = \phi_i = 0$, polarised parallel to the strips the reflection coefficient is

$$\begin{aligned} R_{\theta\theta} &= \frac{1}{1+jt} \\ t &= -\frac{2s}{\lambda} \ln \left(\cos \left(\frac{\pi}{2} \left(1 - \frac{w}{s} \right) \right) \right) \end{aligned} \quad (2.2-64)$$

and for polarisation orthogonal to the strips one gets

$$\begin{aligned} R_{\phi\phi} &= \frac{jt'}{1+jt'} \\ t' &= -\frac{2s}{\lambda} \ln \left(\sin \left(\frac{\pi}{2} \left(1 - \frac{w}{s} \right) \right) \right) \end{aligned} \quad (2.2-65)$$

where λ is the wavelength. These expressions show that both components

$$R_{\theta\theta,\phi\phi} \rightarrow \begin{cases} 1 & \text{for } \frac{w}{s} \rightarrow 0 \\ 0 & \text{for } \frac{w}{s} \rightarrow 1 \end{cases}, \quad (2.2-66)$$

which is reasonable from a physical point of view. Expressions (2.2-64) and (2.2-65) also show that if the spacing relative to the wavelength, s/λ , is reduced while the ratio between the width and the spacing, w/s , is kept constant, $R_{\theta\theta} \rightarrow 1$ and $R_{\phi\phi} \rightarrow 0$. These are the properties of the ideal grid in Section 2.2.3.4.

A typical value of $w/s = 0.2$ is used to illustrate the dependence of $R_{\theta\theta}$ and $R_{\phi\phi}$ as a function of s/λ in Figure 2.2-38.

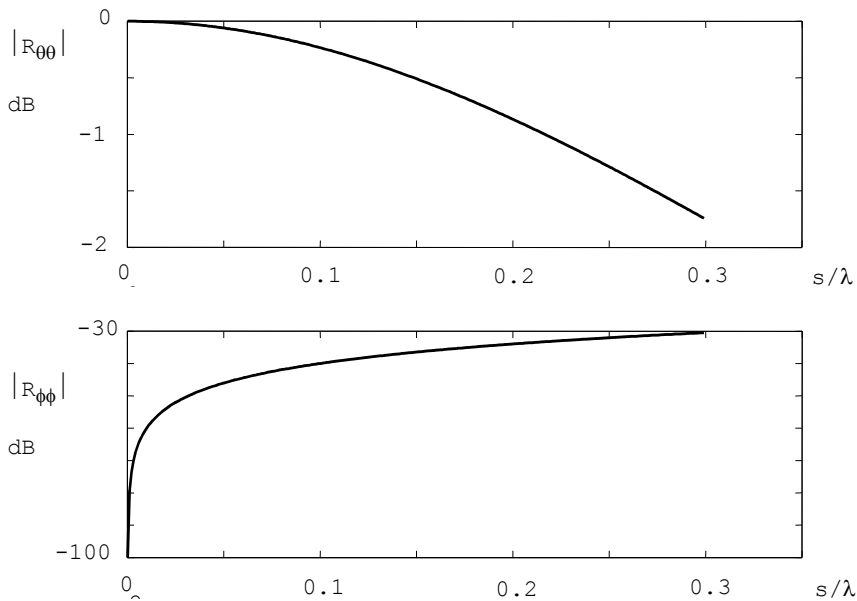


Figure 2.2-38 Reflection from strip grid at normal incidence as a function of the strip spacing s relative to the wavelength λ . The width of the strips is $w = 0.2s$.

The formulas by Nakamura and Ando have been compared to other methods and it has been found that good accuracy is obtained for $s/\lambda < 0.3$.

The angular dependence of the reflection and transmission coefficients is similar to the ideal grid in Section 2.2.3.4. The main difference is that the ideal grid gives no reflection for an incident field polarised orthogonal to the grid whereas the strip grid gives a small reflection as given by expression (2.2-65).

The $x_d y_d$ -plane of the definition coordinate system is the plane of the strips and the x_d -axis is the strip direction. The strip grid is applied to a reflector surface in the same way as for the ideal grid, Figure 2.2-37 in Section 2.2.3.4. The constant strip grid parameters, s and w , are defined in the $x_c y_c$ -plane of the reference coordinate system and the strips are tilted the constant angle α with respect to the x_c -axis. The real strip grid on the reflector is now generated by project-

ing the planar grid along the z_c -direction to the surface. Since the reflector surface is generally curved it means that the local grid spacing and width will vary across the reflector. The approach described here is very important for practical applications since it corresponds to the laser etching technique where the strips are cut out of a continuous thin metal layer deposited on the surface.

Wrinkling problems will occur if the grid is manufactured as a planar strip fabric and then applied to the doubly curved reflector surface. This effect is described in more detail in connection with the tabulated material input in Section 2.2.3.9.

2.2.3.6 Wire grid

The wire grid material consists of a planar sheet of parallel circular cylindrical wires of spacing s . The diameter of the wires is d_0 . It is assumed that $d_0 \ll s$. The reference plane is the plane through the centre lines of the wires.

The wire grid has many similarities with the strip grid and it can be shown that for polarisation parallel to the wires the reflection is equal to that of a strip grid where the strip width $w = 2d_0$ (Butler, 1982). For polarisation orthogonal to the wires the equivalent strip width is $w = \sqrt{2} d_0$ (Johnson and Jasik, 1984, Ch.46). The angular dependence with θ_i and ϕ_i is the same as for the strip grid.

The $x_d y_d$ -plane of the definition coordinate system is the plane of the wires and the x_d -axis is the wire direction. The wire grid is applied to a reflector surface in a similar way as for the strip grid, see Figure 2.2-37 in Section 2.2.3.4. The constant wire grid parameters, s and d_0 , are defined in the $x_c y_c$ -plane of the reference coordinate system and the wires are tilted the constant angle α with respect to the x_c -axis. The real wire grid on the reflector is now generated by projecting the planar grid along the z_c -direction to the surface. Since the reflector surface is generally curved it means that the local wire spacing will vary across the reflector. In contrast to the strip grid where also the strip width varies across the reflec-

tor, the wire diameter d_0 is constant for the wires on the surface.

2.2.3.7 Mesh grid

The mesh grid consists of two orthogonal sets of wires as illustrated in Figure 2.2-39 together with the definition coordinate system. The spacing between the wires is s_x and s_y in the x_d - and y_d -direction, respectively. The wire diameter is d_0 and the two sets of wires are in electrical contact at all the intersection points.

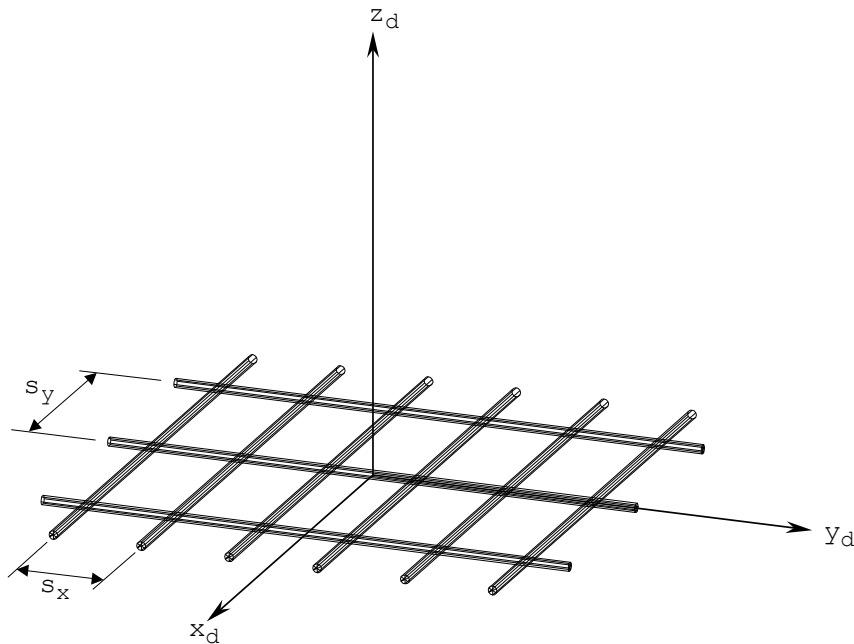


Figure 2.2-39 Mesh grid.

The reflection and transmission coefficients used in GRASP are based on Astrakhan (1968). For incidence in one of the principal planes, for example $\phi_i = 0$, the reflection coefficients are practically identical to those for the wire grid, i.e. $R_{\theta\theta}$ is the same as for the wire grid with spacing s_x and similarly for $R_{\phi\phi}$ in the orthogonal plane.

One of the main purposes of the mesh grid is to model the electrical properties of the tricot mesh of unfurlable antennas. A real mesh is shown in Figure 2.2-40. Although it is obvious that the pattern of the tricot mesh is far from being rectangular, it has been found (Pontoppidan, 1981) that it is possible to define an equivalent rectangular grid which, for any angle of incidence and polarisation, gives the same reflected and transmitted field as the real mesh.

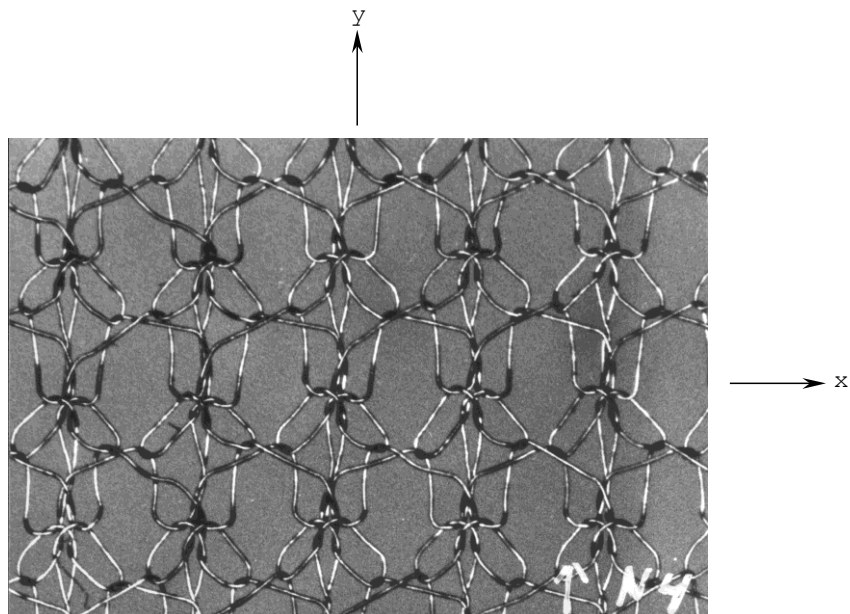


Figure 2.2-40 Tricot mesh. The example shown is made of nickel wire 60 μm in diameter.

The equivalent rectangular grid may be determined as follows. Assume that the power reflection coefficient, R_x , for the mesh in Figure 2.2-40 has been measured for normal incidence with a polarisation parallel to the x -direction. The distance, s_x , between the x -directed wires of the equivalent rectangular grid is now given by (Astrakhan, 1968)

$$s_x = \frac{\lambda \sqrt{1/R_x - 1}}{2 \ln \frac{s_x}{\pi d_0}} , \quad (2.2-67)$$

where λ is the wavelength and d_0 is the wire diameter. (The solution to (2.2-67) for the wire spacing may be determined on a pocket calculator.) A similar relation holds for the wires in the y -direction.

The reflection coefficients for the mesh in Figure 2.2-40 was measured to

$$R_x = 0.932, \quad R_y = 0.999 \quad (2.2-68)$$

at 12 GHz. Expression (2.2-67) gives with $d_0 = 0.06$ mm

$$s_x = 1.59 \text{ mm}, \quad s_y = 0.45 \text{ mm} \quad . \quad (2.2-69)$$

A mesh reflector antenna with unequal reflection coefficients for the x - and y -direction will, in circular polarisation, generate a cross-polar beam similar to the co-polar beam and with an amplitude given by $R_y - R_x / R_y + R_x$. With the numbers in (2.2-68) the cross polarisation is only 29 dB below the co-polar beam.

The mesh grid is applied to a reflector surface as illustrated in Figure 2.2-41. It is assumed that the total mesh is composed of a number of equiangular gore sections. Five sections are shown in Figure 2.2-41. It is possible to rotate the sections the angle ϕ_0 . In each of the gores the bisector, shown dotted in the figure, and the z_c -axis defines a plane and the x_d -axis of the local mesh grid will be parallel to this plane within the entire gore section of the reflector. It must be noted that the local wire spacings are not changed during this projection, in contrast to the strip and wire grids.

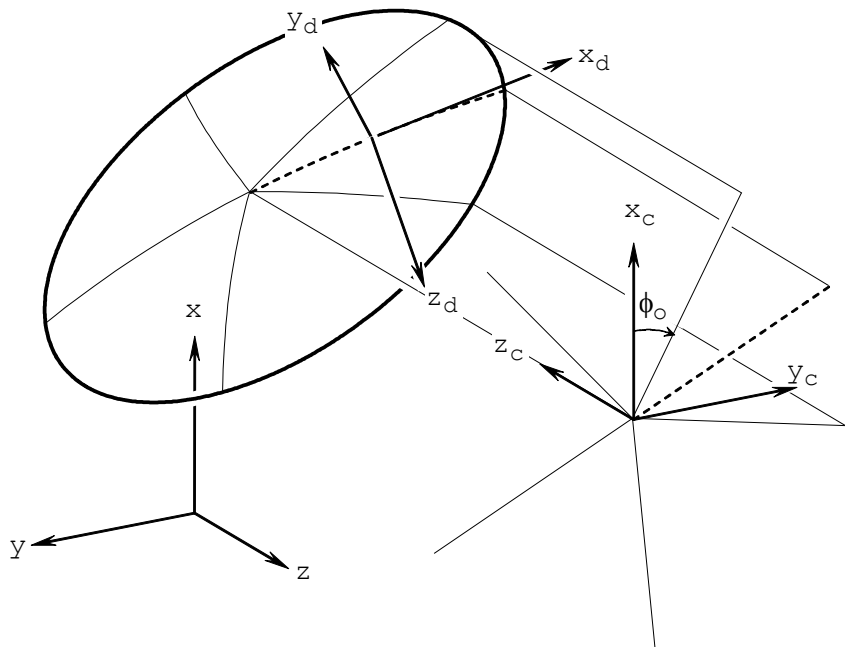


Figure 2.2-41 The reference coordinate system, $x_c y_c z_c$, specifying the local orientation of the mesh definition coordinate system, $x_d y_d z_d$, on the reflector surface.

The number of sections is defined by the user. A minimum of two sections must be applied and in that case the two bisectors become parallel resulting in the same mesh orientation all over the reflector surface.

The mesh grid option is normally used in connection with unfurlable antennas, such as the rib antenna and the truss antenna described in Sections 2.2.1.1.13 and 2.2.1.1.14, respectively, but it may be used for all the reflector surface options available.

2.2.3.8 Dielectric layer

The dielectric layer is a plate of dielectric material of thickness h and with a relative dielectric constant ϵ_r , as illustrated in Figure 2.2-42. This type of material can be used to simulate the effects of a radome or it can be used in combination with

other materials to model the sandwich support structure of a strip grid or the influence of thermal paint on a reflector.

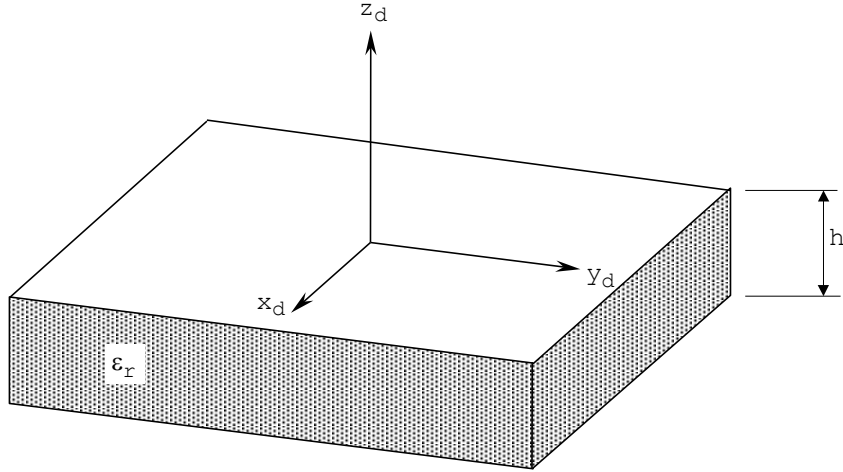


Figure 2.2-42 Dielectric material, relative dielectric constant ϵ_r , thickness h .

The material definition coordinate system is selected such that the $x_d y_d$ -plane is the front surface of the dielectric plate. The reflection and transmission coefficients are given by Born and Wolf (1983) and referred to this plane one obtains for incidence from the front side:

$$r = \frac{(p_2^2 - p_1^2)(1 - e^{-j2\beta})}{(p_1 + p_2)^2 - (p_1 - p_2)^2 e^{-j2\beta}} \quad (2.2-70)$$

$$t = \frac{4p_1 p_2 e^{-j(\beta - kh \cos \theta_i)}}{(p_1 + p_2)^2 - (p_1 - p_2)^2 e^{-j2\beta}} \quad (2.2-71)$$

$$\begin{aligned}
 p_1 &= \cos \theta_i \\
 \beta &= kh\sqrt{\varepsilon_r - \sin^2 \theta_i} \\
 R_{\theta\theta} &= -r \\
 T_{\theta\theta} &= t \\
 \text{with } p_2 &= \frac{\sqrt{\varepsilon_r - \sin^2 \theta_i}}{\varepsilon_r}
 \end{aligned} \tag{2.2-72}$$

$$\begin{aligned}
 R_{\phi\phi} &= r \\
 T_{\phi\phi} &= t \\
 \text{with } p_2 &= \sqrt{\varepsilon_r - \sin^2 \theta_i}
 \end{aligned}$$

where k is the free space wave number, $2\pi/\lambda$. ε_r may be complex to account for losses in the material. For incidence from the back side the above reflection formulas shall be multiplied by $e^{j2kh\cos\theta_i}$, whereas the transmission coefficients are unchanged (this is performed internally in GRASP). The dielectric material is isotropic and therefore the reflection and transmission properties are independent of ϕ_i and all off-diagonal elements are zero.

An application example with a dielectric layer is presented in Section 3.6.2.2.

2.2.3.9 Tabulated reflection and transmission coefficients

It is possible to analyse a reflector antenna with measured or calculated reflection and transmission coefficients. In both cases it is necessary to define a material definition coordinate system and the reflection and transmission coefficients must be given in tabulated form as functions of the incidence angles θ_i and ϕ_i , as defined in Section 2.2.3.1. It will be shown later in this section that the choice of the definition coordinate system can be important and some caution in applying the tabulated input option is advisable.

As for the other non-homogeneous materials it is necessary to specify how the material is applied to the curved reflector surface. Again the reference coordinate system is introduced, as illustrated in Figure 2.2-37, in order to define the local orientation of the x_d -axis of the material definition coordinate system on the surface of the reflector. It should be emphasised that this only determines the local orientation of the material and consequently the local angles of incidence. The reflection and transmission coefficients are as for the original planar sample of the material.

The effects of the choice of the material definition coordinate system will be illustrated by an example. A rotationally symmetric paraboloid with a diameter of 40 units and a focal length of 16 units is selected. Assume that a strip grid has been measured and the x_d -axis was selected as the strip direction. When this material is applied to the curved reflector as described above, the strips will appear as straight lines and a good cross polarisation performance will be achieved. Assume next, that for some reason, the x_d -direction for the measurements was selected at an angle of 60° with respect to the strip direction. This is in principle perfectly acceptable and the new measurements contain exactly the same amount of information as the previous ones. However, when the material is applied to the reflector the x_d -direction remains constant but due to the curvature of the reflector the actual strip direction will vary across the reflector surface. The strip pattern seen from the axis is illustrated in Figure 2.2-43 and the curvature of the strips will increase the cross polarisation significantly.

Superimposed on Figure 2.2-43 is also a contour plot of the strip orientation relative to 60° . The distance between the contours is 1° . It will be noticed that the contour lines are almost symmetric about two axes which are tilted 15° . This means that also the four lobes of the cross polar pattern will be tilted 15° .

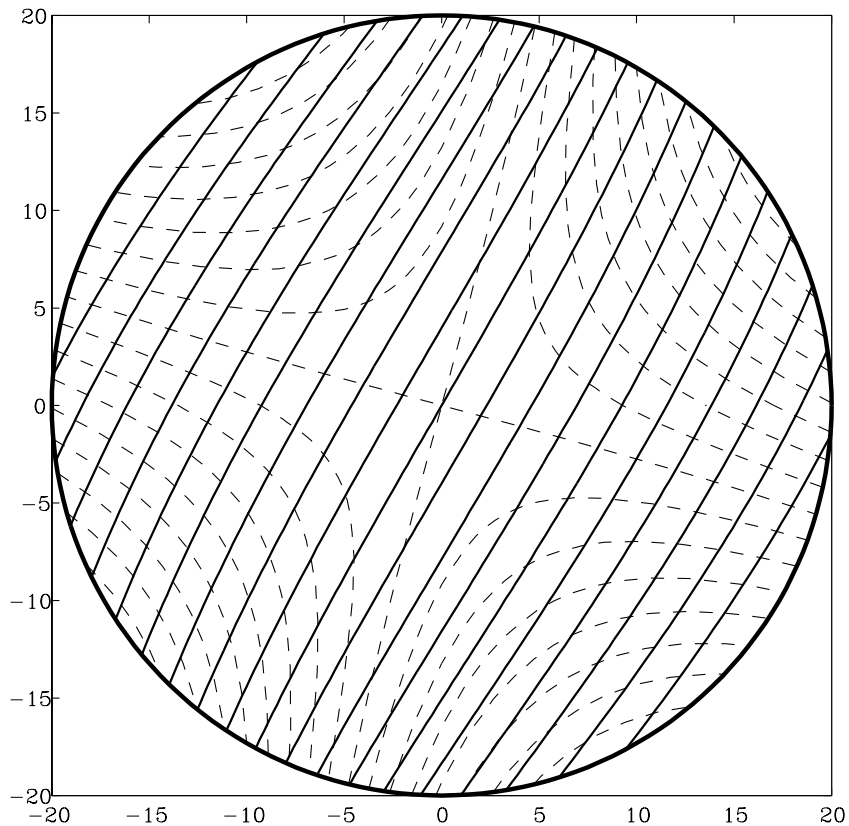


Figure 2.2-43 Apparent strip direction for a measured strip grid where the reference direction is tilted 60° with respect to the strip direction. The contour curves (dotted lines) show the deviation from 60° . The contour spacing is 1° .

It must be pointed out that the one representation of the measured strip grid is not more correct than the other. The ambiguity is coming from the fact that a planar material cannot be bent into the shape of a doubly curved reflector without distortions. The above just describes two different approximations to the real world.

2.2.3.10 Cascading several layers

The different material types described in the previous sections may be combined in order to simulate realistic reflector surface structures. For example

- a painted reflector is modelled as a dielectric layer in front of a perfect conductor
- a polarizer is modelled by a strip grid one eighth of the wavelength in front of a perfect conductor
- a gridded reflector with support structure is modelled by a strip grid in front of one or more dielectric layers
- a reflector made in CFRP is modelled by several closely spaced layers of ideal grids with different orientations.

For each of the layers of a composite material one must specify the material type and the position of the reference coordinate system relative to the mathematical expression describing the surface shape. The layers must be specified in the same order in which they are encountered seen from the front side of the surface.

If all the layers of a composite material are homogeneous, such as dielectrics, the reflection and transmission matrices can be determined exactly by transmission line theory (Uher, Bornemann and Rosenberg, 1993). The same approach is described by Ip and Rahmat-Samii (1998). However, this simple principle of cascading is used for all the layer types in GRASP. The consequence of this approximation is that the resulting combined reflection and transmission coefficients will only be correct if the distance between two nonhomogeneous layers is so large that, by the exit from the first layer, a plane wave has been formed before the entrance to the next. This phenomenon will be illustrated by the following example.

Figure 2.2-44 shows two types of surface materials both constructed from two identical strip grids with spacing $s = 8$ mm and a strip width of $w = 2$ mm. The two grids are separated

the distance d and illuminated by a plane wave at normal incidence and polarised parallel to the strip direction.

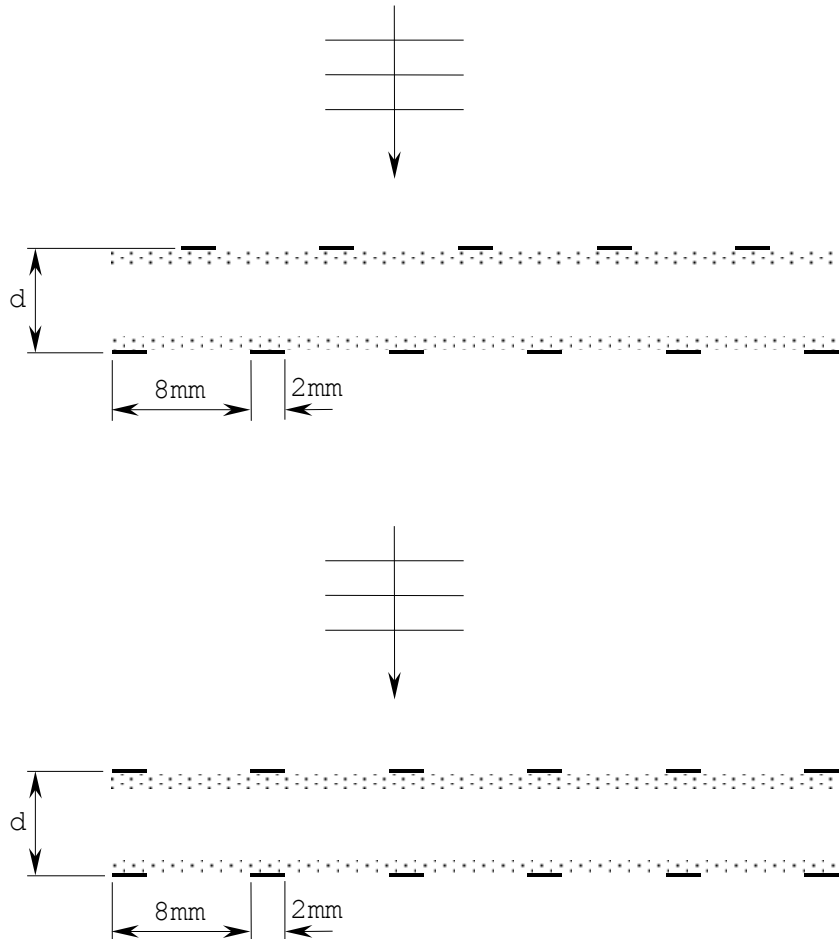


Figure 2.2-44 Two types of composite materials both made of two identical strip grids with spacing 8 mm and strip width 2 mm.
 Top: The two grids are shifted 4 mm
 Bottom: The two grids are aligned.

It is of particular interest to investigate the behaviour of these two models for d approaching zero. It is clear that the top construction in Figure 2.2-44, where the strip layers are shifted, will for $d = 0$ effectively correspond to a single strip layer with a spacing of $s = 4$ mm. On the other hand, the lower construction in Figure 2.2-44 will result in a strip grid with a spacing

of $s = 8$ mm for $d = 0$. In GRASP the actual shift between the two layers is not taken into account and the result becomes erroneous for d small.

The surface material structures in Figure 2.2-44 can be analysed with high precision by means of a Moment-Method solution. This has been implemented by Savi (1997) in the computer program ASG (Analysis of Strip Gratings) and in this program the above mentioned shift is properly taken into account.

Distance between grids mm	GRASP	ASG grids aligned	ASG grids shifted
0	.969	.885 (.890)	.996 (.996)
1	.983	.990	.994
5	.993	.992	.994
10	.978	.975	.975
15	.969	.968	.968
20	.993	.993	.993
25	.977	.975	.975

Table 2.2-2 Reflection coefficients calculated by GRASP and ASG for the two reflector surface types in Figure 2.2-44. The frequency is 10 GHz. The two numbers in parentheses for $d = 0$ are the GRASP result for the corresponding single layer strip grid.

A comparison between the reflection coefficients calculated by GRASP and ASG are shown in Table 2.2-2. The frequency is 10 GHz corresponding to a wavelength of 30 mm. It is seen

that the two ASG-results for $d = 0$ differ considerably and the GRASP-result is somewhere in between. The numbers in parentheses for $d = 0$ are the GRASP-results for the corresponding single strip grids. Already for a distance between the strip grids of $d = 5$ mm the shift between the grids becomes unimportant and the result obtained with GRASP is just as good as the more accurate ASG-solution.

The results presented in Table 2.2-2 are for a very large grid spacing, s , relative to the wavelength. Realistic spacings are in the order of $\lambda/20$ in which case the agreement between ASG and GRASP would be even better. The results therefore seem to indicate that the cascading principle implemented in GRASP is sufficiently accurate for all practical applications.

2.2.4 Struts

Struts are used to support the feed or the subreflector in centre-fed single or dual reflector antennas, respectively. It is possible to analyse the scattering effects from strut elements having circular or polygonal cross-section. The computational techniques are described in Section 3.4.

The struts having circular cross-section are defined by the position of the end points and the radius. The struts having polygonal cross-section are defined by the position of the end points and the shape of the polygonal cross-section. Figure 2.2-45 shows an Open GL plot of a reflector antenna with three rectangular struts.

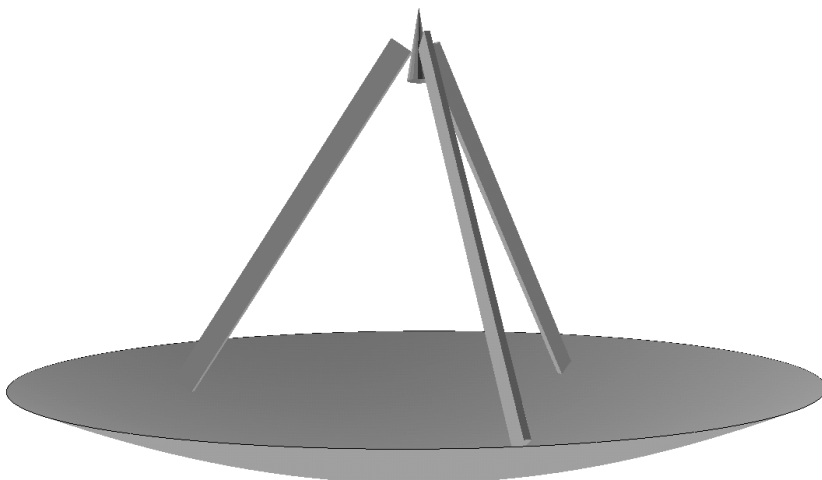


Figure 2.2-45 Front-fed reflector antenna with three polygonal struts to support the feed.

2.3 Feed systems

The feed system is the radiating source of an antenna system in the sense that it carries power to the system. Other sources are also possible, e.g. PO currents, but these originate in an illumination from other elements in the system and only redirect the power already brought into the system. These sources are generated internally in GRASP and will be described in Chapter 3.

The source of the antenna system is here called a feed since typically the antenna system is a reflector antenna. However, GRASP is not restricted to modelling reflector antennas. The feed may just as well be a low gain antenna on a structure, such as a spacecraft, a ship or rural environments, where the structure interacts with the antenna radiation similar to the way reflectors interact with the feed radiation in a reflector antenna system.

In the present section the available feed systems are described. The feed system may consist of one or more feed elements. A special type of feed, a plane wave illumination of the antenna system is also possible. In the following we will first consider the different feed elements, then the plane wave as a feed and, finally, arrays or clusters of feeds.

2.3.1 Feed element types

The feed elements are characterised by their radiation pattern. The most general way to specify a radiation pattern is by means of a table, e.g. measured data.

Another very general description of a feed is the spherical wave expansion which may also be based on a measurement of the complete feed radiation. The advantage of this type of feed element is that the description is accurate and complete. Thus, interpolation errors are not introduced and near-field effects are automatically accounted for.

In the initial design phase of a reflector antenna system an accurate feed model may not be available and a good approximate model may then have to be applied. Many antenna feeds radiate a pattern which resembles a Gaussian beam and can then be modelled by a Gaussian feed, which has the advantage that it describes both the near-field and the far-field effects of the feed in a simple way.

In many cases a crude model of the radiation from the feed suffices, at least for preliminary design work. This is catered for by the simple tapered pattern model, where the radiation from the feed is described by E- and H-plane patterns only. The beam produced is in general elliptical in shape, but the azimuthal (ϕ) variation is inherently limited to $\cos\phi$ and $\sin\phi$ only. The restriction on azimuthal variation has been lifted in the elliptical pattern model.

The list of feed types offered would be inadequate if conventional horns with rectangular or circular aperture cross-sections were not available. These types have further been

supplemented by a hexagonal horn aperture, which lends itself to compact packaging in feed arrays.

Also included in the list of available feed types are models for : a microstrip patch radiator, the helix antenna, the spiral antenna, a half-wave dipole, a Hertzian dipole, and a low gain antenna with a cardioid-shaped pattern.

For all the feed element models the field is normalised to isotropic level (in some cases at the user's choice) such that all subsequent calculations may be expressed in dBi. The normalisation procedure is described in Section 4.1.3.

Some of the feed models mentioned above include the near-field effects from the source, such as the Gaussian feed/beam model and the spherical wave expansion, while other feed models, like the radiating apertures are only valid in the far field. However, for all feed models the user may choose to calculate the near field via an internal spherical wave expansion (SWE) of the far field. With N being the upper radial index in the SWE, the expansion will be valid outside a sphere (the spherical-mode sphere) with radius

$$r_{swe} = N/k , \quad (2.3-1)$$

k being the wave number, and with its centre at the origin of the coordinate system in which the feed is defined.

When the field from a feed shall be evaluated at a short distance from the feed, the SWE is very convenient. Since the SWE is only valid outside the spherical-mode sphere, any attempt to calculate the field inside this sphere will result in a warning being issued. In order to inspect whether all field points are outside the sphere, the user should take advantage of the possibility to make a drawing of the spherical-mode sphere.

At large distances from the feed, the radiated field may be approximated by its far-field. Conventionally this transition occurs at the so-called Rayleigh distance, R , defined as the distance at which the path length error at the edges of a plane aperture of maximum dimension D is less than 22.5° , or

$$R = \frac{2D^2}{\lambda} . \quad (2.3-2)$$

Using the same origin as the spherical-mode sphere, a sphere with radius equal to the Rayleigh distance may similarly be drawn. This can be useful in order to estimate whether a scatterer illuminated by a feed is in its near or far field.

An example for a rectangular horn antenna with aperture dimensions 3λ by 2λ , and hence a maximum aperture dimension of

$$D = 2r_o = \sqrt{3\lambda^2 + 2\lambda^2} \cong 3.6\lambda , \quad (2.3-3)$$

is illustrated in Figure 2.3-1. The radius of the spherical-mode sphere then becomes

$$r_{swe} = N/k \cong r_o + 1.6\lambda = 3.4\lambda \quad (2.3-4)$$

while for the Rayleigh distance we find

$$R = 2D^2/\lambda = 26\lambda . \quad (2.3-5)$$

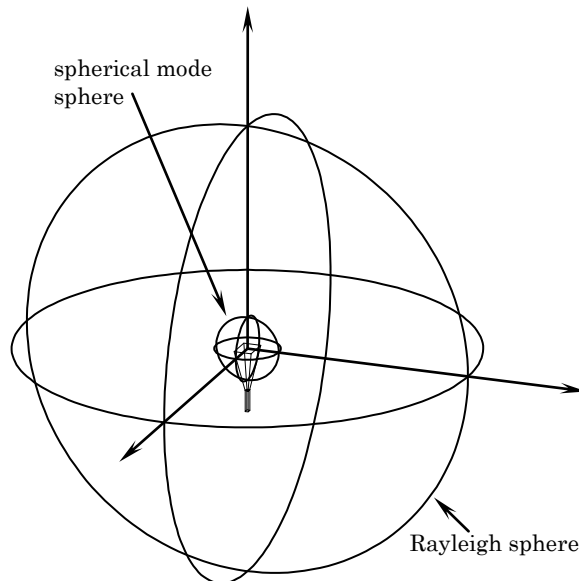


Figure 2.3-1 Illustration of SWE and Rayleigh spheres for a rectangular horn.

The position of feed elements relative to other components in an antenna system is given with reference to a coordinate system. This also determines the direction of radiation and polarisation of the feed.

The feed elements may be combined in feed arrays which are described in Section 2.3.4.

2.3.1.1 *Tabulated pattern*

A general way to represent the radiation from a feed is through tabulated data for its radiation pattern, which may originate from measurements or calculations, the latter performed by GRASP or other electromagnetics software. The radiation pattern data shall contain two orthogonal polarization components, either in the far field or in the near field, given in a regular (θ, ϕ) -grid on a sphere enclosing the source. A sufficiently large part of the radiation from the feed must be available, including at least the main beam region. The data must be represented by complex numbers, i.e. as Real and Imaginary parts, not as amplitude and phase, although the latter representation is the most common format for measured data.

The data shall be organized in polar θ -cuts (i.e. constant ϕ , varying θ), either asymmetrical in the interval $0 \leq \theta \leq \theta_{\max}$ for $\phi = \phi_0$, where θ_{\max} is the maximum polar angle, $\theta_{\max} \leq 180^\circ$, or symmetrical about the pole, i.e. within $-\theta_{\max} \leq \theta \leq \theta_{\max}$, which then includes both the cut for $\phi = \phi_0$ and $\phi = \phi_0 + 180^\circ$.

Unless the user selects otherwise, GRASP will automatically generate a spherical wave expansion of the tabulated data, which then forms the basis for all subsequent calculations with this feed. The expansion coefficients may be stored on file for later use, for example as input to the feed described in Section 2.3.1.2.

2.3.1.1.1 Number of modes included

The spherical wave expansion requires field information for a full sphere and zero values will be inserted for $\theta > \theta_{\max}$, when $\theta_{\max} < 180^\circ$. Further it is required that $\theta = 180^\circ$ is a grid point.

Assume that the tabulated radiation pattern, possibly supplemented with zeros, contains M_ϕ equispaced asymmetric polar cuts, each containing N_θ values equispaced in the interval $0 \leq \theta \leq 180^\circ$. The spherical wave expansion program described in Section 3.10 will generate modal coefficients with indices m and n , where the azimuthal index

$$m = 0, \pm 1, \pm 2, \dots, \pm M , \quad (2.3-6)$$

and the polar index

$$n = 1, 2, \dots, N , \quad (2.3-7)$$

and where the maximum indices are given by

$$M = M_\phi / 2 - 1 \quad (2.3-8)$$

and

$$N = N_\theta - 1 . \quad (2.3-9)$$

In order to be able to regenerate a radiation pattern from tabulated data, the data spacing must fulfil the Nyquist sampling criterion, which results in requirements to the maximum spacing for the tabulated data.

Theoretically, if a radiating or scattering structure is confined within a spherical volume with radius r_o , measured from the reference centre for the tabulated field data (i.e. the centre of rotation for a measured pattern), then the sample spacing shall be $\lambda/2$ or less over this spherical surface. The number of samples for $0^\circ \leq \theta \leq 180^\circ$ is N_θ so we have $N_\theta - 1$ intervals. This gives a minimum value for N_θ

$$N_\theta - 1 = \frac{\pi r_o}{\lambda/2} = kr_o . \quad (2.3-10)$$

The theoretical number of polar modes is therefore $N = N_\theta - 1$. Modal coefficients with a larger polar index will decrease in amplitude for increasing index value. In order to ensure a sufficient accuracy, the number of polar modes, and hence the number of θ -samples, shall be increased so that at least

$$N_\theta - 1 = N = kr_o + \max 3.6\sqrt[3]{kr_o}, 10 \quad (2.3-11)$$

are present (rounded to the nearest larger integer).

When the field level at angles larger than θ_{\max} is low, the field may be truncated at $\theta = \theta_{\max}$. For $\theta_{\max} < 90^\circ$, the circumference of the largest circle in ϕ is $2\pi r_o \sin \theta_{\max} < 2\pi r_o$. On this circle there shall be at least M_ϕ samples spaced by $\lambda/2$, thus M_ϕ is given by

$$M_\phi = \frac{2\pi r_o \sin \theta_{\max}}{\lambda/2} \quad (2.3-12)$$

or, in order to ensure sufficient accuracy similar to (2.3-11),

$$M_\phi = 2N \sin \theta_{\max} \quad . \quad (2.3-13)$$

If the tabulated pattern is not available with spacings in θ and ϕ as required in (2.3-11) and (2.3-13) the regenerated pattern will not be accurate, and aliasing may occur.

The pattern data may be sampled in a denser grid than necessary for the spherical wave expansion. This is especially the case for automatic measurement facilities. Irregularities in the sampled data, resulting from e.g. noise, instrumentation errors or other sources, may show up as higher order harmonics. These may be excluded by the user by restricting the number of modes to what can actually be attributed to the radiation from the source.

It is recommended that the θ -spacing is a divisor in 180° , otherwise the spacing will be changed to include both $\theta = 0^\circ$ and $\theta = 180^\circ$ as grid points. The field values will be interpolated by third order (cubic) polynomial interpolation to the new

sample points within $|\theta| < \theta_{\max}$. For this interpolation to be accurate it is required that the θ -spacing is four times as dense as required by (2.3-11), i.e. less than $\lambda/(8r_o)$.

2.3.1.1.2 Cut adjustment

The data point for $\theta = 0^\circ$ shall appear in all cuts. When the data originate in measurements it may happen that the field values in the different cuts are not the same at $\theta = 0^\circ$. If the field is given in linear or circular field components it is possible to impose an on-axis-adjustment. In that case all field values in a cut are corrected with a factor, such that the co-polar value at $\theta = 0^\circ$ becomes the same as for the first cut.

2.3.1.1.3 Time factor

The time factor of the data may be specified as either $e^{j\omega t}$ or $e^{-i\omega t}$. In the latter case the input will be complex conjugated to the internal $e^{j\omega t}$ notation. In measurements most equipment works according to $e^{j\omega t}$. This can be checked by increasing the measurement distance slightly. When the time dependence is $e^{j\omega t}$, the phase dependence is given by e^{-jkr} and the phase will decrease when the distance is increased.

2.3.1.1.4 Phase reference

It is possible to adjust the phase reference point for far-field input only. In all the feed models the phase reference is always the origin of the coordinate system in which the feed is specified. For tabulated measured data the phase reference point is the point of rotation for the measurements, which most likely does not coincide with the phase centre for the measured data. Since the radiated field propagates with phase fronts with origin in the phase centre, the best results are obtained when distances and directions are referred to this point. For a reflector antenna for example the phase centre of the feed and not the centre of rotation from an arbitrary measurement shall be positioned in the reflector focus.

The situation is depicted in Figure 2.3-2. Assume that the point O is the phase centre of the feed. This point is therefore selected as the origin of the feed coordinate system. Assume further that the tabulated input data are pattern measurements around the point M .

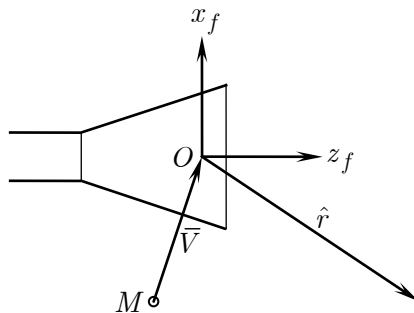


Figure 2.3-2 Repositioning of phase reference point.

Let the tabulated input data around M be denoted E_{far}^M . This data may be referred to the feed coordinate system origin by

$$E_{far}^O = E_{far}^M e^{-jk\bar{V}\cdot\hat{r}} , \quad (2.3-14)$$

where \bar{V} is the vector from M to O and \hat{r} is a unit vector in the far-field direction.

After being read from file the tabulated far field is multiplied by the factor $e^{-jk\bar{V}\cdot\hat{r}}$, and the resultant field is then the basis for the subsequent spherical wave expansion.

2.3.1.1.5 Normalisation

Finally, the input data can be normalised to dBi or the data can be scaled by a complex factor. The normalisation assumes that all radiated power is contained within the angular region defined by the tabulated data. This is not necessarily the entire sphere, as the range in θ can be limited.

2.3.1.2 *Feed defined by spherical wave expansion*

This model calculates the near field or the far field from a feed defined by a set of spherical wave coefficients stored in a file. These coefficients may have been generated from a measured or calculated pattern via the feed described in Section 2.3.1.1 or they can be generated directly by GRASP using any of the available electromagnetic sources as input. The theory for the spherical wave expansion is described in detail in Section 3.10.

2.3.1.2.1 *Number of modes included*

The number of modes in a spherical wave expansion is characterised by the maximum polar index, N , and the maximum azimuthal index M . It may be desirable to reduce the number of modes to less than those present in the data file, for example, if the number of modes in the file is larger than prescribed by the physical extent of the antenna's minimum sphere. A reduced mode set will decrease the computation time for the field and may increase the accuracy of the field computations, since modes in excess may contribute to the numerical noise of the computations.

The maximum indices for the polar and azimuthal modes to be used in the evaluation of the expansion are user controlled. Further, selected azimuthal modes may be excluded from the calculations, allowing for mode filtering.

Another possibility for excluding azimuthal modes from participating in the calculations is by their relative power content. Let P_m denote the power of all modes with the same azimuthal index $|m|$. Then, if the power of that mode relative to the total power in the set of spherical wave coefficients is less than a specified power threshold level P_t , the mode will be excluded. In other words, modes for which

$$P_m < P_t \sum_{m=-n}^n P_m \quad (2.3-15)$$

do not take part in the calculations. The relative power threshold P_t is a non-negative number less than 1.

2.3.1.2.2 *Phase reference*

The phase is calculated with respect to the centre of the sphere of the spherical expansion. This centre is the origin of the coordinate system in which the feed is defined. If the spherical expansion originates in measurements then the centre is also the centre of the sphere over which the measurements were carried out, i.e. the centre of rotation in a conventional set-up. If the spherical expansion is obtained from calculations of a field on a sphere, it is the centre of this sphere, which defines the phase reference.

2.3.1.2.3 *Normalisation*

The spherical-wave coefficients from the input file may be normalised so that the total radiated power equals 4π watt. Following this normalisation, the patterns will be expressed in dBi. If no normalisation is carried out, the power content in the input spherical-wave coefficients is retained.

2.3.1.3 *Gaussian beam*

The Gaussian feed concept provides a good model of the feed's far field as well as its near field, which is important e.g. when a reflector is in the near-field of its feed horn. Therefore, the internal spherical wave expansion calculation is not needed for this model.

2.3.1.3.1 *The source model*

The Gaussian feed is a point source radiating a tapered beam. This is obtained by positioning the source in complex space. The field of the source satisfies Maxwell's equations in the near field as well as in the far field.

The point source is a z -directed Huygens source, which consists of an electrical x -directed short dipole (a Hertzian dipole) and a y -directed short magnetic dipole, cf. Figure 2.3-3. The choice of the Huygens source entails the added advantage that in any direction its polarisation is co-polar to the linear x -

polarisation, as defined according to Ludwig's 3rd definition, cf. Section 4.1.4.1.

The complete field expressions for the electric and magnetic short dipoles are well known (e.g. Stratton, 1941 or Hansen, 1988. Expressions for the z -directed short dipoles are given in Section 2.3.1.11) but lengthy, and we will only give the expression for the Huygens source at large distances r ,

$$\bar{E}(r, \theta, \phi) = E_0 \frac{e^{-jkr}}{r} (1 + \cos \theta) (\cos \phi \hat{\theta} - \sin \phi \hat{\phi}) , \quad (2.3-16)$$

where E_0 is a constant.

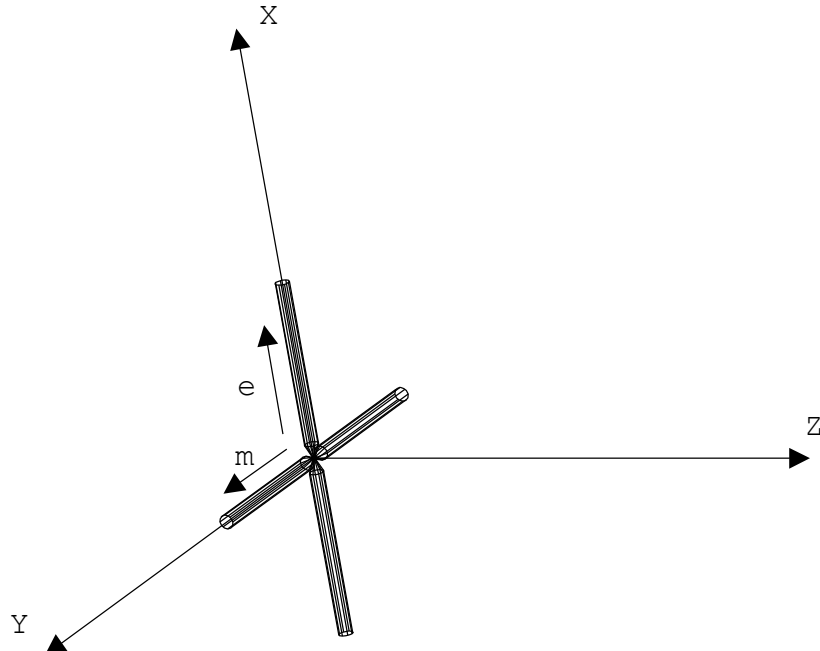


Figure 2.3-3 The Huygens source consisting of an electric and a magnetic dipole.

When a source is located at a point with the complex position $(x, y, z) = (0, 0, -jb)$ it will generate a Gaussian beam in the positive z -direction. The distance b is denoted the imaginary displacement. We will examine this by considering the field from a scalar point source

$$u = \frac{e^{-jkR}}{R} \quad , \quad (2.3-17)$$

where R is the distance from the source to the field point. The function u represents an exact solution to Helmholtz' equation for complex source points and/or field points and it has the same R -dependence as appears in (2.3-16). It is therefore well suited for investigating the properties of the Gaussian beam.

The distance R is in general a complex quantity. Obviously, only field points in real space are of practical interest and we will therefore investigate (2.3-17) in more detail for real field points $P(x, y, z)$.

The distance from the source to the field point is then

$$R = \sqrt{x^2 + y^2 + z^2 - b^2 + j2bz} \quad . \quad (2.3-18)$$

The field is seen to be rotationally symmetric around the z -axis and for later use we introduce

$$\rho^2 = x^2 + y^2 \quad . \quad (2.3-19)$$

If we express P in spherical $r\theta\phi$ -coordinates we have

$$z = r \cos \theta \quad (2.3-20)$$

and if P is in the far field, $b \ll r = \sqrt{x^2 + y^2 + z^2}$, we find

$$\begin{aligned} R &\cong \sqrt{r^2 + j2br \cos \theta} \\ &\cong r + jb \cos \theta \end{aligned} \quad (2.3-21)$$

which inserted into (2.3-17) gives the expression for the field at far field points

$$u = e^{kb \cos \theta} \frac{e^{-jkr}}{r} \quad . \quad (2.3-22)$$

This expression shows that the complex point source radiates a beam in the positive z -direction and the beam width is controlled by the parameter b .

The field from a scalar point source, (2.3-17), modifies for far field points to (2.3-22) when the source is moved into the complex space. It can be shown, that (2.3-16) in the same way modifies to

$$\bar{E}(r, \theta, \phi) = N_f \frac{e^{-jkr}}{kr} e^{kb \cos \theta} (1 + \cos \theta) (\cos \phi \hat{\theta} - \sin \phi \hat{\phi}) \quad (2.3-23)$$

for far field points when the Huygens source is moved to the complex position $(x, y, z) = (0, 0, -jb)$. The normalisation constant, which normalises the field to dBi is denoted N_f .

From the above expression it is seen that the beam width is controlled by the parameter b . The far-field taper at a given angle θ can be determined from (2.3-23). If the taper is specified to A dB ($A < 0$) at the angle θ , this is obtained for

$$b = \frac{20 \log((1 + \cos \theta)/2) - A}{20 k(1 - \cos \theta) \log e} , \quad (2.3-24)$$

and A expressed by b is

$$A = 20 \log((1 + \cos \theta)/2) - 20 b k (1 - \cos \theta) \log e . \quad (2.3-25)$$

2.3.1.3.2 Comparison to an accurate feed model

It is interesting now to compare the field from a realistic feed horn with that of the complex source. Figure 2.3-4 shows near-field patterns as well as the far-field pattern of a conical corrugated feed horn under balanced conditions. The aperture diameter is 5λ and the half flare angle is 9° . The field is plotted on spheres with radius r_m and centre at the far-field phase centre. The similar plots of the field from a complex source point are shown in Figure 2.3-5, the quantity b being determined such that the far-field taper at $\theta = 15^\circ$ is the same for the two cases, i.e. 12.6 dB giving a b of 6.7λ .

Comparing Figure 2.3-4 and Figure 2.3-5 it is seen that within the main beam region down to about 10-15 dB below the peak (the usual region used for illumination of the subreflector in a reflector antenna system) the complex source point model

yields results that are completely satisfactory for practical applications.

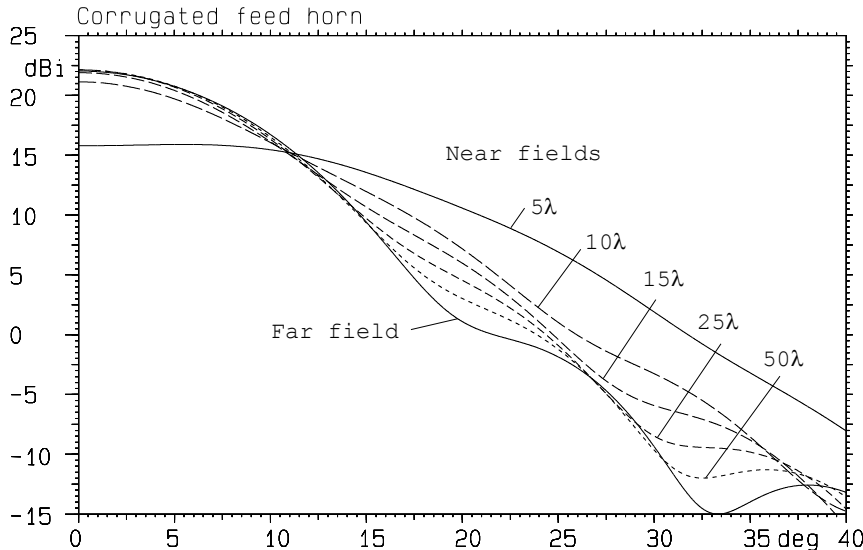


Figure 2.3-4 Fields of conical corrugated feed horn at different near field sphere radii.

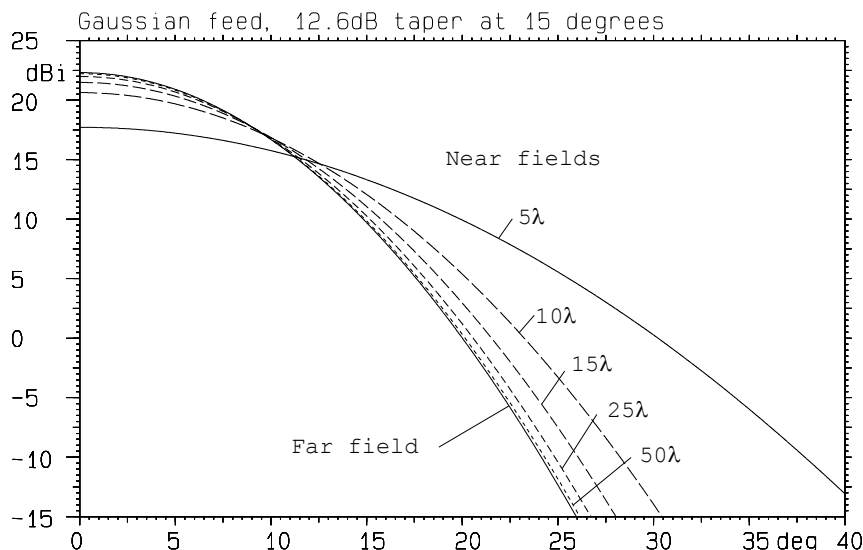


Figure 2.3-5 Fields of complex source point, corresponding to corrugated feed horn above.

2.3.1.3.3 *Near-field properties of the complex point source*

Let us again consider the field from the simple scalar source, (2.3-17). For near-field points in the plane $z = 0$ we have

$$\begin{aligned} R &= \sqrt{\rho^2 - b^2} , \quad \text{for } \rho > b \\ &= j\sqrt{b^2 - \rho^2} , \quad \text{for } \rho < b \end{aligned} \quad (2.3-26)$$

As practically all power is carried within $\rho < b$ we apply the latter expression and obtain for the near field

$$u = \frac{1}{j\sqrt{b^2 - \rho^2}} e^{k\sqrt{b^2 - \rho^2}} \quad (2.3-27)$$

and if we normalise this field to unity for $\rho = 0$ the normalised field may be written as

$$u_n = \frac{1}{\sqrt{1 - \rho^2/b^2}} e^{kb(\sqrt{1-\rho^2/b^2}-1)} \quad (2.3-28)$$

Figure 2.3-6 shows a plot of u_n as a function of ρ/λ for $b = 2\lambda, 5\lambda$ and 10λ . The expressions for u and u_n become singular at $\rho = b$ but ρ must be very close to b before the singular factor is important. For example, for $\rho = 0.99999b$ the singular factor has increased to only 220 while the exponential term is $3.5 \cdot 10^{-6}$, even for b as low as 2λ . The product of the two terms is therefore still small and the effect is invisible in the figure.

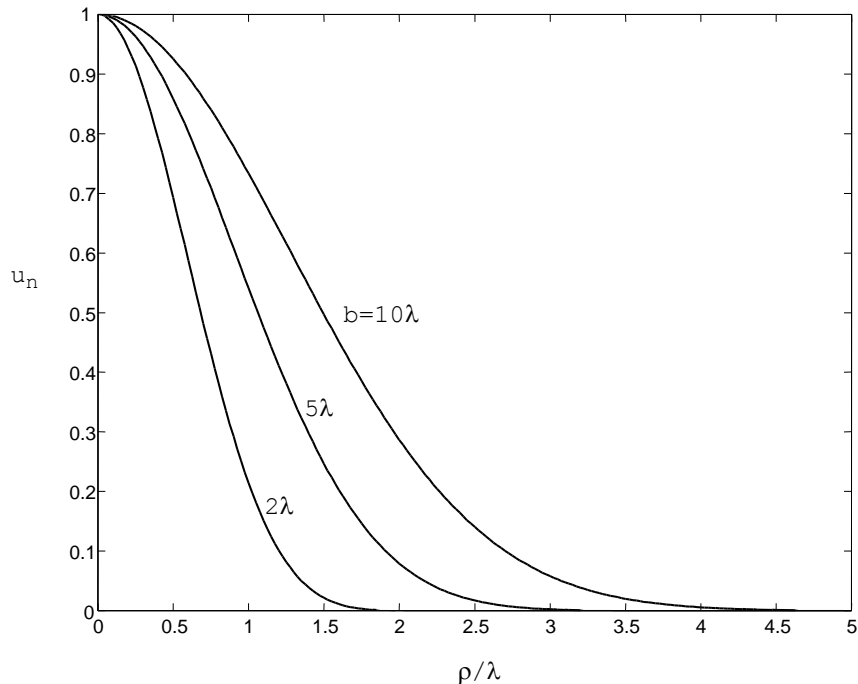


Figure 2.3-6 Normalised field u_n in plane $z=0$ for a point source located at $(0,0,-jb)$, $b = 2\lambda$, 5λ and 10λ .

2.3.1.3.4 Gaussian beams

We will now demonstrate that the near field of the complex point source agrees with the usual Gaussian beam formulas. In the so-called paraxial region (near the axis), $z^2 + b^2 \gg \rho^2$, we have by definition (2.3-18)

$$R = \sqrt{\rho^2 + z + jb^2} = z + jb \sqrt{1 + \frac{\rho^2}{z + jb^2}} \quad (2.3-29)$$

$$\cong z + jb + \frac{1}{2} \frac{\rho^2}{z^2 + b^2} \frac{z - jb}{z + jb}$$

which gives

$$\frac{e^{-jkR}}{R} \cong -\frac{j}{b} e^{kb} \frac{w_o}{w} \exp\left(-\frac{\rho^2}{w^2} - j \frac{k\rho^2}{2R_c} - j kz - \Phi\right) \quad (2.3-30)$$

where

$$w^2(z) = w_0^2 \left(1 + \left(\frac{z}{b}\right)^2\right), \quad w_0^2 = \frac{2b}{k} \quad (2.3-31)$$

$$R_c(z) = z \left(1 + \left(\frac{b}{z}\right)^2\right) \quad (2.3-32)$$

$$\Phi(z) = \text{Arc tan} \frac{z}{b} \quad (2.3-33)$$

Alternatively, if the beam radius, w , and the radius of curvature, R_c , are given at a point on the beam, these equations may be inverted to give the beam radius at the waist

$$w_o = \frac{w}{\sqrt{1 + \left(\frac{kw^2}{2R_c}\right)^2}}, \quad (2.3-34)$$

and the distance to the waist

$$z = \frac{R_c}{1 + \left(\frac{2R_c}{kw^2}\right)^2}. \quad (2.3-35)$$

Note that R_c is positive for a divergent beam and negative for a convergent beam.

From (2.3-30) it is seen that the cross-sectional amplitude distribution of the beam, $\exp(-\rho^2/w^2)$, is similar at any cross section, but its extent and the radius of curvature vary along the path of the beam. This cross-sectional amplitude distribution is Gaussian and the beam radius, w , is defined by the relative amplitude $1/e$ which is for $\rho = w$ as given by (2.3-31). The beam has its minimum radius, the beam waist, for $z = 0$ and it is given by $w = w_0$.

The phase varies with ρ as $\exp(-jk\rho^2/2R_c)$, i.e. as a spherical wave front with radius of curvature R_c given by (2.3-32). The centre of curvature of the beam field is located b^2/z behind the waist. At the beam waist, $z = 0$, the radius of curvature of the wave front is infinite. For increasing z the radius of curvature decreases to its minimum value $R_c = 2b$ for $z = b$. For large z the centre of curvature converges towards $z = 0$.

A typical beam is illustrated in Figure 2.3-7. The two points, F_1 and F_2 , are located the distance b from the beam axis. From (2.3-17) it can be shown that the surfaces of constant phase are ellipsoids, which in the cut of the figure are ellipses with focal points F_1 and F_2 . The ellipsoids are obtained by rotating the figure around the beam axis. The orthogonal curves in the figure (hyperbolas with the same foci) represent surfaces of constant amplitude.

The discussion above, including Figure 2.3-7, is based on the isotropic field of (2.3-17), and the additional distance independent amplitude factor $1 + \cos\theta$ of the Huygens source, cf. (2.3-23), is not included.

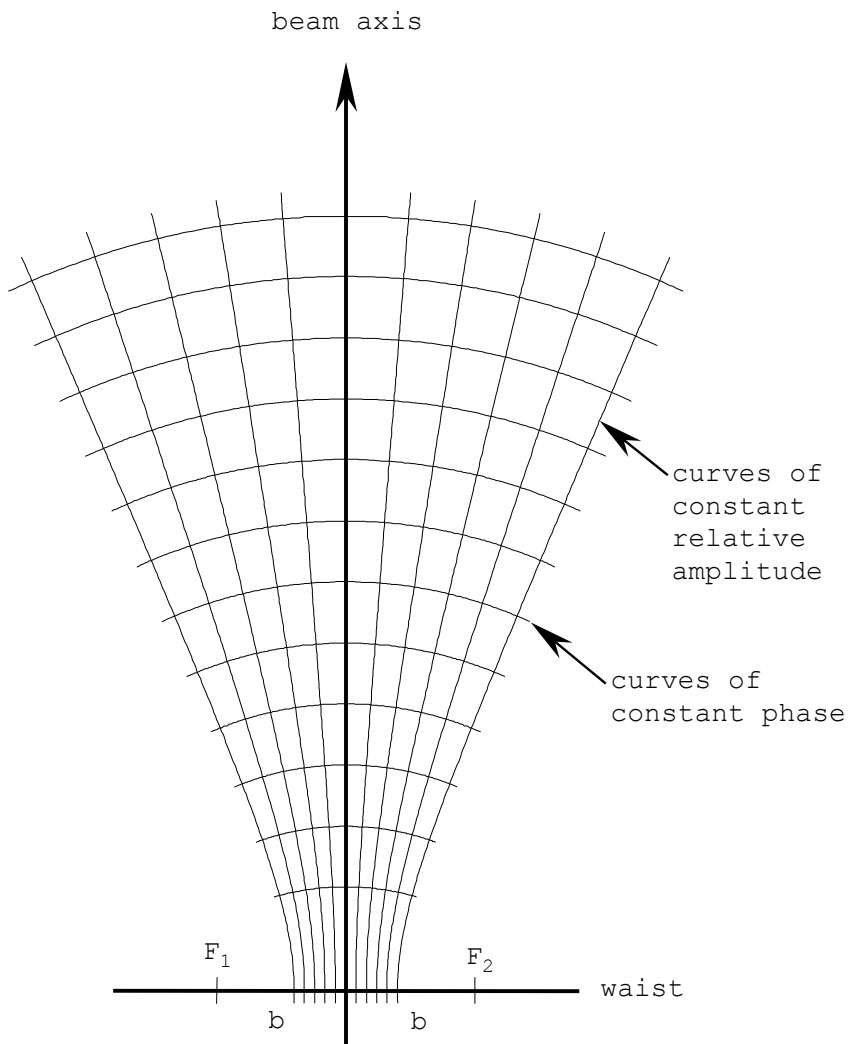


Figure 2.3-7 A typical Gaussian beam. The beam is rotationally symmetric around the axis.

2.3.1.3.5 *Definitions of a complex point source in GRASP*

A complex point source can be defined in two ways in GRASP:

- by specifying the taper A at the angle θ (far field specification) in which case the imaginary displacement b is calculated from (2.3-24), or

- by specifying the beam radius, w in (2.3-31) and the radius of curvature, R_c in (2.3-32) (near field specification). If the Gaussian beam is supposed to model a corrugated horn of flare angle θ_o and aperture diameter D_h , see Figure 2.3-8, it can be shown that for small values of θ_o the beam radius in the aperture is $w = 0.32D_h$ while the radius of curvature is equal to the slant length.

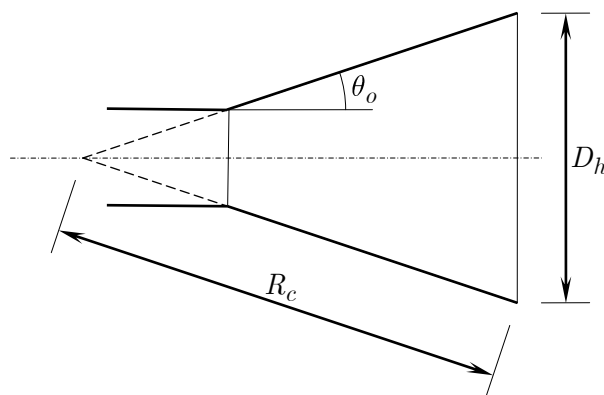


Figure 2.3-8 Horn parameters for the specification of an equivalent Gaussian beam.

For both options the polarisation can be specified by the user to be linear along the x - or the y -axis, or to be right- or left-hand circular.

2.3.1.3.6 *Forced far-field calculations*

For some applications, e.g. in GTD calculations, the far field from the feed is required, even though the field point may be in the near field from the feed. When imposing this forced far-field determination, the field at a finite distance will be calculated as the far field multiplied by e^{-jkr} / kr . This offers the possibility to check whether a reflector or a field point is in the near or in the far field from the illuminating source. First, the field is calculated by the Gaussian beam with its near-field

capabilities enabled and next the field is calculated as a forced far field. If the patterns are different the field point is in the near-field zone of the source.

2.3.1.4 Simple tapered pattern

An elementary, yet very useful feed model is provided by the simple tapered pattern, which is specified by its taper (or beam width) in E- and H-planes. It is possible to specify different E- and H-plane tapers and thereby generate an elliptical beam. This feed model is particularly useful for small, rotationally symmetric feeds with an $m = 1$ excitation, such as a conical horn fed by a TE_{11} circular waveguide mode.

2.3.1.4.1 Feed model

The feed pattern is described by the amplitude function $A(\theta, \phi)$, which is normalised to isotropic level. The main direction is the z -axis, $\theta = 0^\circ$. In the xz -plane, $\phi = 0^\circ$, the pattern function, $A(\theta, \phi)$, is described by

$$A(\theta, 0^\circ) = A_0 \cdot 10^{\left(\frac{A_x}{20} \theta/\theta_0 - 2\right)}, \quad 0^\circ \leq \theta < 180^\circ, \quad (2.3-36)$$

where A_x is the amplitude level in dB at $\theta = \theta_0$ relative to the maximum level and A_0 is a normalisation constant. The pattern is described in a similar way in the yz -plane by $A(\theta, 90^\circ)$ and defined by the relative amplitude level A_y at the same angle, $\theta = \theta_0$. In the normal case both A_x and A_y are negative resulting in an ordinary beam with maximum for $\theta = 0^\circ$.

The radiated far field for a feed linearly polarised in the x -direction is now given by

$$\bar{E} = A(\theta, 0^\circ) \cos \phi \hat{\theta} - A(\theta, 90^\circ) \sin \phi \hat{\phi} \quad (2.3-37)$$

It is also possible to specify A_x and A_y to positive values or zero. This may be used in a front-fed reflector system to model an approximately constant amplitude of the aperture illumination. The values of A_x and A_y shall then be chosen such

that the inverse taper compensates for the distance attenuation from the feed to the reflector. In all cases the feed radiation continues beyond the angle θ_0 .

With A_x and A_y being equal, the model will radiate a circularly symmetric beam with no cross polarisation at all. When A_x and A_y are different, the beam will be elliptically shaped and the cross polarisation will have its maximum in the 45° planes. If the difference between A_x and A_y is large, the pattern is distorted away from the elliptical shape and the elliptical pattern, Section 2.3.1.5, provides a better model. A comparison between the simple tapered pattern and the elliptical feed is described in connection with Figure 2.3-9.

2.3.1.4.2 *Polarisation*

The user specifies the polarisation, which can be linear along the x - or the y -axis, or right or left hand circular.

2.3.1.4.3 *Normalisation*

The normalisation constant A_0 is found by pattern integration. In the usual case where both A_x and A_y are negative, the integration is carried out down to 40 dB below the maximum level. If either A_x or A_y is positive or zero, the integration is carried out up to θ_0 . Nevertheless, the field is still generated according to (2.3-36), also for $\theta > \theta_0$.

2.3.1.4.4 *Cross polarisation*

A cross-polarisation may be specified. The cross-polar pattern is a replica of the co-polar pattern apart from the relative level and phase, which are to be specified.

2.3.1.5 *Elliptical pattern*

Another simple feed model is provided by the elliptical pattern, which is specified by different tapers in two orthogonal directions to generate an elliptical beam. The field generated by this model contains no cross polarisation at all.

2.3.1.5.1 Feed model

The feed pattern is given by the amplitude function $A(\theta, \phi)$, which is normalised to isotropic level. The main direction is the z -axis, $\theta = 0^\circ$. The pattern function is described by

$$A(\theta, \phi) = A_0 \frac{e^{-1-\cos\theta}}{1+\cos\theta} e^{\alpha \cos^2 \phi + \beta \sin^2 \phi} . \quad (2.3-38)$$

$0^\circ \leq \theta \leq 180^\circ, \quad 0^\circ \leq \phi \leq 360^\circ$

Here α is defined by the amplitude level, A_{dB} , in the zx -plane at $\theta = \theta_{zx}$ relative to the maximum level. The pattern is described in a similar way in the zy -plane, where β is defined by the same relative amplitude level in dB, A_{dB} , but at the angle $\theta = \theta_{zy}$. In the normal case A_{dB} is negative resulting in a beam with maximum for $\theta = 0^\circ$ and with the parameter α given by

$$\alpha = \frac{\log \frac{1+\cos\theta_{zx}}{2} - A_{dB}/20}{1-\cos\theta_{zx} \log e} . \quad (2.3-39)$$

β is given correspondingly.

The radiated far field for a feed linearly polarised in the x -direction is now given by

$$\bar{E} = A(\theta, \phi)(\cos\phi \hat{\theta} - \sin\phi \hat{\phi}) . \quad (2.3-40)$$

It is also possible to specify A_{dB} to a positive value or zero. This may be used in a front-fed reflector system to model an approximately constant amplitude of the aperture illumination. The value of A_{dB} shall then be chosen such that the inverse taper compensates for the distance attenuation from the feed to the reflector.

In all cases the feed radiation continues beyond the angles θ_{zx} and θ_{zy} .

2.3.1.5.2 *Polarisation*

The user specifies the polarisation, which can be linear along any direction, or right or left hand circular.

2.3.1.5.3 *Normalisation*

The normalisation constant A_0 in (2.3-38) is found by pattern integration. In the usual case where A_{dB} is negative, the integration is carried out down to 100 dB below the maximum level. If A_{dB} is positive or zero, the integration is carried out up to the maximum value of θ_{zx} and θ_{zy} .

2.3.1.5.4 *Comparison between simple tapered pattern and elliptical pattern*

Both the simple tapered pattern and the elliptical pattern can be used to model a feed with non-rotational symmetry. The main difference is that the simple tapered pattern is restricted to $m = 1$ modes.

A contour plot of the co-polar radiation is shown in a uv -grid in Figure 2.3-9. Both the simple tapered pattern and the elliptical pattern are selected such that the taper is -20 dB at 30° in the zx -plane and at 15° in the yz -plane. The contour curves are nice ellipses for the elliptical pattern but of more complicated shapes for the simple tapered pattern.

The spherical wave expansion for this example shows that the maximum number of n-modes is around 30 for both feeds. The maximum index for m-modes is 1 for the simple tapered pattern by definition, and it is around 19 for the elliptical pattern. The cross polarisation vanishes for the elliptical pattern, whereas the simple tapered pattern generates four lobes 12.5 dB below the co-polar peak in the 45° planes about 13.5° from boresight.

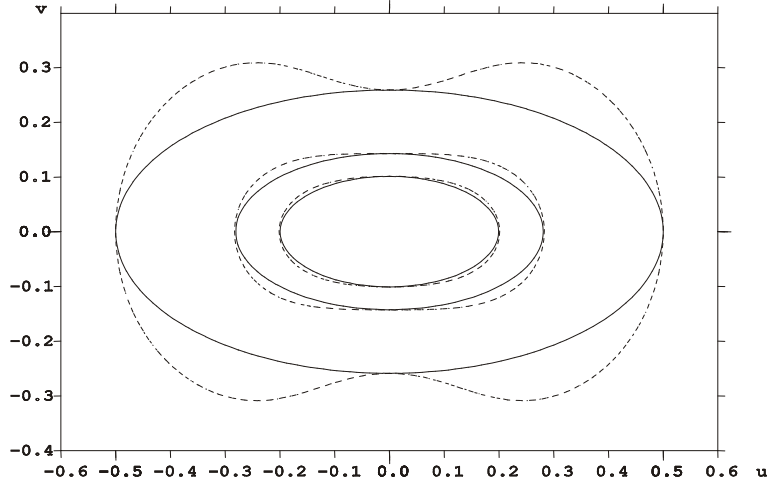


Figure 2.3.9 Contour plot in uv -grid of radiation from elliptical pattern (full line) and simple tapered pattern (dotted line).
Contour levels are 3, 6 and 20 dB below peak.

2.3.1.6 *Radiation from simple apertures*

This section describes simple models of typical feed horns for reflectors, namely

- the rectangular horn (Section 2.3.1.6.2)
- the conical horn (Section 2.3.1.6.3)
- the open-ended circular waveguide with the fundamental TE_{11} mode (Section 2.3.1.6.4)
- the Potter horn (Section 2.3.1.6.5)
- the horn with hexagonal aperture (Section 2.3.1.6.6)

With a knowledge of the aperture field distribution in terms of waveguide modes for the specific horn, the radiation from these horns can be calculated using standard aperture theory. For a horn with a non-zero flare angle, a quadratic phase factor takes care of the aperture phase error. In addition the horn aperture may be placed in an infinite ground plane.

When a horn flare is specified, the phase centre will not, in general, coincide with the centre of the horn aperture. The GTD procedure used in GRASP assumes however that the feed is a point source, and that the rays emanate from the phase reference point. Therefore, a phase correction which allows the user to move the feed along its axis to bring the feed phase centre to coincide with the origin of the feed coordinate system is provided.

For multi-feed applications, the program is able to deal with feeds of different dimensions or with different combinations of modes simultaneously.

First we will describe the common features for these aperture models, next the specific horns will be described in the sections given in the list above.

2.3.1.6.1 *Determination of the far field*

The far field from an aperture is derived by Risser (1949). The aperture is assumed to be that of an open-ended waveguide with the same, but arbitrary, cross section as the specified horn aperture.

An aperture integration of the modal waveguide field incident from the waveguide to the aperture yields

$$E_\theta = \frac{jkK}{4\pi} 1 + t \cos\theta \quad N_x \cos\phi + N_y \sin\phi \quad (2.3-41)$$

$$E_\phi = \frac{jkK}{4\pi} \cos\theta + t \quad -N_x \sin\phi + N_y \cos\phi \quad (2.3-42)$$

where the factor e^{-jkr}/kr has been suppressed. The modal radiation vector $\bar{N} = N_x \hat{x} + N_y \hat{y}$ is given by the integral of the transverse electric field \bar{E}^i over the aperture area A as

$$\begin{aligned} \bar{N} &= \int_A \bar{E}_i e^{jk(x \sin\theta \cos\phi + y \sin\theta \sin\phi)} dx dy \\ &= \int_A \bar{E}_i e^{jk\rho \sin\theta \cos\phi' - \phi} d\phi' \rho d\rho \end{aligned} \quad (2.3-43)$$

where the integration is carried out over the aperture in rectangular and in circular coordinates, respectively. The aperture electric field \bar{E}_i may include a phase factor when a horn flare is modelled. In (2.3-41) and (2.3-42) t is defined by

$$t = \begin{cases} k_g / k & \text{for TE modes} \\ k / k_g & \text{for TM modes} \end{cases} . \quad (2.3-44)$$

The longitudinal waveguide wavenumber k_g depends on the free-space wavenumber k and the modal transverse wavenumber $k_t = 2\pi / \lambda_c$, λ_c being the cut-off wavelength, i.e.,

$$k_g = \sqrt{k^2 - k_t^2} . \quad (2.3-45)$$

Waveguide modes below cut-off, $k^2 - k_t^2 < 0$, are not permitted.

The factor K in (2.3-41) and (2.3-42) is a normalisation factor, determined so that the total radiated power is 4π watt, whereby the field is given relative to isotropic level (in dBi). The normalisation is carried out by an integration of the transverse electric aperture field, E_{ti} ,

$$\int_A |E_{ti}|^2 da = 4\pi, \quad (2.3-46)$$

such that the normalisation factor K is given by

$$K = 1/\sqrt{t} . \quad (2.3-47)$$

If the horn aperture contains more than one mode, the excitation amplitude and phase of each mode shall be given. Each mode will be normalised as described above. After the amplitudes of all modes have been specified the sum of the square of the amplitudes is normalised to unity. As the modes are orthogonal the total radiated power remains 4π watt and the field is directly given in dBi.

The feed may be mounted in a ground plane by using

$$E_\theta^{gp}(\theta, \phi) = E_\theta^{fs}(\theta, \phi) + E_\theta^{fs}(\pi - \theta, \phi) \quad (2.3-48)$$

$$E_{\phi}^{gp}(\theta, \phi) = E_{\phi}^{fs}(\theta, \phi) - E_{\phi}^{fs}(\pi - \theta, \phi) \quad (2.3-49)$$

where E_{θ}^{fs} and E_{ϕ}^{fs} apply for the feed in free space, cf. Equations (2.3-41) and (2.3-42).

2.3.1.6.2 *Rectangular horn*

The traditional notation for waveguides and modes is followed here. This means that the waveguide dimensions are a and b along the x - and y -axis, respectively, and that the fundamental TE_{10} mode is y -polarised.

The mathematical description of the modes may be found in a textbook for waveguide modes and will not be given here, see for example Risser (1949, pp. 341-347), where also the expressions for \bar{N} , (2.3-43), may be found.

The polarisation is linear as given by the specified modes. For square apertures it is possible to obtain circular polarisation by adding a TE_{10} and a TE_{01} mode in phase quadrature.

For small feed elements the power normalisation based on the aperture integration (2.3-46) is inaccurate. For this reason the routine will automatically re-normalise the radiated power to 4π watt by numerical integration of the radiated field over the complete far-field sphere.

In the formulas of Section 2.3.1.6.1 the field in the aperture is assumed to be the undistorted waveguide field with the actual cross section. When the horn has a flare, the resultant phase curvature may be approximated by a quadratic phase term. This approximation is generally accepted and allows the radiation pattern to be expressed in a closed form by means of Fresnel integrals. Mathematical details are given in standard textbooks - e.g. Compton and Collin (1969).

The flare of the horn is specified by the slant flare lengths R_1 and R_2 in the xz -plane and the yz -plane, respectively, as shown in Figure 2.3-10. The quadratic phase curvature in the aperture is introduced by multiplication by the factor

$$e^{-jk\left(\frac{x^2}{2R_1} + \frac{y^2}{2R_2}\right)} . \quad (2.3-50)$$

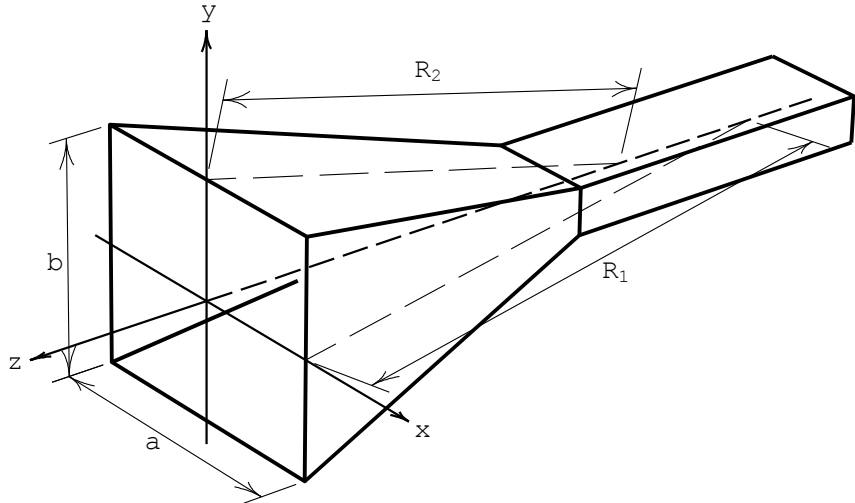


Figure 2.3-10 The general rectangular horn and the definition of the flare lengths R_1 and R_2 .

By default, the aperture of the rectangular horn is placed symmetrically in the xy -plane of the feed coordinate system and the phase of the calculated feed field is referred to the origin of this coordinate system. For horns with a flare the best-fit phase centre is positioned inside the aperture and it is possible to take this effect into account. The user may specify the distance, d , from the aperture to the phase centre. This distance is measured positive along the z -axis of the feed coordinate system and d is therefore negative in all practical cases. The phase of the feed far field is modified by the factor

$$e^{jkd(1-\cos\theta)} . \quad (2.3-51)$$

The above principles concerning the position of a feed are illustrated by the example shown in Figure 2.3-11 where a square pyramidal horn is considered. The side lengths of the aperture are $a = b = 4 \lambda$ and the flare lengths are $R_1 = R_2 = 8 \lambda$.

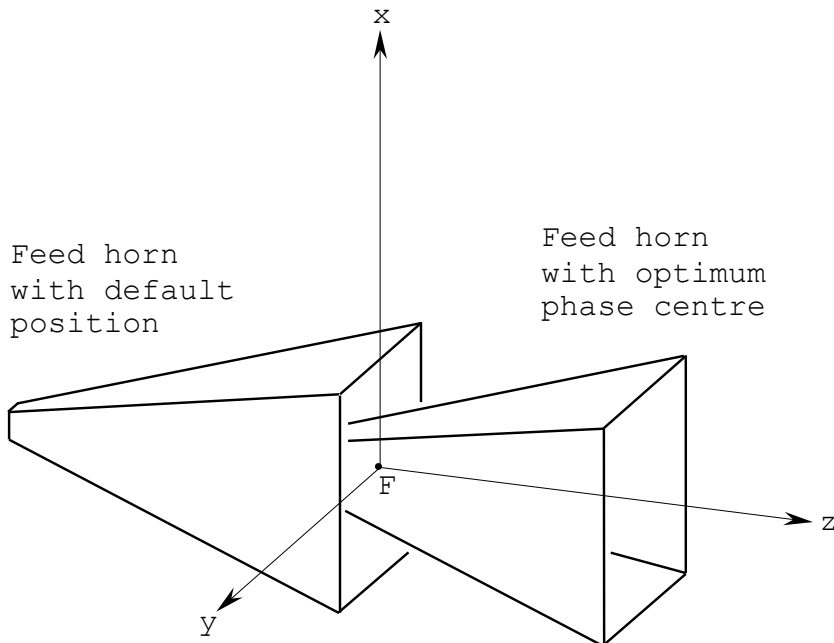


Figure 2.3-11 Square pyramidal feed with aperture side of 4λ and flare lengths of 8λ .

It is assumed that the horn is intended to be used as a feed for a paraboloidal reflector with focal point F . This point is therefore selected as the origin of the feed coordinate system.

By default, the horn will be located with the aperture in the xy -plane. The E- and H-plane patterns of the amplitude are shown in Figure 2.3-12 and the phases are shown in Figure 2.3-13.

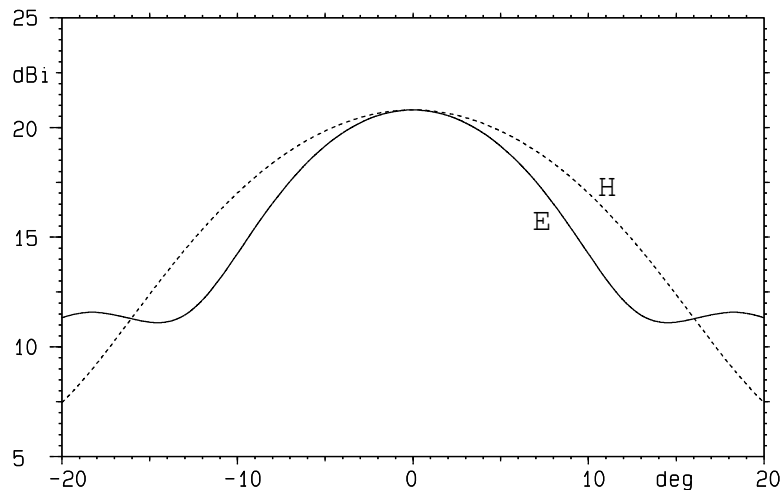


Figure 2.3-12 E- and H-plane patterns for the square horn in Figure 2.3-11.

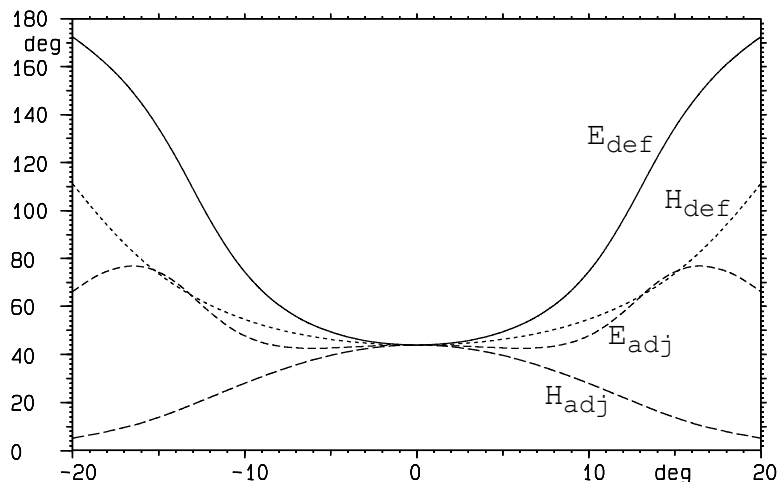


Figure 2.3-13 Phase patterns for the horn in Figure 2.3-11. The two curves for the horn in the default position are labelled with the subscript “def”, and the results for the horn with phase centre in the origin are labelled “adj”.

It is now assumed that the part of the pattern used for the illumination of the reflector extends from the feed axis and out to 15° . The phase patterns show that the phase on axis is 44° . For the default feed at 15° off-axis the phases are 135° and 73° .

in the E- and H-plane, respectively, or 104° in average. This corresponds to a phase increase of 60° relative to the phase on axis. This phase change shall be compensated by moving the horn forward. The distance is determined by (2.3-51) such that $kd(1 - \cos 15^\circ) = -60^\circ$ which gives $d = -4.9\lambda$. This new horn position is also shown in Figure 2.3-11 and the resulting phase patterns are plotted in Figure 2.3-13. It is evident that the phase variation is considerably reduced.

2.3.1.6.3 Conical horn

The description of the conical horn follows the traditional notation for circular waveguides. Thus, the radius of the circular waveguide is denoted a and the circular waveguide modes by TE_{mn} and TM_{mn} with m being the azimuthal mode index, and n the radial mode index. The mode indices are restricted to $0 \leq m \leq 5$ and $1 \leq n \leq 5$.

The far-field expressions given by (2.3-41) through (2.3-43) are evaluated analytically by Risser (1949, pp. 336-341) for the case with no flare.

When the horn has a flare, this may be included by introducing a quadratic phase deviation over the circular aperture,

$$e^{-jk\left(\sqrt{\rho_1^2 + \rho^2} - \rho_1\right)}, \quad (2.3-52)$$

where ρ is the radial position in the aperture, $0 \leq \rho \leq a$, and ρ_1 is the distance along the axis from the aperture plane to the apex of the flare cone.

In this case, the ρ -integration cannot be carried out analytically and it is then performed numerically by means of Romberg's method. The Bessel functions, $J_0(x)$ and $J_1(x)$, are evaluated by fast polynomial approximations. Bessel functions with higher index corresponding to higher order modes are obtained by recurrence.

The modal fields are linearly polarised and the polarisation is chosen such that a TE_{11} mode is polarised along the y -axis and a TM_{11} mode along the x -axis.

In addition to this, the modes may be freely rotated and the rotation may be specified separately for each mode. A mode with $m > 0$ which is rotated an odd multiple of $\pi/2m$ is orthogonal to the original mode. Only orthogonal modes should be specified for the power normalisation to remain valid.

Circular polarisation with arbitrary axial ratio may be modelled by two orthogonal TE_{11} modes in phase quadrature.

In the following sections special applications of the conical horn are given, namely the fundamental TE_{11} mode in an open-ended waveguide, and the Potter horn which has a low cross polarisation.

The normalisation of the circular waveguide feed is based on the description given in Section 2.3.1.6.1 such that the total radiated power is 4π watt and the field is given in dBi.

2.3.1.6.4 *Fundamental mode waveguide*

The fundamental mode waveguide is a simplified version of the conical horn. This feed is defined as an open-ended circular waveguide excited with the fundamental TE_{11} mode. The polarisation may be specified as linear along the x - or the y -axis or as right- or left-hand circular.

The field is normalised to dBi.

2.3.1.6.5 *Potter horn*

The Potter horn is a conical horn excited in the fundamental TE_{11} circular waveguide mode. A properly designed step discontinuity at the throat end of the horn excites the TM_{11} mode with the right amplitude and phase. The two modes propagate towards the horn aperture with different propagation constants. At the aperture the amplitude ratio of the two modes, TM_{11} / TE_{11} , is 0.4 with zero phase difference. This re-

sults in a horn with low sidelobes and low cross-polarisation, at the expense of a narrow bandwidth.

The polarisation may be either linear along the x- or y-axis, or right- or left-hand circular.

2.3.1.6.6 *Hexagonal horn*

Hexagonal horns are feeds with regular hexagonal apertures, which find application in compact feed arrays. The hexagonal aperture is placed in a local feed coordinate system as shown in Figure 2.3-14.

For the hexagonal waveguide cross section no analytic solution is available to Helmholtz' equation so that instead the finite element program IFEM (Pontoppidan, 1971) has been utilised to derive the eigenvalues and the generating fields for a number of modes. These aperture field data are included in the program code. An interface routine converts the aperture field data into azimuthal far-field pattern modes for aperture dimensions and modal combinations specified by the user. The azimuthal pattern modes are defined as for the tabulated pattern described in Section 2.3.1.1.

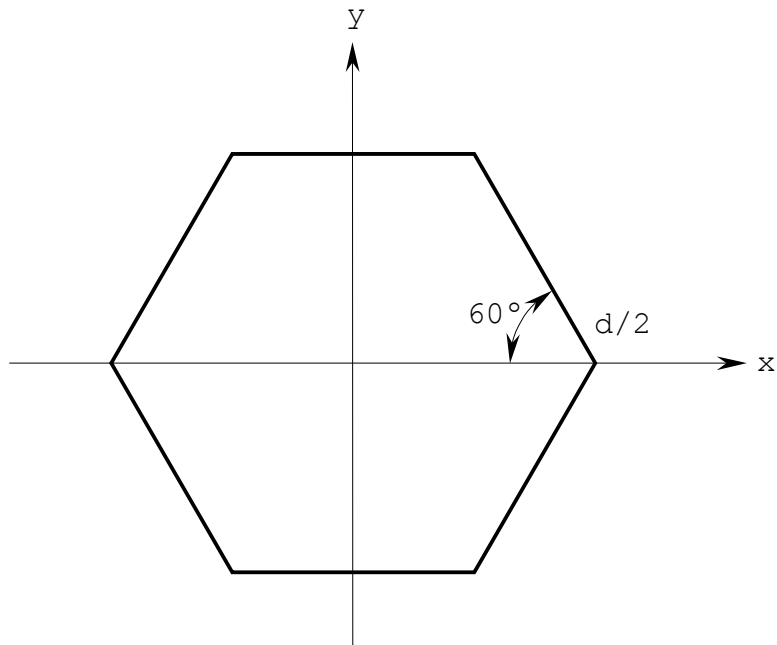


Figure 2.3-14 Regular hexagonal aperture.

Table 2.3-1 lists the 12 lowest eigenvalues determined for the regular hexagonal waveguide. The mode classification is derived from the one applicable to the circular cylindrical guide: the first index gives the azimuthal variation and the second the radial. The 12 modes are part of the software. The transverse wavenumbers are normalised with the radius $d/2$ of the circumscribing circle.

Mode type	Eigenvalues		
	IFEM	Bauer & Reiss	Exact
TE_{11b}	2.0108	-	-
TE_{11a}	2.0116	-	-
TM_{01}	2.6757	2.67495	-
TE_{21a}	3.2970	-	-
TE_{21b}	3.2990	-	-
TE_{01}	4.1891	-	4.18879
TE_{31b}	4.1907	-	4.18879
TM_{11b}	4.2590	4.25814	-
TM_{11a}	4.2590	4.25814	-
TE_{31a}	4.9901	-	-
TM_{21b}	5.6968	5.69666	-
TM_{21a}	5.6996	5.69666	-

Table 2.3-1 Eigenvalues for regular hexagonal waveguide.

Comparisons may be carried out with TM eigenvalues determined by Bauer and Reiss (1978) and exact results for the equilateral triangular waveguide (Schelkunoff, 1943, pp. 392-394). For modes with $m > 0$, the two orthogonal modes indicated by the suffixes a and b appear. These modes are degenerate except for TE_{31} . The differences in the table are due to numerical inaccuracies. For m equal to 1 and 2, the b -mode may be obtained by superposition of two a -modes rotated 60° and 120° . For $m = 3$, the modes repeat themselves by a 60° rotation so that no new mode can be obtained by superposition.

The modes TE_{01} and TM_{11} are not degenerate as in the circular guide.

The mode patterns are shown in Figure 2.3-15.

It may be noted that the approach adopted is general and may be extended to any other waveguide cross section with symmetries about the x -axis and the y -axis by replacing the data for the modal eigenvalues and eigenfunctions.

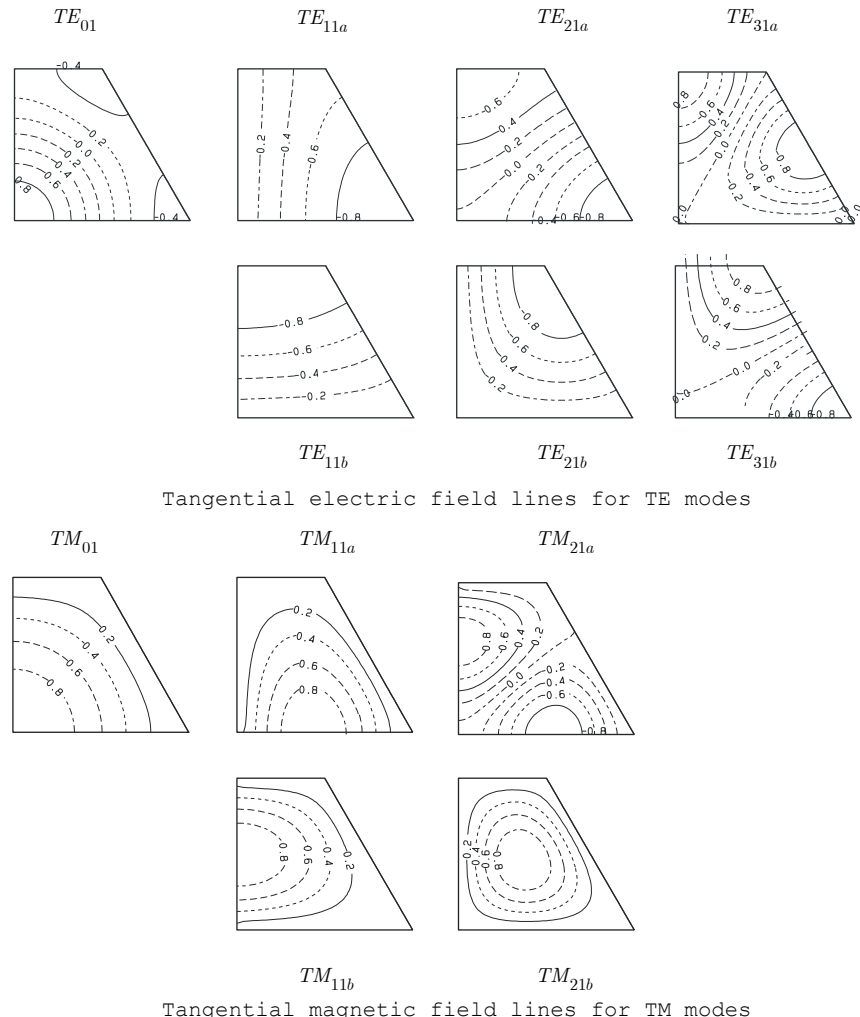


Figure 2.3-15 Transverse modal field in 1st quadrant of a hexagonal waveguide.

2.3.1.7 Microstrip feed

This feed model uses the simple Cavity Model (Bahl and Bhartia, 1982, pp. 86-91) with a TM_{11} cavity mode to approximate the performance of a circular microstrip patch radiator with an arbitrary radius, see Figure 2.3-16.

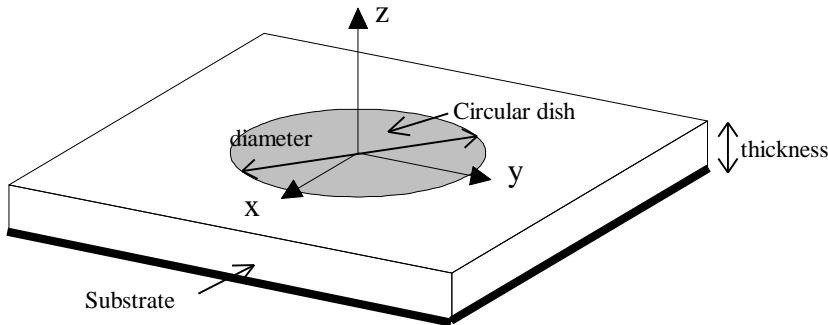


Figure 2.3-16 Circular disk microstrip antenna.

The effective radius

$$a_e = a \left[1 + \frac{2h}{\pi a \varepsilon_r} \left(\frac{\pi a}{2h} + 1.7726 \right) \right]^{1/2} \quad (2.3-53)$$

is used to account for the fringe waves along the edge of the patch. In (2.3-53), a is the patch radius, ε_r the relative dielectric constant and h the thickness of the substrate. The resonant wavelength of the patch is

$$\lambda_o = 2\pi\sqrt{\varepsilon_r}a_e / 1.841 \quad . \quad (2.3-54)$$

The normalised electric far field is derived from

$$E_\theta = 2K a_x \cos \phi + a_y \sin \phi \quad J_1' \quad ka \sin \theta \quad (2.3-55)$$

$$E_\phi = 2K -a_x \sin \phi + a_y \cos \phi \quad \frac{J_1}{ka \sin \theta} \cos \theta \quad (2.3-56)$$

where a_x and a_y are complex numbers specifying the linear polarisation components along the x - and the y -axis. Thus, any polarisation may be simulated. The factor

$$K = \frac{V_{gn} \sqrt{2/P_1}}{|a_x|^2 + |a_y|^2}^{\frac{1}{2}} \quad (2.3-57)$$

where

$$P_1 = \int_0^{\pi/2} \left(J_o^2 \ ka \sin \theta + J_2^2 \ ka \sin \theta - \frac{2}{ka^2} J_1^2 \ ka \sin \theta \right) \sin \theta d\theta \quad (2.3-58)$$

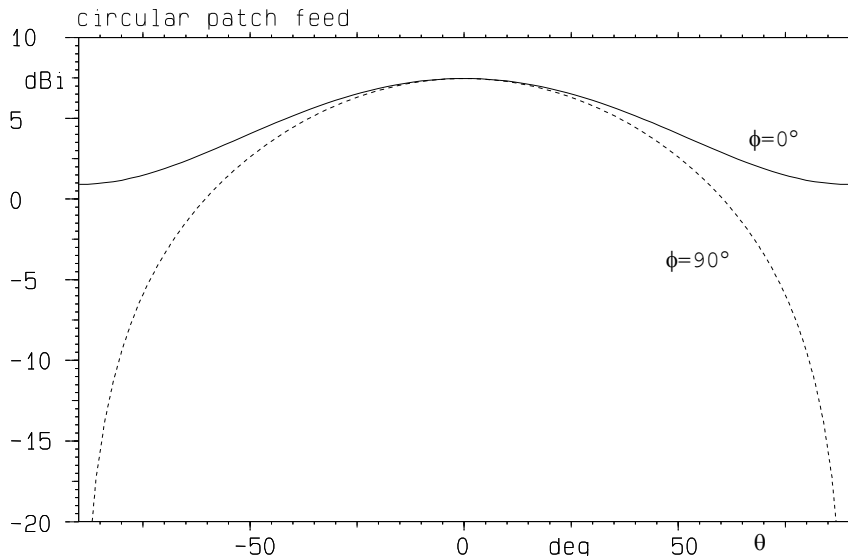


Figure 2.3-17 Far field from x -polarised circular patch antenna.

normalises for $V_{gn} = 1$ the field to isotropic level (James et al., 1981, Eq. 4.34). To account for losses, a value of V_{gn} less than one should be specified to obtain a realistic gain value. Mutual coupling and mismatch losses are not accounted for.

Figure 2.3-17 shows the far field in the principal planes, $\phi = 0^\circ$ and $\phi = 90^\circ$, for an antenna with the parameters: radius $a = .2\lambda$, thickness $h = .03\lambda$, dielectric constant $\varepsilon_r = 2$, and polarised in x -direction. Note that the field is zero in the lower hemisphere, $\theta > 90^\circ$.

2.3.1.8 Axial-mode monofilar helix feed

This feed model approximates the far field of a monofilar helix antenna radiating in axial mode.

The helix antenna is illustrated in Figure 2.3-18.

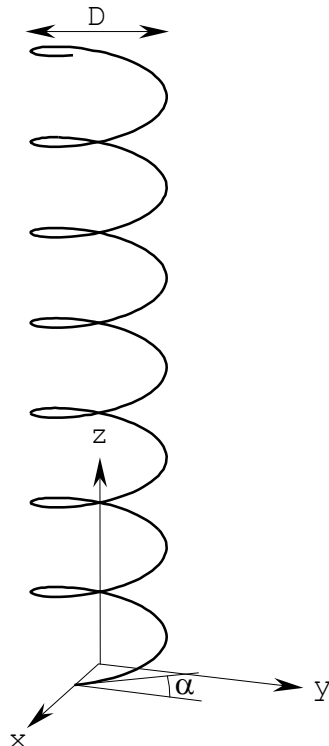


Figure 2.3-18 Monofilar right-hand helix with $\alpha = 12.5^\circ$ and $N = 7$.

The analytical model is based upon the approximations proposed by Kraus (1950) for the helix antenna radiating in the axial mode, and the far field equations developed by Elliott (1981).

A uniform current

$$I(\psi) = I_0 e^{-j(k/p)(L/2\pi)\psi} \quad (2.3-59)$$

is assumed to propagate along the wire. The phase velocity relative to the speed of light is p . The length of one turn of the wire is L . The angle ψ specifies the position on the wire segment.

The primary parameters of the helix are

D - the helix diameter

α - the pitch angle of the helix and

N - the number of turns.

The secondary helix parameters are the axial height of one turn

$$S = \pi D \tan(\alpha), \quad (2.3-60)$$

the circumference of the helix

$$C = \pi D \quad (2.3-61)$$

and the wire length along one turn

$$L = \pi D \sqrt{1 + \tan^2 \alpha} . \quad (2.3-62)$$

The relative phase velocity $p = v/c$ of the current along the wire is determined from the Hansen-Woodyard condition for increased endfire radiation

$$p = \frac{L}{S + \lambda \ln(1 + 1/2N)} . \quad (2.3-63)$$

Experiments have shown that if the circumference of the helix is approximately one wavelength, and if there are several turns per wavelength, a primary component of the current on the helix is a wave travelling along the wire at approximately the speed of light, and the radiation generates a beam in the direction of the axis of the helix and essentially circularly po-

larised. The solution implemented in GRASP is restricted to the interval $0.8\lambda \leq \pi D \leq 1.2\lambda$.

The far-field in the direction θ, ϕ is then determined from the vector potential

$$A_\theta \theta, \phi = f \theta g_1 \theta, \phi \quad (2.3-64)$$

$$A_\phi \theta, \phi = f \theta g_2 \theta, \phi \quad (2.3-65)$$

$$f \theta = \sum_{n=1}^N e^{-j2\pi nh \theta} \quad (2.3-66)$$

$$g_1(\theta, \phi) =$$

$$- I_0 \int_0^{2\pi} e^{-jh(\theta)\psi} a \cos \theta \sin \psi - \phi + b \sin \theta e^{jka \sin \theta \cos \psi - \phi} d\psi \quad (2.3-67)$$

$$g_2 \theta, \phi = I_0 \int_0^{2\pi} e^{-jh(\theta)\psi} a \cos \psi - \phi e^{jka \sin \theta \cos \psi - \phi} d\psi \quad (2.3-68)$$

and

$$a = D/2 \quad (2.3-69)$$

$$b = S/2\pi \quad (2.3-70)$$

$$h \theta = L/p - S \cos \theta / \lambda . \quad (2.3-71)$$

Each of the components is evaluated separately using the substitution

$$e^{jka \sin \theta \cos \psi - \phi} = \sum_{m=-\infty}^{\infty} j^m J_m k a \sin \theta e^{-jm\psi} e^{-jm\phi} \quad (2.3-72)$$

We retain only the fundamental term corresponding to $m = 0$ and obtain

$$g_1 \theta, \phi = -K J_o k a \sin \theta \int_0^{2\pi} e^{-jh \theta \psi} a \cos \theta \sin \psi - \phi + b \sin \theta d\psi \quad (2.3-73)$$

$$g_2 \theta, \phi = K J_o k a \sin \theta \int_0^{2\pi} e^{-jh \theta \psi} a \cos \psi - \phi d\psi \quad (2.3-74)$$

The electric far field is determined directly by the θ - and ϕ -components of the vector potential. The normalisation constant K appearing in (2.3-73) and (2.3-74) is determined by pattern integration.

The assumption of a uniform current distribution with an optimum phase distribution will lead to predicted gain values that are difficult to achieve by real antenna systems. In practice, non-uniform current distributions will be generated near the feed point and the helix termination and give rise to wide-angle radiation and a reduced gain. The details of the actual currents depend upon the feeding arrangement including the finite ground plane, which is neglected in this model. The backward travelling axial-mode current distribution reflected at the helix termination is also neglected. Thus, a major contribution to the cross polarisation degradation is omitted.

The co-polar far field from (2.3-64) and (2.3-65) is compared with measurements in Figure 2.3-19. The measurement is performed by King and Wong (1980) at the peak gain frequency of 925 MHz and on a helix antenna with $\alpha = 12.8^\circ$, $D = 4.23$ inches and $N = 5, 18$ and 35 . The first column of Figure 2.3-19 shows the calculated major and minor elliptical component and the second column is the measured results presented as a spinning dipole pattern. The limits of the spinning dipole are given by the major and minor components.

The main beam and the sidelobe levels and directions are seen to be calculated accurately, especially for helix antennas with many turns. The missing nulls of the measured pattern are due to the actual tapered current distribution, since the total current at the end of the helix is perforce zero. The far field performance in the backward direction is mainly a result of the damped wave travelling back towards the ground plane

and the configuration of the ground plane. Both of these effects are neglected in the calculated field.

At frequencies a few percent above the peak gain frequency, the pattern begins to deteriorate as seen in Figure 2.3-20. The frequencies correspond to a circumference of $.82\lambda$, 1.04λ and 1.20λ which are in the limit of the allowed interval $[0.8\lambda, 1.2\lambda]$. The changes in the calculated field are very small compared to the changes of the measured field. Mainly the beamwidth is narrowing rapidly from 40.5° to 22.5° in the measured pattern whereas for the calculated pattern the change is only from 32.0° to 26.4° .

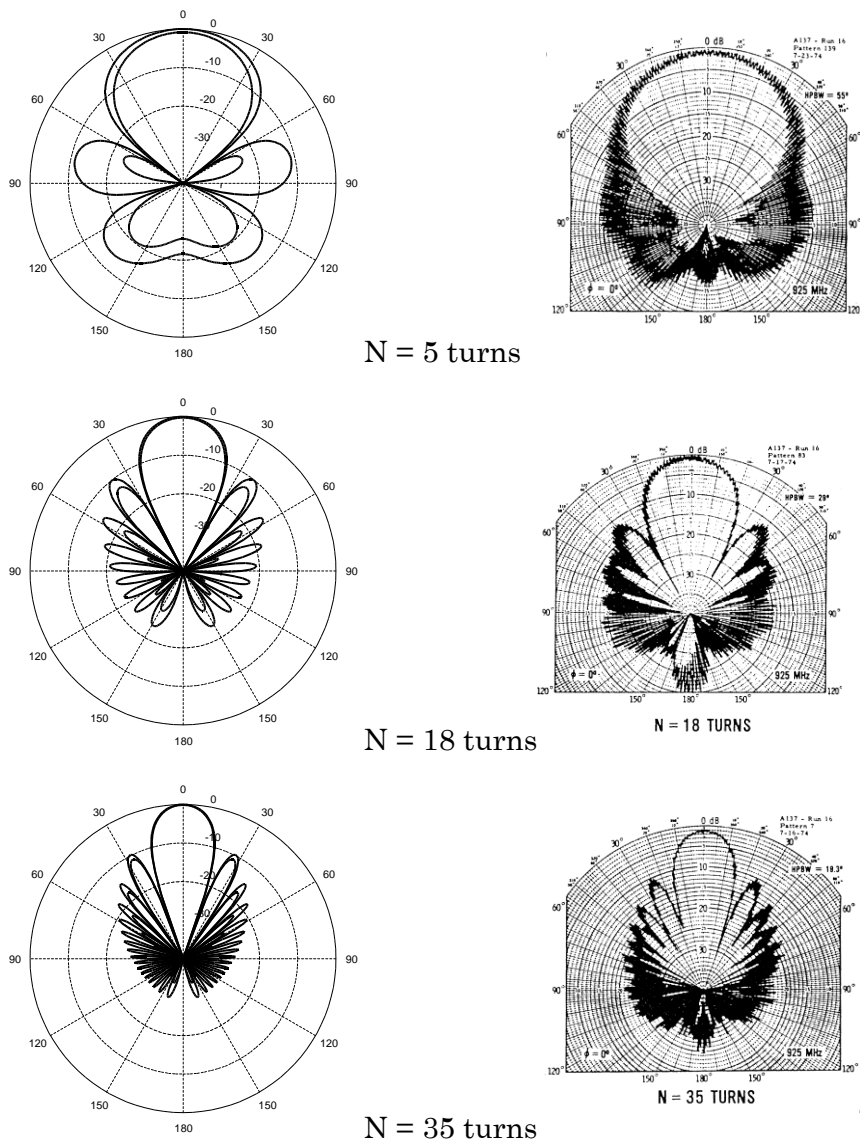


Figure 2.3-19 Comparisons between calculated (left) and measured (right) 5, 18 and 35 turn helix, 4.23 inch diameter and 12.8° pitch angle. Frequency 925 MHz.

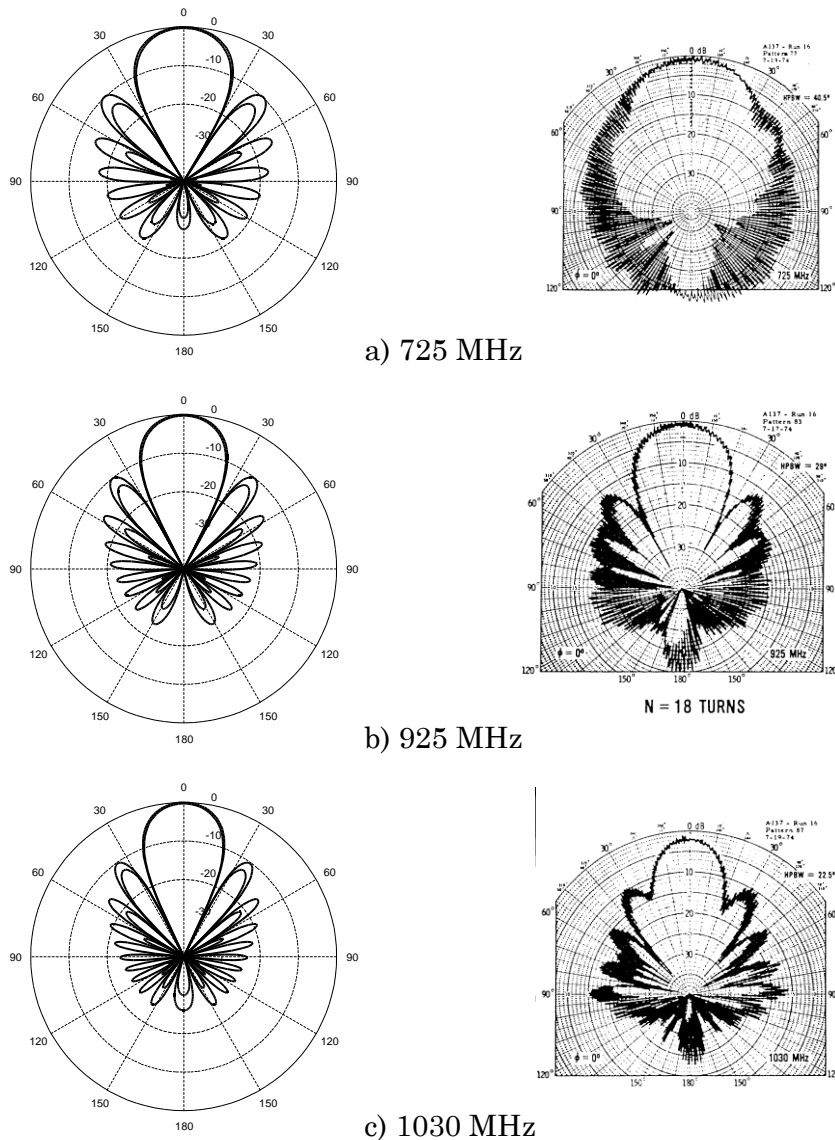


Figure 2.3-20 Comparisons between calculated (left) and measured (right) 18 turn helix, 4.23 inch diameter and 12.8° pitch angle at 3 frequencies.

2.3.1.9 Bifilar equi-angular spiral feed

This feed models the bifilar planar equi-angular spiral antenna based on the assumption that the current along the wire decays with the square root of the length along the wire. A

loss factor and the effect of an infinite ground plane below the spiral element may be included. The plane of the spiral is the xy -plane of the feed coordinate system.

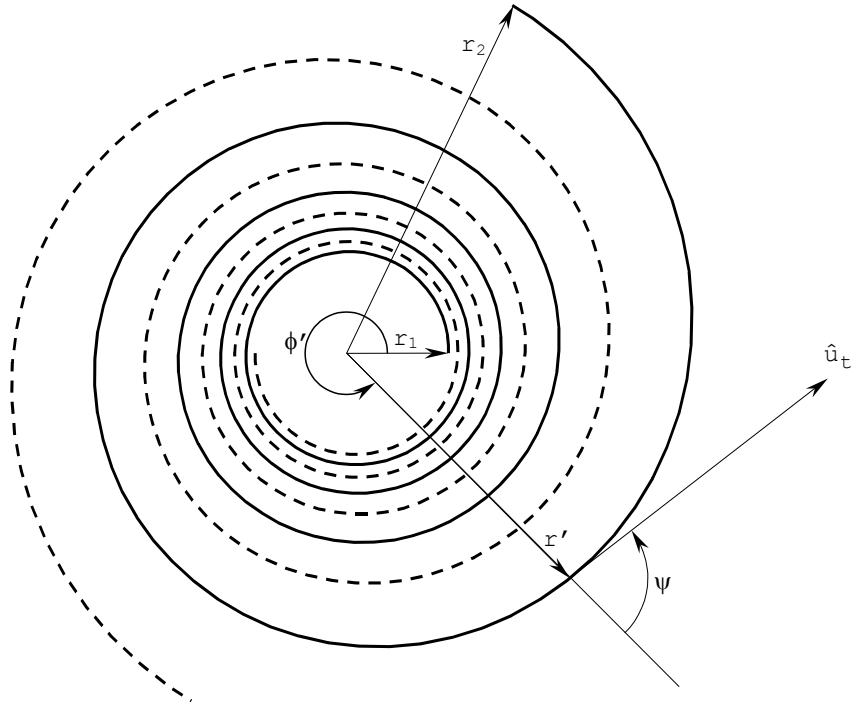


Figure 2.3-21 Bifilar equi-angular spiral.

It is assumed that the spiral on Figure 2.3-21 is equi-angular, i.e. given by the polar equation

$$r' \phi' = r_1 e^{a\phi'} . \quad (2.3-75)$$

The exponential spiral constant, a , determines the density of the spiral winding. A positive sign of a will generate a right-hand spiral radiating right-hand circular polarisation. We define the following secondary spiral parameters

$$\text{Spiral expansion ratio: } \frac{r'(\phi' + 2\pi)}{r'(\phi')} = e^{2\pi a} \quad (2.3-76)$$

$$\text{Spiral angle: } \psi = \operatorname{Arctg} \frac{1}{a} \quad (2.3-77)$$

$$\text{Length along wire: } s' \phi' = [r' \phi' - r_1] \sqrt{1 + 1/a^2} \quad (2.3-78)$$

$$\text{Number of turns: } n(\phi') = \frac{\phi'}{2\pi} \quad (2.3-79)$$

$$\text{Total number of turns: } N = \frac{\ln(r_2/r_1)}{2\pi a} . \quad (2.3-80)$$

The currents along the two spiral arms are parallel to the tangent

$$\hat{u}_t = \cos \phi' + \psi, \sin \phi' + \psi, 0 . \quad (2.3-81)$$

Given an anti-phase current distribution $I s'$ along the wire, the far-field vector potential becomes

$$\bar{A} = 2K'' \int_{\text{arm}} I s' \hat{u}_t \cos kr' \sin \theta \cos \phi - \phi' ds' \quad (2.3-82)$$

where the symbol K'' has absorbed a number of constants.

Using expression (2.3-72) in (2.3-82) leads to a Fourier series representation of the far field in terms of only even-numbered azimuthal modes. Because of the small size of the spiral antenna measured in wavelengths, only the fundamental $m=0$ term is retained. Following Laxpati and Mittra (1967), we substitute for the rectangular components of \hat{u}_t :

$$u_{tx} = \frac{1}{2} e^{j\psi} e^{j \ln r'/r_1 / a} + \frac{1}{2} e^{-j\psi} e^{-j \ln r'/r_1 / a} \quad (2.3-83)$$

$$u_{ty} = \frac{-j}{2} e^{j\psi} e^{j \ln r'/r_1 / a} + \frac{j}{2} e^{-j\psi} e^{-j \ln r'/r_1 / a} . \quad (2.3-84)$$

The current distribution is approximated by (Laxpati and Mittra, 1967):

$$\begin{aligned} I(s') &\approx I_0 H_1^{(2)}(ks') \\ &\approx I_0 \frac{1}{\sqrt{r'}} e^{-jkr' \sqrt{1+1/a^2}} . \end{aligned} \quad (2.3-85)$$

This equation shows that the current distribution has a slow-wave character in the radial direction. Early experimental work indicated an exponential decay constant $\alpha \approx 1/3\lambda$ along the wire (Curtis, 1960). The far-field vector potential is then approximated by

$$A_x = K' e^{j\psi} I_+ + e^{-j\psi} I_- \quad (2.3-86)$$

$$A_y = jK' -e^{j\psi} I_+ + e^{-j\psi} I_- \quad (2.3-87)$$

where the symbols I_{\pm} denote the integrals

$$I_{\pm} = \int_{r_1}^{r_2} \frac{1}{\sqrt{r'}} J_o kr' \sin \theta e^{j[\pm \ln r'/r_1 / a - kr' \sqrt{1+1/a^2}]} dr' \quad (2.3-88)$$

Dependent upon the sign of a , the phase of either I_+ or I_- will have a stationary point at

$$r_o = \frac{\lambda}{2\pi} \frac{1}{\sqrt{1+a^2}} \quad . \quad (2.3-89)$$

This point indicates the location of the active region from which the radiation takes place (Cubley and Hayre, 1971). For good performance of a spiral antenna, this point should be well inside the region between the internal spiral radius r_1 and the external spiral radius r_2 . In the software, the integral (2.3-88) may be evaluated either by numerical integration or asymptotically by a saddle-point contribution, if any, and two end-point contributions. In general, the much faster asymptotic evaluation will be adequate bearing in mind the other approximations made. The electric far field for the spiral radiating in free space is determined by

$$E_\theta \sim K \left[I_+ e^{j\psi-\phi} + I_- e^{-j\psi-\phi} \right] \cos \theta \quad (2.3-90)$$

$$E_\phi \sim jK \left[-I_+ e^{j\psi-\phi} + I_- e^{-j\psi-\phi} \right], \quad (2.3-91)$$

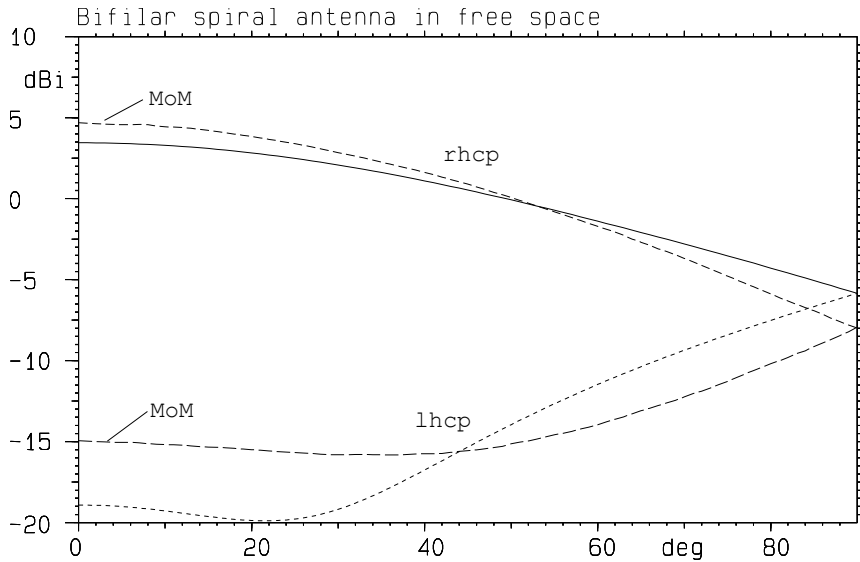
where the normalisation constant K is determined by pattern integration. The spiral antenna is only a practical antenna element when it is backed by a cavity or mounted above a ground plane. The software models these situations by placing the spiral a distance h above an infinite ground plane. The phase reference point in this case is the projection of the spiral centre into the ground plane.

The top figures in Figure 2.3-22 compare co- and cross-polar performance predictions obtained from (2.3-90) and (2.3-91) and a method-of-moments calculation for a spiral in free space with the following parameters

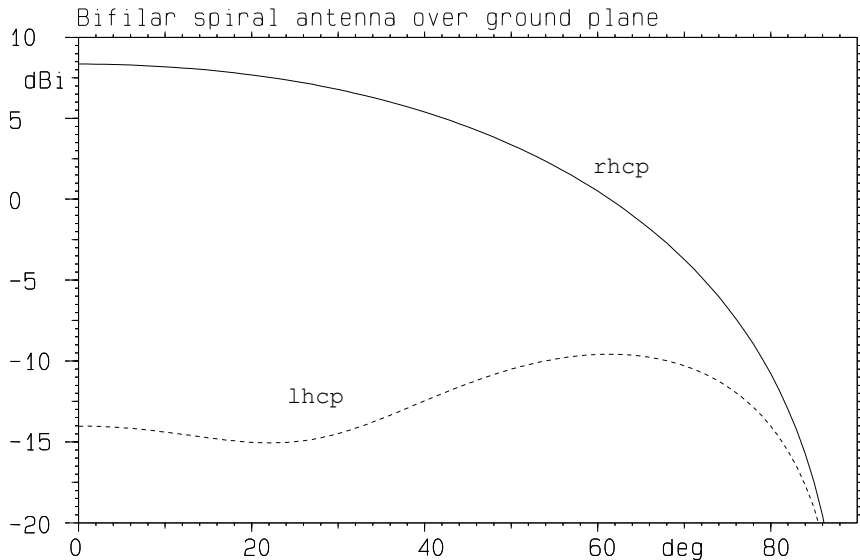
internal radius: $r_1 = 0.1 \lambda$

external radius: $r_2 = 0.4 \lambda$

spiral constant: $a = 0.070875$.



a) Comparisons between MoM and simple model in free space



b) Simple model over ground plane, $h = \lambda/4$

Figure 2.3-22 Equiangular spiral antenna.

$$r_1 = 0.1\lambda; r_2 = 0.4\lambda; \alpha = 0.070875.$$

This gives a spiral angle of 85.95° , 3.11 turns per spiral arm, a length of 4.24λ per arm and an active region at $r_o = 0.16\lambda$. In the method-of-moments calculation, a piece-wise linear approximation to the equi-angular spiral was used. The agree-

ment is acceptable with the major disagreements occurring in the cross-polar fields: The method-of-moments calculation includes the linear segment connecting the two arms and takes the current wave reflected at the outer end of the spiral into account. The latter effect is known to be a major source of cross polarisation in the spiral antenna. The bottom figure shows the pattern of the spiral element placed $h = 0.25\lambda$ above an infinite ground plane.

2.3.1.10 Halfwave dipole

This routine allows the user to specify a simple half wave dipole with the radiation pattern shown in Figure 2.3-23. The dipole is oriented in z -direction of the local feed coordinate system.

The simple model may be used to simulate a large number of antenna systems such as crossed dipoles above ground plane, quasi omni-directional Lindenblad arrays and biconic dipoles. A typical Lindenblad array and its radiation pattern are shown in Figure 2.3-24.

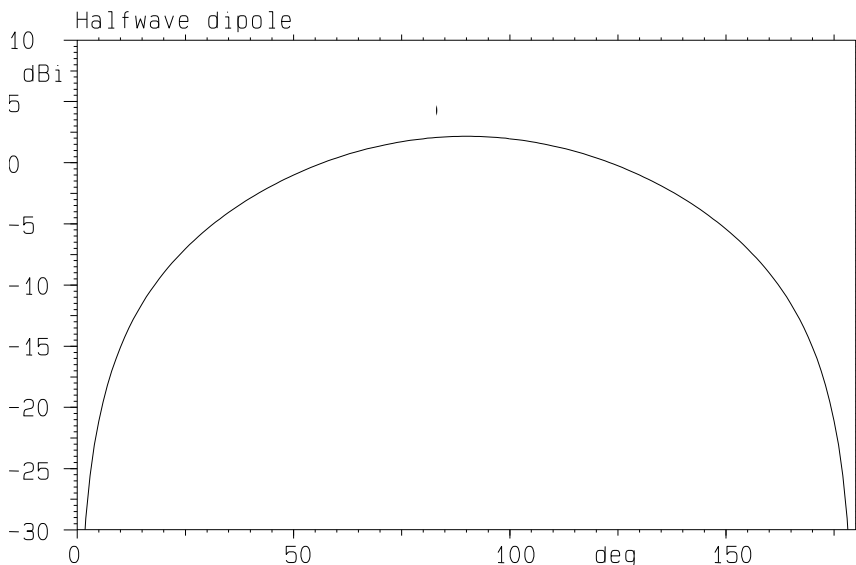


Figure 2.3-23 θ -component for the half wave dipole antenna pattern.

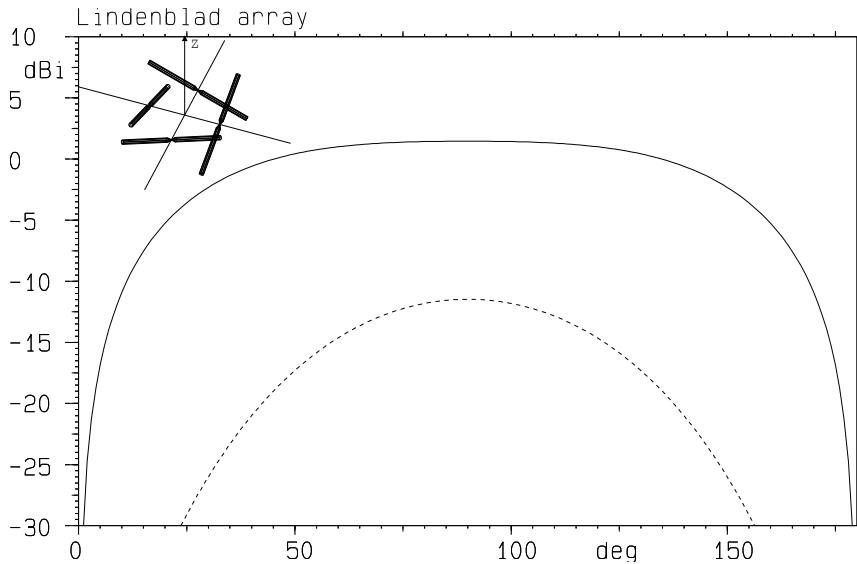


Figure 2.3-24 Lindenblad array with 4 half wave dipoles. Co-polar (RHC) and cross-polar (LHC) components.

2.3.1.11 Hertzian dipole

This feed models the field from an electric or magnetic Hertzian dipole, also known as elementary dipoles. The dipole may be oriented along the x -, y -, or z -direction of the local feed coordinate system.

The field from the z -directed electric Hertzian dipole is

$$\begin{aligned} \bar{E}(r, \theta, \phi) = E_0^e & \left(\hat{\theta} \sin \theta \left(\frac{1}{kr} - \frac{j}{kr^2} - \frac{1}{kr^3} \right) \right. \\ & \left. - \hat{r} \cos \theta \left(\frac{j^2}{kr^2} + \frac{2}{kr^3} \right) \right) e^{-jkr} \end{aligned} \quad (2.3-92)$$

$$\bar{H}(r, \theta, \phi) = \frac{E_0^e}{\zeta} \hat{\phi} \sin \theta \left(\frac{1}{kr} - \frac{j}{kr^2} \right) e^{-jkr} \quad (2.3-93)$$

where ζ is the intrinsic impedance of free space. Similarly, the field from the z -directed magnetic Hertzian dipole is

$$\bar{E} \ r, \theta, \phi = -E_0^m \hat{\phi} \sin \theta \left(\frac{1}{kr} - \frac{j}{kr^2} \right) e^{-jkr} \quad (2.3-94)$$

$$\begin{aligned} \bar{H} \ r, \theta, \phi &= \frac{E_0^m}{\zeta} \left(\hat{\theta} \sin \theta \left(\frac{1}{kr} - \frac{j}{kr^2} - \frac{1}{kr^3} \right) \right. \\ &\quad \left. - \hat{r} \cos \theta \left(\frac{j2}{kr^2} + \frac{2}{kr^3} \right) \right) e^{-jkr} \end{aligned} \quad (2.3-95)$$

In GRASP, E_0^e and E_0^m are normalised such that the Hertzian dipoles radiate a total power of 4π watt.

A Huygens source (as shown in Figure 2.3-3) may be formed by combining an x -directed electric Hertzian dipole and a y -directed magnetic Hertzian dipole. Both dipoles must be excited by the real factor $1/\sqrt{2}$ for the Huygens source to radiate a pattern with the maximum in the positive z -direction with a total power of 4π watt.

2.3.1.12 Cardioid pattern

This feed model approximates a typical cardioid-shaped circularly polarised satellite telemetry and telecommand antenna pattern. The pattern consists of two lobes, a forward directed co-polar lobe and a backward directed cross-polar lobe. The sense of the co-polar polarisation and the relative level of the back radiation shall be specified. The half-power beamwidth is specified by the user for each of the lobes assuming a pattern function of the shape

$$f(\theta) = K |1 \pm \cos \theta|^n / 2^n \quad (2.3-96)$$

where the power n depends upon the beamwidth specified. The constant K normalises the pattern to isotropic level.

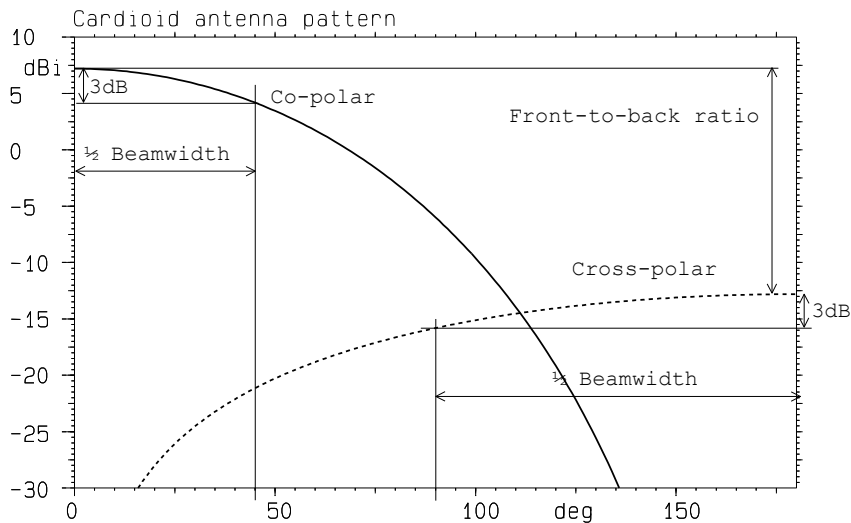


Figure 2.3-25 Cardioid antenna pattern.

Figure 2.3-25 illustrates by an example the cardioid pattern and the parameters to be specified: The co- and cross-polar half power beamwidth is 90° and 180° , respectively, and the front-to-back ratio is 20 dB.

2.3.1.13 Hybrid mode conical horn

The hybrid mode horn model is based on a standard corrugated conical horn connected to a smooth circular waveguide. The model assumes that the corrugation geometry is such that the horn is operated under the balanced-hybrid condition and that the horn semi flare angle does not exceed 20° (Clarricoats and Olver, 1984). The waveguide diameter, $2a'$, and the aperture diameter, $2a$, as well as the axial length, L (aperture to apex), of the horn are shown in Figure 2.3-26.

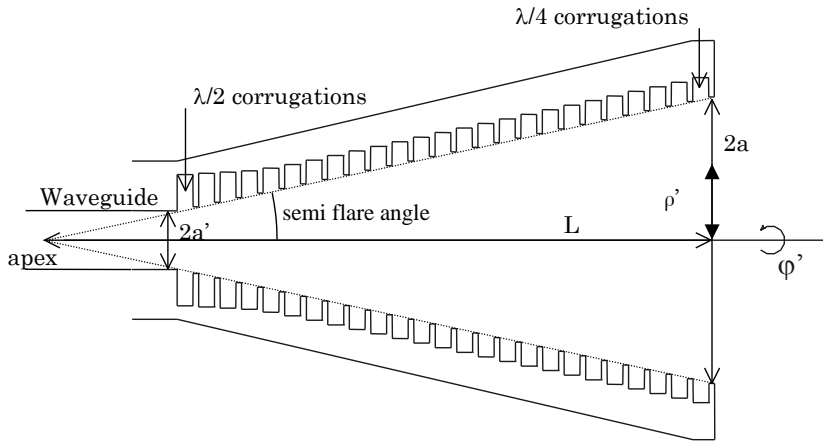


Figure 2.3-26 Typical corrugated horn geometry.

Hybrid modes in corrugated horns can exhibit low-frequency as well as high-frequency cut-off properties. Whereas low-frequency cut-off is determined by the inner diameter of the corrugated horn, high frequency cut-off occurs in a non-trivial manner (Clarricoats and Olver, 1984). In the present model, only the hybrid modes HE_{mn} ($1 \leq m \leq 8$ and $1 \leq n \leq 8$), EH_{mn} ($1 \leq m \leq 8$ and $2 \leq n \leq 8$) and the cylindrical modes TE_{0n} ($1 \leq n \leq 8$) and TM_{0n} ($2 \leq n \leq 8$) are supported (m is the azimuthal mode index and n is the radial mode index). Notice that for well designed horn geometries EH_{m1} -modes as well as the TM_{01} -mode are high-frequency cut-off and therefore not included in the model.

Assuming that the influence of a horn flare can be approximated by a quadratic phase distribution over the aperture, the aperture electric fields for the HE_{mn} -, EH_{mn} - and TM_{0n} -modes may be expressed in xy -components as:

$$\begin{aligned}
 E_x = E_0 & [\bar{\Delta} - \beta / k J_{m+1}(K\rho') \cos m + 1 \phi' \\
 & + \bar{\Delta} + \beta / k J_{m-1}(K\rho') \cos m - 1 \phi'] \\
 & e^{-jk\sqrt{L^2 + \rho'^2} - jk\left(\sqrt{L^2 + \rho'^2} - L\right)}
 \end{aligned} \tag{2.3-97}$$

and

$$E_y = E_0 [\bar{\Delta} - \beta/k J_{m+1}(K\rho') \sin m+1 \phi' \\ - \bar{\Delta} + \beta/k J_{m-1}(K\rho') \sin m-1 \phi'] e^{-jk(\sqrt{L^2+\rho'^2}-L)} \quad (2.3-98)$$

while for the TE_{0n} -modes the aperture fields are given by:

$$E_x = -E_0 J_1(K\rho') \sin \phi' e^{-jk(\sqrt{L^2+\rho'^2}-L)} \quad (2.3-99)$$

and

$$E_y = E_0 J_1(K\rho') \cos \phi' e^{-jk(\sqrt{L^2+\rho'^2}-L)} . \quad (2.3-100)$$

Here K and β are, respectively, the transversal and the longitudinal propagation constants, related to the free space propagation constant k as $k^2 = \beta^2 + K^2$. $J_m(x)$ is the cylindrical Bessel function.

The hybrid factor $\bar{\Delta}$ depends on the corrugation depth and the mode type. ϕ' and ρ' are the azimuth angle and radial position in the aperture, respectively.

The values of K , β/k , a , a' and $\bar{\Delta}$ control the modes that are able to propagate. For example, the value of K for the EH_{45} -mode is found by dividing the 4'th zero of J_5 with a . Furthermore, $\bar{\Delta} = -1$ for EH-modes and $\bar{\Delta} = +1$ for HE-modes. At the aperture $\beta/k \cong 1$. This information is used to find the aperture fields.

If the corrugation depth is constant and equal to $\lambda/4$ along the horn, then the cut-off frequencies are given by simple rules. The table below shows how the modes are named as well as checked for cut-off. To determine whether the EH_{45} -mode is cut-off the 5'th zero of J_4' is compared to ka' , and if ka' is smaller than this zero, the mode is cut-off. For further details see Clarricoats and Olver (1984).

Mode	K determined by	$\bar{\Delta}$	β/k	Low freq. cut-off, n 'th zero of
EH_{mn}	$(n-1)$ 'th zero of $J_{m+1} \text{ } Ka$	-1	~ 1	$J_m \text{ } ' \text{ } ka'$
HE_{mn}	n 'th zero of $J_{m-1} \text{ } Ka$	1	~ 1	$J_m \text{ } k \text{ } a' + \lambda/4$
TM_{0n}	$(n-1)$ 'th zero of $J_0 \text{ } ' \text{ } Ka$	0	~ 1	$J_0 \text{ } k \text{ } a' + \lambda/4$
TE_{0n}	n 'th zero of $J_0 \text{ } ' \text{ } Ka$		~ 1	$J_0 \text{ } ' \text{ } ka'$

Table 2.3-2 Characteristics of modes of the hybrid mode horn

The far-fields are found by numerical integration over the aperture coordinates ϕ' and ρ' .

The horn aperture may be embedded in an infinite ground plane which means that the tangential components of the electric fields must vanish for $\theta = 90^\circ$.

In addition to this, the modes may be freely rotated and the rotation may be specified separately for each mode. A mode with $m > 0$ which is rotated an odd multiple of $\pi/(2m)$ is orthogonal to the original mode.

The normalisation of the fields radiated by the hybrid feed is such that the total radiated power is 4π watt.

2.3.2 Electromagnetic source generated by a planar tabulated field

The “Equivalence Principle” of electromagnetic fields is used in GRASP in the tabulated_planar_source module and it allows the user to apply a near field defined on a plane as a source input. This may be useful when for example the horn aperture field or a near field on a plane in a beam waveguide

is known. The source can then be used to find the horn radiation pattern or to propagate the radiation through the beam waveguide.

A consequence of the Equivalence Principle is that when a source is radiating from behind an infinite plane, a set of tangential currents on this plane can be used to find the field anywhere in front of the plane. In some cases and with approximations in the accuracy this principle may be used also to determine the field behind the plane in the source region.

Assume that the sources are located in the region behind the plane $z = 0$, and that they radiate the electric and magnetic fields, \bar{E} and \bar{H} . The equivalent electric currents in the $z = 0$ -plane defined by

$$\bar{J}_e = 2\hat{z} \times \bar{H} \quad (2.3-101)$$

will radiate the exact field in front of the plane, $z > 0$, but the field is invalid in the region behind the plane, $z < 0$. Similarly, the equivalent magnetic currents

$$\bar{J}_m = -2\hat{z} \times \bar{E} \quad (2.3-102)$$

will radiate the exact field in front of the plane, but the field is invalid in the region behind the plane. It is also possible to combine equivalent electric and magnetic currents defined by

$$\begin{aligned} \bar{J}_e &= \hat{z} \times \bar{H} \\ \bar{J}_m &= -\hat{z} \times \bar{E} \end{aligned}, \quad (2.3-103)$$

which will radiate the exact field in front of the plane and the field is zero in the region behind the plane.

The planar near field can be given in either a circular or a rectangular region as a set of radial cuts or a rectangular xy -grid, respectively. An electric field, a magnetic field or both can be specified. If only an electric field or a magnetic field is specified the radiated field corresponds to a current distribution radiating in an aperture in a ground plane. The field is thus only determined in front of the plane.

If both an electric and a magnetic field are specified the radiated field corresponds to a finite current distribution radiating in free space and this means that also the field behind the plane can be determined. However, this will only give approximate results since the region behind the plane is not source free.

The accuracy of the model depends on how the actual field is truncated by the circular or rectangular region in which the input field is given. If the intensity of the field has decreased to practically zero outside the input region, the exact radiation pattern for $z > 0$ can be found regardless whether only the E-field, only the H-field or both fields have been specified.

An example of the model is shown for a horn aperture field distribution in Figure 2.3-27. Assume first that the E-field or the H-field is given as input at $z = 0$ on the horn aperture and that the field values on the outer horn structure are small. Then the model will provide a good approximation for $z > 0$ but it will be invalid for $z < 0$. In the case where both the E-field and the H-field are given as input at $z = 0$ on the horn aperture, the model is also an acceptable approximation for $z < 0$, except inside the horn.

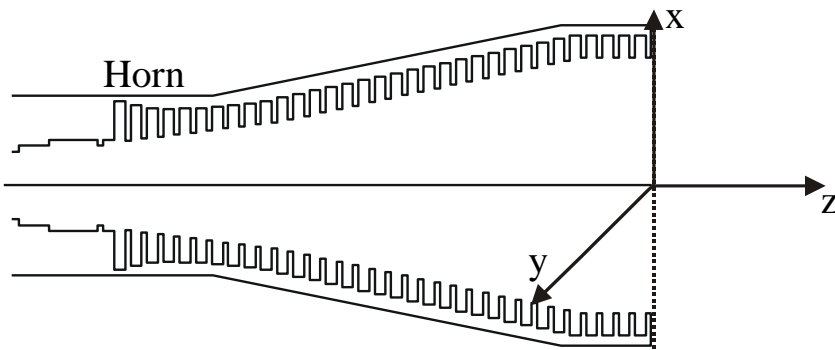


Figure 2.3-27 Illustration of the use of the tabulated planar source model for a horn aperture.

For both file types an interpolation is necessary for computing the field at the points required by Gaussian integration (see Sections 3.1.2.1 and 3.1.2.2). Hereafter the equivalent cur-

rents on the xy -plane are computed by (2.3-101), (2.3-102) or (2.3-103). Once the currents are determined the far field or the near field can be determined from the radiation integrals in Section 3.1.2.

If a grid file is specified, the field in the equally distributed points is interpolated by a two-dimensional cubic interpolation.

In a cut file, the field is specified on a set of radial cuts and must be interpolated to find the field in the xy -plane for $\rho \leq \rho_{\max}$, where ρ_{\max} is the radius of the circular region in which the cuts are given. This is done by a combination of Fourier interpolation in ϕ and cubic interpolation in ρ . First, the field is converted to $\rho\phi$ -components:

$$\bar{E}_t = \hat{\rho}E_\rho + \hat{\phi}E_\phi \quad (2.3-104)$$

where \bar{E}_t denotes the tangential component of the E-field vector. The field can be then be found in all other cuts by computing its Fourier coefficients. This is illustrated for the component E_ρ , which can be written as

$$E_\rho(\rho, \phi) = \sum_{m=-M}^M c_m(\rho) e^{jm\phi} \quad (2.3-105)$$

where the coefficients c_m depend on ρ , but not on ϕ . It is here assumed that the field has a maximum angular variation given by $e^{jM\phi}$. The Fourier coefficients are found from the orthogonality integral

$$c_m(\rho) = \frac{1}{2\pi} \int_0^{2\pi} E_\rho(\rho, \phi) e^{-jm\phi} d\phi \quad (2.3-106)$$

which can be approximated by

$$c_m(\rho) \cong \frac{1}{2\pi} \sum_{r=1}^N E_{\rho,r} e^{-jm(r-1)2\pi/N} \frac{2\pi}{N} \quad (2.3-107)$$

where $E_{\rho,r}$ is the value of the field in the different cuts and N is the number of cuts.

The approximation (2.3-107) becomes exact if $N \geq 2M + 1$. Once the Fourier coefficients are determined cubic interpolation is used to find $c_m(\rho)$ for all values of $\rho \leq \rho_{\max}$.

The field from the tabulated planar source can be normalised such that the total radiated power is 4π watt and the field is given in dBi.

2.3.3 Plane wave illumination

A plane wave in GRASP is defined in an *xyz*-coordinate system. The wave travels in the positive *z*-direction and the phase is referred to the origin of the coordinate system. The plane wave field exists at any near-field point in space and the amplitude is defined by means of the radius of a circle in the *xy*-plane such that the power radiated through this circle is 4π watt. The polarisation can be linear or circular.

The plane wave feature is very useful to investigate the focal region of a reflector antenna or to determine the scattering properties of an object.

2.3.4 Arrays of radiating elements

A collection of feed elements may be combined into feed arrays in GRASP. The location of the individual elements is specified in a feed array coordinate system. Two types of feed arrays are available:

- Regular grid arrays
- Irregular arrays

The regular grid arrays are planar, i.e. the feed elements are all located in the *xy*-plane of the feed array coordinate system. The feeds are arranged regularly in a hexagonal or rectangular grid.

For the irregular arrays the feed element locations can be anywhere.

For both types of arrays the individual feeds can be assigned a particular feed element type described in Section 2.3.1.

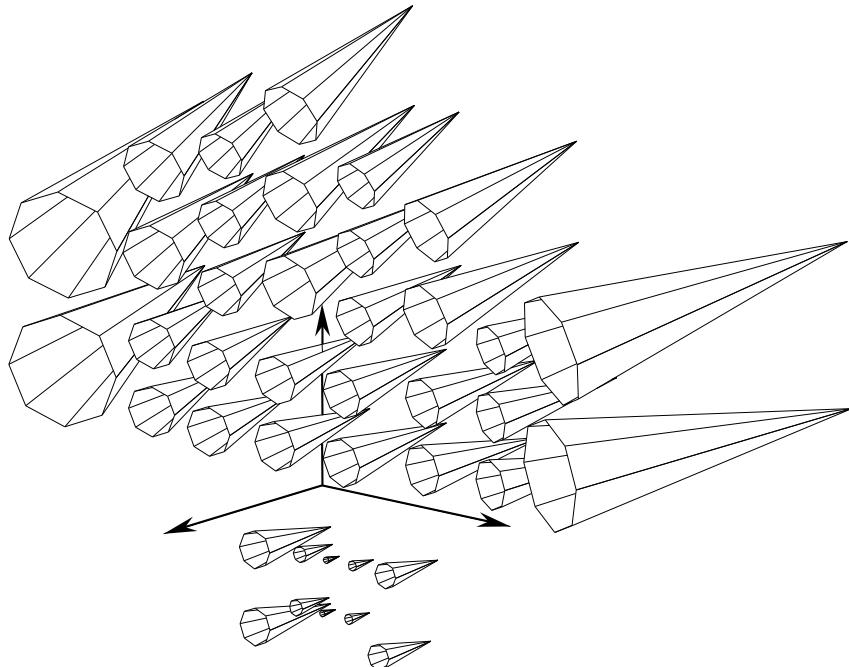


Figure 2.3-28 Irregular feed array.

Figure 2.3-28 shows an irregular feed array containing feeds of different sizes and orientation. It must be pointed out that all the feeds in the same array will operate at the same frequencies. If feeds are operating at different frequencies they must therefore be defined in different arrays.

The orientation of each individual feed element is defined by the three orientation angles θ , ϕ and ψ , as defined in Section 2.1, relative to the array coordinate system.

For both the regular and the irregular array it is possible to input the feed element positions and orientations from a file. This option is certainly preferable if more than a few feeds are to be investigated.

The radiation from the feed array can be calculated on an element-by-element basis. This means that each feed is excited one at a time and the computed field will contain the same

number of beams as there are elements in the array. The feeds are normalised to 4π watt and the calculated element beams will therefore be normalised to dBi.

It is also possible to treat the field from the array as a composite beam where the user inputs the excitations, b_i , of the individual elements. The normalisation for arrays of feed elements is discussed in Section 4.1.3. It is found that if power coupling between the feeds can be neglected, the amplitude excitations must satisfy

$$\sum_{i=1}^N |b_i|^2 = 1 \quad , \quad (2.3-108)$$

where N is the number of elements, and the composite radiated beam will be expressed in dBi.

3. ANALYSIS METHODS

This chapter describes the various analysis methods used in GRASP. The most fundamental approach, Physical Optics for perfect conductors, is described in Section 3.1 together with the integration grids for different boundary types. Here also the convergence properties are discussed and the new automatic convergence procedure is presented. The correction to Physical Optics, Physical Theory of Diffraction, is described in Section 3.2.

The special problems related to gaps and struts are treated in Sections 3.3 and 3.4, respectively.

Section 3.5 presents the necessary modifications and approximations when Physical Optics is used for scatterers which cannot be considered perfectly conducting.

Ray techniques, Geometrical Optics and Geometrical Theory of Diffraction, are described in Section 3.6.

Special techniques involving the direction of the incident field are explained in Section 3.7. A number of illustrative application examples are presented in Section 3.8.

Gaussian beam analysis is a new feature in GRASP. The underlying principles are summarised in Section 3.9.

A Spherical Wave Expansion program is now fully integrated with GRASP and the basic concepts are presented in Section 3.10.

3.1 Physical Optics

A scattering problem consists of a known incident field and a scatterer with known geometry and electrical surface properties. The goal is to compute the total radiated field. A useful field, denoted the scattered field, is defined by the relation

$$\bar{E} = \bar{E}^i + \bar{E}^s \quad (3.1-1)$$

where \bar{E}^i is the incident electrical field, \bar{E} is the total field and \bar{E}^s is the scattered field. If the surfaces of the scatterer are perfectly conducting the scattered field is generated by the induced surface currents on the scatterer. For non-perfectly conducting surfaces, as those described in Section 2.2.3, a set of equivalent electric and magnetic surface currents can be computed which exactly radiates the scattered field.

The scattering analysis can be considered as a three step procedure where the first step is to calculate the induced or equivalent surface currents, the second step is to calculate the field radiated by these currents and the third step is to add the incident and the scattered field to obtain the total field. Of these steps the first is the most difficult and in general it will involve techniques such as the method of moments that become very time-consuming for large scatterers. Physical optics is a simple method that gives an approximation to the surface currents valid for perfectly conducting scatterers which are large in terms of wavelengths. The second step involves no further approximations since the radiation integral of the surface currents can be computed by numerical integration with high precision. If the surfaces of the scatterer are not perfectly conducting, but reflection and transmission coefficients are known, the physical optics method can be modified to give an approximation to the equivalent electric and magnetic surface currents.

3.1.1 Induced surface currents

In the physical optics approximation it is assumed that the surface current in a specific point on a curved, but perfectly conducting scatterer is the same as the surface current on an infinite planar surface which is tangent to the scattering surface at this point.

The induced currents on a perfectly conducting infinite plane surface illuminated by an arbitrary incoming field are given by the well-known formula (Collin and Zucker, 1969)

$$\bar{J}^e = 2\hat{n} \times \bar{H}^i \quad (3.1-2)$$

which constitutes the physical optics approximation. Here \bar{J}^e is the induced electric current, \hat{n} is the unit surface normal (pointing outward on the illuminated side of the surface) and \bar{H}^i is the incident magnetic field. At points on the scatterer which are not directly illuminated by the incident field the surface currents are approximated with zero.

The equation (3.1-2) is simple to derive for an incident plane wave but it is valid for any kind of incident field as explained below. For a curved surface (3.1-2) is a good approximation to the actual current if the dimensions of the scattering surface and its radius of curvature are sufficiently large measured in wavelengths. For simple surface shapes physical optics is often used for scatterers down to five wavelengths in diameter.

In order to show that (3.1-2) is valid for a general incident field we consider two plane waves with different amplitudes and direction of propagation incident on an infinite planar surface. They will induce the currents \bar{J}_1^e and \bar{J}_2^e , respectively, given by

$$\begin{aligned}\bar{J}_1^e &= 2\hat{n} \times \bar{H}_1^i \\ \bar{J}_2^e &= 2\hat{n} \times \bar{H}_2^i\end{aligned}\tag{3.1-3}$$

where \bar{H}_1^i and \bar{H}_2^i are the magnetic fields of the two incident plane waves. The total surface current is found by adding the two equations in (3.1-3) which gives

$$\bar{J}^e = \bar{J}_1^e + \bar{J}_2^e = 2\hat{n} \times (\bar{H}_1^i + \bar{H}_2^i) = 2\hat{n} \times \bar{H}^i\tag{3.1-4}$$

where \bar{H}^i is now the total incident field. It is seen that this equation has the same form as (3.1-2). An incident field consisting of an arbitrary number of incident plane waves can be treated in the same way which shows that (3.1-2) is valid for a general incident field.

The expressions presented above are valid for perfectly conducting scatterers. For reflectors with material properties it is possible to use the PO approach with equivalent electric and magnetic currents. This is described in detail in Section 3.5.

In GRASP, the induced currents are calculated from either (3.1-2) or (3.5-2), depending on the properties of the reflector surface material. The surface normal is always chosen in such a way that it points into the half-space where the source is located, see Figure 3.1-1.

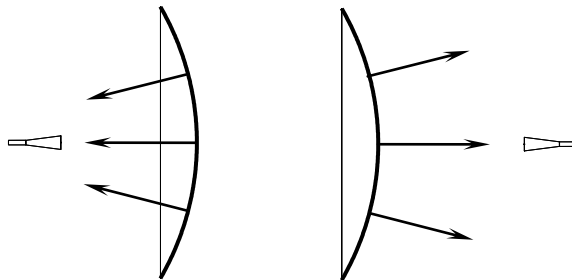


Figure 3.1-1 The reflector normal is at any point directed towards the half-space where the source is located.

In certain cases a reflector may create a shadow region on itself for a given source location, dividing the reflector into an illuminated region S and a shadowed region S' . This is illustrated in Figure 3.1-2.

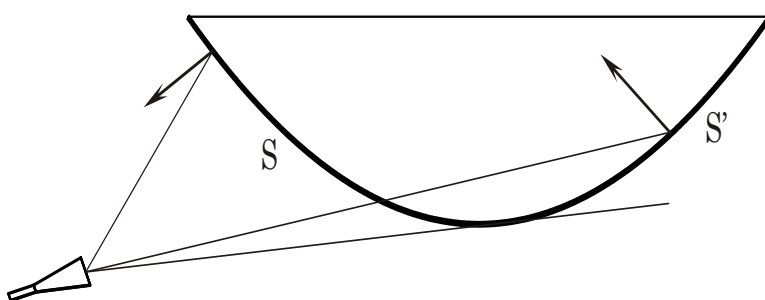


Figure 3.1-2 For a given source and reflector location it is possible to define an illuminated region S and a shadowed region S' .

PO implies that the currents are set to zero in the shadowed region, creating a shadow boundary on the reflector surface where the PO currents are abruptly terminated. To keep track of the precise location of the shadow boundary would significantly affect the computation time in a general analysis program like GRASP and is therefore not done. Instead, the PO currents are calculated on the entire reflector surface, resulting in currents that may constitute a poor approximation to the actual currents in the shadowed region. In the shadow region, the surface normal is chosen as indicated in Figure 3.1-2.

In order to solve a problem that involves self-shadowing of the above type the user may try to divide the reflector up into smaller segments, some of which are illuminated and some which are not.

It is noted that a special approach is taken when modelling PO currents on struts, see Section 3.4.

3.1.2 Surface integral

According to Collin and Zucker (1969) the radiated field from a set of induced or equivalent currents can be computed from

$$\begin{aligned}\bar{A}^e &= \frac{\mu}{4\pi} \iint_B \bar{J}^e(\bar{r}') \frac{e^{-jkR}}{R} ds' \\ \bar{A}^m &= \frac{\varepsilon}{4\pi} \iint_B \bar{J}^m(\bar{r}') \frac{e^{-jkR}}{R} ds'\end{aligned}\tag{3.1-5}$$

$$\begin{aligned}\bar{E} &= -j\omega \left(\bar{A}^e + \frac{1}{k^2} \nabla \cdot \bar{A}^e \right) - \frac{1}{\varepsilon} \nabla \times \bar{A}^m \\ \bar{H} &= \frac{1}{\mu} \nabla \times \bar{A}^e - j\omega \left(\bar{A}^m + \frac{1}{k^2} \nabla \cdot \bar{A}^m \right)\end{aligned}\tag{3.1-6}$$

Here \bar{A}^e is the electric vector potential, \bar{A}^m is the magnetic vector potential and ε and μ are the permittivity and permeability, respectively. The parameter ω is the angular frequency and k is the wavenumber which is related to the wavelength λ by $k = 2\pi/\lambda$. The distance R is given by $R = |\bar{r} - \bar{r}'|$ where

\bar{r} is the observation point and \bar{r}' is the integration variable running over the surface. The integration region B in (3.1-5) denotes integration over the scatterer surface. From (3.1-6) the radiated electric and magnetic field is found by applying the various differential operators on \bar{A}^e and \bar{A}^m . The result becomes

$$\begin{aligned}\bar{E}(\bar{r}) = & \frac{\zeta}{4\pi} \iint_B (\bar{J}^e \left(-\frac{j}{kR} - \frac{1}{k^2 R^2} + \frac{j}{k^3 R^3} \right) \\ & + (\bar{J}^e \cdot \hat{R}) \hat{R} \left(\frac{j}{kR} + \frac{3}{k^2 R^2} - \frac{3j}{k^3 R^3} \right)) e^{-jkR} k^2 ds' \quad (3.1-7) \\ & - \frac{1}{4\pi} \iint_B \bar{J}^m \times \hat{R} \frac{1}{k^2 R^2} (1 + jkR) e^{-jkR} k^2 ds',\end{aligned}$$

$$\begin{aligned}\bar{H}(\bar{r}) = & \frac{1}{4\pi} \iint_B \bar{J}^e \times \hat{R} \frac{1}{k^2 R^2} (1 + jkR) e^{-jkR} k^2 ds' \\ & + \frac{1}{4\pi\zeta} \iint_B (\bar{J}^m \left(-\frac{j}{kR} - \frac{1}{k^2 R^2} + \frac{j}{k^3 R^3} \right) \\ & + (\bar{J}^m \cdot \hat{R}) \hat{R} \left(\frac{j}{kR} + \frac{3}{k^2 R^2} - \frac{3j}{k^3 R^3} \right)) e^{-jkR} k^2 ds' \quad (3.1-8)\end{aligned}$$

where

$$\hat{R} = \frac{\bar{R}}{R} = \frac{\bar{r} - \bar{r}'}{\|\bar{r} - \bar{r}'\|} \quad (3.1-9)$$

and ζ is the free-space impedance, $\zeta = \sqrt{\mu/\epsilon}$.

It is seen that (3.1-7) and (3.1-8) satisfy the duality principle such that they are invariant under the substitutions

$$\begin{aligned}\bar{E} & \rightarrow -\zeta \bar{H} \\ \bar{H} & \rightarrow \frac{1}{\zeta} \bar{E} \\ \bar{J}^e & \rightarrow -\frac{1}{\zeta} \bar{J}^m \\ \bar{J}^m & \rightarrow \zeta \bar{J}^e\end{aligned}. \quad (3.1-10)$$

The far field is defined by

$$\bar{E}_{far} = \lim_{r \rightarrow \infty} (\bar{E}(\bar{r}) kr e^{jkr}) \quad (3.1-11)$$

$$\bar{H}_{far} = \lim_{r \rightarrow \infty} (\bar{H}(\bar{r}) kr e^{jkr}) \quad (3.1-12)$$

where $r = |\bar{r}|$.

Inserting (3.1-7) and (3.1-8) in these definitions gives

$$\begin{aligned} \bar{E}_{far} &= -\frac{j\zeta}{4\pi} \iint_B (\bar{J}^e - (\bar{J}^e \cdot \hat{r})\hat{r}) e^{jk\bar{r} \cdot \hat{r}} k^2 ds' \\ &\quad + \frac{j}{4\pi} \hat{r} \times \iint_B \bar{J}^m e^{jk\bar{r} \cdot \hat{r}} k^2 ds' \end{aligned} \quad (3.1-13)$$

$$\begin{aligned} \bar{H}_{far} &= -\frac{j}{4\pi} \hat{r} \times \iint_B \bar{J}^e e^{jk\bar{r} \cdot \hat{r}} k^2 ds' \\ &\quad - \frac{j}{4\pi\zeta} \iint_B (\bar{J}^m - (\bar{J}^m \cdot \hat{r})\hat{r}) e^{jk\bar{r} \cdot \hat{r}} k^2 ds' \end{aligned} \quad (3.1-14)$$

where \hat{r} is the far-field direction $\hat{r} = \bar{r} / |\bar{r}|$.

It is seen that (3.1-13) and (3.1-14) satisfy the relations

$$\begin{aligned} \bar{E}_{far} &= \zeta \bar{H}_{far} \times \hat{r} \\ \zeta \bar{H}_{far} &= \hat{r} \times \bar{E}_{far} . \end{aligned} \quad (3.1-15)$$

which expresses the well-known connection between the E- and H-field for a plane wave propagating in the direction \hat{r} .

The near field and far field is calculated by numerical integration of (3.1-7), (3.1-8) and (3.1-13), (3.1-14), but in order to obtain an efficient procedure these surface integrals must be transformed into standard two-dimensional integrals on a plane. The procedure is illustrated by the scalar surface integral

$$I = \iint_B f(x', y') ds' . \quad (3.1-16)$$

It is assumed that the surface is defined by a function g of two variables

$$z' = g(x', y') \quad , \quad (3.1-17)$$

where x' , y' and z' are rectangular coordinates in a suitable coordinate system. The radiation integrals (3.1-7), (3.1-8) and (3.1-13), (3.1-14) are reduced to the form (3.1-16) by use of

$$\bar{r}' = (x', y', g(x', y')) \quad . \quad (3.1-18)$$

The surface element is given by

$$ds' = |\bar{N}| dx' dy' \quad (3.1-19)$$

where \bar{N} is the surface normal

$$\bar{N} = \left(-\frac{\partial g}{\partial x'}, -\frac{\partial g}{\partial y'}, 1 \right) \quad (3.1-20)$$

$$|\bar{N}| = \sqrt{1 + \left(\frac{\partial g}{\partial x'} \right)^2 + \left(\frac{\partial g}{\partial y'} \right)^2} \quad (3.1-21)$$

such that the integral (3.1-16) can be written as

$$I = \iint_D f(x', y') |\bar{N}| dx' dy' \quad . \quad (3.1-22)$$

Here the integration area D is the projection of the surface onto the $x'y'$ -plane. The further reduction of the integral depends on the rim of the surface which can either be a general smooth curve, a parallelogram or a triangle as described in the following sub-sections.

3.1.2.1 Polar grid

A typical reflector rim is a smooth curve (e.g. a circle) which can be represented in polar coordinates as shown in Figure 3.1-3.

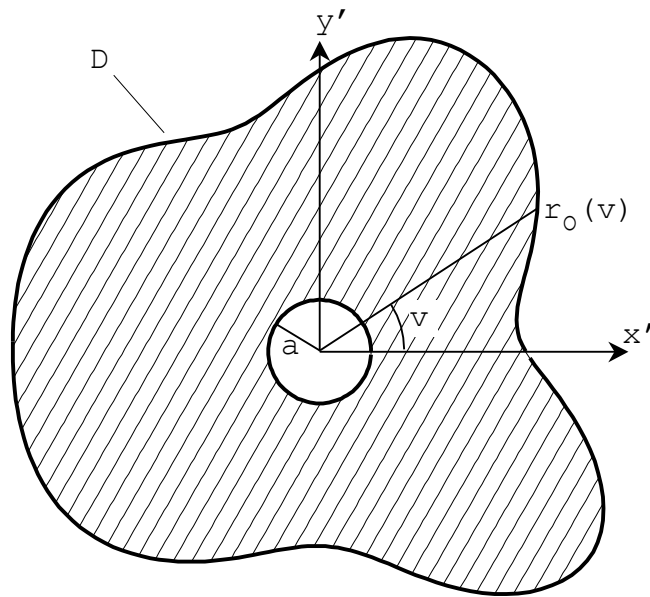


Figure 3.1-3 Integration area D in the $x'y'$ -plane with a smooth rim curve.

The integration area is bounded by an aperture blocking circle with radius a and a rim curve specified by a function $r_0(v)$. Transformation of (3.1-22) to the polar rv coordinates gives

$$\begin{aligned} x'(r, v) &= r \cos v \\ y'(r, v) &= r \sin v \end{aligned} \tag{3.1-23}$$

$$I = \iint_E f(r \cos v, r \sin v) |\bar{N}| r dr dv \tag{3.1-24}$$

with the integration area E shown in Figure 3.1-4.

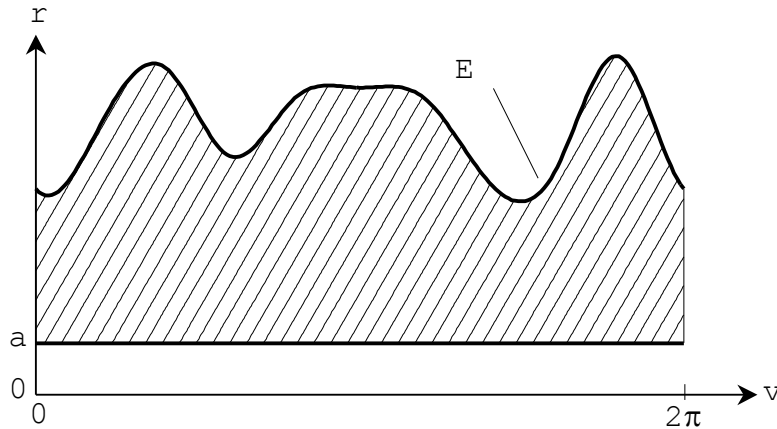


Figure 3.1-4 Integration area E in the rv -plane.

Next, the integration area is transformed to scaled polar coordinates ρ and ϕ defined by

$$\begin{aligned} r(\rho, \phi) &= \rho r_0(\phi) - a + a \\ v(\rho, \phi) &= \phi . \end{aligned} \quad (3.1-25)$$

It is seen that for a given value of v (or ϕ), $\rho = 0$ gives $r(\rho, \phi) = a$, and $\rho = 1$ gives $r(\rho, \phi) = r_0(\phi)$. The integration area E is therefore transformed to a rectangular area with side lengths 1 and 2π in the $\rho\phi$ -plane. The integral becomes

$$\begin{aligned} I &= \iint_F f(r(\rho, \phi) \cos \phi, r(\rho, \phi) \sin \phi) \\ &\quad |\bar{N}| r(\rho, \phi) \left| \det \frac{\partial(r, v)}{\partial(\rho, \phi)} \right| d\rho d\phi \end{aligned} \quad (3.1-26)$$

where the Jacobian is given by

$$\begin{aligned} \left| \det \frac{\partial(r, v)}{\partial(\rho, \phi)} \right| &= \left| \det \begin{pmatrix} \partial r / \partial \rho & \partial r / \partial \phi \\ \partial v / \partial \rho & \partial v / \partial \phi \end{pmatrix} \right| \\ &= \left| \det \begin{pmatrix} r_0(\phi) - a & \rho dr_0 / d\phi \\ 0 & 1 \end{pmatrix} \right| \\ &= |r_0(\phi) - a| . \end{aligned} \quad (3.1-27)$$

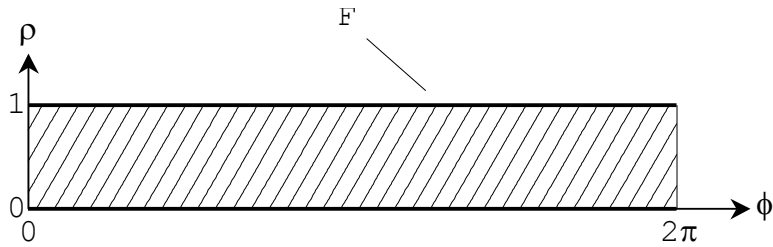


Figure 3.1-5 Integration area F in the $\rho\phi$ -plane.

Now, the integration area is rectangular as shown in Figure 3.1-5 such that the integral can be written in terms of one-dimensional integrals with constant limits

$$I = \int_0^{2\pi} \int_0^1 f(r(\rho, \phi) \cos \phi, r(\rho, \phi) \sin \phi) |\bar{N}| r(\rho, \phi) |r_0(\phi) - a| d\rho d\phi \quad (3.1-28)$$

For the numerical calculation of this integral the trapezoidal rule is used for the ϕ -integration and the rule of Gauss for the ρ -integration. Despite its simplicity the trapezoidal rule is very efficient when the integrand is periodic and the integral is calculated over a whole period. The weights and abscissas are calculated by a simple algorithm from Davis & Rabinowitz (1984).

A trapezoidal-Gauss integration grid on a circular aperture is shown in Figure 3.1-6. The number of points in the ϕ -integral is $N_\phi = 19$ and the number of points in the ρ -integral is $N_r = 8$.

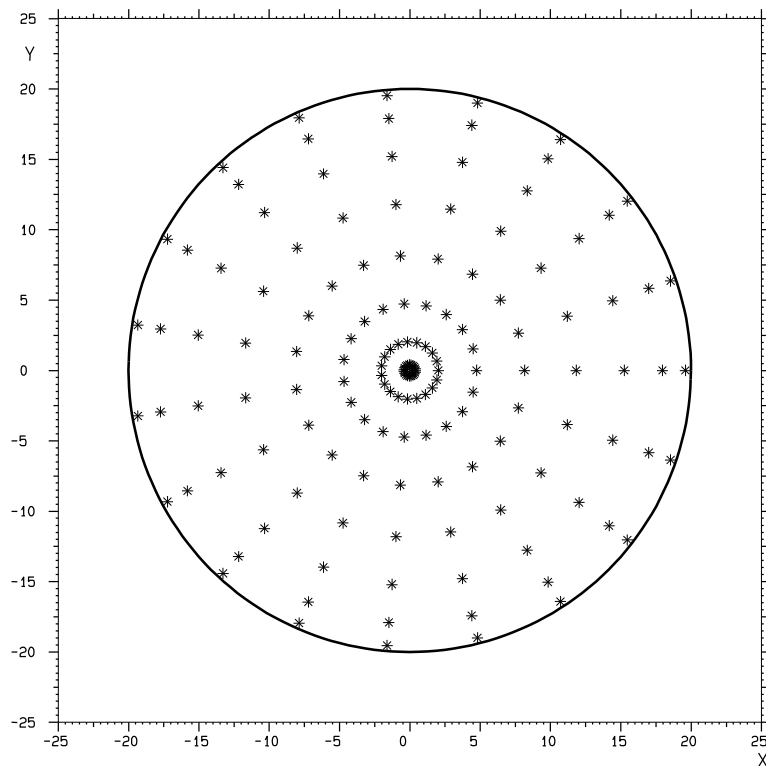


Figure 3.1-6 Integration grid for fixed N_ϕ .

$N_\phi = po2 = 19$, $N_r = pol = 8$. Number of points = 152.

It is seen that the density of points near the centre is unnecessarily high which can be avoided if N_ϕ is a function of ρ . If N_ϕ is a constant and $N_\phi \propto \rho$ is chosen as

$$N_\phi(\rho) = \text{nint} \left[\max \left(N_\phi, 10 - 10 \sqrt{\rho} \right) + 10 \right] \quad (3.1-29)$$

(where the function $\text{nint}(x)$ denotes the nearest integer to x), the same precision of the integral is obtained as when a constant N_ϕ equal to N_ϕ' is used. This reduced integration grid is shown in Figure 3.1-7.

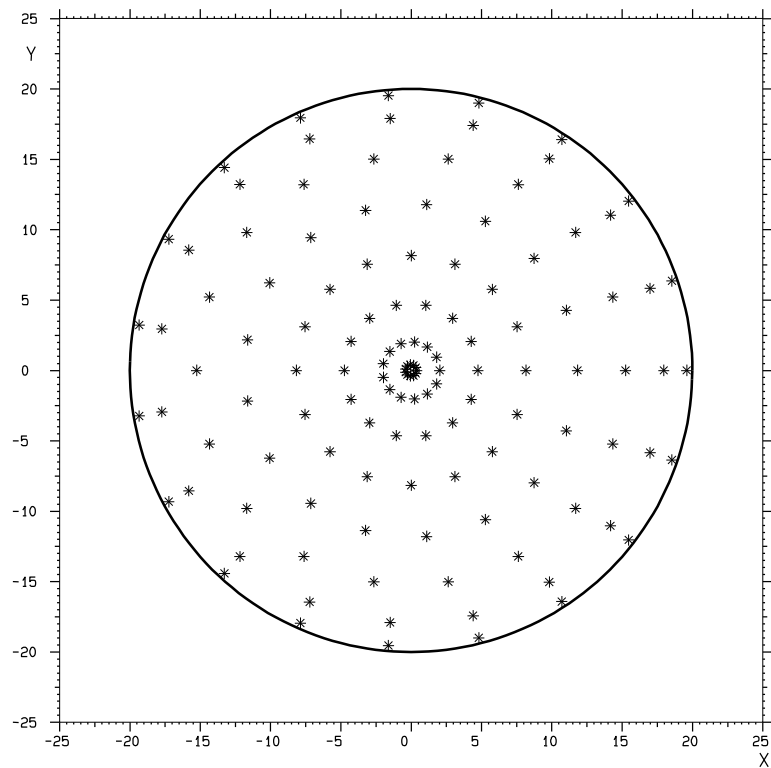


Figure 3.1-7 Reduced integration grid.

$N_\phi = po2 = 19$, $N_r = pol = 8$. Number of points = 127.

If the aperture has a circular blocking area the integration points will be distributed as shown in Figure 3.1-8. The thinning algorithm for the ϕ -integration becomes slightly more complicated than (3.1-29) and N_r denotes the number of radial integration points from the rim of the blocking circle to the rim of the reflector.

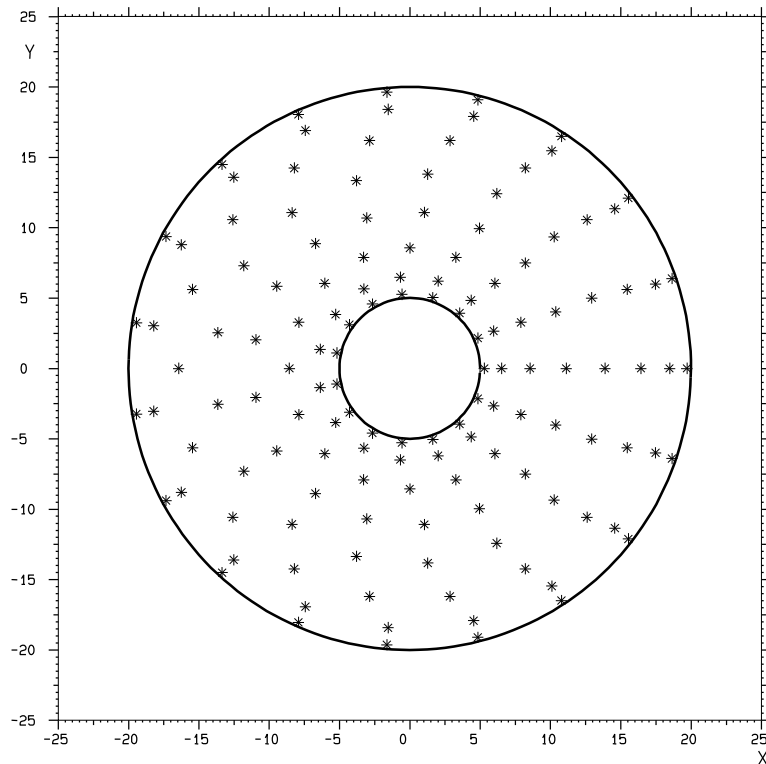


Figure 3.1-8 Reduced integration grid with circular blocking.

$N_\phi' = po2 = 19$, $N_r = pol = 8$. Number of points = 136.

In the physical optics classes in the integration grid density is specified by the variables pol and $po2$ which, for the polar grid, are connected to the variables above by

$$\begin{aligned} pol &= N_r \\ po2 &= N_\phi' . \end{aligned} \quad (3.1-30)$$

3.1.2.2 *Rectangular and parallelogram grid*

If the scatterer is a reflector with rectangular rim or a plane parallelogram a special integration grid is used as described in this section. In the following only the parallelogram is treated since the rectangle is a special case.

A parallelogram is shown in Figure 3.1-9 with the two side vectors \bar{v}_1 and \bar{v}_2 given from a corner point \bar{r}_0' . The interior points in the parallelogram can be parameterised by the coordinates ξ and η through

$$\begin{aligned}\bar{r}' &= \bar{r}_0' + \xi\bar{v}_1 + \eta\bar{v}_2 \\ 0 &\leq \xi \leq 1 \\ 0 &\leq \eta \leq 1\end{aligned}\tag{3.1-31}$$

and the Jacobian becomes

$$\left| \det \frac{\partial(x', y')}{\partial(\xi, \eta)} \right| = |\bar{v}_1 \times \bar{v}_2| \tag{3.1-32}$$

so that the integral (3.1-22) can be written

$$I = \int_0^1 \int_0^1 f(x'(\xi, \eta), y'(\xi, \eta)) |\bar{N}| |\bar{v}_1 \times \bar{v}_2| d\xi d\eta \quad . \tag{3.1-33}$$

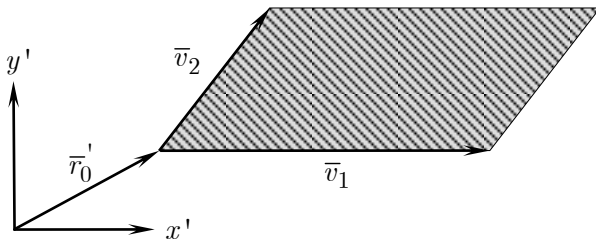


Figure 3.1-9 Integration over a parallelogram.

For both ξ and η the integration procedure of Gauss is used and a typical integration grid is shown in Figure 3.1-10.

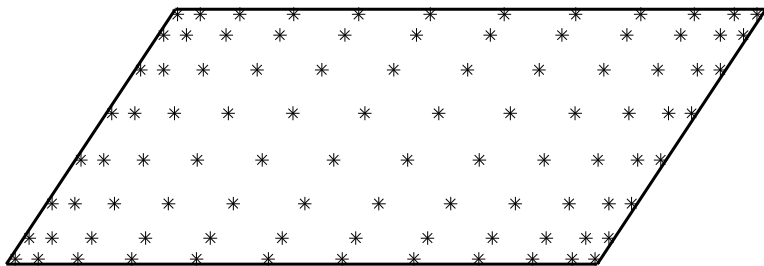


Figure 3.1-10 Integration grid on a parallelogram.
 $pol = 12, po2 = 8$. Number of points = 96.

The integration grid density is specified by the variables pol and $po2$ such that

$$pol = \text{Number of points along } \bar{v}_1$$

$$po2 = \text{Number of points along } \bar{v}_2 . \quad (3.1-34)$$

3.1.2.3 *Triangular grid*

When the scatterer is a flat triangular plate or a reflector with a triangular rim the physical optics integration is carried out in the following way.

If the scatterer is a triangular plate a coordinate system $x'y'z'$ is chosen such that the plane triangle is located in the $x'y'$ -plane with one corner point in the origin and the longest side of the triangle along the positive x' -axis. The sides of the triangle is numbered 1,2 and 3 corresponding to the vectors \bar{v}_1 , \bar{v}_2 and \bar{v}_3 along the sides of the triangle. The numbering is chosen such that \bar{v}_1 and \bar{v}_2 starts at the origin, \bar{v}_1 is located along the longest side and $\bar{v}_1 = \bar{v}_2 + \bar{v}_3$ as shown in Figure 3.1-11.

If the scatterer is a reflector with a triangular rim the same procedure is chosen apart from the $x'y'$ -plane now being parallel to the xy -plane of the reflector coordinate system in which the triangular rim is defined.

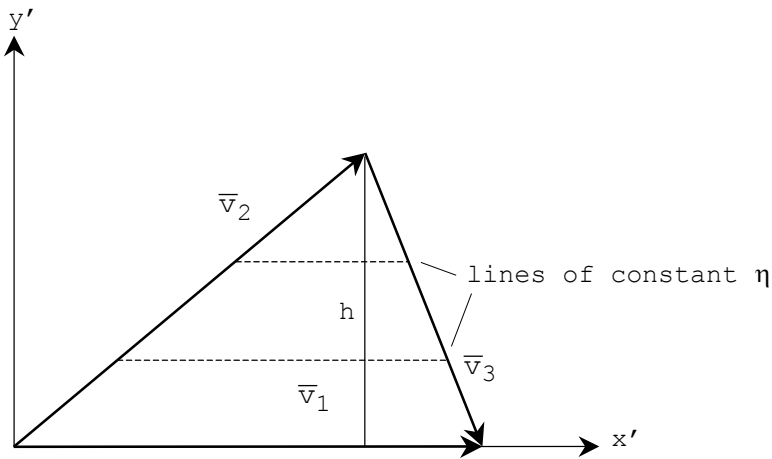


Figure 3.1-11 Local coordinate system for triangle integration.

The base g and height h of the triangle with respect to the longest side can then be computed by

$$\begin{aligned} g &= \bar{v}_1 \cdot \hat{x}' \\ h &= \bar{v}_2 \cdot \hat{y}' . \end{aligned} \quad (3.1-35)$$

It is also seen that the slope of the side along \bar{v}_2 is given by

$$\alpha = \frac{\bar{v}_2 \cdot \hat{y}'}{\bar{v}_2 \cdot \hat{x}'} . \quad (3.1-36)$$

The equation of the line along side No. 2 becomes

$$x' = \alpha y' \quad (3.1-37)$$

and

$$x' = g - \left(\frac{g}{h} - \alpha \right) y' \quad (3.1-38)$$

for the line along side No. 3. A parameterisation of the points inside the triangle can now be defined by the two parameters, ξ and η where

$$\begin{aligned} 0 &\leq \xi \leq 1 \\ 0 &\leq \eta \leq 1 . \end{aligned} \quad (3.1-39)$$

The parameterisation is defined such that a fixed value of η with ξ running from 0 to 1 gives the points on the line $y' = h\eta$, starting from the intersection of this line with side No. 2 and ending at the intersection with side No. 3 as indicated by the dashed lines in Figure 3.1-11. The relations are explicitly given by

$$\begin{aligned} y' &= h\eta \\ x' &= ah\eta + g(1 - \eta)\xi \end{aligned} . \quad (3.1-40)$$

The Jacobian becomes

$$\left| \det \frac{\partial(x', y')}{\partial(\xi, \eta)} \right| = |hg(1 - \eta)| \quad (3.1-41)$$

and the integral (3.1-22) can be written as

$$I = \int_0^1 \int_0^1 f(x'(\xi, \eta), y'(\xi, \eta)) |\bar{N}| |hg(1 - \eta)| d\xi d\eta . \quad (3.1-42)$$

Gaussian integration is used for both ξ and η in (3.1-42).

A typical distribution of integration points is shown in Figure 3.1-12 where the number of integration points N_ξ along ξ is reduced when η increases according to

$$N_\xi(\eta) = \max 10, \text{nint}(N_{\xi \text{ max}} \sqrt{1 - \eta}) , \quad (3.1-43)$$

where $N_{\xi \text{ max}}$ is the maximum number of integration points along the longest side and the function $\text{nint}(x)$ denotes the nearest integer to x .

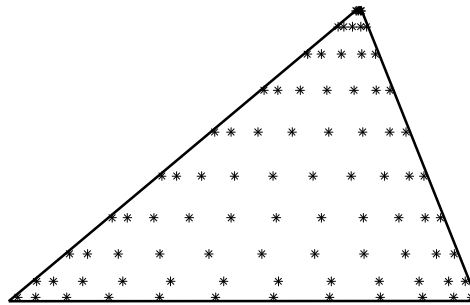


Figure 3.1-12 Integration grid for triangle.

$pol = 10$, $po2 = 12$. Number of points = 86.

The integration grid density is specified by the variables pol and $po2$ such that

$$\begin{aligned}
 pol &= \text{Number of points along the height} \\
 &\quad \text{orthogonal to the longest side} \\
 po2 &= \text{Maximum number of points} \\
 &\quad \text{along the longest side}
 \end{aligned} \tag{3.1-44}$$

3.1.3 Convergence of the physical optics integral

3.1.3.1 General convergence properties

The physical optics integration grid is specified by the two variables pol and $po2$. The values of these variables can either be determined automatically by GRASP, as will be described in the next section, or they can be set to suitable values by the user. Too small values of pol and $po2$ will result in inaccurate fields since the PO integral has not converged, and large values, on the other hand, will take more computation time than necessary. For simple cases (e.g. focused single reflector systems) it is possible to use a set of explicit rules, described below, but otherwise a convergence test must be carried out.

In general the physical optics integral is easiest to calculate for focused reflectors and close to the main lobe because the integrand in the PO integral is then a slowly varying function of the integration variables. As the observation point moves

into the side-lobe region the integrand becomes increasingly oscillatory which requires a finer integration grid resulting in longer computation time.

For some scatterer types it is possible to give simple rules for estimating $po1$ and $po2$. If the scatterer is a focused reflector with circular rim the PO integral will converge if (cf. (3.1-30))

$$po1 = \text{nint } z / 2.4 , \quad po2 = \text{nint } z \quad (3.1-45)$$

where

$$z = 1.09 \cdot \pi \frac{D}{\lambda} \sin \theta_o + 10 . \quad (3.1-46)$$

The function nint gives the nearest integer to the argument, D is the reflector diameter, λ is the wavelength and θ_o is the maximum angle from the beam centre at which the integration shall be converged. This estimate of $po2$ can also be used for PTD integration. If the aperture is defocused it may be necessary with up to two times these values as illustrated in Figure 3.1-13 where a circular reflector is illuminated by an incident field which propagates nearly parallel to the plane of the rim and the observation direction is the opposite of the incident field. This is the worst-case situation because the integrand of the PO-integral varies with a whole period when the integration point on the reflector is moved $\lambda/2$ in the direction of the incident field. Since at least one sample per period is needed the spacing $\Delta\ell$ between the integration points must satisfy

$$\Delta\ell < \lambda/2 . \quad (3.1-47)$$

Along the rim of the reflector the spacing between the integration points is given by

$$\Delta\ell = \frac{2\pi R}{N_\phi} , \quad (3.1-48)$$

where R is the reflector radius and $N_\phi = po2$. From $D = 2R$ and the two relations above it is seen that

$$po2 > 2\pi \frac{D}{\lambda} \quad (3.1-49)$$

which is approximately the double of (3.1-45) for $\theta_o = 90^\circ$. In this situation also $po1$ should be doubled.

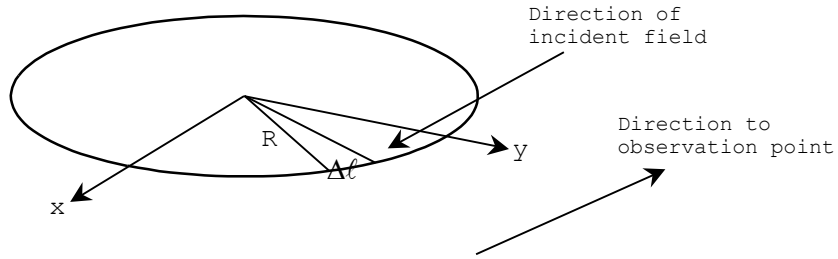


Figure 3.1-13 Worst-case PO integration with circular reflector rim.

If the scatterer is a focused reflector with rectangular rim $po1$ and $po2$ can be estimated from (cf. (3.1-34))

$$\begin{aligned} po1 &= \text{nint}\left(1.75 \cdot \frac{D_x}{\lambda} \sin \theta_x + 10\right) \\ po2 &= \text{nint}\left(1.75 \cdot \frac{D_y}{\lambda} \sin \theta_y + 10\right) , \end{aligned} \quad (3.1-50)$$

where D_x and D_y are the reflector dimensions along \bar{v}_1 and \bar{v}_2 , respectively, in Figure 3.1-9. The PO integral will converge from the beam centre up to the angle θ_x away from the z -axis towards the x -axis and the angle θ_y away from the z -axis towards the y -axis. As for the circular rim the worst-case situation may require the double values

$$\begin{aligned} po1 &= 3.5 \cdot \frac{D_x}{\lambda} \\ po2 &= 3.5 \cdot \frac{D_y}{\lambda} . \end{aligned} \quad (3.1-51)$$

In more general cases as e.g. a dual reflector system, where the incident field on the main reflector may be very complicat-

ed because it comes from the subreflector instead of a simple feed, it is not possible to give simple rules for the integration grid. To this end the procedure described in the following section is developed.

3.1.3.2 *Automatic convergence procedure*

The density of the PO integration grid is given by the two numbers pol and $po2$ and the values necessary to obtain a convergent solution depend both on the current distribution on the reflector and on the location of the output points. In GRASP an automatic procedure has been developed to assure that a convergent result is achieved. This procedure is described in the following.

The output points for a PO integration can be either the field points specified as cuts or grids in Section 4.2 or it can be the integration grid points on another reflector. In both cases the automatic convergence procedure operates in the same way. At the start a representative subset of the output points, in the following called the test points, is selected.

The calculations start with the values $pol = po2 = 10$ and the field is calculated at the desired test points. Hereafter, pol is doubled to $pol = 20$ and the field is re-calculated. This doubling of pol is continued until the field is converged. If the fields for e.g. $pol = 40$ and $pol = 80$ differ by less than $10^{field accuracy/20}$ relative to the maximum field values at all the requested test points the convergence is deemed acceptable. The value of “field accuracy” is given by the user and it defines the required accuracy of the calculations. If for example field accuracy is -80 dB this means that the field error due to convergence is at least 80 dB below the maximum value of the field at any of the field points. A field accuracy of -80 dB corresponds to ripples of ± 1 dB at the -60 dB level.

The smallest acceptable value of pol is now known to be contained in the interval from 20 to 40. The interval may be further narrowed by selecting the centre point, $pol = 30$, and compare the result to the field obtained for $pol = 80$. This bi-

section can be continued until a satisfactory value for $po1$ is determined. Next, $po1$ is reset to 10 and the same procedure is carried out for $po2$. These convergence calculations will run very fast because only one of the parameters $po1$ and $po2$ is greater than 10.

Now, the reflector parameters are determined to e.g. $po1 = 35$ and $po2 = 55$ and the currents are then calculated with these values and stored on file. It is then assured that these currents will provide the required accuracy on all the specified output points. If the reflector is the first in a sequence of PO calculations the currents will generate the input field on the following reflector for which the same convergence procedure can now be applied.

The procedure described above can be used for any number of reflectors. In the following the automatic convergence method will be illustrated for a single-reflector system.

An offset single-reflector system is shown in Figure 3.1-14. The diameter of the reflector is $D = 40 \lambda$, the focal length is $f = 20 \lambda$ and the offset of the centre point is $x_0 = 40 \lambda$. The objective is to calculate the far-field radiation pattern all around the antenna in the plane of symmetry, i.e. $-180^\circ < \theta < 180^\circ$ and $\phi = 0^\circ$. In order to obtain the correct determination of all the side lobes an angular spacing of less than $0.25\lambda/D = 0.36^\circ$ is necessary.

Some of the calculated radiation patterns are shown in Figure 3.1-15. For the convergence tests an output field containing only eleven test points from -180° to $+180^\circ$ with a spacing of 36° is used as a representative subset. The integration grid parameters $po1$ and $po2$ determined for different field accuracies are summarised in Table 3.1-1. The right-most column in the table shows the product, $po1*po2$, which is an indication of the computer time required to calculate the pattern.

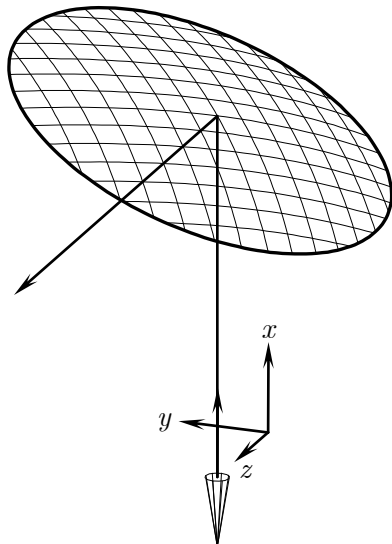


Figure 3.1-14 Single offset reflector for automatic convergence investigations.

Field accuracy, dB below maximum	pol	$po2$	$pol*po2$
-20	35	93	3255
-40	85	260	22100
-60	93	295	27435
-80	97	310	30070
-100	100	315	31500
-200	100	315	31500

Table 3.1-1 The integration grid parameters pol and $po2$ as a function of the required convergence accuracy.

The results show that even with the most crude field accuracy, -20 dB, the whole region around the main beam from -30° to $+120^\circ$ is completely converged. Figure 3.1-15 also demonstrates that in the remaining part of the pattern the convergence errors are 20 dB or more below the peak. When the field accuracy is increased it is seen that the most difficult direction

is around $\phi = -135^\circ$ but when the field accuracy is -100 dB also this direction has fully converged. Table 3.1-1 also illustrates the rate of convergence. Increasing the accuracy from -20 dB to -40 dB increases the computer time by a factor 7. Increasing the accuracy from -40 dB to -60 dB adds 25% in computer time while increasing the accuracy further from -60 to -100 dB results in only a 15% increase of computer time.

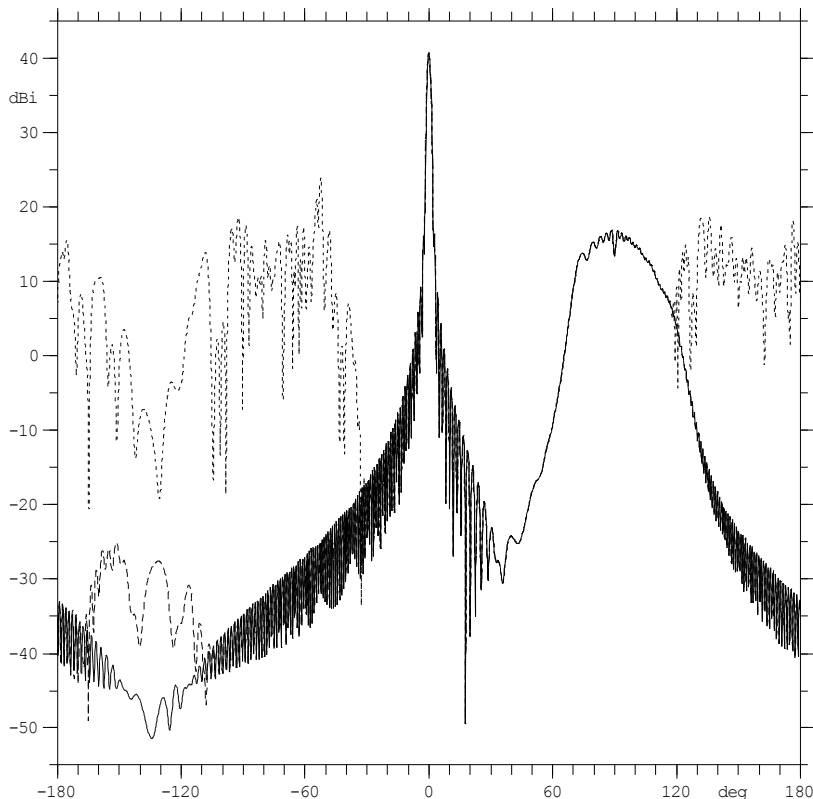


Figure 3.1-15 Radiation patterns for the antenna in Figure 3.1-14 with different field accuracy requirements to the convergence.
 Full line: field accuracy, -100 dB
 Long dots: field accuracy, -60 dB
 Small dots: field accuracy, -20 dB

It should be noted that only the scattered field from the reflector is tested. In order to get the correct pattern, especially in

the region behind the reflector around $\theta = 90^\circ$, the feed pattern must be added. Let us assume, as an example, that the feed pattern has a gain of 20 dBi and the total field in this direction is required with an accuracy of ± 1 dB at the 0 dBi level. This means that the error level shall be at the -20 dBi level which is 60 dB below the main beam peak. The field accuracy for the automatic procedure shall therefore be specified to -60 dB.

The automatic convergence procedure is very fast and it will normally not affect the total computer time to any significant extent. However, if many runs have to be performed with the same integration grid, and especially if the incident field is a large file of currents, it is recommended to switch off the automatic convergence procedure once the correct values of pol and $po2$ have been determined.

The convergence properties and the automatic convergence procedure for PO calculations described above are also applicable to calculations involving PTD, gaps and struts described in Sections 3.2 to 3.4.

3.1.4 Spillover calculation

When the induced PO currents are computed on a scatterer surface it is also possible to request a calculation of the power contained in the incident field. This power is computed by integrating Poynting's vector \bar{P} over the surface

$$\bar{P} = \frac{1}{2} \operatorname{Re}(\bar{E} \times \bar{H}^*) , \quad (3.1-52)$$

where Re denotes the real part and * the complex conjugate. The power ΔW hitting a surface element with area Δs becomes

$$\Delta W = -\bar{P} \cdot \hat{n} \Delta s , \quad (3.1-53)$$

where \bar{P} is the Poynting vector of the incident field and \hat{n} is the unit surface normal pointing towards the illuminated side of the surface. The total power W on the surface becomes

$$W = - \iint_B \bar{P}(\bar{r}') \cdot \hat{n}(\bar{r}') \, ds' , \quad (3.1-54)$$

which is a surface integral with the integration variable \bar{r}' . The integral can be reduced to the standard form (3.1-22) and evaluated numerically as described in Section 3.1.2.

The spillover in dB is defined as

$$\text{spillover} = 10 \log_{10} \frac{4\pi}{W} , \quad (3.1-55)$$

where the factor 4π originates from the normalisation of the feed to the power 4π watt (see Section 4.1.3). Since both the E- and H-field are used in the spillover calculation the computation time for the incident field is doubled compared to standard calculation of the PO currents where only the H-field is needed. The reason for the selected spillover definition is that it is much more efficient and accurate to calculate the power hitting a reflector than to attempt to calculate the total power in all other directions.

One consequence of the definition (3.1-55) is that in a multi-reflector system the spillover for a given reflector will include the spillover past all the preceding reflectors in the system.

3.2 Physical Theory of Diffraction

As explained in Section 3.1 physical optics gives an approximation to the scattered field

$$\bar{E}^s \cong \bar{E}^{PO} . \quad (3.2-1)$$

The physical optics currents approximate the induced currents on a scatterer derived from scattering by an infinite planar surface. Thus, the special behaviour of the currents close to an edge of the scatterer is not modelled by physical optics. In the Physical Theory of Diffraction, PTD, the difference between the exact induced currents and the PO currents is approximated by considering the induced currents on an infinite per-

fectly conducting half plane illuminated by a plane wave. These PTD currents are therefore a correction to the PO currents such that the radiated PTD field is a correction which must be added to the PO field for obtaining the scattered field

$$\bar{E}^s \simeq \bar{E}^{PO} + \bar{E}^{PTD} . \quad (3.2-2)$$

The PTD implemented in GRASP is based on Johansen (1996). The PTD contribution is calculated by integrating so-called PTD equivalent edge currents along the illuminated part of the edges of the scattering structure. These currents are determined from an integration of the fringe wave current (the exact current minus the PO current) along incremental strips on the canonical wedge or half plane. The incremental strips may be either infinite or of finite length as discussed by Johansen.

In GRASP, the infinite incremental strips are used for reflectors, whereas incremental strips of finite length are used for flat plates (hence, different PTD expressions are used for a flat plate and a reflector having a plane surface). The length of the strips is chosen to conform with the physical dimensions of the flat plates. For both reflectors and flat plates, the PTD contributions are based on the canonical half plane modelling.

The reader is referred to Johansen (1996) for the PTD expressions.

In the case of infinite strips and half plane modelling - as used for reflectors - the PTD expressions reduce to those reported previously by Shore and Yaghjian (1988) and listed below. These PTD contributions can conveniently be separated in a TE and a TM component of the following form

$$d\bar{E}^{TM} = dz' E_z^i \frac{e^{-jkr}}{4\pi r} \frac{\sin \theta}{\sin^2 \theta_o} \frac{2 \sin \frac{\phi_o}{2}}{\left| \cos \frac{\phi_o}{2} \right| + \sin \frac{\alpha}{2}} \hat{\theta} \quad (3.2-3)$$

$$\begin{aligned}
 d\bar{E}^{TE} = dz' \zeta H_z^i \frac{e^{-jkr}}{4\pi r} \frac{1}{\sin \theta_o} \frac{\text{SIGN}(\pi - \phi_o)}{\sin \frac{\alpha}{2} \left(\left| \cos \frac{\phi_o}{2} \right| + \sin \frac{\alpha}{2} \right)} \\
 \left[\left(\cos \phi \cos \theta + \cot \theta_o \sin \theta \left(1 + 2 \left| \cos \frac{\phi_o}{2} \right| \sin \frac{\alpha}{2} \right) \right) \hat{\theta} \right. \\
 \left. - \sin \phi \hat{\phi} \right] \quad (3.2-4)
 \end{aligned}$$

where dz' is the incremental arc length along the edge giving the contributions $d\bar{E}^{TM}$ and $d\bar{E}^{TE}$ to the PTD field. The constant ζ is the impedance of free space and E_z^i and H_z^i denote the z -components of the incident field. The angles θ_o and ϕ_o define the direction of the incident field and r , θ and ϕ are the polar coordinates of the observation point as illustrated in Figure 3.2-1. The special angle α is defined through

$$\sin \frac{\alpha}{2} = \sqrt{\frac{1 - \sin \theta \cos \phi \sin \theta_o + \cos \theta_o \cos \theta}{2 \sin^2 \theta_o}}. \quad (3.2-5)$$

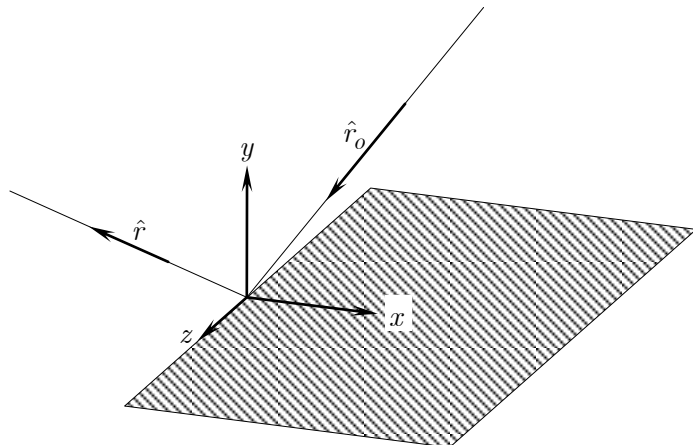


Figure 3.2-1 PTD analysis.

Direction of incident field

$$\hat{r}_o = -(\sin \theta_o \cos \phi_o, \sin \theta_o \sin \phi_o, \cos \theta_o).$$

Direction of observation point

$$\hat{r} = (\sin \theta \cos \phi, \sin \theta \sin \phi, \cos \theta).$$

All angles and vectors are referred to a local edge coordinate system as shown in the figure.

The PTD field depends on the direction of the incident field and the PTD approximation is only valid if the incident field at the edge locally behaves as a plane wave. As explained in Section 3.1.1 PO does not have this limitation.

The default in GRASP is that the direction of propagation of the incident field is computed from Poynting's vector (3.1-52) such that

$$\hat{r}_o = \frac{\bar{P}}{|\bar{P}|}. \quad (3.2-6)$$

If the incident field comes from an extended source (e.g. a feed array or a set of PO currents) the user can choose to calculate the PTD contribution from each of its elements separately. This may be time consuming, but will give a more accurate result.

PTD is not available for non-perfectly conducting scatterers.

3.3 Reflector with gaps

For reflectors built of panels, the physical optics calculation is performed panel by panel, i.e. over the actual reflecting surface.

The currents radiate a field which to some extent takes into account the influence of the gaps. However, the PO currents on a specific panel are independent of the presence of the other panels, as $\bar{J}^{PO} = 2\hat{n} \times \bar{H}^i$ only depends on the incident field. As a result, the coupling between currents on adjacent panels is not taken into account.

In addition, the special behaviour of the currents close to the panel edges is not modelled by PO. Therefore, in GRASP it is possible to add to the PO field, a PTD-field that better models the behaviour of the currents close to the panel edges.

The PTD is divided into two contributions depending on whether the panel edge is part of the reflector outer edge or is part of an inter-panel gap. The PTD-contribution used at the reflector outer edge is the same as described in Section 3.2. The PTD-contribution used at the gaps is approximated by considering the induced currents on the canonical problem of plane-wave scattering by a slit in an infinite ground plane as described below.

3.3.1 The PTD-gap contribution

The canonical problem, configuration 1, is shown in Figure 3.3-1. A plane wave is illuminating a slit of width w in an infinite ground plane. The desired field is the PTD-contribution, \bar{E}_1^{PTD} , from this configuration, i.e. the total field minus the PO-field.

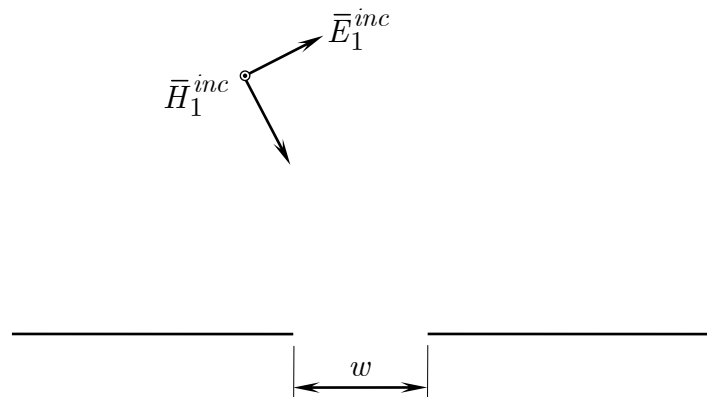


Figure 3.3-1 Configuration 1: a slit of width w in an infinite plane.

Using Babinet's principle, the solution to this canonical problem is related to the dual problem, configuration 2, of plane-wave scattering by a two-dimensional (2D) strip, cf. Figure 3.3-2.

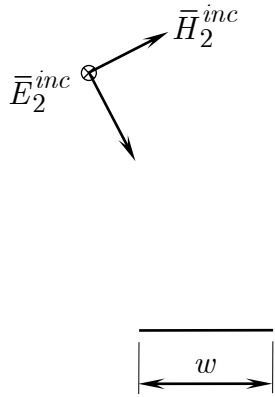


Figure 3.3-2 Configuration 2: a strip of width w .

If the incident plane waves in the two configurations are related as

$$\bar{E}_1^{inc}, \zeta \bar{H}_1^{inc} = \zeta \bar{H}_2^{inc}, -\bar{E}_2^{inc} \quad (3.3-1)$$

then the desired PTD field from configuration 1 can be shown to be

$$\begin{aligned} \bar{E}_1^{PTD} &= \bar{E}_1^{PO} \text{ Gap} + \Gamma \zeta \bar{H}_2^{scat} \\ &= \Gamma \zeta \bar{H}_2^{PTD} + \bar{E}_1^{PO} \text{ Gap} + \Gamma \zeta \bar{H}_2^{PO} . \end{aligned} \quad (3.3-2)$$

In this equation, \bar{E}_1^{PO} Gap is the PO field due to the incident field of configuration 1, but for the dual scattering configuration, i.e. for the infinite strip. Further, \bar{H}_2^{PO} and \bar{H}_2^{PTD} are the PO and PTD fields from configuration 2, and Γ is a factor which equals +1 if the source and observation points are on the same side of the infinite ground plane, and -1 if they are on opposite sides. All three contributions on the right-hand side of (3.3-2) are calculated for 2D-problems with finite cross-section, as opposed to the contribution on the left-hand side where the cross-section is of infinite extent.

The calculation of the right-hand side of (3.3-2) is further divided into two cases: If the gap (and thus the strip) is narrow-

er than 0.32λ , then a narrow-gap approximation is used. Otherwise a wide-gap approximation is used.

The narrow-gap approximation uses the approximation of \bar{H}_2^{scat} and $\bar{E}_1^{PO} Gap$ reported by Shore and Yaghjian (1988). The PTD-contributions are formulated as Incremental Length Diffraction Coefficients (ILDCs), which are distributed along the central curve of the actual gap.

The wide-gap approximation uses the same approximation of \bar{H}_2^{PTD} as used for plates, cf. Section 3.2. Hence, this PTD-contribution is formulated as ILDCs distributed along both edges of the gap. The ILDCs use incremental strips proportional to w and thus of finite length, cf. Section 3.2. The contributions \bar{H}_2^{PO} and $\bar{E}_1^{PO} Gap$ are calculated by integrating physical optics currents distributed in a two-dimensional grid conforming with the actual gap width and length.

3.3.2 Integration Grids

In the GRASP input, the integration grid to be used for the PTD-gap contributions is specified by the variables *ptd1* and *ptd2*.

If the narrow-gap approximation is used, then *ptd1* specifies the number of integration points (ILDCs) along the central gap curve. The variable *ptd2* is not used.

If the wide-gap approximation is used, there are two integration grids used. One grid is used to calculate \bar{H}_2^{PO} and $\bar{E}_1^{PO} Gap$. The variables *ptd1* and *ptd2* define the two-dimensional grid conforming with the gap, with *ptd1* points along the gap and *ptd2* points across the gap. The other grid is used to calculate \bar{H}_2^{PTD} and uses *ptd1* points (ILDCs) along each of the two edges of the gap.

For all integration grids the integration procedure of Gauss is used.

3.3.3 Numerical Example

A Panels in Polar Grid reflector, cf. Section 2.2.1.4, with gaps is analysed. The scattering configuration is shown in Figure 3.3-3. The paraboloidal antenna has a focal length, $F = 8\lambda$, and a diameter, $D = 20\lambda$, λ being the wavelength. The feed is a Huygens source located at the focus with the electric dipole x -directed and the magnetic dipole y -directed.

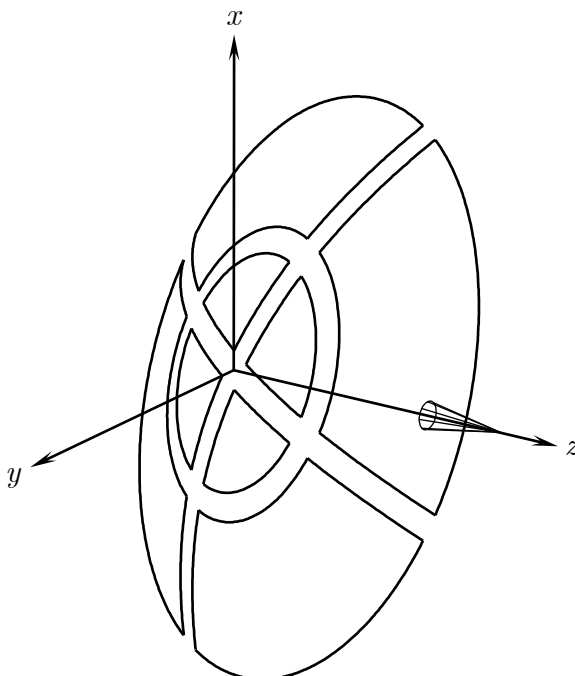


Figure 3.3-3 Paraboloidal front-fed reflector with radial and azimuthal gaps.

The configuration has an azimuthal gap halfway in angular measure from the centre of the paraboloid, $2u = 32.01^\circ$, and four radial gaps at the azimuthal angles $\phi = \pm 45^\circ$, $\phi = \pm 135^\circ$ (i.e. two "diameter-gaps"). The gap width is fixed to 1λ .

The gap layout considered is not realistic due to the presence of the gaps at the centre of the reflector, but is used since it is

identical to the one considered in Shore and Yaghjian (1993). Also, the gap widths are too large for a realistic antenna.

In the upper half of Figure 3.3-4, the field in the $\phi = 0$ cut is shown from the boresight direction at $\theta = 0$ to the back lobe of the antenna at $\theta = 180^\circ$. The pattern obtained by the GRASP PO/PTD-modelling is shown in full line. The pattern obtained by a Method of Moments solution is shown in dotted line. For reference, the corresponding patterns for a reflector without gaps are shown in the lower part of Figure 3.3-4.

The presence of the wide gaps significantly changes the pattern. In particular the field penetrating the reflector is clearly visible as the field level is significantly raised close to the back-lobe. In the major part of the pattern there is a very good agreement between the patterns obtained by PO/PTD and by Method of Moments. In a region close to the antenna aperture plane, $\theta = 90^\circ$, the patterns differ, as multiple scattering phenomena and the reflector self-shadowing are not taken into account in the PO/PTD solution.

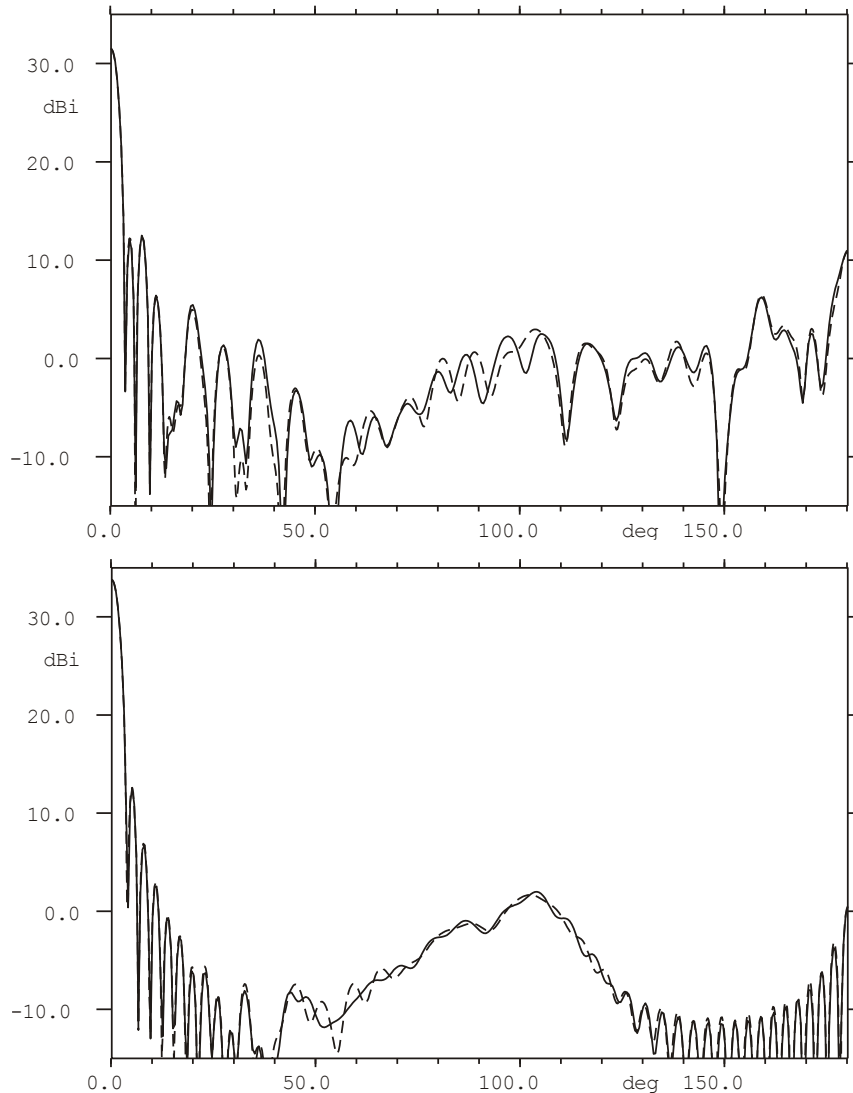


Figure 3.3-4 Radiation pattern in the xz -plane for the antenna in Figure 3.3-3. The full line curve is the result predicted by GRASP and the dotted line is a Moment-Method solution.
Top figure: gap width $w = 1\lambda$.
Bottom figure: gap width $w = 0$, (solid reflector).

3.4 Strut calculations

Struts in single and dual reflector antennas are used to support the feed system and subreflector in rotationally symmetric systems. These struts may have a serious impact on the antenna performance. The efficiency and cross-polarisation is degraded and the sidelobe level is increased.

3.4.1 Typical strut contributions

The three most important mechanisms by which the strut scattering influences the antenna radiation are described below and shown in Figure 3.4-1:

1. Illumination of the struts by the reflected field from the main reflector.
2. Shadowing and changes of the main reflector currents caused by direct feed illumination of the struts.
3. Reflection in the main reflector of the scattered field from the struts, where the incident field on the strut comes from the main reflector.

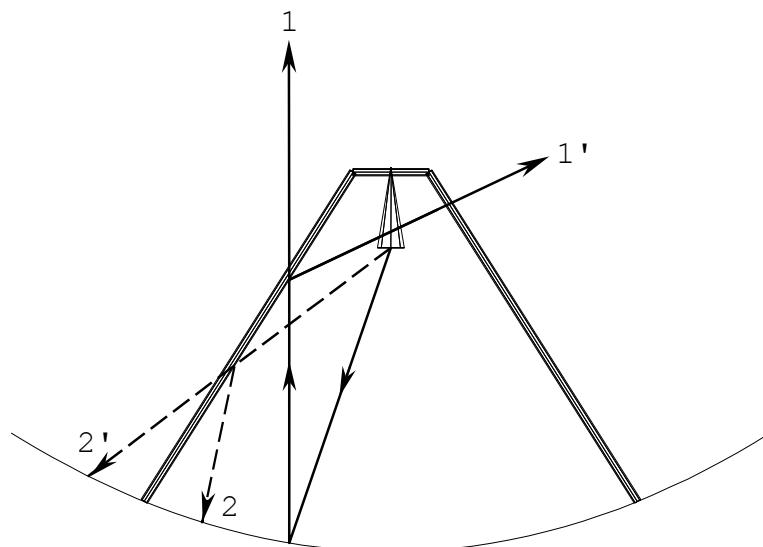


Figure 3.4-1 a Strut scattering of type 1 and 2.

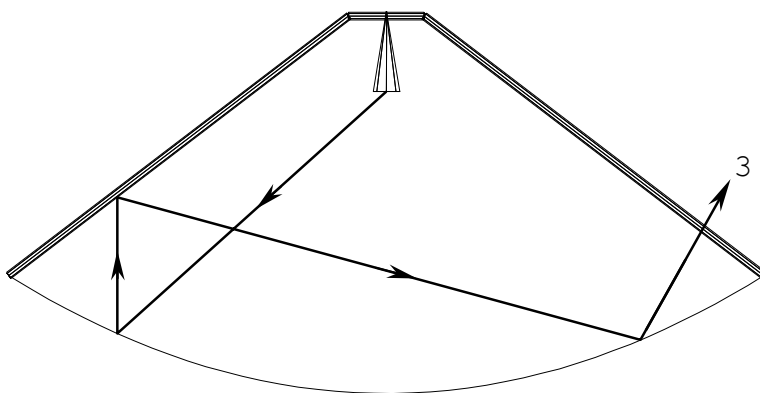


Figure 3.4-1 b Strut scattering of type 3.

The degradation of the peak gain (efficiency) is mainly due to the effects (1) and (2) of which (2) is only important in a system where the struts are not supported by the outer edge of the main reflector as in Figure 3.4-1a. The side-lobes will mainly be affected by the strut scattering (1') and (3) where (3) is only important in a configuration as shown in Figure 3.4-1b. Although these scattering effects are illustrated for a single reflector system they will also be the dominant effects in a dual reflector system where the feed is replaced by the subreflector.

3.4.2 Computational approach for circular struts

Two types of analyses for circular struts are presented in the following: 1) a simple PO approach which is especially useful for struts which are thick relative to the wavelength and 2) a canonical solution for struts with diameters in the order of the wavelength.

An accurate prediction of the effects of the struts both on the main lobe and on the sidelobes can be achieved by taking the current distribution along the circumference of the strut into account. This is relatively simple for a circular strut because the canonical problem (plane wave incidence on an infinite circular cylinder) has a simple solution in series form. For thick

struts the current distribution can alternatively be found by the simple PO approximation.

3.4.2.1 Simple PO

If the circular strut is large in terms of the wavelength the standard PO method can be used as for normal reflector surfaces. The circular strut is modelled as a circular cylinder and the surface currents on the illuminated surface side are found using the PO approximation

$$\bar{J} = 2\hat{n} \times \bar{H} \quad (3.4-1)$$

where \hat{n} is the unit surface normal (pointing outward) and \bar{H} is the total incident magnetic field from the source. The integral of the PO currents is evaluated numerically by the standard method using the trapezoidal rule for ϕ variation in the circular cross section and the rule of Gauss for the variation in length. A trapezoidal-Gauss integration grid on a circular strut is shown in Figure 3.4-2. The number of equidistant points around the circle is $N_\phi = 18$ and the number of points partitioning the length is $N_l = 20$.

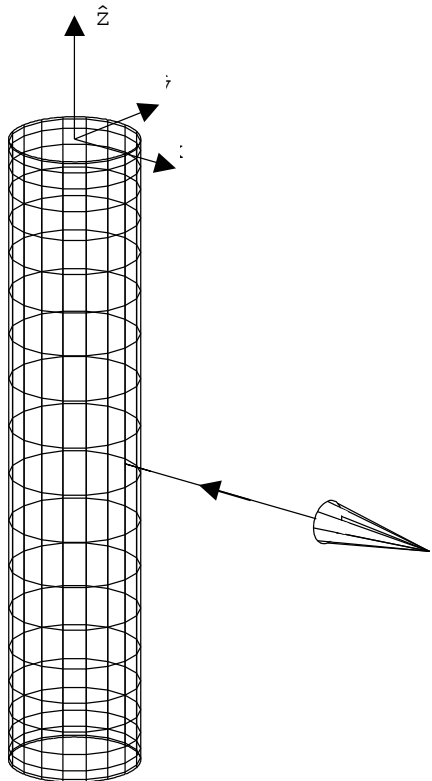


Figure 3.4-2 Integration grid on circular strut.

The user must specify the values of N_ϕ and N_l . The number of grid points necessary for convergence can be estimated by

$$N_l = 3L/\lambda \quad (3.4-2)$$

$$N_\phi = 16a/\lambda + 4 \quad (3.4-3)$$

where L is the strut length, a the radius and λ is the wavelength. In special cases it may be necessary to determine the density of the integration grid by a convergence test using the above values as start.

The currents in points on the shadow side of the strut are set to zero in a PO calculation. Therefore, the PO approach is only valid for thick struts. The shadow side is determined by the inequality

$$\hat{n} \cdot \bar{P} > 0. \quad (3.4-4)$$

where \bar{P} is the Poynting vector, $\bar{P} = \frac{1}{2} \operatorname{Re}(\bar{E} \times \bar{H}^*)$.

3.4.2.2 Canonical solution

A better prediction of the currents on the struts, especially on the shadow side of thin struts, is achieved using the canonical solution for circular cylinders. The scattered field from a plane wave incident on an infinite circular cylinder has a simple solution in series form, which is used to obtain the current distribution along the circumference of the strut.

3.4.2.2.1 Plane wave incidence

A local coordinate system is placed with the z -axis along the axis of the cylinder, as shown in Figure 3.4-3. A plane wave is incident from the direction θ_o, ϕ_o in this coordinate system.

The surface currents become for an incident TM-field

$$\bar{J}_{TM} = \hat{z} E_z^{ic} \frac{2}{\pi k a \sin^2 \theta_o} \sum_{m=-\infty}^{\infty} \frac{j^m e^{jm \phi - \phi_o}}{H_m^2 k a \sin \theta_o} \quad (3.4-5)$$

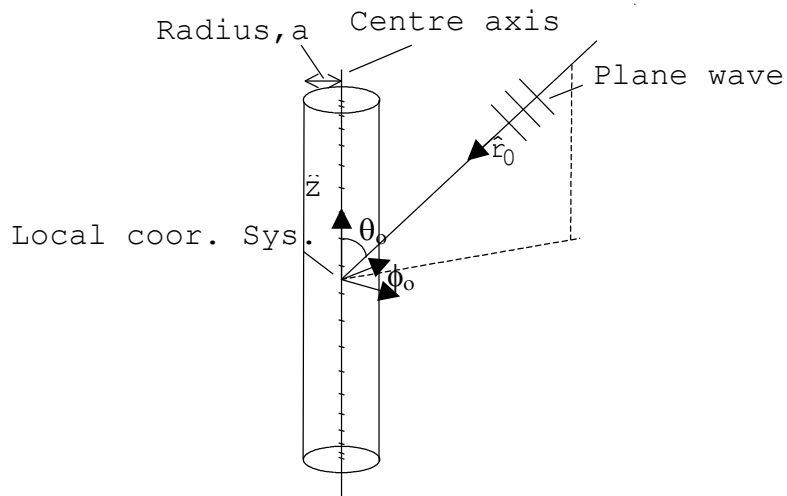


Figure 3.4-3 Plane wave incidence on strut.

and for an incident TE-field

$$\begin{aligned}\bar{J}_{TE} = & \hat{z} H_z^{ic} \frac{2j \cos \theta_o}{\pi k a^2 \sin^3 \theta_o} \sum_{m=-\infty}^{\infty} \frac{m j^m e^{jm \phi - \phi_o}}{H_m^2, k a \sin \theta_o} \\ & + \hat{\phi} H_z^{ic} \frac{2j}{\pi k a \sin \theta_o} \sum_{m=-\infty}^{\infty} \frac{j^m e^{jm \phi - \phi_o}}{H_m^2, k a \sin \theta_o}\end{aligned}\quad (3.4-6)$$

In expressions (3.4-5) and (3.4-6) the GRASP units are used, cf. Section 4.1.1.

3.4.2.2.2 Spherical wave incidence

If the incident field on the strut has a spherical phase front the illumination of the strut surface is quite different and the strut gives rise to a much wider shadow region, see Figure 3.4-4.

However, the canonical solution for a plane wave incidence can still give a good approximation to the induced surface currents. In a specific point on the cylinder the incident E and H field are calculated. The direction of propagation \hat{r}_o in this point is found from Poynting's vector. It is then assumed that the current in this point is the same as the current on an infinite cylinder illuminated by a plane wave with the same direction of propagation, amplitude and phase.

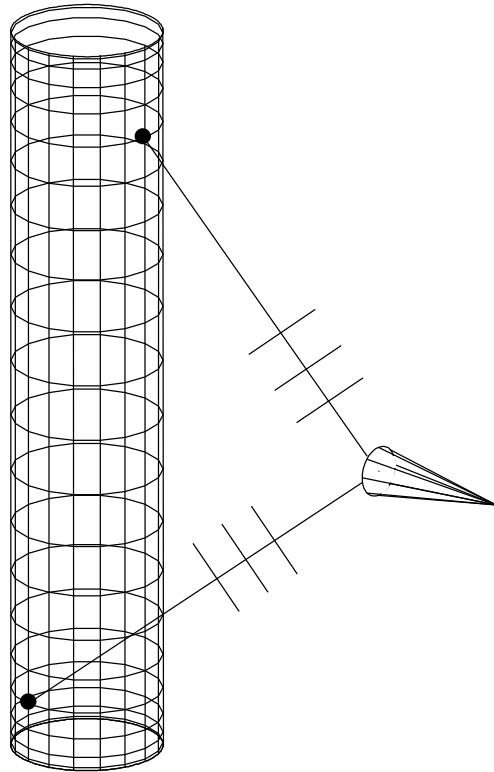


Figure 3.4-4 Field incidence from point source.

The field on the axis of the cylinder of this equivalent plane wave \bar{E}^{Pw} is related to the incident field \bar{E}^i from the near field source on the surface by the phase correction

$$\bar{E}^{Pw} = \bar{E}^i e^{-jk\hat{r}_o \cdot \bar{u}} \quad (3.4-7)$$

as illustrated in Figure 3.4-5. The formulas (3.4-5) and (3.4-6) can then be used to calculate all the surface currents.

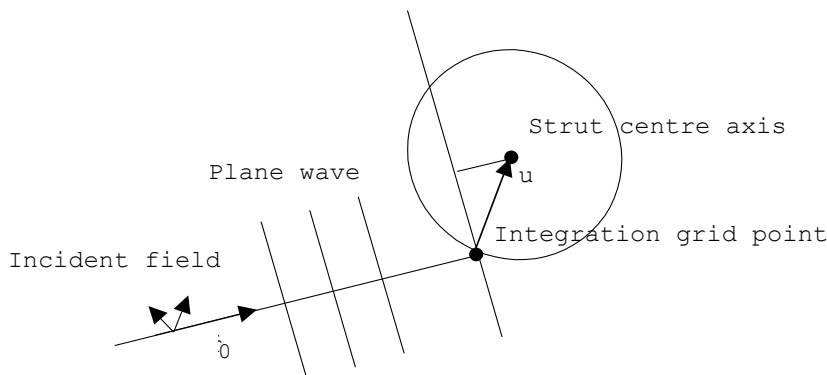


Figure 3.4-5 Phase correction of incident field to strut centre axis.

3.4.2.3 Comparison between methods

As a first case an infinite circular cylinder of diameter $D = 6\lambda$ illuminated by a plane wave polarised parallel to the cylinder is described. The situation is illustrated in Figure 3.4-6.

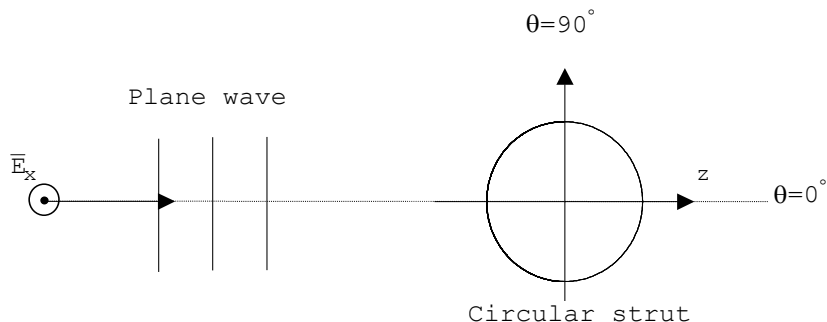


Figure 3.4-6 Plane wave incidence on circular strut.

Figure 3.4-7 shows the calculated far field in the plane orthogonal to the strut. In addition to the simple PO and the canonical solution described above also the exact solution (based on the series expansion) and the Geometrical Optics field are shown.

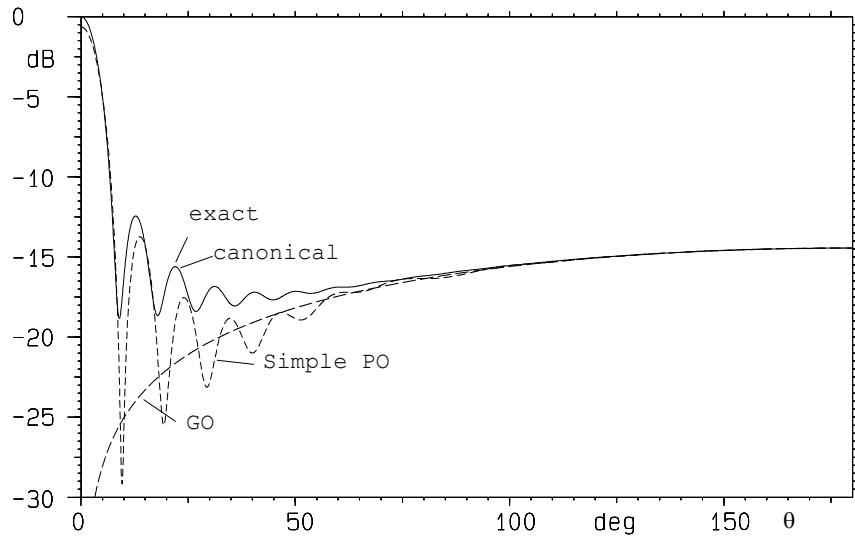


Figure 3.4-7 Far fields from circular strut, $D = 6\lambda$, illuminated by a plane wave.

It is seen that the canonical and the exact series solution for the scattered field are identical. Since the canonical solution is based on calculated currents on the strut this just indicates that the numerical integration is converged. The geometrical optics (GO) approach is only adequate for the backward half plane, $90^\circ < \theta < 270^\circ$, due to the lack of creeping wave contributions. The simple PO method is able to generate the large amplitude in the forward direction, but the amplitude of the lobes in the region, $10^\circ < \theta < 90^\circ$, is still too small. This is a consequence of the missing surface currents on the shadow side of the strut. The currents in a cross section of the strut are shown in Figure 3.4-8. The PO currents are in good agreement with the canonical solution on the illuminated side but decrease to zero in the shadow region, $0^\circ < \theta < 90^\circ$.

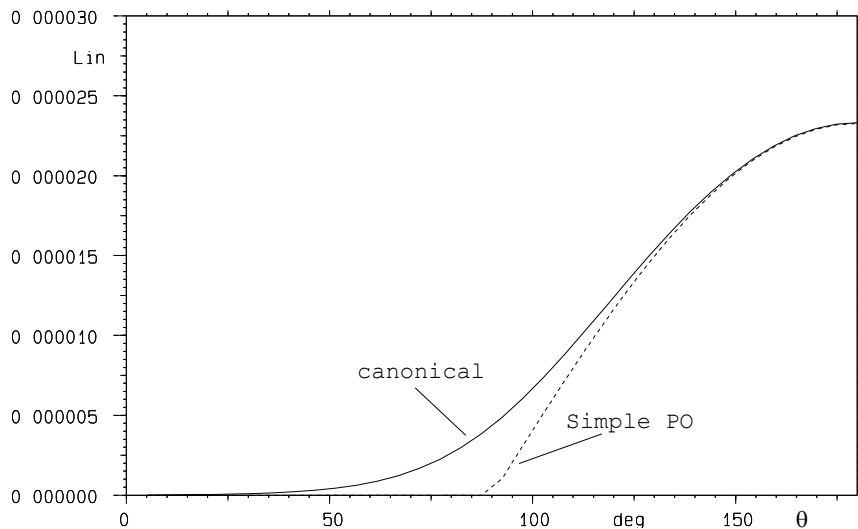


Figure 3.4-8 Total surface currents on cross section of circular strut.

The difference between the two methods in relation to the thickness of the struts is illustrated in the following for three different wavelengths and for a strut illuminated by both a plane wave and a dipole feed, see Figure 3.4-9.

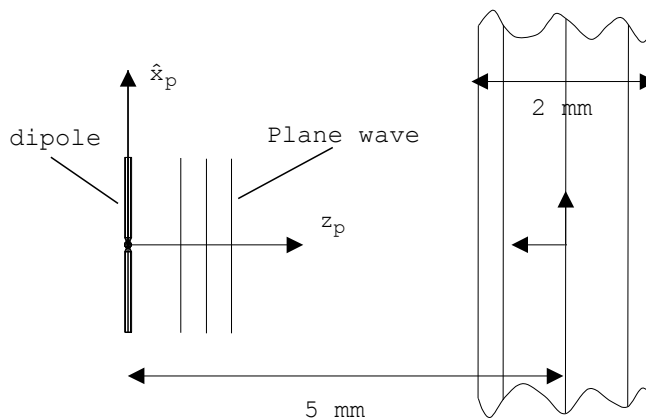


Figure 3.4-9 Geometry of circular strut illuminated by plane wave or dipole feed.

The scattered fields for the three different strut diameters are calculated in the plane orthogonal to the strut, as illustrated in Figure 3.4-10. The strut is illuminated by both a plane wave

and a dipole and the scattered fields are calculated with the simple PO as well as the canonical solution. The results are presented in Figure 3.4-11 and in Figure 3.4-12 for the plane wave and the dipole, respectively. The incident field is polarised parallel to the strut and orthogonal to the strut and the results are presented in top and bottom part of the graphs, respectively.

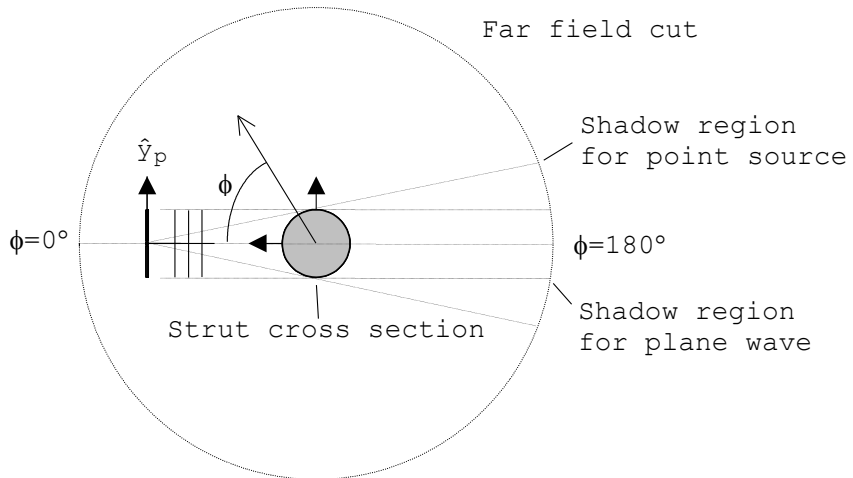


Figure 3.4-10 Circular strut in top view.

The accuracy of the simple PO solution increases with increasing strut diameters, because the amplitude of the generated currents on the shadow side is decreasing. The remaining large sidelobes in the PO solution and especially for the y -polarised illumination are due to the large discontinuity of the current distribution near the shadow region of the strut. Furthermore, the PO solution is unable to predict the current differences for x - and y -polarised illumination on the shadow boundary. The PO field is actually exactly the same for both x - and y -polarised illumination at $\phi = 180^\circ$. This is most evident for the thin strut, $D = .5\lambda$, where the difference between the canonical solution and the PO method is largest.

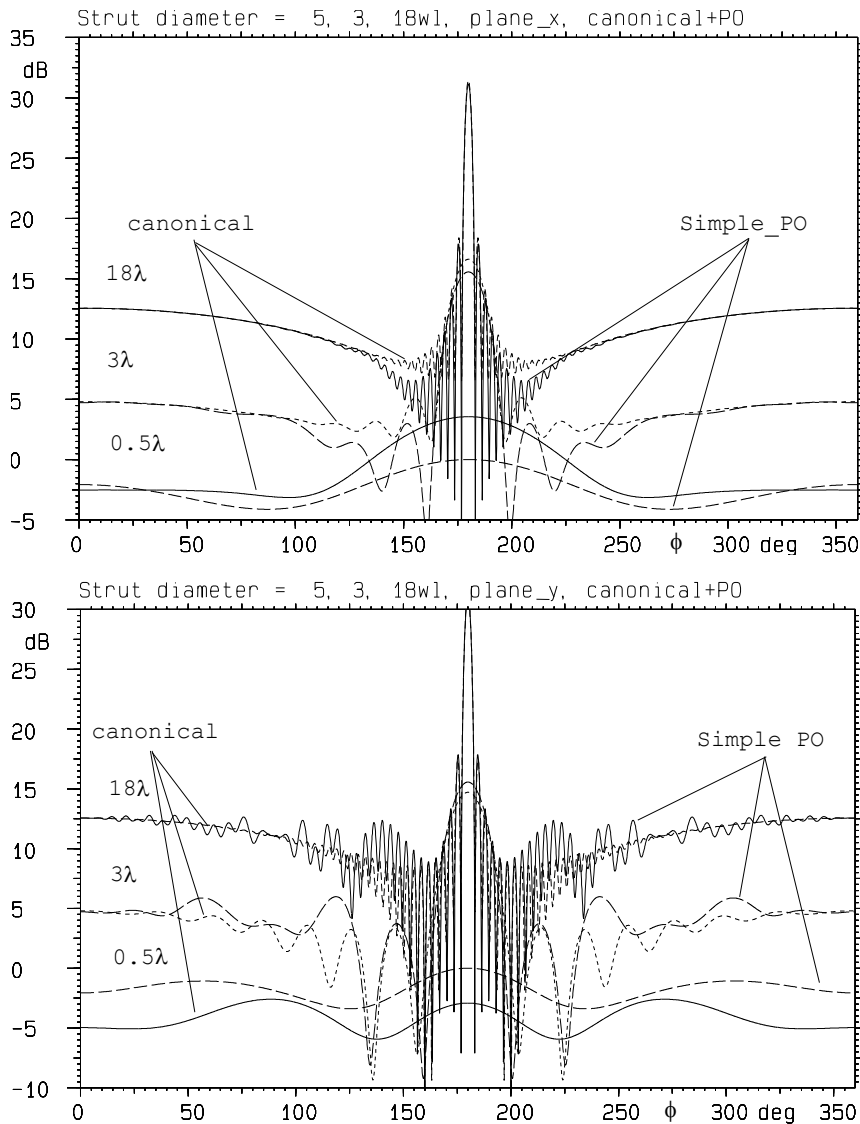


Figure 3.4-11 Far fields from circular strut, $D = .5\lambda, 3\lambda, 18\lambda$, illuminated by a plane wave and calculated by the canonical and the simple PO solution.

Top: polarisation parallel to the strut

Bottom: polarisation orthogonal to the strut

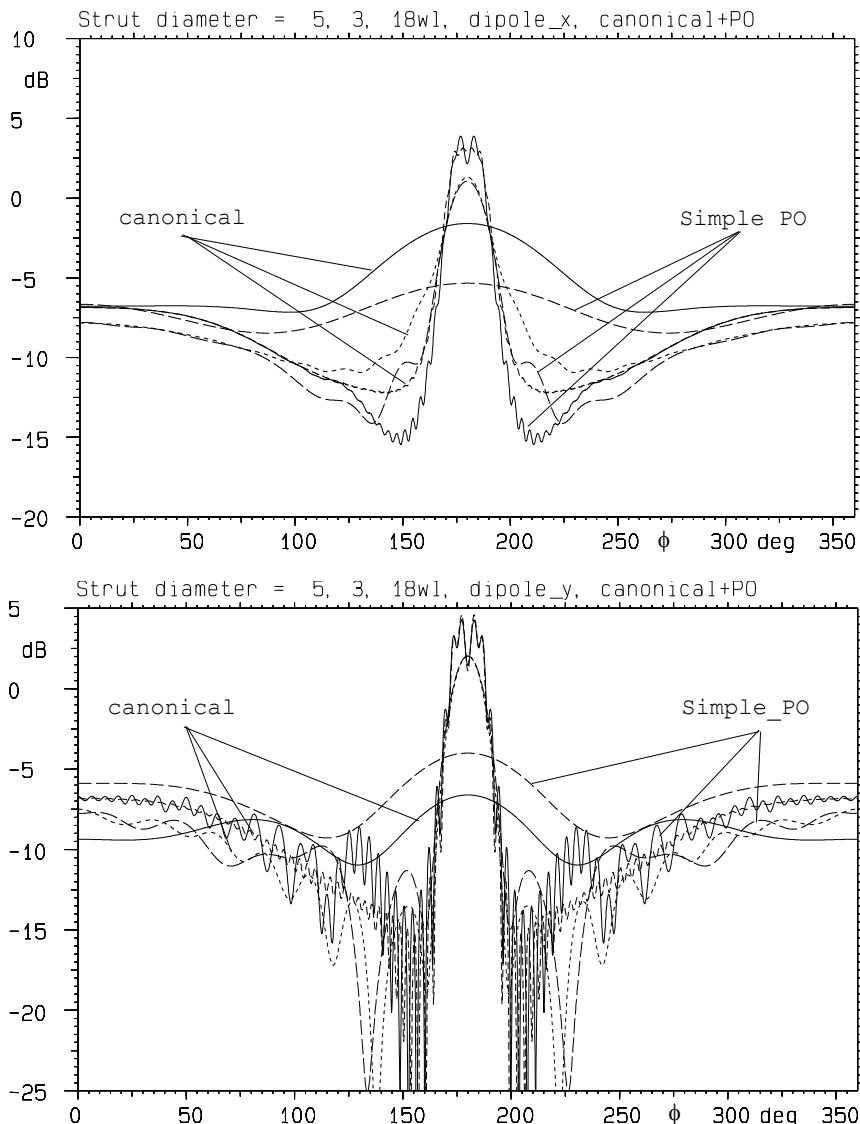


Figure 3.4-12 Far fields from circular strut, $D = .5\lambda$, 3λ , 18λ , illuminated by a dipole and calculated by the canonical and the simple PO solution.
 Top: polarisation parallel to the strut
 Bottom: polarisation orthogonal to the strut

The oscillations in the main lobe for $D = 18\lambda$ in Figure 3.4-12 can be interpreted as interference between the creeping waves travelling around the cylinder.

The results presented in Figure 3.4-11 and Figure 3.4-12 indicate that for struts thicker than 3 wavelengths the simple PO approach is sufficient for most practical applications, both for plane wave and spherical wave incidence.

3.4.3 Computational approach for polygonal struts

The scattering model used for polygonal struts (as introduced in Section 2.2.4) is based on PO and PTD.

When the cross section dimensions of the polygonal strut are large in terms of wavelengths, the standard PO method can be used to estimate the scattering from the strut. However, when the dimensions of the strut are decreased, the diffraction by the edges of the strut must be better modelled in order to obtain a satisfactory result.

This is accomplished using PTD. The diffraction from a specific edge of the strut is taken to be the same as the diffraction from a canonical wedge that locally conform with the strut. The PTD theory, like PO, is a high-frequency theory, and hence the dimensions of the strut must still be in the order of wavelengths for the approximations made to be justified. However, the model provides reasonably accurate results even for a strut with dimensions in the order of the wavelength. For thinner struts, the PO and PTD theories predict inaccurate results, and in GRASP the struts should be replaced by circular struts, cf. Section 3.4.2.

The PO and PTD theories for the polygonal strut are discussed in more details in the following sections.

3.4.3.1 *PO*

If the dimensions of the polygonal strut are large in terms of wavelengths, a good approximation of the induced surface currents is provided by the PO approximation

$$\bar{J} = \begin{cases} 2\hat{n} \times \bar{H}^i, & \text{if illuminated} \\ 0, & \text{otherwise} \end{cases} \quad (3.4-8)$$

where \hat{n} is the outward normal vector and \bar{H}^i is the total incident magnetic field. The illuminated sides are defined by the inequality

$$\hat{n} \cdot \bar{P} < 0. \quad (3.4-9)$$

If the source is a point source, \bar{P} is the direction from the source. Otherwise, \bar{P} is the Poynting vector $\bar{P} = \frac{1}{2} \operatorname{Re}(\bar{E} \times \bar{H}^*)$.

The field radiated by the PO currents is calculated as described in Section 3.1.2. A rectangular integration grid - as described in Section 3.1.2.2 - is used on each side of the strut parallel to the strut axis. The polygonal end-sides of the strut are not taken into account in the analysis.

The number of PO points necessary for convergence can be estimated by

$$\begin{aligned} n_{\text{length}} &= 3.5 L / \lambda \\ n_{\phi} &= 3.5 d / \lambda \end{aligned} \quad (3.4-10)$$

where L is the length of the strut, d is the width of the side considered and λ is the wavelength.

3.4.3.2 PTD

A more accurate calculation can be achieved by adding to the PO field a PTD field which more accurately models the diffraction arising from the illuminated edges of the scatterer.

The PTD implemented for polygonal struts is based on the work by Johansen (1996). The wedge modelling and incremental strips of finite length is used, c.f. Section 3.2.

Each illuminated edge gives rise to a diffraction which is taken to be the same as the diffraction from a canonical wedge that locally conforms with the two adjoining sides of the strut. Only the edges of the strut parallel to the strut axis are included in the analysis.

The number of PTD points, ptd , necessary for convergence can be estimated as n_length for the PO calculations, i.e.

$$ptd = 3.5L / \lambda \quad (3.4-11)$$

where L is the length of the strut and λ is the wavelength.

3.4.3.2.1 *On the propagation through the wedge*

The PTD expressions reported by Johansen are derived from the canonical problem of plane-wave illumination of an infinite wedge with an exterior wedge angle of $N\pi$ ($1 < N \leq 2$), as shown in Figure 3.4-13. In the canonical problem the illumination must be from the exterior region, $0 < \phi_o < N\pi$, and the observation also in the exterior region, $0 < \phi < N\pi$. The total field is zero in the interior region.

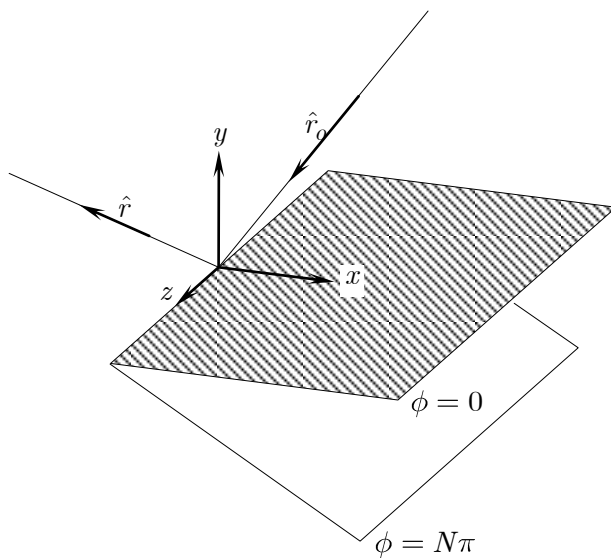


Figure 3.4-13 PTD analysis for a wedge.

Direction of incident field

$$\hat{r}_o = -(\sin \theta_o \cos \phi_o, \sin \theta_o \sin \phi_o, \cos \theta_o).$$

Direction of observation point

$$\hat{r} = (\sin \theta \cos \phi, \sin \theta \sin \phi, \cos \theta).$$

When using the wedge to locally model the diffraction from the edges of the struts, the above-mentioned restrictions are not necessarily fulfilled. As an example, the triangular strut of Figure 3.4-14 is considered.

For this strut, the direction of incidence is from the outside at edge 1 and 2, whereas it is from the inside at edge 3. Clearly, if an edge is illuminated from the inside, then the two adjoining sides, s_2 and s_3 in Figure 3.4-14, are also illuminated from the inside, and hence the PO currents are identically zero on these sides. In this case, the PTD contribution is set to be identically zero.

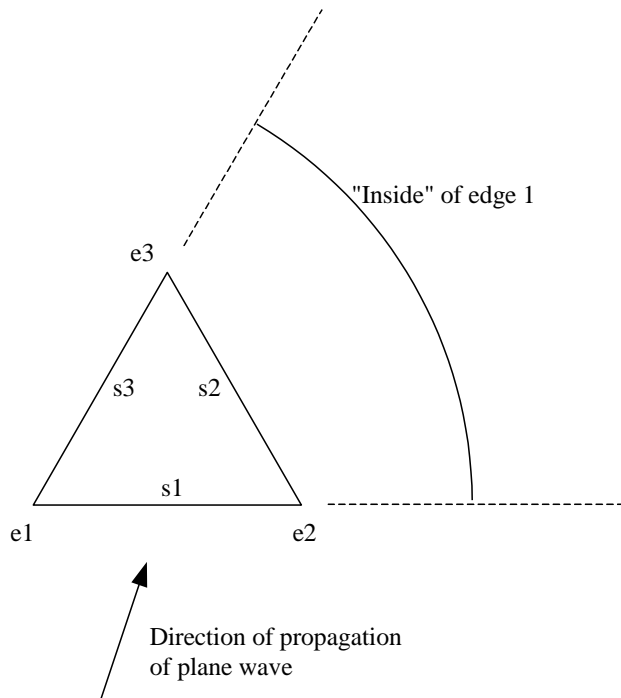


Figure 3.4-14 Triangular strut under plane wave illumination.

For the two illuminated edges, e_1 and e_2 , there are regions where the observation points are located inside the wedge, as illustrated in Figure 3.4-14. It is emphasised that the incident field as well as the PO field contribute in these regions (for example to form the shadow zone of side s_1). In particular, the

PO from side $s1$ gives rise to an erroneous (half plane) diffraction from $e1$ and $e2$. The total field can be significantly improved by adding a PTD contribution.

The PTD contribution is defined by extending the validity of the PTD expressions to observation points inside the wedge. Inspecting the PTD expressions, it is observed that the azimuthal angle of observation, ϕ , only appears as $\sin\phi$ or $\cos\phi$. Hence, extending the ϕ -range in the lower or upper end yields identical results. It is emphasised that even though the extension of the ϕ -range is not explicitly discussed in Johansen (1996), it has been used in the calculations presented in the paper.

3.4.3.3 Examples

In the following the scattering by the polygonal struts is exemplified. First, the plane-wave scattering from a strut with a square cross-section is analysed using PO alone and using PO plus PTD. The results are compared to an integral equation solution. Next, the scattering from struts having fixed cross-section area but varying number of sides is considered.

All configurations considered in this section are as shown in Figure 3.4-15. The corners of the polygon defining the cross section of the strut are specified by n equidistant points $n > 2$ located on a circle with radius R_n i.e. the corners are given by

$$(x_p, y_p) = R_n \left(\cos \left[p \frac{2\pi}{n} + \delta \right], \sin \left[p \frac{2\pi}{n} + \delta \right] \right) \quad (3.4-12)$$

where $p = 1, 2, \dots, n$, and δ is an arbitrary angle.

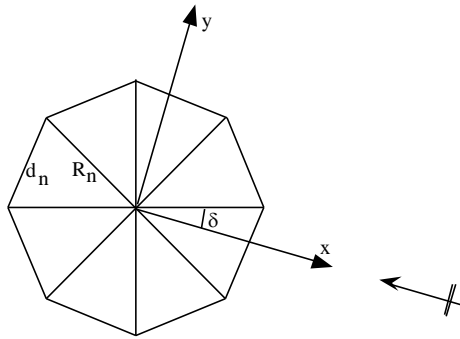


Figure 3.4-15 Polygonal cross section with $n = 8$.

In all the configurations considered in this chapter, the strut is illuminated by a plane wave propagating in the direction of the negative x -axis. The plane wave is polarised perpendicular to the cylinder axis.

We wish to compare the scattering from struts having identical area of the cross section. Assuming that the area shall be the same as for a circular strut with radius R_c , then R_n is given as

$$R_n = \frac{R_c}{\sqrt{\frac{\sin(2\pi/n)}{(2\pi/n)}}}. \quad (3.4-13)$$

The length, d_n , of the sides of the polygon is

$$d_n = 2R_n \sin \frac{\pi}{n}. \quad (3.4-14)$$

The following three strut dimensions are considered:

$R_c = 10\lambda$, $R_c = 2\lambda$, and $R_c = 0.5\lambda$.

3.4.3.3.1 *The square cylinder*

The scattering configuration for the square cylinder is shown in Figure 3.4-16. The scattered field as a function of the polar angle ϕ is calculated using PO, PO+PTD and an integral

equation solved by the method of moments (MoM) and the results are shown in Figure 3.4-17.

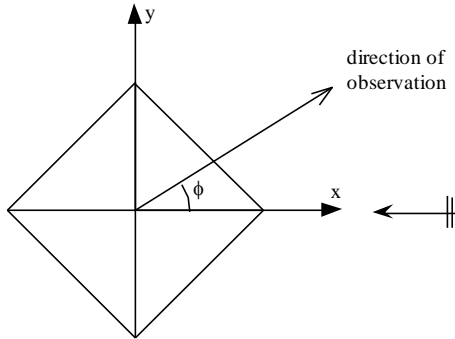


Figure 3.4-16 The square cylinder.

As the scattering configuration is symmetric with respect to the x -axis, only the ϕ -interval from 0° to 180° is shown.

The square has two main scattering effects: I) It shadows the incident plane wave in the backward direction, $\phi \approx 180^\circ$, and II) it reflects the plane wave in the two illuminated sides of the square in the directions $\phi = 90^\circ$ (and $\phi = 270^\circ$). The two effects are clearly visible in the plot.

For $R_c = 10\lambda$ (the top plot of the figures) the PO result has the same overall lobe characteristics as the MoM solution. However, the fine details of the results differ especially around $\phi = 135^\circ$. Adding the PTD contribution to the PO yields a result in almost perfect agreement with the MoM result.

For $R_c = 2\lambda$ (the centre plot of the figures) the differences between the PO and the MoM results are larger. Again, the inclusion of PTD yields a very close agreement with the MoM result. For $R_c = 0.5\lambda$ (the bottom plot of the figures) where the side length is smaller than the wavelength, the same conclusions are true.

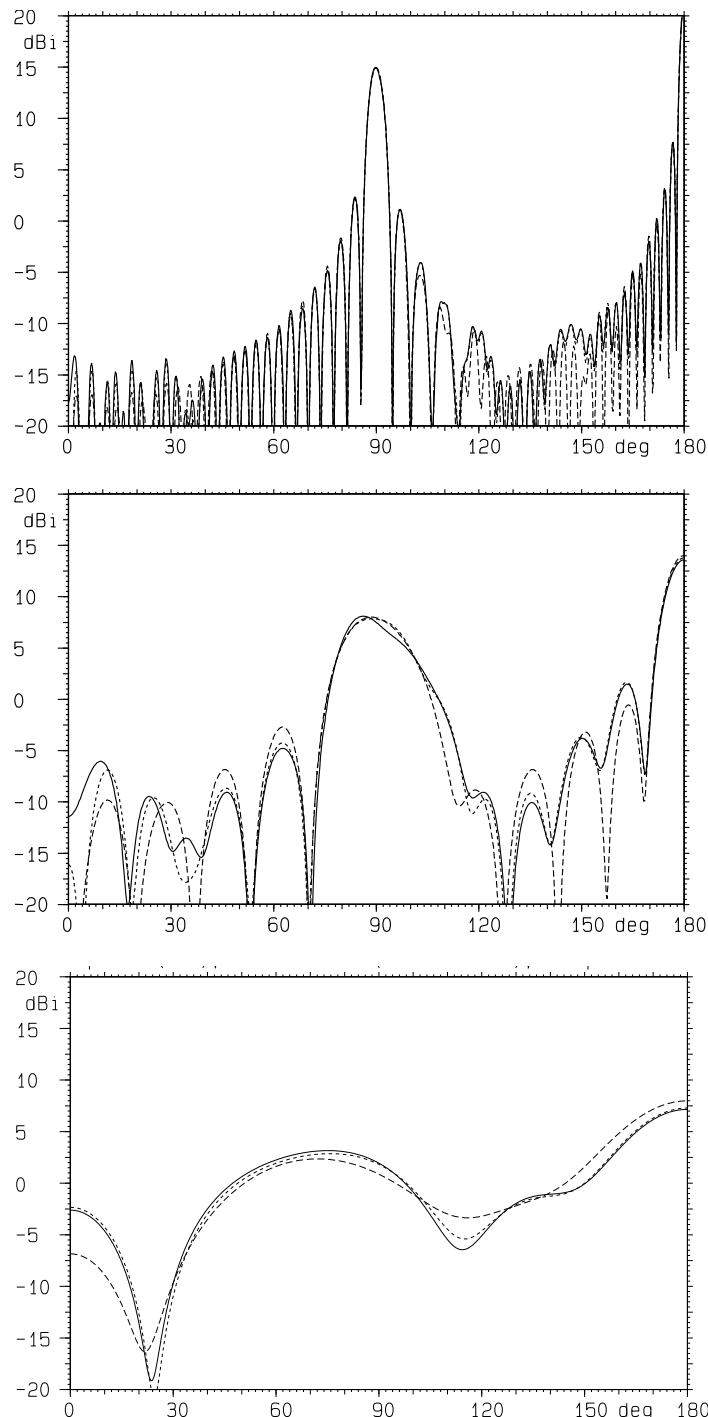


Figure 3.4-17 Scattering by a square cylinder calculated by MoM (full line), PO+PTD (short dots) and PO (long dots).

In all cases, it is observed that the inclusion of PTD improves the accuracy of the scattered field prediction.

In general, the results for the plane wave polarised parallel to the strut (not shown) are in better agreement with the MoM results. For this polarisation the boundary condition on the surface requires the tangential E-field to vanish, which tends to reduce the interaction between the edges.

3.4.3.3.2 Square to circular cylinder

In the following, the scattering is compared for struts having identical cross-section area and varying number of sides.

In Figure 3.4-18, the scattering is compared for a circular strut, a polygonal strut with $n = 16$, and a square strut ($n = 4$). Three dimensions are considered : $R_c = 10\lambda$, $R_c = 2\lambda$, and $R_c = 0.5\lambda$.

The square cylinder (identical to the one considered in the previous section) has a single reflecting side contributing to the plot. The strut with $n = 16$ has four reflecting sides contributing to the plot corresponding to reflection directions of $\phi = 22.5^\circ, 67.5^\circ, 112.5^\circ$ and 157.5° . As the four sides have different projected length, the scattering lobes are of different width. Especially, two of the four sides have very small projected lengths (they are almost parallel to the direction of incidence of the plane wave), and consequently two of the four lobes are only barely visible. Clearly, increasing the number of sides will produce a pattern without the dominating reflection lobes.

It is seen that the scattering from the circular and the square cylinder is only similar in the shadow region. For the polygonal strut with $n = 16$ the scattering is more similar to the circular strut, especially in the region where the reflection lobes are interfering. The same conclusion is true for the smaller struts with $R_c = 2\lambda$ and $R_c = 0.5\lambda$. The result for $R_c = 2\lambda$ yields the best overall agreement between the scattering from the circular and the polygonal ($n = 16$) strut. This is due to the fact, that the side length is so small (sub-wavelength) that the

scattering from the two objects is practically the same, but still so large that the PTD expressions are valid.

For the plane wave polarised parallel to the strut (not shown) the agreement is better between the results for the polygonal strut with $n = 16$ and the circular strut.

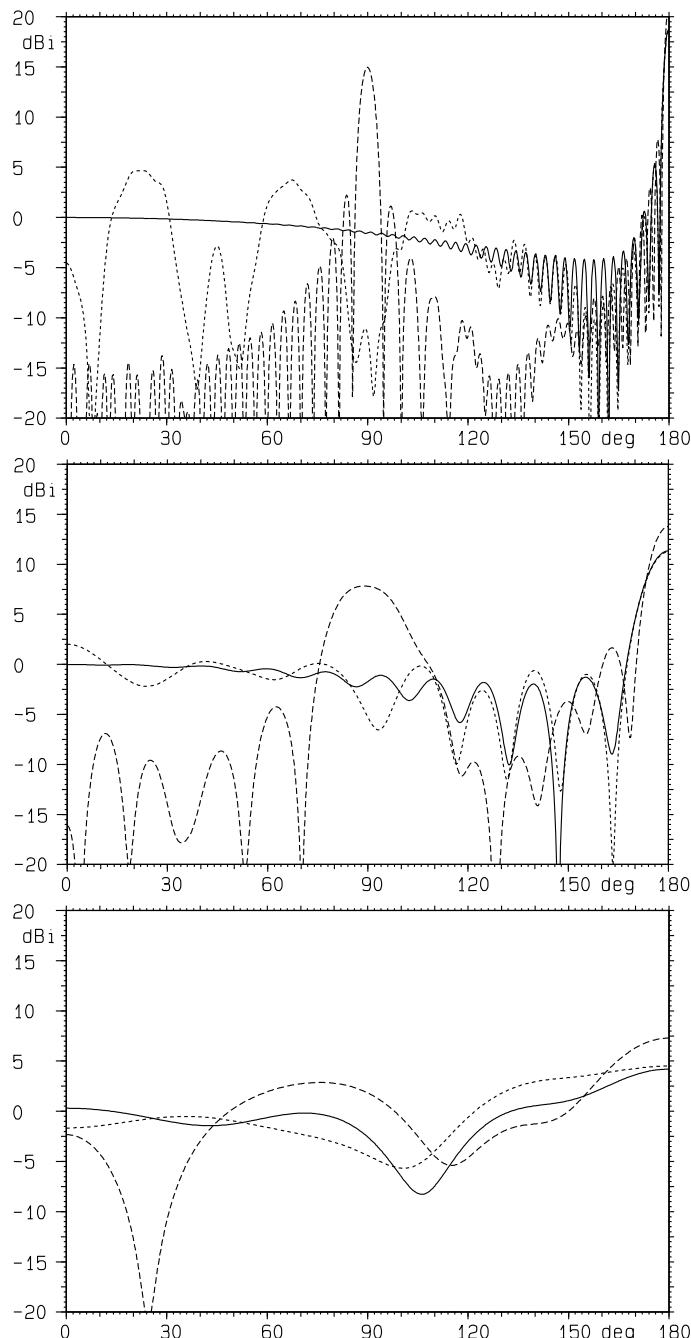


Figure 3.4-18 Scattering from circular and polygonal struts by PO+PTD.
full line: circular strut
long dots: polygonal strut with $n = 4$
short dots: polygonal strut with $n = 16$

3.5 Physical Optics for scatterers with material properties

If the scattering surface is not perfectly conducting, but the reflection and transmission coefficients are known (see Section 2.2.3) a method similar to physical optics can be used to compute a set of equivalent electric and magnetic currents which approximate the exact equivalent currents radiating the scattered field. For derivation of this approximation we consider an infinite planar surface of finite thickness with known incident field and reflection and transmission coefficients as shown in Figure 3.5-1. The incident, reflected and transmitted electric and magnetic fields are marked by the superscripts i , r and t , respectively.

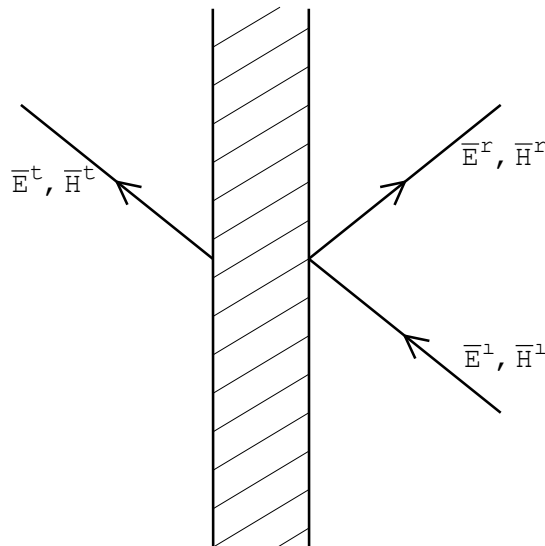


Figure 3.5-1 Non-perfectly conducting surface.

If the incident field is subtracted from the fields on both sides of the surface the equivalence principle may be applied so that the surface can be replaced by two current sheets as shown in Figure 3.5-2 where the equivalent currents exactly radiates the scattered field defined by (3.1-1).

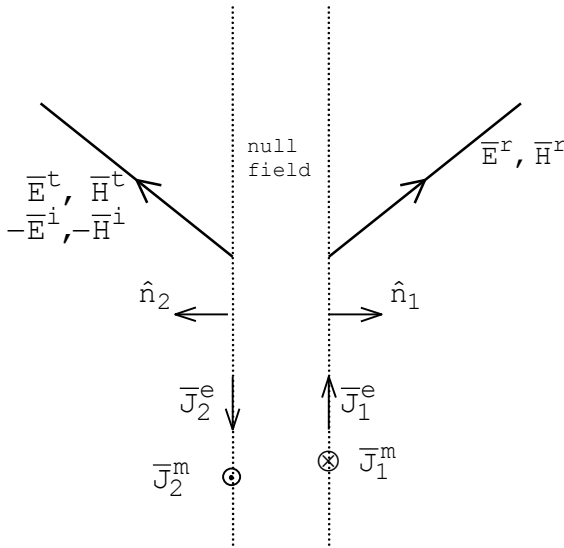


Figure 3.5-2 Equivalent currents radiating the scattered field.

From the reflection and transmission coefficients the reflected and transmitted field can be computed and the equivalent currents can then be found from the electromagnetic boundary conditions which give

$$\begin{aligned} \bar{J}_1^e &= \hat{n}_1 \times \bar{H}^r, & \bar{J}_1^m &= -\hat{n}_1 \times \bar{E}^r \\ \bar{J}_2^e &= \hat{n}_2 \times (\bar{H}^t - \bar{H}^i), & \bar{J}_2^m &= -\hat{n}_2 \times (\bar{E}^t - \bar{E}^i), \end{aligned} \quad (3.5-1)$$

where \bar{J}^m denotes magnetic currents.

Due to the plane wave assumption the phase of the transmitted field may be referred to the front surface such that only one sheet of equivalent currents is needed. Using $\hat{n}_2 = -\hat{n}_1$ we obtain

$$\begin{aligned} \bar{J}^e &= \bar{J}_1^e + \bar{J}_2^e = \hat{n}_1 \times (\bar{H}^i + \bar{H}^r - \bar{H}^t) \\ \bar{J}^m &= \bar{J}_1^m + \bar{J}_2^m = -\hat{n}_1 \times (\bar{E}^i + \bar{E}^r - \bar{E}^t) \end{aligned} \quad . \quad (3.5-2)$$

When the scattering surface is curved and of finite extent the currents (3.5-2) are an approximation to the exact equivalent currents. For a perfectly conducting surface the transmitted

field is zero and the tangential components of the incident and reflected field are either equal (H-field) or opposite (E-field) such that \bar{J}^e in (3.5-2) reduces to (3.1-2) and \bar{J}^m becomes zero. An important complication for the non-perfectly conducting surface is that the reflection and transmission coefficients usually depend on the angle of incidence which means that it is necessary to know the direction of propagation of the incident field, cf. Section 3.7. As explained above this restriction is not necessary for the physical optics approximation (3.1-2) on a perfectly conducting surface.

The numerical procedure employed to calculate the field from a reflector with material properties places the equivalent current sheet (3.5-2) at the mathematical surface of the reflector, and it uses the incident field at this surface as source for the induced currents. The layer with the given material properties can be placed at any distance from the mathematical surface, and this may give rise to some peculiarities in the field computations. An example will illustrate the issue further.

Consider the two reflector systems shown in Figure 3.5-3. Both are circular discs with a diameter of 40λ and both are illuminated by a feed placed 40λ in front of it. Feed 1 is for Reflector 1 and Feed 2 is for Reflector 2. The two systems are displaced 5λ relative to one another, with Reflector 1 placed in the (x, y) -plane.

The scattered far field from these two systems are identical, apart from an obvious phase difference due to the displacement. But we will now model them in two different ways:

Reflector 1 is modelled as a reflector with no special material properties, which means that it by default is perfectly conducting. It is placed in the (x, y) -plane. Reflector 2 is modelled as a reflector with surface material, which is perfectly conducting. The mathematical surface is placed in the (x, y) -plane but the surface material is displaced 5λ to model the desired configuration.

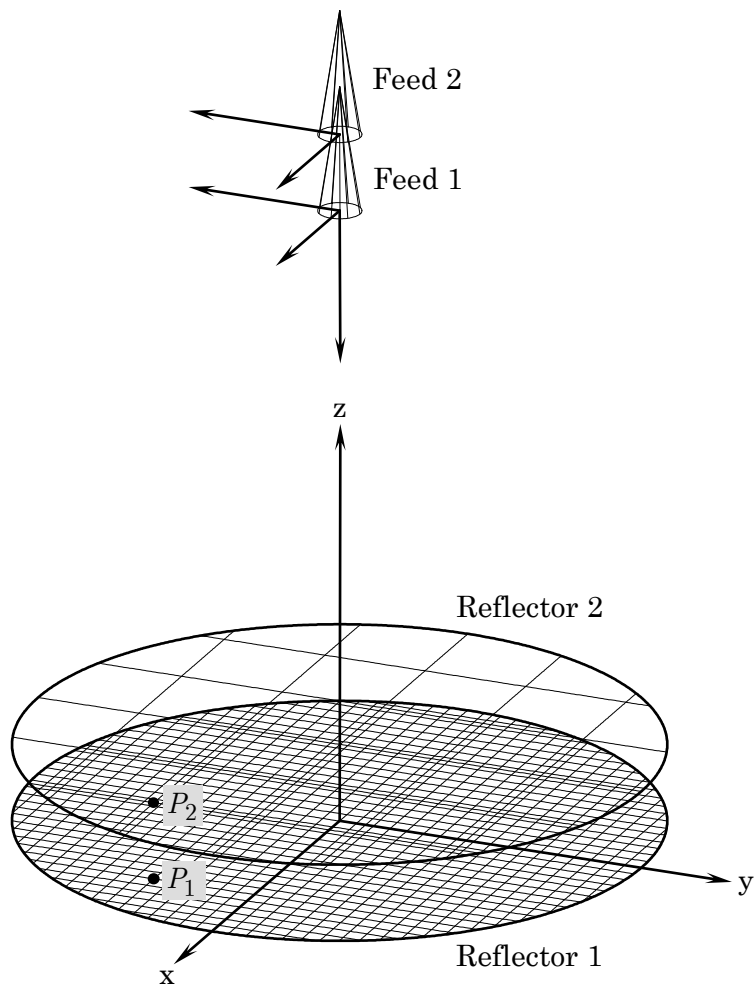


Figure 3.5-3 Two reflector configurations used to illustrate the influence of a reflector surface material displacement.

Because the mathematical surface for the reflectors are in both cases the (x, y) -plane, the PO currents will be computed in this plane, as exemplified by point P_1 in Figure 3.5-3. For Reflector 1 the incident field from Feed 1 is calculated and the PO currents are derived in the usual way.

For Reflector 2 the currents are again calculated in P_1 using as source the incident field from Feed 2, as given by (3.5-2). The incident and reflected fields are referred to the (x, y) -plane, which in effect corresponds to a phase modification of the reflected field by a factor $e^{j2ks\cos\theta_i}$, where s is the distance from the (x, y) -plane to the layer.

This phase modification will correct for the fact that the "true" induced currents are located at a distance of 5λ from the (x, y) -plane. However, this current is caused by the field from Feed 2 at the location P_2 , which is not the same as the field from Feed 2 at P_1 . The difference in the field from Feed 1 at P_1 and P_2 is not accounted for in the procedure, and therefore the computed field for Reflector 2 is not correct.

Figure 3.5-4 shows the computed patterns for both reflectors and they are clearly distinct, with the results for Reflector 1 being the more accurate of the two. The example is chosen to exaggerate, while in practice layers with different material properties are typically confined to a small region very close to the mathematical surface. However, the example shows that for thick structures one should select the position of the mathematical reflector surface such that it coincides with the dominant reflection layer of the structure.

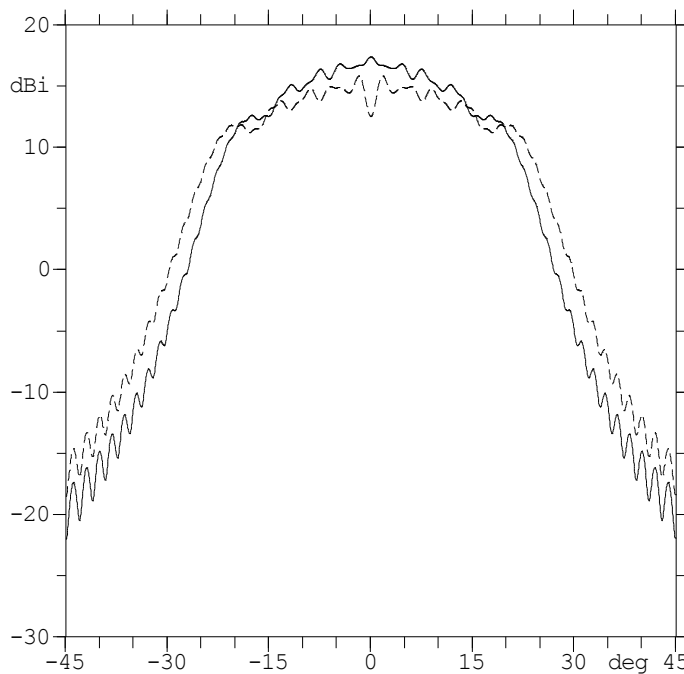


Figure 3.5-4 Far field radiation patterns for the two configurations in Figure 3.5-3.

Solid line: Reflector 1 and Feed 1

Dotted line: Reflector 2 and Feed 2

3.6 Ray-optical methods

The PO-techniques described in the previous section are very accurate and they may be used in all regions of the space surrounding the antenna, both in front of the antenna and behind it. However, as the frequency increases the density of the integration grids must be finer and the computation time will increase. For antenna systems containing two or more reflectors the computation time will increase with the fourth power of the frequency in order to obtain accurate results in the same angular region. It is therefore essential also to have ray-optical methods available to take over when the structures become very large in wavelengths.

This section describes the ray-optical methods available in GRASP, i.e. the direct and the reflected rays and the singly

diffracted rays. All higher order diffractions are not implemented in GRASP in the standard version.

A typical antenna configuration is shown in Figure 3.6-1 where a paraboloid is illuminated by a feed at the focus and the field point F is situated somewhere in front of the reflector surface.

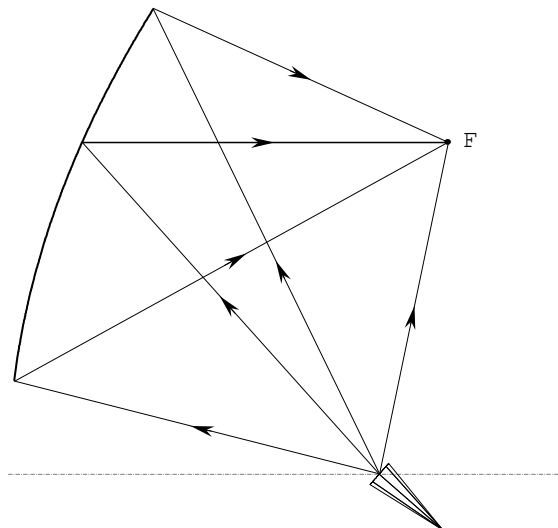


Figure 3.6-1 Optical rays in the near field of a reflector antenna.

The rays to be taken into account are the direct ray from the feed, the ray reflected from the main reflector and the diffracted rays from the reflector edge. The direct ray will for most field points be of negligible amplitude. The most important ray is the reflected ray but also the diffracted rays are important, especially when the field point approaches the boundary of the reflected rays where the diffraction contributions will ensure continuity of the total field. All higher order rays such as doubly diffracted rays are neglected.

The GTD calculation is carried out in three steps

- selection of significant rays
- ray tracing
- field calculation

The selection of the significant rays is necessary in order to determine the important field contributions and to avoid unnecessary computations. If for example one wants to determine the field behind a reflector it is superfluous (but not erroneous) to attempt to calculate the reflected field since it cannot exist behind the reflector.

Once the significant rays have been identified the next step is the ray tracing, i.e. the determination of the points of reflection and diffraction. This is often the most difficult task in ray-optical methods, and once it is solved the field calculations are straightforward, see for example Kouyoumjian and Pathak, 1974.

Reflected and diffracted rays are treated separately in the following two subsections.

3.6.1 Geometrical Optics

The Geometrical Optics (GO) component in GRASP are the direct ray from the source and the reflected ray from a reflector surface. In case of surface material parameters the direct ray will represent the field transmitted through the surface.

The determination of the reflection point R for the source point S and the field point F is illustrated in Figure 3.6-2.

The path length from S to F via R is denoted L . The reflection point is found by requiring that L is stationary, that is

$$\begin{aligned}\frac{\partial L}{\partial x} &= 0 \\ \frac{\partial L}{\partial y} &= 0\end{aligned}\tag{3.6-1}$$

Expressions (3.6-1) are valid regardless of whether the ray path length is a minimum, maximum or a saddle point. This latter property implies that if the source point and the field point are located on either side of the reflector surface the solution to (3.6-1) is a shadow point and the procedure can

therefore be used to check whether the direct ray is shadowed by the reflector.

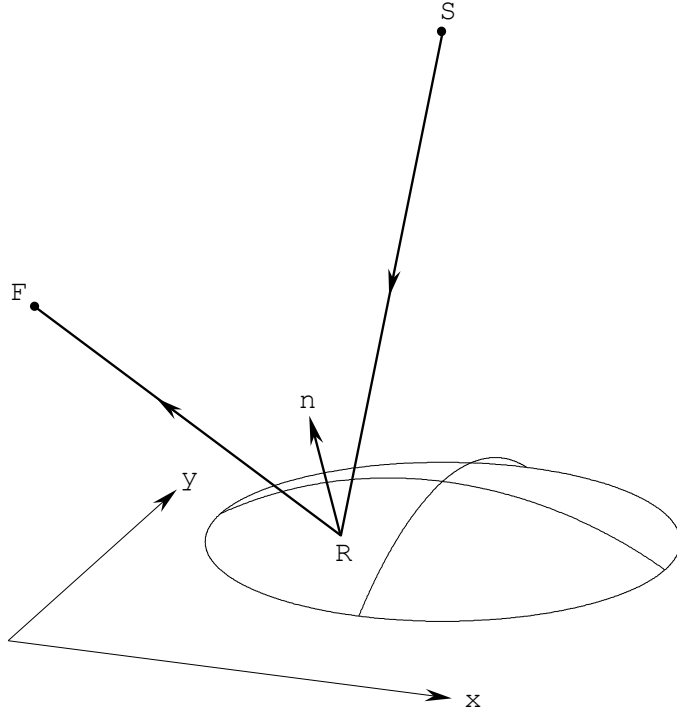


Figure 3.6-2 Reflection point.

An efficient way to solve the non-linear equation system (3.6-1) numerically is to determine the minimum value for the function

$$F = \left(\frac{\partial L}{\partial x} \right)^2 + \left(\frac{\partial L}{\partial y} \right)^2 \quad (3.6-2)$$

and the method proposed by Powell (1970) is used in GRASP. This method is an iterative procedure which is a mixture between standard Newton iteration and search along the direction of the negative gradient of F . Newton iteration converges very fast if the starting point is close to the reflection point, but the convergence is not guaranteed. On the other hand it is certain that F decreases in the direction of the negative gradient. If Newton iteration does not give a sufficient decrease of

F , Powell's procedure starts to search in a direction that interpolates between the Newton direction and the negative gradient direction. The weight between the two directions is adjusted by the procedure such that the next point in the iteration is only accepted if the value of F decreases. The procedure has guaranteed convergence to a local minimum of F and is normally very fast since the negative gradient search only comes into effect in special situations. For reflection point search the procedure must be slightly modified to take into account the rim of the reflector and to stop the search if the procedure repeatedly suggest that the next iteration point is outside the rim.

Once the minimum is found it is checked that $F=0$. The method works normally well with the centre of the rim as the starting point for the numerical search (simple ray tracing).

On rare occasions it may happen that the simple ray tracing fails. An example is depicted in Figure 3.6-3 where a spherical reflector is illuminated by a feed which is located half the radius from the centre. The figure shows that the rays reflected at the centre of the reflector are parallel to the axis and therefore these rays create a caustic in the far field in this direction. The rays reflected from points away from the centre area are tilted into off-axis directions and the figure clearly shows that only one reflection point is possible for each far-field direction up to about 50° from the axis. Above this angle reflected rays do not exist. Although the configuration is quite uncomplicated it turns out that the simple ray tracing with starting point at the centre will find no reflection points. The reason for this is identified by means of Figure 3.6-4 which shows the path length L from the feed to the reflector and further on to a plane tilted the angle θ with respect to the x -axis. The reflection point for the far field direction θ is then found as the minimum value for F given by (3.6-2).

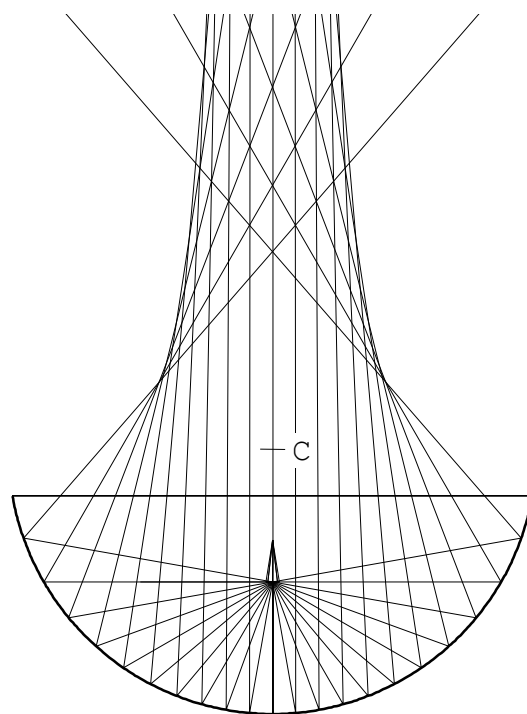


Figure 3.6-3 Spherical reflector of radius R . Feed located at $R/2$ from the centre.

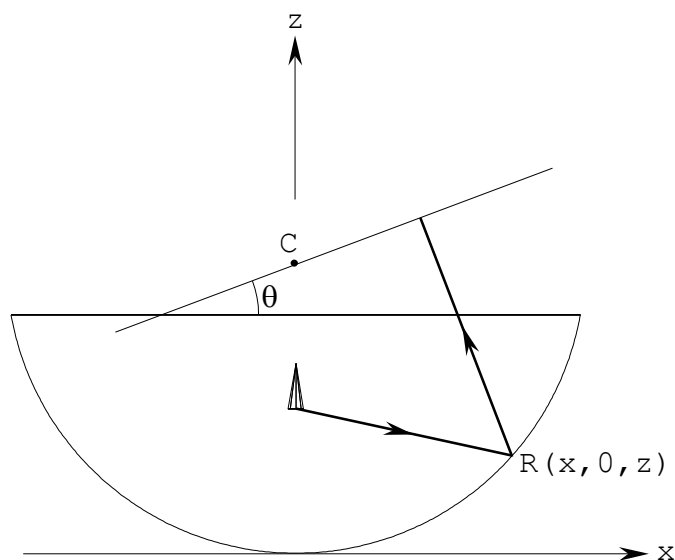


Figure 3.6-4 Path length for rays from the feed via the reflector to a plane tilted θ .

Figure 3.6-5 shows L and $\partial L/\partial x^2$ for $\theta = 20^\circ$ in the plane of symmetry, where $\partial L/\partial y = 0$. It is clear that the correct reflection point is located around $x = 7.5$. However, the function $\partial L/\partial x^2$ also has a local minimum around $x = -1.5$ and since the search is started at $x = 0$ this minimum will be found and then rejected because the function value is not zero.

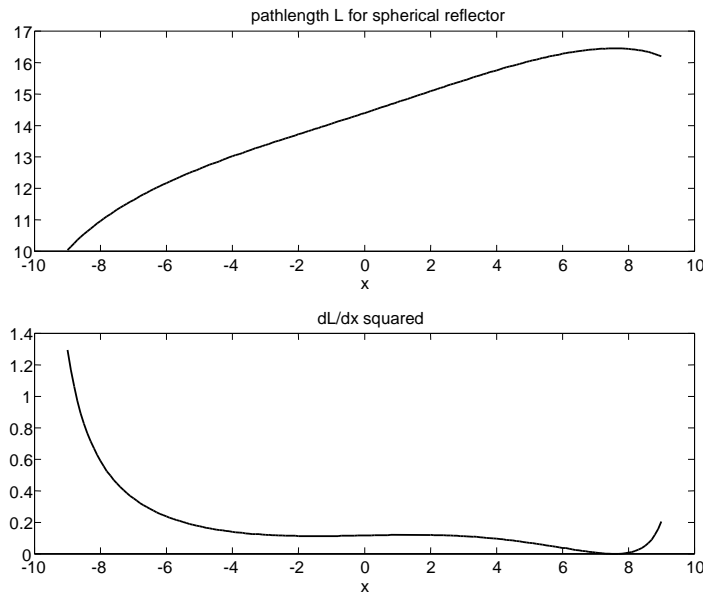


Figure 3.6-5 The ray path length in the plane of symmetry for the spherical reflector in Figure 3.6-3 and for $\theta = 20^\circ$

Top: L
Bottom: $\partial L/\partial x^2$.

This problem of determining the reflection point when starting at the centre of the reflector may be solved by the so-called advanced ray tracing also available in GRASP. In this method the reflector surface is sampled at a large pre-defined number of test points. The function F in (3.6-2) is evaluated at each test point and the search procedure is started at the point with the lowest F -value. This approach has proven to work properly in all cases.

The GO-result for the configuration in Figure 3.6-3 obtained with advanced ray tracing is shown in Figure 3.6-6 for a feed taper of -20 dB at 110°. It is seen that there is a caustic at the axis and the reflected rays disappear at about 51.6°. This result is independent of the frequency. For information also the calculated results with GTD and PO with $\lambda = 0.03R$ are included on the figure. One will notice that the PO-result differs from GTD on the axial caustic but in all other regions of the pattern the two methods are practically identical.

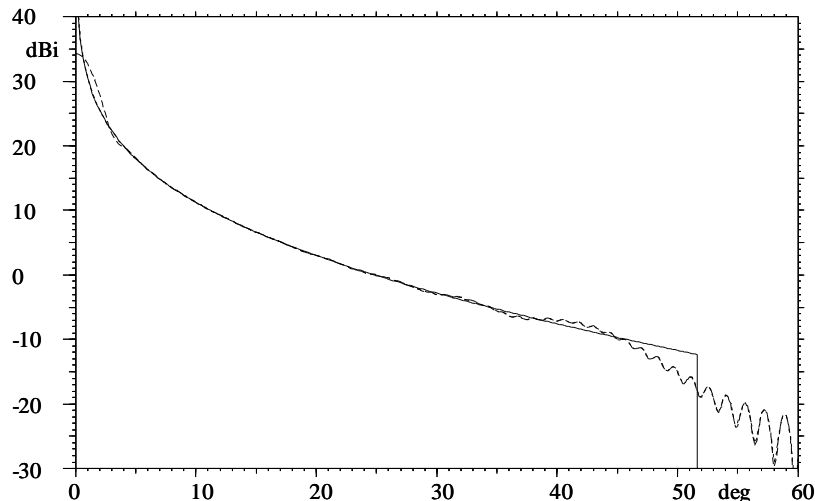


Figure 3.6-6 Calculated patterns for the reflector antenna in Figure 3.6-3. The feed has a standard pattern with a taper of -20 dB at 110°.
 full line: GO
 short dots: GTD ($R = 33.3\lambda$)
 long dots: PO ($R = 33.3\lambda$).

3.6.2 Geometrical Theory of Diffraction

The ray tracing for the edge-diffracted rays is carried out as illustrated in Figure 3.6-7.

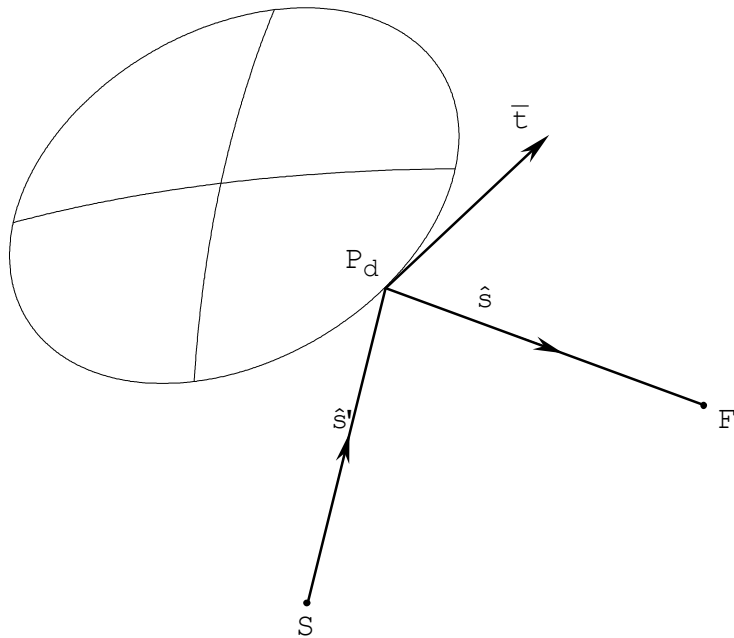


Figure 3.6-7 Ray tracing of edge-diffracted rays.

Assume that the reflector rim is given by

$$\begin{aligned} x &= f(t) \\ y &= g(t) \end{aligned} \quad (3.6-3)$$

where $0 \leq t \leq 1$. Expression (3.6-3) is a projection of the rim on the xy -plane where S and F are the position of the feed and the field point, respectively, and P_d is the diffraction point to be determined. \hat{s}' and \hat{s} are unit vectors in the direction from S to P_d and from P_d to F , respectively. \bar{t} is a tangent vector to the edge given by

$$\bar{t} = \left(\frac{dx}{dt}, \frac{dy}{dt}, \frac{dz}{dt} \right) \quad (3.6-4)$$

where

$$z(t) = F(x(t), y(t)) \quad (3.6-5)$$

and $F(x, y)$ is the reflector surface expression. P_d is a diffraction point if

$$\bar{t} \cdot (\hat{s}' - \hat{s}) = 0 . \quad (3.6-6)$$

The left hand side of (3.6-6) is a function of t and the equation is solved by a standard one-dimensional root finding procedure.

The number of diffraction points on the reflector edge depends on the actual geometrical structure; it is usually 2 or 4 but up to 8 diffraction points on the same edge can be found in GRASP.

When the ray tracing has been performed the field is calculated by standard GTD (Kouyoumjian and Pathak, 1974).

3.6.2.1 Caustic corrections

The diffracted rays may give rise to caustics in particular directions. An automatic caustic correction procedure will be activated if a field point approaches a caustic as described in the following.

The location of the caustics for typical antenna systems are described in Section 6.4 and application examples involving caustic field points are presented in Section 3.8. The diffracted field, \bar{E}^d , from a curved edge is given by

$$\bar{E}^d = \bar{E}^i \cdot \bar{\mathbf{D}} A \frac{e^{-jks}}{s} \quad (3.6-7)$$

where \bar{E}^i is the incident field, $\bar{\mathbf{D}}$ the dyadic diffraction coefficient and the divergence factor

$$A = \sqrt{\rho s / (\rho + s)} , \quad (3.6-8)$$

where s is the distance from the diffraction point to the field point (see Figure 3.6-7) and where ρ , the caustic distance, is determined by

$$\frac{1}{\rho} = \frac{1}{s'} - \frac{\hat{n} \cdot (\hat{s}' - \hat{s})}{a \sin^2 \beta} \quad (3.6-9)$$

where s' is the distance from the feed to the diffraction point and \hat{n} is a unit normal vector to the edge. \hat{s}' and \hat{s} are unit vectors in the direction of incidence and diffraction, respectively, a is the radius of curvature of the rim at P_d and β is the angle between the tangent \hat{t} and the incident or the diffracted ray.

The caustic occurs for field points where ρ approaches $-s$. The divergence factor (3.6-8) will increase to infinity and the GTD formulation becomes invalid. The problem may be solved by the so-called equivalent currents (Knott and Senior, 1974). These currents are determined by the incident field and the diffraction coefficients for the edge, and the diffracted field is determined by a line integral along the edge. This approach is very similar to the PTD extension in the PO formulation.

The equivalent current approach is a relatively complicated process and for the present purpose a quicker, although more approximate, solution is preferable. The reason is that the GTD approach is often very useful to compute the incident field from one reflector on another reflector where then PO is going to be applied. The caustic point from the first reflector will only be one out of many integration grid points on the second reflector surface. A very accurate description of the caustic field is therefore not necessary, the important point is to remove the singularity.

The general approximate caustic correction factor is derived by analogy to a specific case where the caustic field is known, namely a circular cylinder illuminated by a source on the axis as shown in Figure 3.6-8.

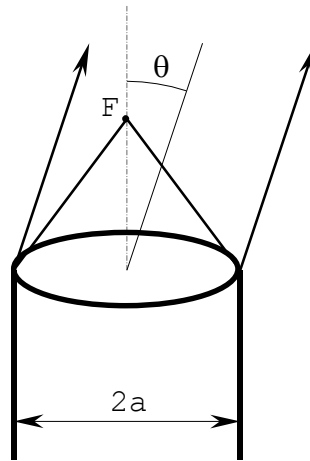


Figure 3.6-8 Circular cylinder with feed on axis.

It is assumed that the source is an isotropic radiator. The far field in directions close to the axis may be approximated by (Keller, 1957)

$$E = J_o \ u \quad (3.6-10)$$

where

$$u = k a \sin \theta \quad (3.6-11)$$

and a is the radius of the cylinder.

The asymptotic form of (3.6-10) (which corresponds to a GTD solution) is

$$E_a = \sqrt{2/\pi u} \cos(u - \pi/4) \quad (3.6-12)$$

which is seen to diverge for $\theta \rightarrow 0$. The asymptotic solution (3.6-12) must therefore be multiplied by the caustic correction factor

$$F_c = \frac{E}{E_a} = \sqrt{\pi u / 2} \ J_o \ u / \cos(u - \pi/4) \quad (3.6-13)$$

in order to obtain the desired finite solution (3.6-10) near the caustic direction $\theta = 0$. The caustic distance for the two rays in Figure 3.6-8 is from (3.6-9)

$$\rho = a / \sin \theta \quad (3.6-14)$$

which inserted into (3.6-11) gives

$$u = k\rho \sin^2 \theta \quad . \quad (3.6-15)$$

It is seen that, by means of (3.6-15), the caustic correction factor (3.6-13) is expressed by the caustic distance for the diffracted rays and the angle between the far-field direction and the caustic direction.

In order to arrive at the caustic correction factor for the general, curved edge it is reasonable to assume that the same angular dependence close to the caustic direction will be valid. Therefore, the correction factor will be calculated by (3.6-13) where u is given by (3.6-15) and where ρ is determined by (3.6-14). The angle θ in (3.6-15) is the angle between the far-field direction \hat{s} and the caustic direction \hat{s}_c for the particular point of diffraction. For far-field points \hat{s}_c is determined from (3.6-9) by

$$\frac{1}{s'} - \frac{\hat{n} \cdot (\hat{s}' - \hat{s}_c)}{a \sin^2 \beta} = 0 \quad (3.6-16)$$

which together with the law of diffraction

$$\hat{t} \cdot \hat{s}' = \hat{t} \cdot \hat{s}_c \quad (3.6-17)$$

specifies the unit vector \hat{s}_c .

The above derivation has been carried out for far-field points. In the near field (3.6-13) and (3.6-17) still apply whereas (3.6-15) and (3.6-16) should be replaced by

$$u = k \frac{\rho s}{\rho + s} \sin^2 \theta \quad (3.6-18)$$

and

$$\frac{1}{s'} - \frac{\hat{n} \cdot (\hat{s}' - \hat{s}_c)}{a \sin^2 \beta} = \frac{1}{s} \quad (3.6-19)$$

respectively.

Figure 3.6-9 shows the caustic correction factor for $0 \leq u \leq 1$. $F_c = 0.98$ for $u = 1$ and for $u > 1$ no correction is applied.

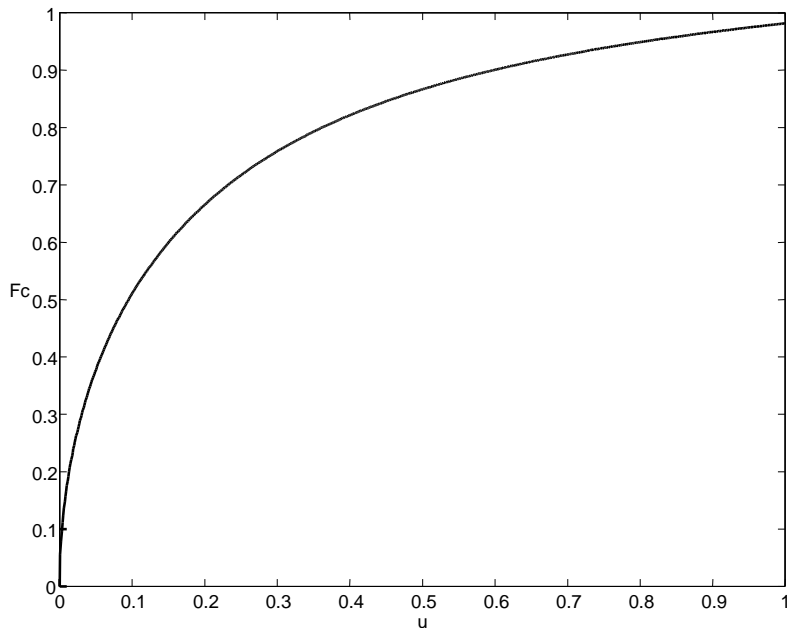


Figure 3.6-9 Caustic correction factor.

The caustic correction presented here is well suited for general numerical calculations since it limits the diffracted field close to a caustic direction independent of the type of caustic. Furthermore, it is simple and requires almost no additional computer time.

3.6.2.2 GTD for scatterers with material properties

One of the effects of the edge diffracted field is to create a continuous field across a reflection boundary (RB) and a shadow boundary (SB) of a scattering body, hence, where the reflected ray and the direct ray from the source are switched off. This situation is shown in Figure 3.6-10.

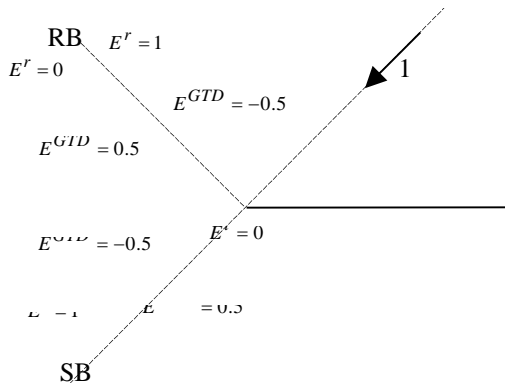


Figure 3.6-10 Diffraction on the edge of a perfect conductor

A ray with unity amplitude is diffracted in the left edge of a perfectly conducting plate. The reflected field, E^r , has unity amplitude inside the reflector boundary and is zero outside. The transmitted field has unity amplitude outside the shadow boundary and is zero inside the shadow boundary. To compensate for this discontinuity the diffracted field, E^{GTD} , must have the amplitude ± 0.5 around the boundaries.

If the perfect conductor is replaced by a partly reflecting and partly transmitting plate, the situation is as shown in Figure 3.6-11.

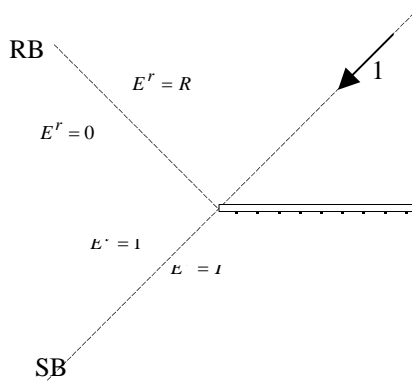


Figure 3.6-11 Edge diffraction on a non-perfectly conducting plate

The reflection/transmission coefficients are R and T, hence the reflected field inside the reflection boundary and the transmitted field inside the shadow boundary are modified accordingly.

The problem now consists in adapting the existing GTD algorithms, valid for perfect conductors, to surfaces that have specified reflection and transmission coefficients. Two separate cases, one for the reflection boundary and one for the shadow boundary, are considered. In Figure 3.6-12 the method for treating the reflection boundary is outlined.

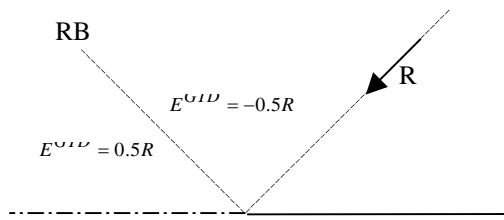


Figure 3.6-12 Diffraction at the RB edge of a non-perfectly conducting plate

As the reflected field inside the reflection boundary has the amplitude R, the existing algorithms for calculating the diffracted field can be used with the assumption that the incident field is scaled from unity to R.

As regards the shadow boundary the method is illustrated in Figure 3.6-13.

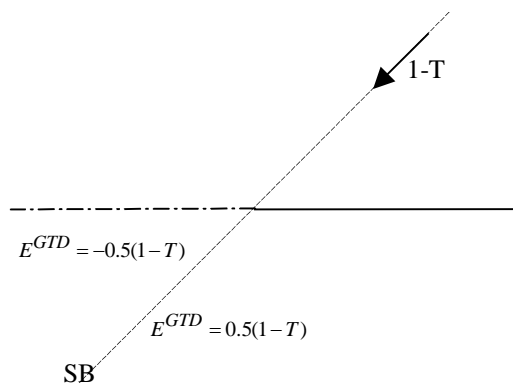


Figure 3.6-13 Diffraction at the SB edge of a non-perfectly conducting plate

As shown in Figure 3.6-11 the transmitted field, E^t , has unity amplitude outside the shadow boundary and the amplitude T inside the shadow boundary, hence, an amplitude change of 1-T. If the amplitude of the incident field is modified to 1-T, the diffraction coefficients valid for the perfect conductor case can be applied here.

In order to solve the discontinuity problem at the reflection and shadow boundaries of the non-perfectly conducting plate in Figure 3.6-11 the two approaches are used as illustrated in Figure 3.6-12 and Figure 3.6-13. The dash-dot line in these two figures indicate where the switch from one approach to the other is done. This switch will give rise to a discontinuity in the GTD field, however, at the boundary line the GTD field is low compared to the direct field so the discontinuity in the total field will be negligible.

To show the validity of the method the geometry shown in Figure 3.6-14 has been analysed. The source is a Hertzian dipole illuminating a flat reflector with a diameter of 20 cm. The dipole is located 10 cm above the plate. The total field (direct field from dipole and scattered field from plate) is calculated in the cut perpendicular to the dipole. The wavelength is 1 cm.

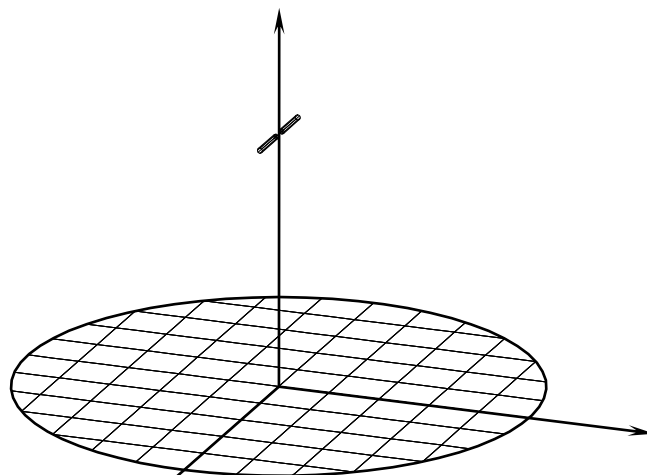


Figure 3.6-14 Geometry used in validity check

In the first case the reflector is assumed to be a perfect conductor (metallic plate). The result of the analysis is shown in Figure 3.6-15.

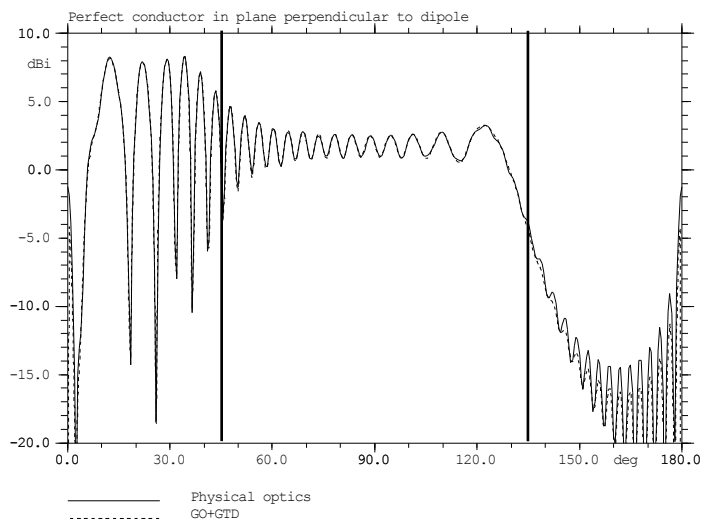


Figure 3.6-15 Field from dipole and perfect conductor. The angular location of the reflection boundary (RB) and the shadow boundary (SB) are marked by thick lines.

In the interval up to 45° (RB) a strong interference pattern is seen due to the dipole field being added/subtracted to its own image in the metallic plate. Beyond the reflection boundary the diffracted field interferes with the direct ray from the dipole and beyond 135° (SB) only the two diffracted rays are present. The field calculated by Physical Optics and by GO/GTD are almost identical. For the calculation of the GTD component the model in Figure 3.6-10 is used.

If the perfect conductor is replaced by a perfect absorber, cf. Section 2.2.3.2.2, the field is as shown in Figure 3.6-16.

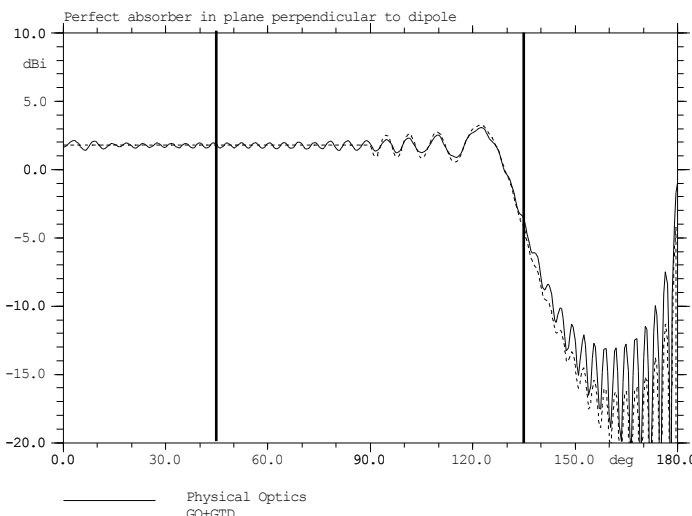


Figure 3.6-16 Field from dipole and perfect absorber. The angular location of the reflection boundary (RB) and the shadow boundary (SB) are marked by thick lines.

As there is no reflected/diffracted field from the plate the total field up to 90° is the dipole field which is constant. In this interval, hence across the reflection boundary, the model in Figure 3.6-12 is used with $R = 0$. Beyond 90° the model in Figure 3.6-13 is used with $T = 0$, hence $1 - T = 1$. For this reason the pattern is the same as that obtained for the perfect conductor where the source amplitude is also unity (Figure 3.6-10). This ensures the continuity across the shadow

boundary as in Figure 3.6-15. The Physical Optics field (solid line) has a small ripple around the constant value of the dipole field due to the fact that the PO field from the absorber is not zero.

As the third case the scatterer is specified as a dielectric plate, cf. Section 2.2.3.8, with a thickness of 1 cm $\approx 1\lambda$ and a dielectric constant of 3. The field is shown in Figure 3.6-17.

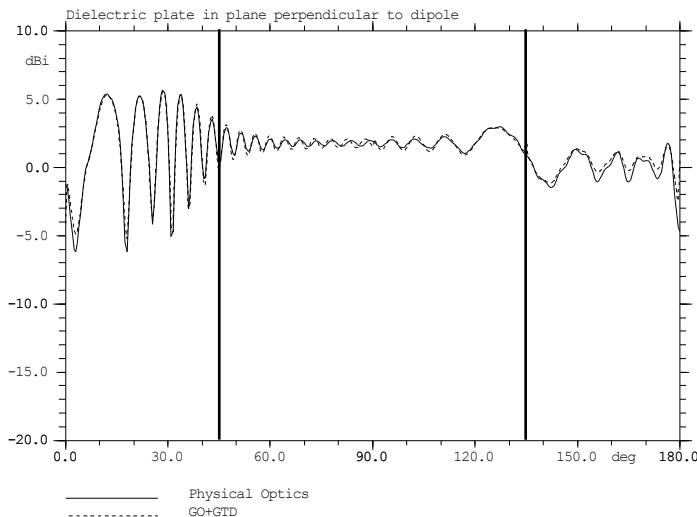


Figure 3.6-17 Field from dipole and dielectric plate. The angular location of the reflection boundary (RB) and the shadow boundary (SB) are marked by thick lines.

The GTD component is calculated from the models in Figure 3.6-12 and Figure 3.6-13 inserting as R and T values the reflection/transmission values at the reflector edge. In Figure 3.6-17 no discontinuity is seen at the reflection boundary (45°) but at 90° where the GTD model is changed a small step is present.

3.7 Special techniques involving the direction of the incident field

Some of the analysis methods employed in GRASP require the direction of incidence for the field to be known. This is for example the case in GTD computations where it is assumed that the field is a ray field coming from a specific direction. The same applies to PTD currents, which can only be computed when a direction of incidence is given. A third example is a reflector surface made from non-perfectly conducting materials, in which case the formulation of the scattering problem, be it in terms of PO or GO, involves the direction of incidence.

If the incident field comes from a simple point source it is straightforward to specify the angle of incidence. However, many sources are more complex than this. A PO current distribution cannot in general be said to originate from a single point. Similar with an array of feed elements or the GTD field from a reflector antenna.

To cope with these cases a special feature has been implemented in GRASP. Each source object of the type in question has a special attribute called "ray_output". Depending on the source it may take the value "all", "none", "spherical", or "plane". The value of ray_output does not affect the computation of the field, it only provides information about the direction of propagation at the location of the field point. The normal mode of operation is that ray_output is "none", in which case the direction of incidence is determined from Poynting's vector

$$\bar{P} = \frac{1}{2} \operatorname{Re} \bar{E} \times \bar{H}^* . \quad (3.7-1)$$

It is noted that this requires knowledge of both the electric and the magnetic field which can be seen on the computation time.

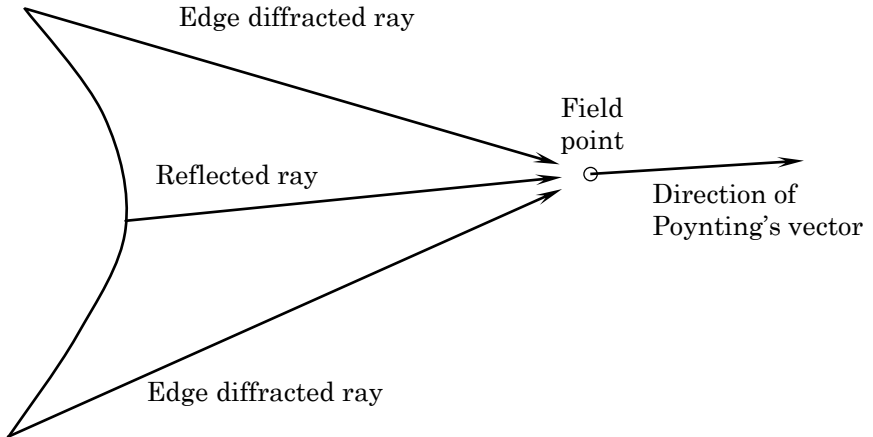


Figure 3.7-1 Illustrating the principles of finding the direction of incidence.

To illustrate the procedure let us consider Figure 3.7-1, and assume that we need to calculate the field from the reflector at the field point. Furthermore, we need the direction of incidence at the field point, because there is a reflector located there (not shown in the figure), which consists of a polarisation-sensitive grid. The field from the first reflector shall be calculated by GTD.

At the field point there are three rays, a reflected ray and two edge diffracted rays. Poynting's vector will have almost the same direction as the reflected ray, only slightly modified by the edge-diffracted field. If the `ray_output` is set to "none", then the total field would be calculated by summing all ray components, calculate Poynting's vector and assume that the field comes from a single ray in this direction.

The problem could instead be treated as three independent sources, all of which are true ray fields and thus have no ambiguity in the direction of incidence. This can be achieved by setting the value of `ray_output` to "all" instead on "none". A more accurate description is then obtained, and as it will be seen in one of the examples of Section 5, it is possible to ob-

serve differences between the two approaches, although at a very low field level. For most practical calculations it will be sufficient to use the default value of `ray_output` ("none").

The above example describes the concept by looking at the GTD field from a single reflector. However, the same approach is applicable to e.g. an array where, by setting the value of `ray_output` to "all", the contribution from each individual element of the array can be calculated separately rather than calculating the composite field. In a similar manner a PO current distribution can be viewed as an array of current elements, each of which acts as a point source.

There are two more options for the value of `ray_output`. These are "spherical" and "plane". The effect of `ray_output` = "spherical" is that the direction of propagation of the field at the field point is assumed to originate from the origin of a coordinate system specified by the user. This makes it possible to use a PO current distribution as a source for a subsequent GTD calculation, which is not allowed when `ray_output` = "none". It could be useful and speed up computations in cases where the behaviour of the source field is known in advance, for example the current distribution on a hyperboloidal subreflector illuminated by a point-source feed at the focus.

When `ray_output` = "plane" the direction of propagation of the field at the field point is assumed to be parallel to the z -axis of a coordinate system specified by the user.

It is difficult to say in general which method should be used, because it depends very much in the problem under consideration. If computing time is of no concern then the `ray_output` = "all" should be used since this is the most accurate approach to the problem. However, in very many cases it will be a most reasonable assumption to use the direction of Poynting's vector (`ray_output` = "none"), and thereby save computing time. It is left to the user of GRASP to make the final and appropriate decision, based on the actual geometry of interest.

3.8 Examples illustrating PO and GTD

The analysis methods described in the above paragraphs will be further illustrated in the following, by applying them to a fairly simple parabolic reflector antenna design. It will be shown how close agreement can be obtained between the two methods, and some guidelines will be established to help choosing the most appropriate method for a given design.

First the geometry is outlined followed by a comparison between GTD and PO in the main beam and first few sidelobes. We then investigate the wide-angle pattern and show how it is possible to obtain good agreement also in this region. For all the examples the automatic convergence procedure described in Section 3.1.3.2 has been used to determine the necessary density of the PO integration grid.

3.8.1 Single offset reflector geometry

An offset paraboloid is chosen, with a diameter $D = 40\lambda$ and a focal length $f = 32\lambda$ as shown in Figure 3.8-1. A clearance of $D' = 10\lambda$ ensures a blockage-free design. The feed is a Gaussian beam, as described in Section 2.3.1.3.5, with a taper of 12 dB at the edge of the reflector corresponding to an angle of 29.1° and linearly polarised in the symmetry plane of the antenna. It is directed towards the aperture centre point on the reflector which is also the origin of the output coordinate system. With this pointing the feed axis forms an angle of 50.2° with the reflector axis.

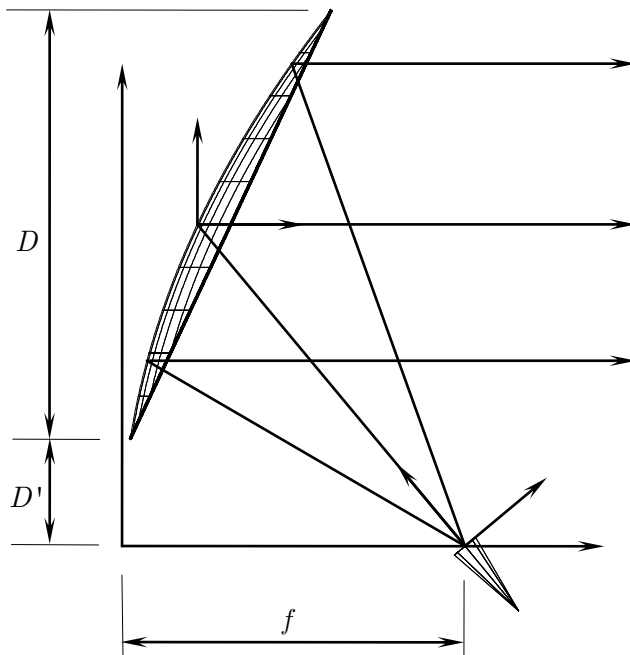


Figure 3.8-1 Geometry of single offset parabolic reflector antenna, $D = 40\lambda$, $f = 32\lambda$, $D' = 10\lambda$.

The reflected field from the surface will form a caustic in the far field in the boresight direction. The edge diffracted rays will, as described in Section 6.4, generate a caustic hyperbola in the symmetry plane where the one asymptotic direction is the boresight, $\theta = 0^\circ$, and the other may be found from Section 6.4 and equation (6.1-15) which with the actual parameters gives $\theta = 129.8^\circ$.

3.8.2 Calculation of main beam and near-in sidelobes

The calculated radiation pattern near the main beam maximum is shown in Figure 3.8-2. The GTD solution deviates significantly from the PO results in the main beam and up to the first two sidelobes. This is of course to be expected since, as

earlier indicated, the main-beam region is a caustic for the reflected rays and PO is the only valid prediction tool here.

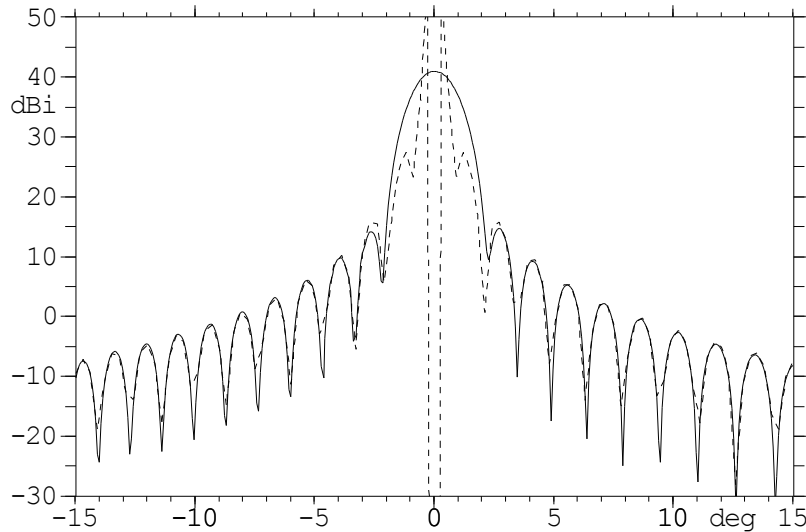


Figure 3.8-2 Far-field radiation pattern in the plane of symmetry. Full line: PO, dotted line: GTD.

In the further-out sidelobe region the GTD and the PO results are in perfect agreement, and from an accuracy point of view either method could be selected. The above results are somewhat depending on the taper of the feed, but as a general rule of thumb it is reasonable to say that GTD can be used from an angle θ , where

$$\frac{D}{\lambda} \sin \theta = 4.7 . \quad (3.8-1)$$

The above patterns were computed on a notebook computer within fractions of a second for both the PO and the GTD predictions. Thus the actual choice of method is not critical for computation-time considerations, as for near-in sidelobes it is just as fast to use PO as it is to use GTD. It is when very wide-angle patterns are considered that GTD may have its greatest advantage, as we shall see in the next section.

3.8.3 Wide-angle pattern prediction by PO and GTD

It is commonly argued that GTD is more accurate than PO in the far-out sidelobe region. As we shall see in the following, it is in fact possible to obtain extremely accurate results by means of PO, also in the far-out sidelobes. This may, however, come at a considerable price in terms of CPU time.

Figure 3.8-3 shows the PO and the GTD patterns in the upper half space of the antenna in Figure 3.8-1.

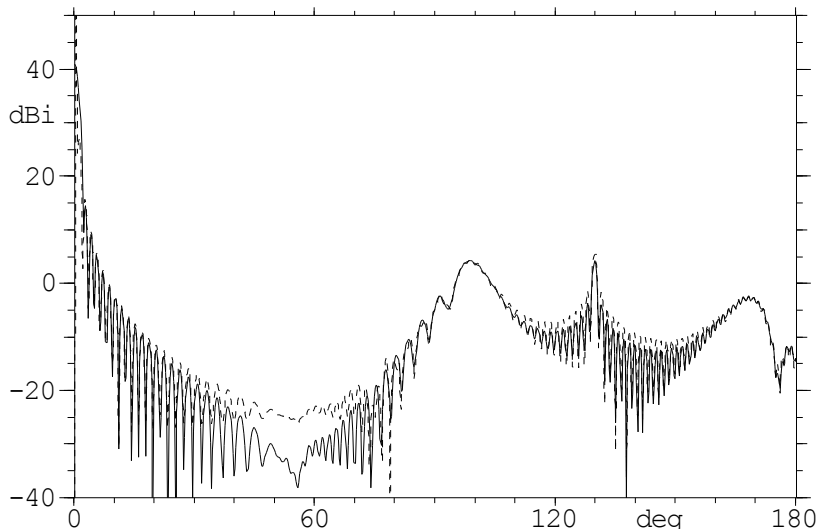


Figure 3.8-3 Upper half of symmetry plane pattern.
Full line: PO, dotted line: GTD.

The first characteristic feature of the patterns is the rather high increase in the sidelobes at 90° . This is where the feed becomes visible and contributes to the total pattern with a contribution that is larger than the sidelobes from the reflector scattered pattern. It drops off again, corresponding to the region where it is shadowed by the reflector. It is important to note that whereas the GTD method inherently takes the shadowing effect into account by only adding the direct ray from the feed when it is not shadowed by the reflector, the PO method requires that the feed field is added to the scattered

field from the reflector at any point in space. Usually, it is not important to add the feed field when PO is used to calculate the pattern in the main-beam direction since the feed radiation is significantly lower. But this is far from the case in the rear direction of the reflector. If we had not added the feed contribution we would have obtained a scattered pattern that in this direction would closely resemble that of the feed main lobe.

Another interesting characteristic is the peak at $\theta = 130^\circ$ caused by the caustic of the diffracted rays, an angle that was earlier calculated to 129.8° .

In the above calculations only the induced currents were considered in the PO solution. As described in Section 3.2 the PO currents are inaccurate near the edge of the reflector, and PTD may be used to improve the accuracy. Figure 3.8-4 shows the difference when PTD is added to the PO solution. Now there is extremely good agreement between GTD and PO+PTD also in the region from $\theta = 30^\circ$ to $\theta = 75^\circ$.

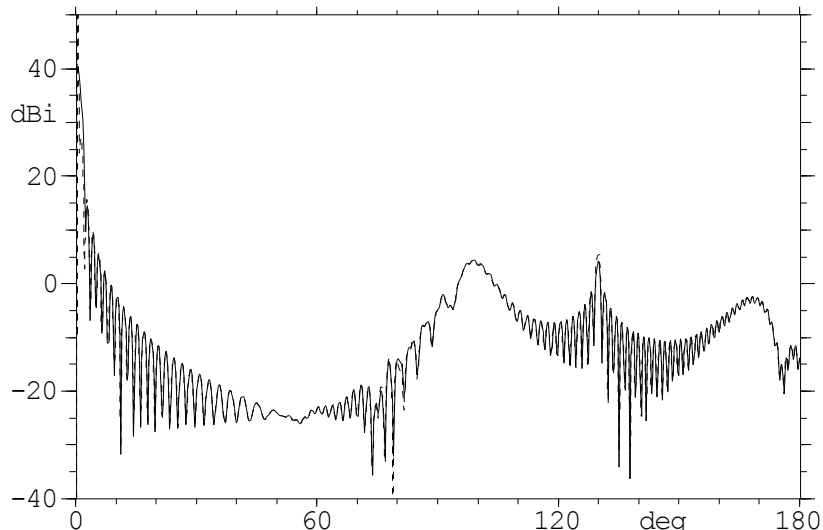


Figure 3.8-4 Upper half of symmetry plane pattern.
Full line: PO+PTD, dotted line: GTD.

3.8.4 The significance of an accurate feed model in PO calculations

The calculations presented above have shown that the secondary pattern is extremely well predicted all over the far-field sphere. In the shadow region the total field is generated by a superposition of the scattered field from the reflector and the direct field from the feed. These two contributions are almost equal in amplitude but of opposite phase and it is of utmost importance that the correct feed model is used since otherwise it will not be possible to make the two contributions cancel out.

In GRASP all feed models are described by a spherical wave expansion such that not only the far field but also the near field from the feed is correct. This is in contrast to previous versions where the far field pattern was accepted for most of the feed models. The importance of the correct near field is illustrated in Figure 3.8-5 which shows a close-up of the patterns in the shadow region behind the reflector, i.e. for $110^\circ < \theta < 150^\circ$. The figure shows the GTD solution and two PO+PTD solutions, one with the correct near field and one where the far-field pattern of the feed is used.

It is seen that the GTD solution and the PO+PTD result with the near-field feed model are in perfect agreement with just a minor discrepancy in the direction of the caustic, a region where GTD is known to be less accurate.

GTD and PO+PTD with the far-field feed model disagree by as much as 5 dB on some of the lobes. Such differences at a level which is only about 45 dB below peak may in some cases not be satisfactory, and the example here demonstrates that this problem has been eliminated by the correct near-field model of the feeds.

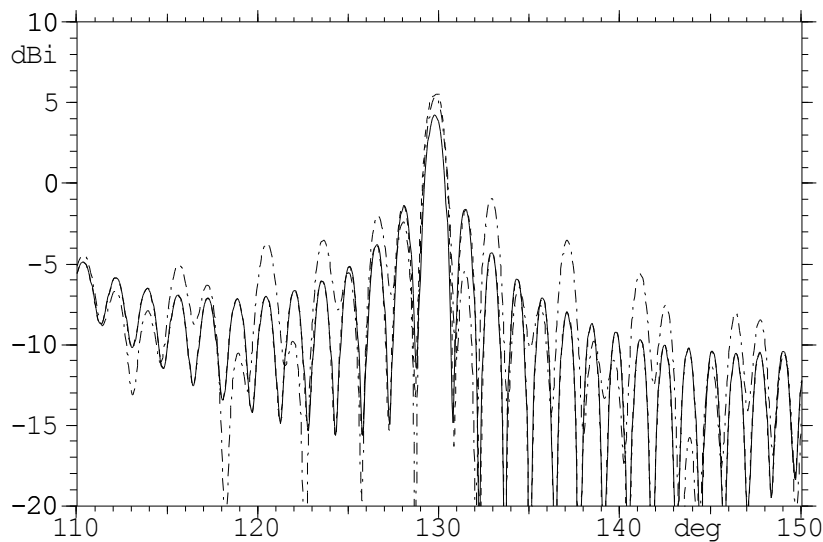


Figure 3.8-5 Close look at the rear pattern in the symmetry plane.

Full line: PO+PTD, near-field feed

Dot-and dash line: PO+PTD, far-field feed

Dotted line: GTD.

3.8.5 Near-field predictions

While the above calculations and associated considerations all have been for far fields, both PO and GTD are applicable to near-field calculations as well. It should be noted that the reflected ray caustic in the far-field boresight direction does not exist in the near field, and thus GTD (with GO) can be used at any point. Caustics due to diffracted rays are in general present and may cause deviations between GTD and PO, but they do not represent a computational problem due the caustic correction explained in Section 3.6.2.1.

The near field of the offset parabolic reflector is presented in Figure 3.8-6. An excellent agreement between the two methods is observed, even at the centre of the aperture where the diffracted field has a caustic.

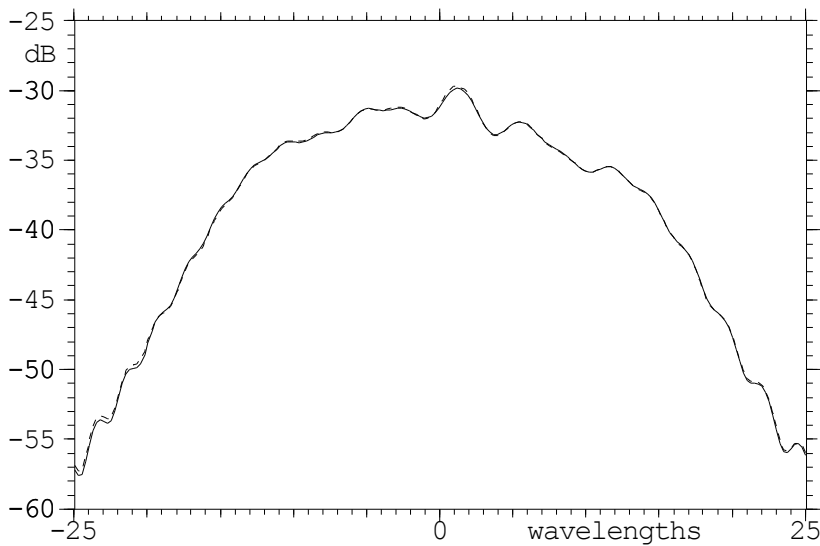


Figure 3.8-6 Near-field pattern calculated 80λ in front of the aperture,
Full line: PO+PTD, dotted line: GTD.

The near field can be calculated as close to the reflector as desired, though field points on the surface should be avoided. For focusing reflectors there is a maximum distance for which GTD should be applied due to the caustic of the reflected rays. This distance has been found to be

$$R_{\max} = \frac{1}{4} D(D/\lambda) \quad (3.8-2)$$

above which GTD fails in the boresight direction.

3.8.6 Guidelines on selecting PO or GTD

We have shown in the preceding sections that PO and GTD can be used as alternative analysis methods, except for the main-beam direction of a focusing aperture where GTD fails. One may then ask the question: which analysis method should I apply to a particular problem? Some guidelines based on experience are given below.

PO should be used when:

1. The field is calculated at or near a caustic of the reflected field, i.e. in the focusing region of a reflector.
2. When the reflector is in the near field of the feed. GTD always assumes far-field conditions.
3. In dual reflector systems with low cross polarisation requirements. PO is more accurate in predicting the cross polarisation in dual reflector systems due to the subreflectors curvature. GTD may predict a too optimistic pattern.
4. The reflector is shaped. In this case the GTD algorithm may prove incapable of finding all diffraction points, just as there may be more reflection points for one field point.
5. The reflector has an irregular edge. In this case the GTD ray tracing algorithm may fail in finding all diffraction points, just as the inclusion of a corner-diffracted field may be necessary to obtain satisfactory accuracy, an option which is not included in GRASP.

On the other hand, GTD may be more appropriate for:

6. Wide angle pattern of electrically large single reflectors. To obtain the agreement presented in Section 3.8.3 the PO analysis took 5 times longer than the GTD analysis. In this particular case for a 40λ antenna the CPU time is relatively low in both cases. If the antenna was 10 times larger it would be necessary to calculate 10 times as many field points in order to sample the far field appropriately. Since a GTD analysis is almost independent of the antenna size the total CPU time would increase by a factor of 10. As opposed to this, the PO analysis would not only require 10 times more output points, but the integration grid would increase by almost a factor of 100. The estimated increase in CPU time consumption is thus 1000 such that

the ratio between PO and GTD calculations in this case would be around 500.

7. Fast near field calculations, and investigations where it can provide insight into a particular scattering problem if the edge-diffracted and reflected rays fields are observed independently.

3.9 Gaussian beam analysis

The Gaussian feed model, described in Section 2.3.1.3, is well suited for modelling of the field propagation through a beam waveguide (see for example Kitsuregawa, 1990). Let us consider the reflection at Q in an ellipsoidal reflector with foci F_1 and F_2 , see Figure 3.9-1. In this geometry, a conventional point source on the ray F_1Q at the distance z_1 from Q after the reflection at Q will focus at a point on the ray QF_2 at the distance z_2 from Q . z_1 and z_2 satisfies the formula for reflecting systems (Abbe's invariant, Born and Wolf, 1983)

$$\frac{1}{z_1} + \frac{1}{z_2} = \frac{1}{f} \quad (3.9-1)$$

where f may be found from the known special case when $z_1 = r_1 = F_1Q$ and $z_2 = r_2 = F_2Q$ with $r_1 + r_2$ being the length of the major axis of the ellipsoid

$$\frac{1}{r_1} + \frac{1}{r_2} = \frac{1}{f} \quad . \quad (3.9-2)$$

If we place a Gaussian source with imaginary displacement b_1 in A $z_1 = AQ$ it will focus as a Gaussian source with imaginary displacement b_2 in B $z_2 = BQ$. The imaginary displacement was introduced in Section 2.3.1.3.1 for the Gaussian beam feed.

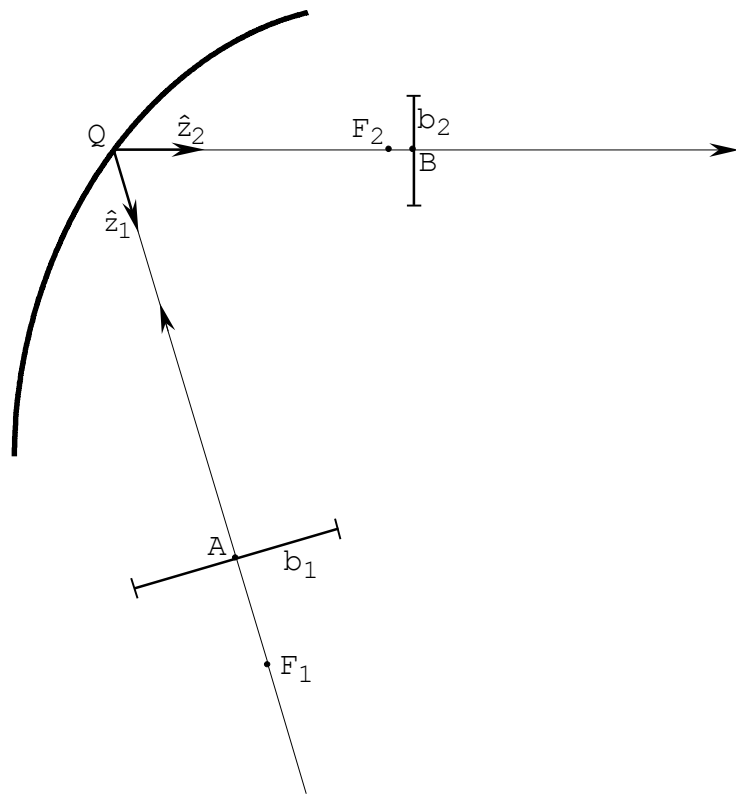


Figure 3.9-1 Reflection in an ellipsoidal reflector at Q .

If we substitute the complex distances for z_1 and z_2 in (3.9-1) we find

$$\frac{1}{z_1 + jb_1} + \frac{1}{z_2 - jb_2} = \frac{1}{f} \quad (3.9-3)$$

which can be used immediately to determine z_2 and b_2 . Expression (3.9-3) is therefore the fundamental equation for the design of a beam waveguide system. The physical implications of (3.9-3) can be further substantiated by the following considerations. Expression (3.9-3) can be rewritten as

$$\frac{z_1 - jb_1}{z_1^2 + b_1^2} + \frac{z_2 + jb_2}{z_2^2 + b_2^2} = \frac{1}{f} \quad . \quad (3.9-4)$$

The real part of (3.9-4) yields

$$\frac{1}{z_1 \sqrt{1+b_1^2/z_1^2}} + \frac{1}{z_2 \sqrt{1+b_2^2/z_2^2}} = \frac{1}{f} \quad . \quad (3.9-5)$$

Applying **(2.3-32)** shows that the radii of curvature, R_1 and R_2 , of the incoming and reflected fields, respectively, at the reflection point Q fulfills (3.9-1)

$$\frac{1}{R_1} + \frac{1}{R_2} = \frac{1}{f} \quad . \quad (3.9-6)$$

This corresponds to the fact that a conventional point source at the distance R_1 from Q will reflect and focus at the distance R_2 from Q . The radii of curvature of the fields of these two sources will be the same as for the two Gaussian sources at the reflection point Q .

The imaginary part of (3.9-4) yields

$$\frac{1}{b_1 \sqrt{1+z_1^2/b_1^2}} = \frac{1}{b_2 \sqrt{1+z_2^2/b_2^2}} \quad (3.9-7)$$

which shows, cf. **(2.3-31)**, that the width of the waist of the incoming Gaussian beam at the reflection point Q is equal to the width of the waist of the reflected beam.

3.10 Spherical wave expansion

The Spherical wave expansion software (SWE) was previously an add-on to GRASP. It is now implemented as an integrated part of GRASP.

The main advantage for the user is that it is then possible to make an automatic spherical wave expansion of all feeds and it is not necessary to require that the reflector is in the far field of the feed. In this case the spherical wave expansion coefficients will only be stored internally in GRASP during the computations. However, the spherical wave expansion coefficients can be calculated and stored for any radiating electromagnetic source for which the field can be specified on a sphere around it.

The techniques employed to calculate a spherical wave expansion are treated in detail by Hansen (1988). It is implicitly assumed that the input field (E_θ and E_ϕ) is known at any point (θ, ϕ) on a sphere with constant radius r , which is infinite in case of far-field input. Usually, the input field will be given in a finite number of cuts with constant ϕ each containing a finite number of θ -values. These cuts are then input to the tabulated pattern model in Section 2.3.1.1, which in turn is used as input for the spherical wave expansion.

When an electromagnetic source is specified by its spherical wave expansion the field may be determined accurately outside a sphere surrounding the source. The near field as well as the far field may be determined accurately from this model. In this context, the source may be any kind of radiating source, e.g. a feed horn or a subreflector or even a complete antenna. This source model is thus well suited when the illuminated object is in the near field of the radiating source. In dual reflector systems the subreflector is very often in the near field of the feed horn, and the main reflector is almost always in the near field of the sub.

Such a completely general representation of a source is obtained by means of an expansion in spherical waves as derived in Stratton (1941, pp. 414-420). Stratton applied even and odd modes in ϕ whereby the ϕ -variation is given by $\sin m\phi$ and $\cos m\phi$.

These modes were replaced by complex exponential modes by Jensen (1970, Appendix I) where the ϕ -variation is given by the more handy $\exp -jm\phi$, m being positive as well as negative. In this notation two sets of expansion functions exist (\bar{m}_{mn} and \bar{n}_{mn}) with the coefficients a_{mn} and b_{mn} , respectively. The modes are therefore called the *ab*-modes in the following.

Both of these definitions have the disadvantage that the involved associated Legendre polynomials even for rather small antennas (diameter $\sim 20\lambda$) increase in value beyond the limits for floating point arithmetic in modern computers. Larsen (1980) therefore replaced these with the normalised associated

Legendre polynomials. The Larsen definition further has the advantage that each mode coefficient reflects the power content of the mode. A detailed discussion of the modes is given in Hansen (1988). The notation for the expansion function is reduced to \bar{F}_{smn} and there is only one coefficient, Q_{smn} . These modes are therefore called the Q -modes in the following.

In the following the ab -modes as well as the Q -modes are presented and after this a common discussion of the properties of the spherical modes will be given. But first we will introduce the numbering sequence of the spherical modes.

3.10.1 Theoretical number of modes

The radiation from an antenna may be determined by measurements in a spherical scanner. Alternatively, a calculation over a spherical surface surrounding the antenna may be carried out. In both cases, the centre of the sphere is well defined. The smallest sphere with this centre completely surrounding the antenna is called the minimum sphere. The radius of this minimum sphere is denoted r_o .

The spherical modes have an azimuthal index m and a polar index n . The maximum value, N , of the polar index is determined by kr_o where k is the wavenumber $2\pi/\lambda$. In general sufficient numerical accuracy is obtained (Jensen and Frandsen, 2004) when

$$N = kr_o + \max 3.6\sqrt[3]{kr_o}, 10 , \quad (3.10-1)$$

and this criterion is used whenever a spherical wave expansion is carried out internally in GRASP.

For the azimuthal index m we have the limits

$$-n \leq m \leq n . \quad (3.10-2)$$

For each pair of indices (m, n) there exists two modes given by the ab -coefficients a_{mn} and b_{mn} or the Q -coefficients Q_{smn} , $s = 1, 2$. The total number of modes is then $2N(N+2)$, cf. Hansen (1988).

Summations over the spherical modes can then either be a summation over all m for each n :

$$\sum_{n=1}^N \sum_{m=-n}^n \quad (3.10-3)$$

which is used for the Q -modes. Or the summations may be over the possible n for each m

$$\sum_{m=-N}^N \sum_{\substack{n=|m|, \\ n>0}}^N \quad (3.10-4)$$

which is used in the ab -modes.

The last notation gives the possibility of excluding high order modes with negligible power. The m -modes may be limited to $|m| \leq M \leq N$ where M is input by the user and N is given in (3.10-1); for example an antenna of high degree of rotational symmetry will often have a low value of M , e.g. $M = 5$. Further, for each m , the number of n -modes with significant power may be lower than N and may be determined as a function in m , $N(m)$. For example, the highly rotational antenna will often have $N(m)$ low for even m but $N(m) = N$, N given by (3.10-1), for odd m . M and $N(m)$ may be determined when the spherical modes are calculated. The summation then becomes

$$\sum_{m=-M}^M \sum_{\substack{n=|m|, \\ n>0}}^{N(m)} . \quad (3.10-5)$$

3.10.2 Spherical expansion expressed in the ab -modes

A general electromagnetic field may be written as a spherical wave expansion, which in the notation of the ab -modes may be written as

$$\bar{E} \ r, \theta, \phi = k\sqrt{2\zeta} \sum_{m=-M}^M \sum_{\substack{n=|m| \\ n>0}}^{N(m)} \left\{ \begin{array}{l} a_{mn} \bar{m}_{mn} \ r, \theta, \phi \\ + b_{mn} \bar{n}_{mn} \ r, \theta, \phi \end{array} \right\} \quad (3.10-6)$$

$$\bar{H} \ r, \theta, \phi = jk \sqrt{\frac{2}{\zeta}} \sum_{m=-M}^M \sum_{\substack{n=|m| \\ n>0}}^{N(m)} \left\{ \begin{array}{l} a_{mn} \bar{n}_{mn} \ r, \theta, \phi \\ + b_{mn} \bar{m}_{mn} \ r, \theta, \phi \end{array} \right\} \quad (3.10-7)$$

where a_{mn} and b_{mn} are the spherical-wave expansion coefficients and ζ is the free-space impedance. The complex spherical-wave coefficients, a_{mn} and b_{mn} , as well as the number of modes M and $N(m)$ are stored in a data file.

The spherical vector expansion functions $\bar{m}_{mn} \ r, \theta, \phi$ and $\bar{n}_{mn} \ r, \theta, \phi$ are defined by

$$\begin{aligned} \bar{m}_{mn} \ r, \theta, \phi &= -h_n^2 \ kr \frac{jmP_n^{|m|} \cos \theta}{\sin \theta} e^{-jm\phi} \hat{\theta} \\ &\quad - h_n^2 \ kr \frac{dP_n^{|m|} \cos \theta}{d\theta} e^{-jm\phi} \hat{\phi} \end{aligned} \quad (3.10-8)$$

and

$$\begin{aligned} \bar{n}_{mn} \ r, \theta, \phi &= \frac{n \ n+1}{kr} h_n^2 \ kr \ P_n^{|m|} \ \cos \theta \ e^{-jm\phi} \hat{r} \\ &\quad + \frac{1}{kr} \frac{d}{d \ kr} \ kr h_n^2 \ kr \ \frac{dP_n^{|m|} \ \cos \theta}{d\theta} e^{-jm\phi} \hat{\theta} \\ &\quad - \frac{1}{kr} \frac{d}{d \ kr} \ kr h_n^2 \ kr \ \frac{jm \ P_n^{|m|} \ \cos \theta}{\sin \theta} e^{-jm\phi} \hat{\phi} \end{aligned} \quad (3.10-9)$$

where $P_n^m \ \cos \theta$ are the associated Legendre functions given by

$$P_n^{|m|}(\cos \theta) = (\sin \theta)^{|m|} \frac{d^{|m|} P_n(\cos \theta)}{d(\cos \theta)^{|m|}}, \quad |m| \leq n \quad (3.10-10)$$

in which

$$P_n(\cos \theta) = \frac{1}{2^n n!} \frac{d^n}{d(\cos \theta)^n} (\cos^2 \theta - 1)^n, \quad n \geq 0 \quad (3.10-11)$$

is the Legendre polynomial (Stratton, 1941).

$h_n^{(2)}(kr)$ are the spherical Hankel functions of the second kind as defined in Abramowitz and Stegun (1965) and easiest given by the recursion relation

$$h_{n-1}^{(2)}(kr) + h_{n+1}^{(2)}(kr) = 2n+1 \frac{h_n^{(2)}(kr)}{kr} \quad (3.10-12)$$

and

$$h_0^{(2)}(kr) = j \frac{e^{-jkr}}{kr} \quad (3.10-13)$$

$$h_1^{(2)}(kr) = \left(-1 + j \frac{1}{kr} \right) \frac{e^{-jkr}}{kr} \quad (3.10-14)$$

For the derivatives of the Hankel functions a recurrence relation is

$$\frac{1}{kr} \frac{d}{dkr} kr h_n^{(2)}(kr) = h_{n-1}^{(2)}(kr) - n \frac{h_n^{(2)}(kr)}{kr} . \quad (3.10-15)$$

In the far field kr becomes large and we find

$$h_n^{(2)}(kr) \rightarrow j^{n+1} \frac{e^{-jkr}}{kr} \text{ for } kr \rightarrow \infty \quad (3.10-16)$$

and

$$\frac{1}{kr} \frac{d}{dkr} kr h_n^{(2)}(kr) \rightarrow j^n \frac{e^{-jkr}}{kr} \text{ for } kr \rightarrow \infty . \quad (3.10-17)$$

The power of the mode-expanded field is given by the *ab-* coefficients as

$$P = 4\pi \sum_{m=-M}^M \sum_{\substack{n=|m|, \\ n>0}}^{N_m} \frac{n(n+1)}{2n+1} \frac{n+|m|!}{n-|m|!} |a_{mn}|^2 + |b_{mn}|^2 \quad (3.10-18)$$

3.10.3 Spherical expansion expressed in the Q -modes

The Q -notation of the spherical modes differs from the ab -notation presented above. The functions are different and thus the expansion coefficients are different too.

The general field in the notation of the Q -modes may be written as

$$\bar{E} \ r, \theta, \phi = k\sqrt{\zeta} \sum_{s=1}^2 \sum_{m=-M}^M \sum_{\substack{n=|m| \\ n>0}}^{N_m} Q_{smn} \bar{F}_{smn} \ r, \theta, \phi \quad (3.10-19)$$

$$\bar{H} \ r, \theta, \phi = \frac{jk}{\sqrt{\zeta}} \sum_{s=1}^2 \sum_{m=-M}^M \sum_{\substack{n=|m| \\ n>0}}^{N_m} Q_{smn} \bar{F}_{3-s,m,n} \ r, \theta, \phi \quad (3.10-20)$$

where Q_{smn} are the spherical-wave expansion coefficients for the Q -modes. The expressions follow Hansen (1988).

The spherical vector expansion functions $\bar{F}_{smn} \ r, \theta, \phi$ are defined by two functions $\bar{m}'_{mn} \ r, \theta, \phi$ and $\bar{n}'_{mn} \ r, \theta, \phi$ for $s = 1$ and 2, respectively:

$$\bar{F}_{1mn} \ r, \theta, \phi = \frac{1}{\sqrt{2\pi}} \frac{1}{\sqrt{n \ n + 1}} \left(-\frac{m}{|m|} \right)^m \bar{m}'_{mn} \ r, \theta, \phi \quad (3.10-21)$$

and

$$\bar{F}_{2mn} \ r, \theta, \phi = \frac{1}{\sqrt{2\pi}} \frac{1}{\sqrt{n \ n + 1}} \left(-\frac{m}{|m|} \right)^m \bar{n}'_{mn} \ r, \theta, \phi \quad (3.10-22)$$

where $\bar{m}'_{mn} \ r, \theta, \phi$ and $\bar{n}'_{mn} \ r, \theta, \phi$ are defined as $\bar{m}_{mn} \ r, \theta, \phi$ and $\bar{n}_{mn} \ r, \theta, \phi$ in (3.10-8) and (3.10-9) by replacing the associated Legendre polynomial $P_n^{|m|} \cos \theta$ by the normalised associated Legendre polynomial $\bar{P}_n^{|m|} \cos \theta$, i.e.

$$\begin{aligned} \bar{m}'_{mn} \ r, \theta, \phi &= -h_n^2 \ kr \frac{jm\bar{P}_n^{|m|} \cos \theta}{\sin \theta} e^{-jm\phi} \hat{\theta} \\ &\quad - h_n^2 \ kr \frac{d\bar{P}_n^{|m|} \cos \theta}{d\theta} e^{-jm\phi} \hat{\phi} \end{aligned} \quad (3.10-23)$$

and

$$\begin{aligned}
\bar{n}'_{mn} r, \theta, \phi &= \frac{n(n+1)}{kr} h_n^2 kr \bar{P}_n^{|m|} \cos \theta e^{-jm\phi} \hat{r} \\
&+ \frac{1}{kr} \frac{d}{d(kr)} kr h_n^2 kr \frac{d\bar{P}_n^{|m|}}{d\theta} \cos \theta e^{-jm\phi} \hat{\theta} \\
&- \frac{1}{kr} \frac{d}{d(kr)} kr h_n^2 kr \frac{jm \bar{P}_n^{|m|} \cos \theta}{\sin \theta} e^{-jm\phi} \hat{\phi} \quad (3.10-24)
\end{aligned}$$

The normalised associated Legendre polynomial $\bar{P}_n^{|m|} \cos \theta$ is defined by

$$\bar{P}_n^{|m|} \cos \theta = \sqrt{\frac{2n+1}{2} \frac{(n-m)!}{(n+m)!}} P_n^{|m|} \cos \theta \quad (3.10-25)$$

where $P_n^{|m|} \cos \theta$ is given in (3.10-10).

After these redefinitions the power P of the spherical mode expansion can be written in the simple form

$$P = \frac{1}{2} \sum_{s=1}^2 \sum_{n=1}^N \sum_{m=-n}^n |Q_{smn}|^2 \text{ (watt)} \quad (3.10-26)$$

A general description of the properties of the spherical wave expansion including the $\bar{F}_{smn} r, \theta, \phi$ functions may be found in Hansen (1988).

3.10.4 Field determination

The field is determined directly from the coefficients of the spherical wave expansion. Both far fields and near fields can be determined. Far fields are used for GO and GTD calculations while PO currents are determined from the near-field expressions, including the r -component, of the magnetic field.

4. OUTPUT CAPABILITIES

This chapter describes the output capabilities in GRASP. The units used are defined in Section 4.1 where also the feed normalisation is introduced such that the calculated field can be expressed relative to isotropic level, dBi. This section also presents the polarisation options available in GRASP.

The different possibilities for the location of the field points are presented in Section 4.2, especially the one-dimensional patterns cuts and the two-dimensional field grids. Interpolation techniques are described in Section 4.3, and Section 4.4 contains some special beam analyses available in the Post-processor.

4.1 Definition and normalisation of field components

4.1.1 Field units

The electric and magnetic fields in GRASP are measured in normalised units. The relation between the fields in the standard SI units and the units in GRASP is given by

$$\bar{E} = \frac{1}{k\sqrt{2\zeta}} \bar{E}_{SI} \quad (4.1-1)$$

$$\bar{H} = \frac{1}{k} \sqrt{\frac{\zeta}{2}} \bar{H}_{SI} \quad (4.1-2)$$

$$\bar{J}^e = \frac{1}{k} \sqrt{\frac{\zeta}{2}} \bar{J}_{SI}^e \quad (4.1-3)$$

$$\bar{J}^m = \frac{1}{k\sqrt{2\zeta}} \bar{J}_{SI}^m \quad (4.1-4)$$

where \bar{E}_{SI} , \bar{H}_{SI} , \bar{J}_{SI}^e and \bar{J}_{SI}^m are the electric field, the magnetic field, the electric surface current and the magnetic surface current, respectively, measured in the standard SI units. The fields \bar{E} , \bar{H} , \bar{J}^e and \bar{J}^m are the same quantities in the normalised GRASP units.

A suppressed time factor $e^{j\omega t}$ is assumed for all GRASP output with ω as the cyclic frequency related to the actual frequency ν by $\omega = 2\pi\nu$. The constant k is the wavenumber defined by

$$k = \omega\sqrt{\epsilon\mu} \quad (4.1-5)$$

where ϵ and μ are the free-space permittivity and permeability, respectively. The other constant ζ in (4.1-1) through (4.1-4) is the impedance of free-space

$$\zeta = \sqrt{\mu/\epsilon} \quad (4.1-6)$$

which is measured in ohm. The free-space wavelength λ is defined by

$$\lambda = c/\nu \quad (4.1-7)$$

where c is the speed of light related to ϵ and μ by

$$c = \frac{1}{\sqrt{\epsilon\mu}} \quad (4.1-8)$$

so that k can be expressed as

$$k = 2\pi/\lambda \quad . \quad (4.1-9)$$

Since the units of \bar{E}_{SI} , \bar{H}_{SI} , \bar{J}_{SI}^e and \bar{J}_{SI}^m are

$$[\bar{E}_{SI}] = \text{volts/meter}$$

$$[\bar{H}_{SI}] = \text{ampere/meter}$$

$$[\bar{J}_{SI}^e] = \text{ampere/meter}$$

$$[\bar{J}_{SI}^m] = \text{volts/meter} \quad (4.1-10)$$

it is seen that the unit of \bar{E} , \bar{H} , \bar{J}^e and \bar{J}^m become watt $^{1/2}$. By using these units all constants of nature are avoided in the field equations. Such normalised units are convenient in a computer program where very large or small physical constants (e.g. the speed of light) might give numerical problems.

The power flux per unit area is given by Poynting's vector

$$\bar{P} = \frac{1}{2} \operatorname{Re} \bar{E}_{SI} \times \bar{H}_{SI}^* \quad (4.1-11)$$

where Re denotes the real part and * the complex conjugate. In normalised units Poynting's vector becomes

$$\bar{P} = k^2 \operatorname{Re} \bar{E} \times \bar{H}^* . \quad (4.1-12)$$

If a near field is known to behave approximately as a plane wave propagating in the direction \hat{z} (e.g. an aperture field) the plane wave relation $\bar{H} = \hat{z} \times \bar{E}$ can be used whereby Poynting's vector becomes

$$\bar{P} = k^2 |\bar{E}|^2 \hat{z} = k^2 |\bar{H}|^2 \hat{z} . \quad (4.1-13)$$

This relation can be useful for relating near field data to power flux.

4.1.2 Definition of far field

The far field is defined as the limit

$$\bar{E}_{far} = \lim_{r \rightarrow \infty} (\bar{E} kr e^{jkr}) \quad (4.1-14)$$

$$\bar{H}_{far} = \lim_{r \rightarrow \infty} (\bar{H} kr e^{jkr}) \quad (4.1-15)$$

where r is the distance from the origin of the coordinate system in which the fields \bar{E} and \bar{H} are calculated. The near field is a function of the location of the field point specified by three space coordinates, such as (x, y, z) or r, θ, ϕ . The far field is a function of direction and can thus be specified by two coordinates, e.g. θ, ϕ . It is seen that \bar{E}_{far} and \bar{H}_{far} have the same units, watt $^{1/2}$, as \bar{E} and \bar{H} . In GRASP units the plane wave relations for the far field become

$$\begin{aligned} \bar{E}_{far} &= \bar{H}_{far} \times \hat{r} \\ \bar{H}_{far} &= \hat{r} \times \bar{E}_{far} \end{aligned} \quad (4.1-16)$$

where \hat{r} is the radial unit vector. In an observation point far away from the antenna the power flux per unit area \bar{P} given by (4.1-12) reduces to

$$\bar{P} = k^2 |\bar{E}|^2 \hat{r} = k^2 |\bar{H}|^2 \hat{r} \quad (4.1-17)$$

because of the plane wave relations (4.1-16).

A useful quantity is the radiated power per unit solid angle, P_d , in the far field. It is seen that

$$P_d = \lim_{r \rightarrow \infty} (r^2 \bar{P} \cdot \hat{r}) \quad (4.1-18)$$

and that P_d is a function of the far-field direction. From (4.1-17) and (4.1-18) it is seen that

$$P_d = |\bar{E}_{far}|^2 = |\bar{H}_{far}|^2. \quad (4.1-19)$$

The directivity is defined by

$$\text{directivity} = 4\pi \frac{P_d}{P_{tot}} , \quad (4.1-20)$$

where P_{tot} is the total radiated power from the feed. As explained in Section 4.1.3 the feed power in GRASP is normalised to 4π watt, so that the directivity is related to the far field in GRASP units simply by

$$\text{directivity} = P_d = |\bar{E}_{far}|^2 = |\bar{H}_{far}|^2 . \quad (4.1-21)$$

4.1.3 Feed normalisation

The feed classes in GRASP calculate two vector functions, \bar{f}_E and \bar{f}_H , of the spherical $r\theta\phi$ -coordinates, such that the electric and magnetic near field are given by

$$\begin{aligned} \bar{E} &= \bar{f}_E(r, \theta, \phi) \frac{e^{-jkr}}{kr} \\ \bar{H} &= \bar{f}_H(r, \theta, \phi) \frac{e^{-jkr}}{kr} . \end{aligned} \quad (4.1-22)$$

The classes also calculate the far fields $\bar{E}_{far}(\theta, \phi)$ and $\bar{H}_{far}(\theta, \phi)$ which from the definitions (4.1-14) and (4.1-15) are related to \bar{f}_E and \bar{f}_H through

$$\begin{aligned}\bar{E}_{far}(\theta, \phi) &= \lim_{r \rightarrow \infty} \bar{f}_E(r, \theta, \phi) \\ \bar{H}_{far}(\theta, \phi) &= \lim_{r \rightarrow \infty} \bar{f}_H(r, \theta, \phi)\end{aligned}\quad (4.1-23)$$

where \bar{E}_{far} and \bar{H}_{far} satisfy the plane wave relations (4.1-16).

In the Geometrical Theory of Diffraction (see Section 3.6) it is an inherent assumption that the scatterer is located in the far field from the feed so that the only r -dependency of the incident field is through the factor $e^{-jkr}/(kr)$. When a feed is used as source in a GTD calculation the near field is therefore calculated by

$$\begin{aligned}\bar{E} &= \bar{E}_{far}(\theta, \phi) \frac{e^{-jkr}}{kr} \\ \bar{H} &= \bar{H}_{far}(\theta, \phi) \frac{e^{-jkr}}{kr}\end{aligned}\quad (4.1-24)$$

rather than (4.1-22).

The feeds are normalised to a total power of 4π watt which means that the total power P_{tot} becomes

$$P_{tot} = \iint_A |\bar{E}_{far}(\theta, \phi)|^2 d\omega = 4\pi \quad (4.1-25)$$

where $d\omega$ is a solid angle element and A denotes integration over the whole sphere. Since $d\omega = \sin \theta d\theta d\phi$ we have

$$P_{tot} = \int_0^{2\pi} \int_0^\pi |\bar{E}_{far}(\theta, \phi)|^2 \sin \theta d\theta d\phi = 4\pi \quad . \quad (4.1-26)$$

This normalisation is convenient since the feed directivity is then simply given by (4.1-21). For the plane wave model the normalisation is different since the far field is not defined, see Section 0.

When a source is specified as an array of N feeds the composite field from the array is calculated as the field from each of the feeds multiplied by a user specified excitation factor ε_i

$$\bar{E}(\bar{r}) = \sum_{i=1}^N \varepsilon_i \bar{E}_i(\bar{r}) . \quad (4.1-27)$$

where $\bar{E}_i(\bar{r})$ is the electric near field from feed No. i and $\bar{E}(\bar{r})$ is the total near field. The far field is calculated in the same way by

$$\bar{E}_{far}(\hat{r}) = \sum_{i=1}^N \varepsilon_i \bar{E}_{far, i}(\hat{r}) . \quad (4.1-28)$$

The excitation factor is complex and specified by its phase a_i and amplitude b_i

$$\varepsilon_i = b_i e^{ja_i} . \quad (4.1-29)$$

The total radiated power from the array of feeds becomes

$$P_{tot} = \iint_A \left| \bar{E}_{far}(\theta, \phi) \right|^2 \sin \theta d\theta d\phi \quad (4.1-30)$$

and if power coupling between the feeds can be neglected the radiated power can be calculated as

$$P_{tot} = 4\pi \sum_{i=1}^N b_i^2 \quad (4.1-31)$$

since each of the fields $\bar{E}_{far, i}(\bar{r})$ contains a power of 4π watt. If the user specifies the feed amplitudes such that

$$\sum_{i=1}^N b_i^2 = 1 \quad (4.1-32)$$

the feed array is normalised to a total power of 4π watt and the relation (4.1-21) between the antenna far field and directivity will be valid.

If the elements are closely spaced the power coupling cannot be neglected. Assume for example that an array consists of two identical half-wave dipoles. The amplitude excitation according to (4.1-32) becomes $1/\sqrt{2}$ for each element. If the dipoles are parallel and located close to each other the field at any point will be $2/\sqrt{2}$ times the radiation from a single dipole and the total radiated power will be $(2/\sqrt{2})^2 = 2$ times the power from a single dipole.

If the distance between the elements is larger than about 1.2λ the power coupling can normally be neglected. If this is not the case, a normalisation can be done in the following way: first, the radiation pattern from the feed array is calculated in a number of polar cuts containing the z -axis of the feed array coordinate system. These cuts are then input to the tabulated pattern feed model, see Section 2.3.1.1, which has the capability of normalising the input pattern.

4.1.4 Polarisation

In this section the polarisation convention used in GRASP is described. The near fields and far fields are treated separately because a near field has three vector components whereas a far field can be completely characterised by two transversal components. In the following only E-field polarisation is described, but all the different polarisation options are also available for the H-field.

4.1.4.1 Far fields

A far field has no radial component and may be decomposed along any two polarisation vectors \hat{e}_1 and \hat{e}_2 which are mutually orthogonal and also orthogonal to the far-field direction \hat{r}

$$\bar{E}_{far} = E_1 \hat{e}_1 + E_2 \hat{e}_2 . \quad (4.1-33)$$

The two polarisation vectors \hat{e}_1 and \hat{e}_2 are functions of the far-field direction θ, ϕ . The polarisation components can be calculated from

$$\begin{aligned} E_1 &= \bar{E}_{far} \cdot \hat{e}_1^* \\ E_2 &= \bar{E}_{far} \cdot \hat{e}_2^* . \end{aligned} \quad (4.1-34)$$

In the GRASP Post-processor the polarisation components can be displayed graphically in dB as

$$E_1 \text{ in dB} = 20 \log |E_1| . \quad (4.1-35)$$

From (4.1-21) it is seen that the polarisation components are related to the directivity by

$$\text{directivity} = |E_1|^2 + |E_2|^2 . \quad (4.1-36)$$

The different far-field polarisation options in GRASP are given through the definitions of \hat{e}_1 and \hat{e}_2 and will be explained in the following. All vectors are referred to the coordinate system in which the field is computed, namely the output coordinate system with unit vectors \hat{x} , \hat{y} and \hat{z} .

The most basic far-field polarisation, the $\theta\phi$ polarisation, is based on the spherical coordinates θ and ϕ with the polarisation components defined by

$$\bar{E}_{far} = E_\theta \hat{\theta} + E_\phi \hat{\phi} , \quad (4.1-37)$$

where $\hat{\theta}$ and $\hat{\phi}$ are the usual spherical unit vectors

$$\begin{aligned} \hat{\theta} &= \hat{x} \cos \theta \cos \phi + \hat{y} \cos \theta \sin \phi - \hat{z} \sin \theta \\ \hat{\phi} &= -\hat{x} \sin \phi + \hat{y} \cos \phi . \end{aligned} \quad (4.1-38)$$

The directions of the polarisations $\hat{\theta}$ and $\hat{\phi}$ are shown in Figure 4.1-1(a) in the region around the z -axis out to $\theta = 60^\circ$.

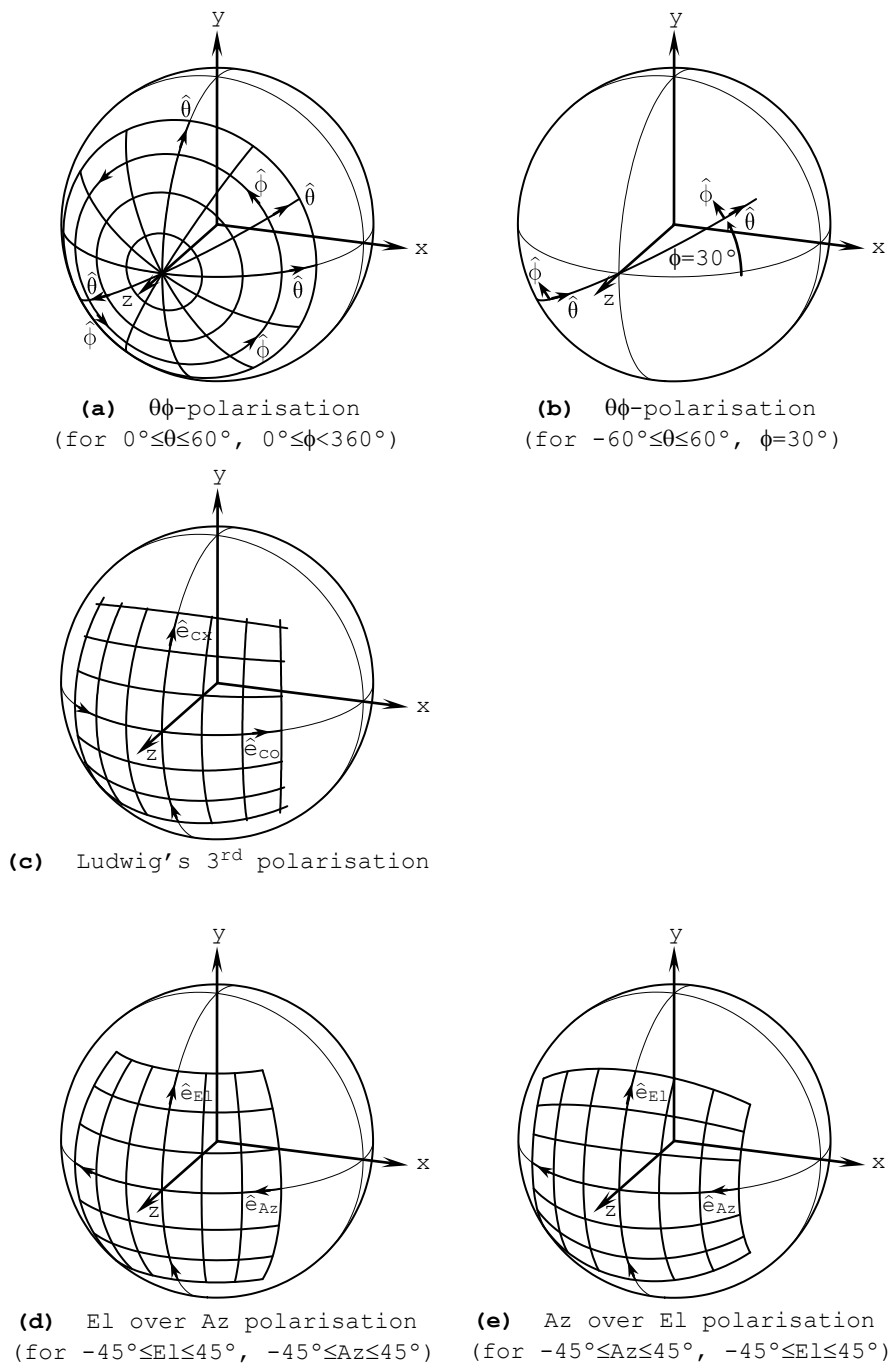


Figure 4.1-1 Polarisation directions on a sphere.

These $\theta\phi$ -components will be discontinuous through the point $\theta = 0^\circ$ (and $\theta = 180^\circ$) with the usual convention $0^\circ \leq \theta \leq 180^\circ$ for θ . To avoid this, a polar pattern cut (i.e. ϕ is constant and θ is varying) in GRASP may contain negative values of θ so that a cut may start at $\theta = -60^\circ$ and end at $\theta = +60^\circ$ passing through $\theta = 0^\circ$, cf. Figure 4.1-1(b). The value of ϕ is kept constant for all points in the cut ($\phi = 30^\circ$ in Figure 4.1-1(b)) so that the vectors (4.1-38) become continuous resulting in continuous polarisation components E_θ and E_ϕ . For contour plots containing $\theta = 0^\circ$ or $\theta = 180^\circ$ the components will, however, be discontinuous.

Linear polarisation is defined according to the so-called *Ludwig's 3rd definition* (Ludwig, 1973)

$$\bar{E}_{far} = E_{co}\hat{e}_{co} + E_{cx}\hat{e}_{cx} \quad (4.1-39)$$

with

$$\begin{aligned} \hat{e}_{co} &= \hat{\theta} \cos \phi - \hat{\phi} \sin \phi \\ \hat{e}_{cx} &= \hat{\theta} \sin \phi + \hat{\phi} \cos \phi . \end{aligned} \quad (4.1-40)$$

These vectors are continuous at $\theta = 0^\circ$ and the only pole is located at $\theta = 180^\circ$.

The polarisation directions \hat{e}_{co} and \hat{e}_{cx} are shown in Figure 4.1-1(c) in the region around the z -axis. On the z -axis the polarisations are parallel to x and y , respectively, and follow the shown lines which all pass through the point on the sphere for $\theta = 180^\circ$.

Two additional polarisation definitions are available in the Post Processor, *elevation over azimuth* and *azimuth over elevation*. These polarisation definitions are closely related to output grids of the same names, cf. Section 4.2.2.1, and have special relevance to measurement coordinate systems.

The *elevation over azimuth* polarisation is defined by

$$\bar{E}_{far} = E_{Az}\hat{e}_{Az} + E_{El}\hat{e}_{El} \quad (4.1-41)$$

with

$$\begin{aligned}\hat{e}_{Az} &= -\hat{x} \cos Az - \hat{z} \sin Az \\ \hat{e}_{El} &= \hat{x} \sin Az \sin El + \hat{y} \cos El - \hat{z} \cos Az \sin El .\end{aligned}\quad (4.1-42)$$

These polarisation directions follow the lines shown in Figure 4.1-1(d). The polarisation definition has poles on the y -axis. On the z -axis the azimuth polarisation is directed in the negative x direction while the elevation polarisation is directed in the positive y direction.

The *azimuth over elevation* polarisation is correspondingly defined by

$$\bar{E}_{far} = E_{Az}\hat{e}_{Az} + E_{El}\hat{e}_{El} \quad (4.1-43)$$

but now with

$$\begin{aligned}\hat{e}_{Az} &= -\hat{x} \cos Az - \hat{y} \sin Az \sin El - \hat{z} \sin Az \cos El \\ \hat{e}_{El} &= \hat{y} \cos El - \hat{z} \sin El .\end{aligned}\quad (4.1-44)$$

These polarisation directions follow the lines shown in Figure 4.1-1(e). This polarisation definition has poles on the x -axis. Again, on the positive z -axis the azimuth polarisation is directed along $-x$ while the elevation polarisation is directed along $+y$.

Right hand and left hand circular polarisation are defined by

$$\bar{E}_{far} = E_{rhc}\hat{e}_{rhc} + E_{lhc}\hat{e}_{lhc} , \quad (4.1-45)$$

based on \hat{e}_{co} and \hat{e}_{cx} from (4.1-40)

$$\begin{aligned}\hat{e}_{rhc} &= \frac{1}{\sqrt{2}}(\hat{e}_{co} - j\hat{e}_{cx}) \\ \hat{e}_{lhc} &= \frac{1}{\sqrt{2}}(\hat{e}_{co} + j\hat{e}_{cx}) .\end{aligned}\quad (4.1-46)$$

From these components the *major and minor axes of the polarisation ellipse* can be computed by

$$\begin{aligned} r_{major} &= \frac{1}{\sqrt{2}} \|E_{rhc}| + |E_{lhc}\| \\ r_{minor} &= \frac{1}{\sqrt{2}} \|E_{rhc}| - |E_{lhc}\| \end{aligned} . \quad (4.1-47)$$

Note that

$$\text{directivity} = r_{major}^2 + r_{minor}^2 . \quad (4.1-48)$$

Furthermore, the *tilt angle of the polarisation ellipse* can be computed as the phase of the complex number $\sqrt{E_{rhc}/E_{lhc}}$.

The ratio between two polarisation components is often of interest for satellite communications antennas. This ratio is called *cross-polarisation discrimination* (XPD) and the following types are available in GRASP.

$$\theta\phi\text{-XPD: } E_\theta / E_\phi \text{ and } E_\phi / E_\theta \quad (4.1-49)$$

$$\text{linear-XPD: } E_{co} / E_{cx} \text{ and } E_{cx} / E_{co} \quad (4.1-50)$$

$$\text{circular-XPD: } E_{rhc} / E_{lhc} \text{ and } E_{lhc} / E_{rhc} \quad (4.1-51)$$

$$\text{major-minor-XPD: } r_{major} / r_{minor} \text{ and } r_{minor} / r_{major} \quad (4.1-52)$$

In the Post Processor also an azimuth-elevation XPD may be determined. This is calculated as

$$\text{Az-El-XPD: } E_{Az} / E_{El} \text{ and } E_{El} / E_{Az} \quad (4.1-53)$$

independently of whether E_{Az} and E_{El} are defined according to (4.1-41) or (4.1-43).

A special polarisation type called the *power component* is also available and defined by

$$E_{power} = |\bar{E}_{far}| . \quad (4.1-54)$$

It is seen from (4.1-21) that the square of E_{power} equals the directivity.

4.1.4.2 Near fields

A near field can be decomposed in three general, mutually orthogonal vector components as

$$\bar{E} = E_1 \hat{e}_1 + E_2 \hat{e}_2 + E_3 \hat{e}_3 . \quad (4.1-55)$$

The three polarisation vectors \hat{e}_1 , \hat{e}_2 and \hat{e}_3 are functions of the near-field point. The polarisation components can be calculated from

$$\begin{aligned} E_1 &= \bar{E} \cdot \hat{e}_1^* \\ E_2 &= \bar{E} \cdot \hat{e}_2^* . \\ E_3 &= \bar{E} \cdot \hat{e}_3^* \end{aligned} \quad (4.1-56)$$

The near-field in GRASP can be calculated as a set of points on a sphere, on a circular cylinder or as points on a plane as described in Section 4.2. The available polarisation components are different in each case which will therefore be described separately in the following.

4.1.4.2.1 Near-field points on a sphere

The $r\theta\phi$ -components are defined by

$$\bar{E} = E_\theta \hat{\theta} + E_\phi \hat{\phi} + E_r \hat{r} , \quad (4.1-57)$$

where \hat{r} , $\hat{\theta}$ and $\hat{\phi}$ are the usual spherical unit vectors

$$\begin{aligned} \hat{r} &= \hat{x} \sin \theta \cos \phi + \hat{y} \sin \theta \sin \phi + \hat{z} \cos \theta \\ \hat{\theta} &= \hat{x} \cos \theta \cos \phi + \hat{y} \cos \theta \sin \phi - \hat{z} \sin \theta . \\ \hat{\phi} &= -\hat{x} \sin \phi + \hat{y} \cos \phi \end{aligned} \quad (4.1-58)$$

Linear polarisation is defined similarly to the far-field definition but now includes a radial component

$$\bar{E} = E_{co} \hat{e}_{co} + E_{cx} \hat{e}_{cx} + E_r \hat{r} \quad (4.1-59)$$

with unit vectors defined according to Ludwig's 3rd definition (Ludwig, 1973)

$$\begin{aligned}\hat{e}_{co} &= \hat{\theta} \cos \phi - \hat{\phi} \sin \phi \\ \hat{e}_{cx} &= \hat{\theta} \sin \phi + \hat{\phi} \cos \phi\end{aligned}. \quad (4.1-60)$$

and \hat{r} as in (4.1-58).

Right hand and left hand circular polarisations are defined on the basis of these linear components:

$$\bar{E} = E_{rhc}\hat{e}_{rhc} + E_{lhc}\hat{e}_{lhc} + E_r\hat{r}, \quad (4.1-61)$$

where

$$\begin{aligned}\hat{e}_{rhc} &= \frac{1}{\sqrt{2}}(\hat{e}_{co} - j\hat{e}_{cx}) \\ \hat{e}_{lhc} &= \frac{1}{\sqrt{2}}(\hat{e}_{co} + j\hat{e}_{cx})\end{aligned} \quad (4.1-62)$$

and \hat{r} as in (4.1-58).

The major and minor axes and tilt angle of the polarisation ellipse is computed as in Section 4.1.4.1 for the far field. Also the various XPD options are calculated as for the far field.

For near-field points the special polarisation type called the power component is defined as the power in all three field components,

$$E_{power} = |\bar{E}|. \quad (4.1-63)$$

From (4.1-13) it is seen that if the near field behaves approximately as a plane wave E_{power} is related to Poynting's vector \bar{P} by

$$|\bar{P}| \cong k^2 E_{power}^2. \quad (4.1-64)$$

4.1.4.2.2 Near-field points on a circular cylinder

The field is decomposed in cylindrical coordinates with the unit vectors $\hat{\phi}$, \hat{z} and \hat{r}

$$\begin{aligned}\hat{\phi} &= -\hat{x} \sin \phi + \hat{y} \cos \phi \\ \hat{\rho} &= \hat{x} \cos \phi + \hat{y} \sin \phi\end{aligned}. \quad (4.1-65)$$

Linear polarisation is defined as the two field components tangential to the surface of the cylinder, $E_{co} = E_\phi$ and $E_{cx} = E_z$, and the field along the surface normal, E_ρ ,

$$\bar{E} = E_{co}\hat{\phi} + E_{cx}\hat{z} + E_\rho\hat{\rho} . \quad (4.1-66)$$

Hence the right hand and left hand circular polarisations are defined by

$$\bar{E} = E_{rhc}\hat{e}_{rhc} + E_{lhc}\hat{e}_{lhc} + E_\rho\hat{\rho} , \quad (4.1-67)$$

where

$$\begin{aligned}\hat{e}_{rhc} &= \frac{1}{\sqrt{2}}(\hat{e}_{co} - j\hat{e}_{cx}) = \frac{1}{\sqrt{2}} \hat{\phi} - j\hat{z} \\ \hat{e}_{lhc} &= \frac{1}{\sqrt{2}}(\hat{e}_{co} + j\hat{e}_{cx}) = \frac{1}{\sqrt{2}} \hat{\phi} + j\hat{z}\end{aligned}. \quad (4.1-68)$$

The major and minor axes and tilt angle of the polarisation ellipse is computed as in Section 4.1.4.1 for the far field.

The XPD options for linear, circular and major-minor are calculated as (4.1-50) through (4.1-52), and the power is given by (4.1-63).

4.1.4.2.3 Near-field points on a plane

The $\rho\phi$ -components are defined by

$$\bar{E} = E_\rho\hat{\rho} + E_\phi\hat{\phi} + E_z\hat{z} , \quad (4.1-69)$$

where $\hat{\rho}$, $\hat{\phi}$ and \hat{z} are the cylindrical unit vectors given by (4.1-65).

The linear polarisation components are defined simply by

$$\bar{E} = E_{co}\hat{x} + E_{cx}\hat{y} + E_z\hat{z} \quad (4.1-70)$$

and right hand and left hand circular polarisations are again defined from the linear components by

$$\bar{E} = E_{rhc}\hat{e}_{rhc} + E_{lhc}\hat{e}_{lhc} + E_z\hat{z} \quad , \quad (4.1-71)$$

where

$$\begin{aligned} \hat{e}_{rhc} &= \frac{1}{\sqrt{2}} (\hat{e}_{co} - j\hat{e}_{cx}) = \frac{1}{\sqrt{2}} (\hat{x} - j\hat{y}) \\ \hat{e}_{lhc} &= \frac{1}{\sqrt{2}} (\hat{e}_{co} + j\hat{e}_{cx}) = \frac{1}{\sqrt{2}} (\hat{x} + j\hat{y}) \end{aligned} . \quad (4.1-72)$$

The major and minor axes and tilt angle of the polarisation ellipse is computed as in Section 4.1.4.1 for the far field.

The XPD options for linear, circular and major-minor XPD are calculated as (4.1-50) through (4.1-52) and the new $\rho\phi$ -XPD is given by

$$\rho\phi\text{-XPD: } E_\rho / E_\phi \text{ and } E_\phi / E_\rho . \quad (4.1-73)$$

Finally, the power is calculated from (4.1-63).

4.1.4.2.4 Example illustrating near-field normalisation

In this example we show how the near field computed by GRASP can be related to the radiated power.

A parabolic offset system is considered with diameter 0.5 m, focal length 0.5 m and offset distance 0.3 m as shown in Figure 4.1-2. The feed is linearly polarised in the antennas symmetry plane.

The analysis is carried out with a wavelength of $\lambda = 0.01$ m in the near field from the main reflector and the results are shown in Figure 4.1-3. The two cuts are located in a plane at a distance of 0.25 m in front of the aperture centre and orthogonal to the beam direction. A cut coordinate system is displayed in Figure 4.1-2 of which the x_s - and y_s -axis point along the two cuts. The polarisation component in Figure 4.1-3 is the so-called power component (explained in the preceding section)

which in this case is very similar to the linear co-component in the cut coordinate system.

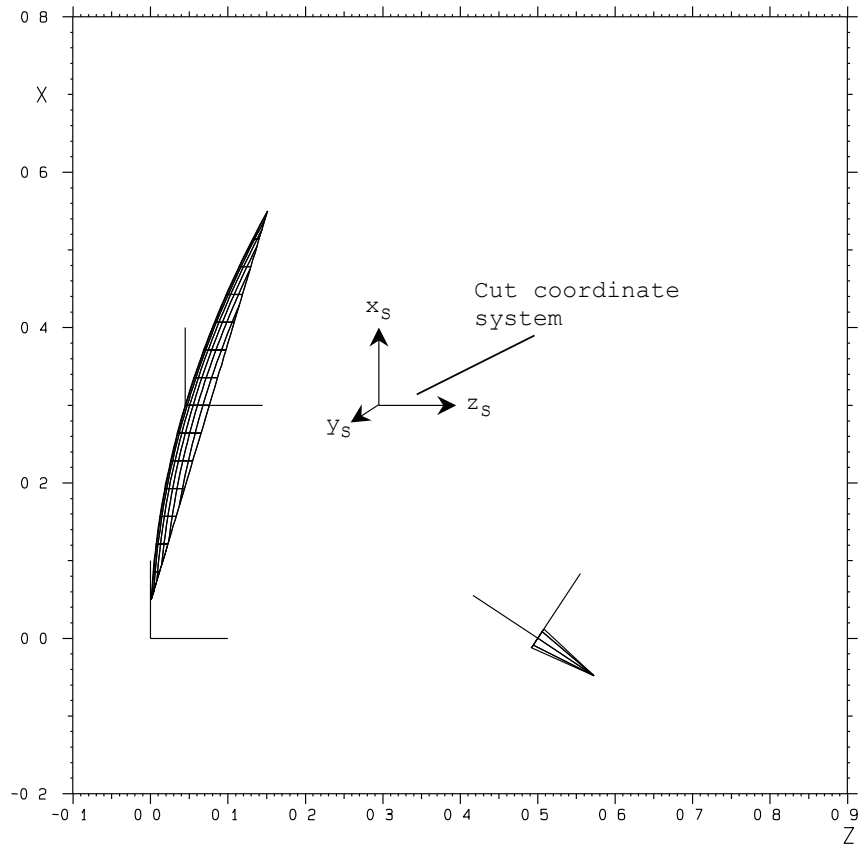


Figure 4.1-2 Offset single reflector system.

It is seen that the power component in dB, $E_{power,dB}$, inside the aperture varies from approximately -50 to -33 dB which can be converted to linear scale through

$$E_{power,dB} = 20 \log E_{power} \quad (4.1-74)$$

and to power flux using (4.1-64). For example the value -40 dB corresponds to $E_{power} = 0.01 \text{ watt}^{1/2}$ and to a power flux of 39.48 watt/m².

An ideal aperture field as predicted by geometrical optics would be uniform inside the aperture and zero outside. In this case the power flux inside the aperture can easily be calculat-

ed as the feed power divided by the area of the aperture. This gives

$$\text{power flux} = |\bar{P}| = \frac{4\pi \text{ watt}}{\pi r^2} = 64.0 \text{ watt/m}^2 \quad (4.1-75)$$

where $r = 0.25 \text{ m}$ is the aperture radius. A feed power of 4π watt is the default in GRASP as explained in Section 4.1.3. From (4.1-64) the value of E_{power} can be computed and its value in dB becomes -37.90 dB.

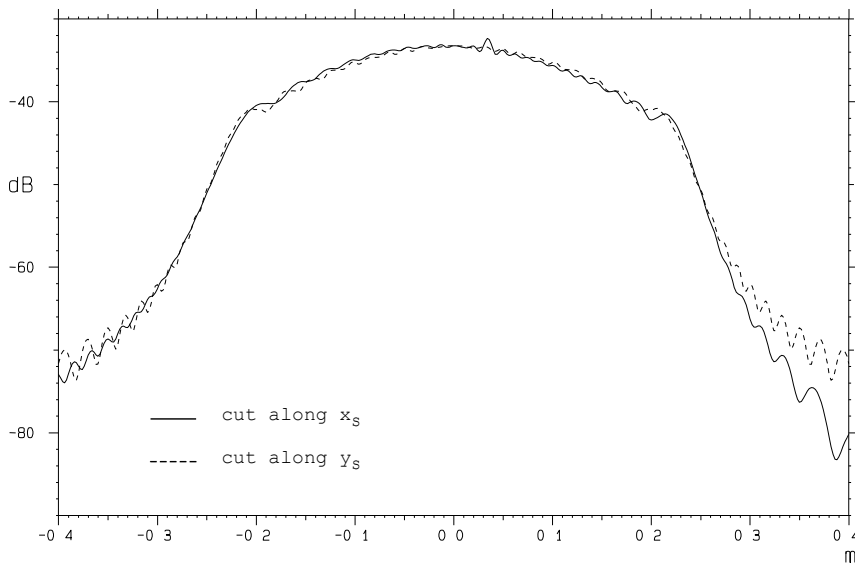


Figure 4.1-3 Near field.

It must be noted that this simple conversion between E_{power} and power flux is only valid when it can be assumed that the near field behaves approximately as a plane wave.

4.1.4.3 Redefinition of the polarisation components

The locations of the calculated field points are defined by the output coordinate system as described in Section 4.2 and in most cases this coordinate system is also used to define the polarisation components. However, sometimes it is preferable to refer the polarisation components to another coordinate sys-

tem. This option is available for output points located in spherical cuts or spherical grids

A typical example of the application of the polarisation coordinate system is illustrated in Figure 4.1-4. A shaped beam has been designed for the coverage of North America and the polarisation is assumed to be linear in a coordinate system with the z -axis pointing towards the centre of the Earth. It may be desirable to calculate some additional cuts through the centre of the beam as shown on the figure and this can be done using an output coordinate system with the z -axis in the direction of this point. However, the polarisation options in this coordinate system will be different from the original polarisation requirement. In order to solve this a special polarisation coordinate system is introduced such that the location of the field points are specified in the output coordinate system but the polarisation components are referred to the polarisation coordinate system. For the example in Figure 4.1-4 the polarisation coordinate system is selected such that the z -axis points towards the centre of the Earth.

Another example where the polarisation coordinate system is useful is when the *elevation over azimuth* and *azimuth over elevation* polarisations, as defined by (4.1-41) and (4.1-43), are considered. These polarisation components can also be obtained from the $\theta\phi$ -components of a polarisation coordinate system where the z -axis is directed along the y -axis and x -axis, respectively, of the output coordinate system. This is clearly seen from Figure 4.1-1. More specifically we have

$$\begin{aligned}\hat{e}_{Az} &= -\hat{\phi} \\ \hat{e}_{El} &= -\hat{\theta}\end{aligned}\tag{4.1-76}$$

for *elevation over azimuth* polarisation and

$$\begin{aligned}\hat{e}_{Az} &= \hat{\theta} \\ \hat{e}_{El} &= -\hat{\phi}\end{aligned}\tag{4.1-77}$$

for *azimuth over elevation* polarisation.

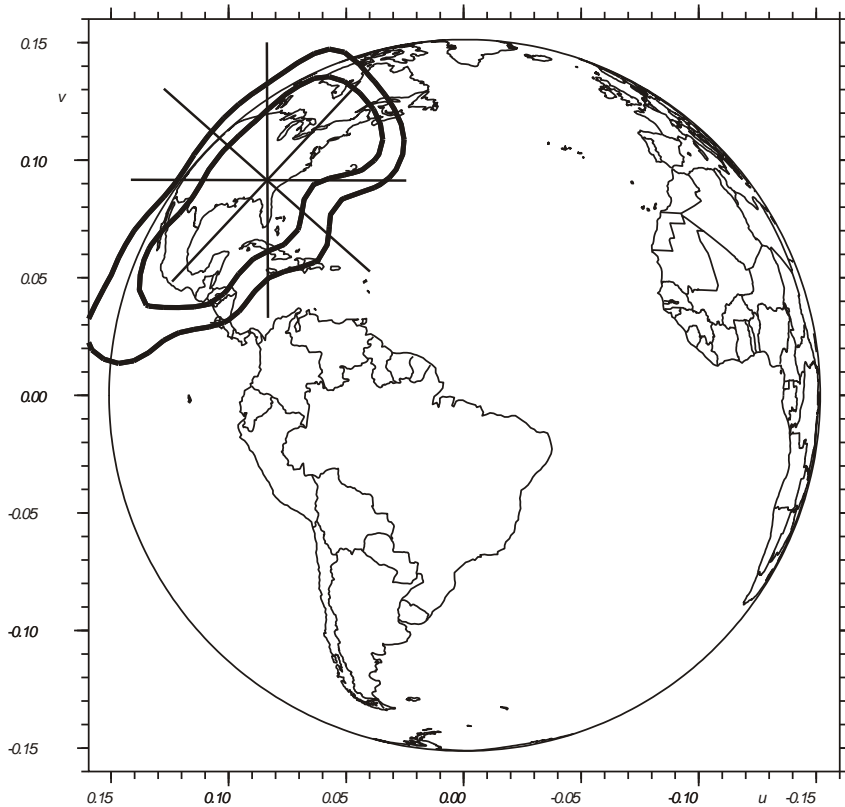


Figure 4.1-4 Shaped beam example illustrating the application of the polarisation coordinate system.

4.2 Output points

This section describes the various possibilities for the location of the output points in GRASP. The two most common options are the one-dimensional pattern cuts and the two-dimensional field grids as presented in the following two sections. It is also possible to calculate the far field at a set of irregularly distributed directions and finally the field can be evaluated directly at the surface of the scatterers.

The output points are specified relative to a user-defined coordinate system, in the following called the output coordinate system, $x_o y_o z_o$. The number of different output objects and output coordinate systems is unlimited.

It is in general preferable to select the origin of the output coordinate system near the expected phase centre of the calculated results. This will improve the interpolation techniques described in Section 4.3.

The plotting facilities in GRASP can also be used to visualise the output points. Near-field points are plotted at their actual position whereas far-field points are plotted at a distance from the output coordinate system origin specified by the user.

4.2.1 One-dimensional cuts

Three types of pattern cuts are available, spherical cuts, cylindrical cuts and planar cuts. The spherical and the planar cuts are illustrated in Figure 4.2-1, the cylindrical cuts in Figure 4.2-2.

The spherical pattern cuts can be used for far-field as well as near-field points and both polar and conical cuts can be specified. Polar cuts are great circles through the z_o -axis, i.e. θ varies for fixed ϕ . Conical cuts are small circles orthogonal to the z_o -axis, i.e. ϕ varies for constant θ .

The cylindrical and the planar pattern cuts are only available for near-field points. The planar cuts are positioned in the plane $z_o = z_d$. Radial and circular cuts are specified similarly to the polar and conical cuts for the spherical case.

The cylindrical pattern cuts follow the usual circular cylindrical coordinate system, i.e. the cuts may be axial cuts parallel to the axis of the cylinder or circular cuts, which are perpendicular to the axis. It shall be noted that the output coordinate system is oriented with the z_o -axis along the axis of the cylinder. Cylindrical cuts are thus best suited for antennas which radiate mainly in the x_oy_o -plane.

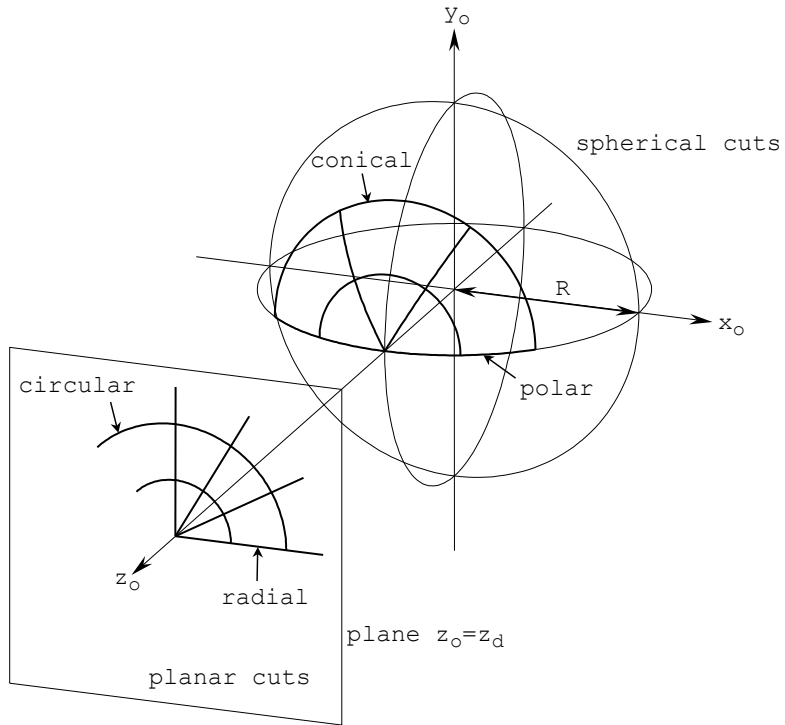


Figure 4.2-1 Spherical and planar pattern cuts.

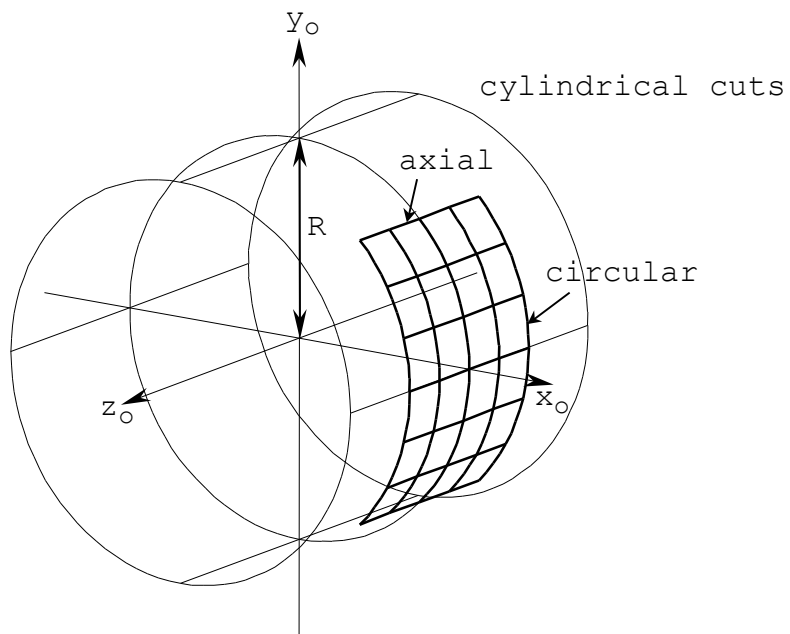


Figure 4.2-2 Cylindrical pattern cuts.

4.2.2 Two-dimensional grids

The two-dimensional grids are available in three forms: spherical for both near-field and far-field points and cylindrical and planar for near-field points only.

4.2.2.1 Spherical grids

For the spherical grids five types of output coordinates are available: 1) uv , 2) $\theta\phi$, 3) *elevation over azimuth*, 4) *elevation and azimuth*, and 5) *azimuth over elevation*. The five types of grids are illustrated in Figure 4.2-3 for approximately the same angular region on the sphere. When a near field on a sphere is requested the user must specify the radius R of the sphere whereas the centre is assumed to be the origin of the $x_0y_0z_0$ -coordinate system. The grids are specified by the minimum and maximum value and the number of points for each of the two grid coordinates.

The most well-known grid is the standard spherical $\theta\phi$ -grid. In this grid the unit vector to the field point is given by

$$\hat{r} = \sin \theta \cos \phi, \sin \theta \sin \phi, \cos \theta \quad (4.2-1)$$

in the output coordinate system, $x_0y_0z_0$.

The field components in directions of $\hat{\theta}$ and $\hat{\phi}$ are defined in Section 4.1.4 on polarisation.

The uv -coordinates are related to the spherical coordinates θ and ϕ by

$$\begin{aligned} u &= \sin \theta \cos \phi \\ v &= \sin \theta \sin \phi \end{aligned}, \quad (4.2-2)$$

and the unit vector to the field point at (u, v) is given by

$$\hat{r} = u, v, \sqrt{1 - u^2 - v^2} \quad . \quad (4.2-3)$$

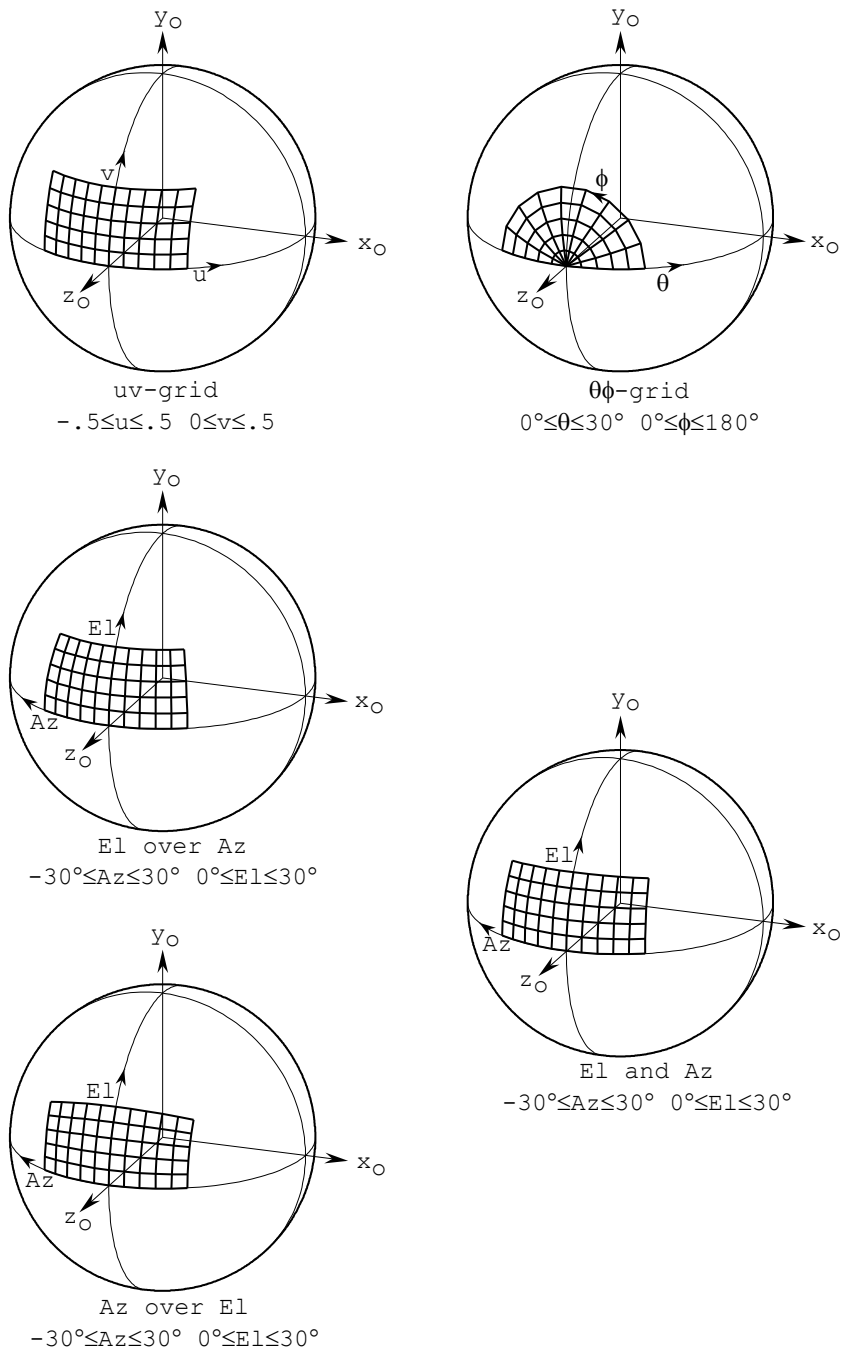


Figure 4.2-3 Spherical two-dimensional output grids.

It is seen that this grid, upon projection on a plane orthogonal to the z_O -axis, will appear as a rectangular grid. All the grids

are generated with equidistant spacing in the applied coordinates, here u and v . Due to the projection in (4.2-2), all points (u, v) are confined to the area within the unit circle

$$u^2 + v^2 \leq 1 \quad (4.2-4)$$

and the grid should not be used for $\theta > 90^\circ$. See also the comments at the end of the present section.

For the *elevation over azimuth* coordinates, El over Az , the unit vector to the field point is given by

$$\hat{r} = (-\sin Az \cos El, \sin El, \cos Az \cos El) . \quad (4.2-5)$$

The grid name, *elevation over azimuth*, is associated with a positioning system where the horizontal elevation axis is mounted above the vertical azimuth axis. When the positioner is rotated an angle Az around the vertical axis and an angle El around the horizontal axis it is pointing in the direction indicated by \hat{r} in (4.2-5).

Points of constant Az will lie in planes containing the y_0 -axis and points of constant El will line in planes that are orthogonal to the y_0 -axis.

It is important to note the difference between the above definition, which applies to the location of a field point, and a measurement set-up involving an *elevation over azimuth* positioner. In such a measurement facility the antenna under test is mounted on the positioner. When the positioner rotates, it is the direction of the antenna axis that is described by (4.2-5) and NOT the location of the point where the field is measured by the probe. In fact, it can be shown that the field point moves in an *azimuth over elevation* grid (see below) relative to the antenna, and as such the measurement data should be compared to predictions made in the *azimuth over elevation* grid. Vice versa, measurements made on an *azimuth over elevation* positioner should be compared to an analysis in an *elevation over azimuth* grid.

The *azimuth over elevation* coordinates are similar to the *elevation over azimuth* coordinates. The unit vector to the field point is

$$\hat{r} = (-\sin Az, \cos Az \sin El, \cos Az \cos El) . \quad (4.2-6)$$

The vertical azimuth axis is now located on top of the horizontal elevation axis. The points of constant *El* will lie in planes containing the x_o -axis and the points of constant *Az* will lie in planes orthogonal to the x_o -axis.

The *elevation and azimuth* coordinates is a mixture of the two preceding options and defined by

$$\begin{aligned} Az &= -\theta \cos \phi \\ El &= \theta \sin \phi \end{aligned} . \quad (4.2-7)$$

Apart from the sign of the first coordinate, this grid also resembles the *uv*-grid, Eq. (4.2-2), especially for small values of θ .

From (4.2-7) it is seen that

$$\theta = \sqrt{Az^2 + El^2} \quad (4.2-8)$$

and insertion in the general (4.2-1) yields for the unit vector to the field point given by (Az, El)

$$\hat{r} = \left(-Az \frac{\sin \theta}{\theta}, El \frac{\sin \theta}{\theta}, \cos \theta \right) . \quad (4.2-9)$$

In all the output grids the coordinate set $(0,0)$ represents the direction of the z_o -axis. Further, the grid spacing is equidistant in the specified grid coordinates.

A special option, which is particularly useful for the analysis of the element beams of a multibeam reflector antenna, is to specify a beam centre direction for each beam. This feature is illustrated in the following and exemplified by *uv*-coordinates. The field is calculated separately for each of the feeds, but the grid point number (i, j) of the *uv*-grid for feed number ℓ is translated by u_ℓ, v_ℓ so that

$$u_i = u'_\ell + u_{\min} + d_u \cdot i - 1 \quad (4.2-10)$$

$$v_i = v'_\ell + v_{\min} + d_v \cdot j - 1 \quad (4.2-11)$$

where i and j run through all the grid points and d_u and d_v are the spacings in the u - and v -directions, respectively. The translation u'_ℓ, v'_ℓ is defined by

$$u'_\ell = d_u \cdot \text{nint } u_\ell / d_u \quad (4.2-12)$$

$$v'_\ell = d_v \cdot \text{nint } v_\ell / d_v , \quad (4.2-13)$$

where u_ℓ and v_ℓ are user specified and the function $\text{nint}(x)$ gives the nearest integer to x . It is seen that the definition (4.2-12) and (4.2-13) of the translation ensures that the grid (4.2-10) and (4.2-11) is translated an integer number of grid spacings so that the fields from the different feeds can be added prior to interpolation by post-processing tools. The option described above is normally applied to translate the uv -grid to the centre of the beam for feed No. ℓ by specifying u_ℓ, v_ℓ as the centre direction for beam No. ℓ .

The output grid re-direction, illustrated above for the uv -coordinates, is valid for all the output options in Figure 4.2-3, but for the $\theta\phi$ -grid it will only be useful in special cases.

As a default, the field is calculated at all the grid points in the rectangular area defined by the maximum and minimum values of the two coordinates. It is also possible, however, to truncate the grid points to an elliptical area where the two axes are identical to the ranges for the rectangular area. This possibility is especially useful for a uv -grid where the maximum values are close to +1 or -1. In this case $u^2 + v^2$ could be larger than 1 unless the elliptical truncation is applied.

4.2.2.2 Cylindrical grid

The cylindrical grid consists of points spaced equidistantly in ϕ and z_o on a circular cylinder of radius R , Figure 4.2-4. ϕ is

the conventional azimuth angle. The vector to a grid point is then given in the output coordinate system by

$$x_o, y_o, z_o = R \cos \phi, R \sin \phi, z_o . \quad (4.2-14)$$

The field components in directions of the cylinder coordinates $\hat{\phi}$ and \hat{z} are defined in Section 4.1.4.2.

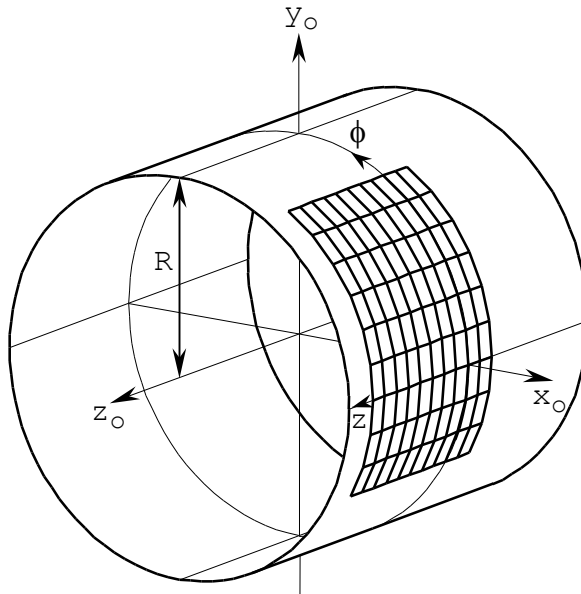


Figure 4.2-4 Cylindrical output grid, $-0.2m \leq z \leq 0.8m$, $-30^\circ \leq \phi \leq 60^\circ$ (a full cylinder is drawn for $-1m \leq z_o \leq 1m$).

4.2.2.3 Planar grid

Two planar grids are possible, an xy -grid and a $\rho\phi$ -grid. Both grids are placed in the plane given by a constant z_o -value, $z_o = z_d$, cf. Figure 4.2-5.

In the xy -grid the field points are spaced equidistantly in x_o and y_o in the output coordinate system.

In the $\rho\phi$ -grid the field points are spaced equidistantly in ρ and ϕ and a vector to a field point is then given by

$$x_o, y_o, z_o = \rho \cos \phi, \rho \sin \phi, z_d . \quad (4.2-15)$$

The field components in directions of the planar coordinates \hat{x} and \hat{y} or $\hat{\rho}$ and $\hat{\phi}$ are defined in Section 4.1.4.2.

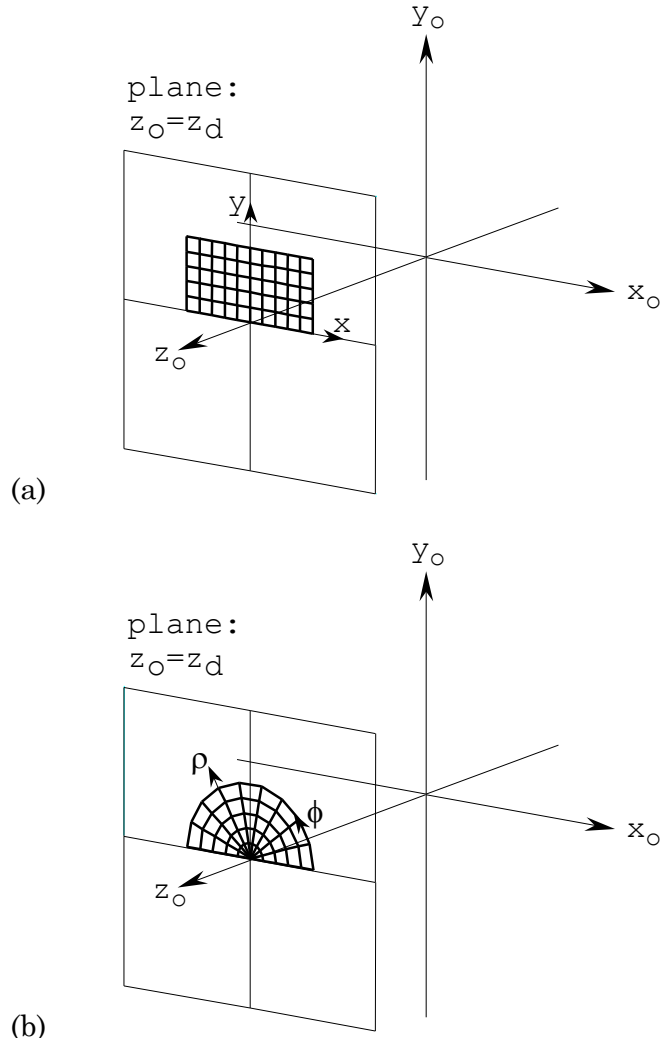


Figure 4.2-5 Planar output grids in the plane $z_o = z_d$.

(a) xy -grid for $-0.5m \leq x \leq 0.5m$,

$0m \leq y \leq 0.5m$; $x = x_o$ and $y = y_o$.

(b) $\rho\phi$ -grid for $0 \leq \rho \leq 0.5 m$, $0^\circ \leq \phi \leq 180^\circ$.

4.2.3 Irregularly spaced output points

It is possible to calculate the field at a number of irregularly distributed stations. This can for example be useful in order to check the performance of an antenna for the major cities of a large geographical area. The station positions must be given by their uv -coordinates and only far-field points are allowed.

4.2.4 Surface points and aperture fields

It is sometimes of interest to calculate the field directly at the surface of a scatterer. The points on the scatterer can be arranged as one-dimensional cuts or two-dimensional grids as described in the following subsections.

The field quantity on the surface can be

- the incident electric field
- the reflected electric field
- the incident magnetic field
- the reflected magnetic field
- the PO currents

The calculated field vectors at points on the surface of the scatterer will be resolved in components according to the axes of a special polarisation coordinate system defined by the user. When the axes of this coordinate system are directed along \hat{x} , \hat{y} and \hat{z} the available field polarisations are the same as those presented in Section 4.1.4.2 for near-field points on a plane, cf. Eqs. (4.1-69) ff. Thus, the components are not necessarily parallel to the surface of the scatterer. Both the incident and reflected, electric or magnetic field components may be determined as well as the electric current on the surface. Also the current is given in the mentioned components.

The above described analysis features are only implemented for ordinary reflectors and flat plates, but not for struts and reflectors with panels.

4.2.4.1 One-dimensional surface cuts

The surface cuts are defined in the coordinate system of the scatterer and they can be radial or circular, as illustrated in Figure 4.2-6 for an offset reflector. It is possible to offset the centre of the cuts by the distances x_0 and y_0 which are measured relative to the rim centre of the scatterer. Figure 4.2-6 also shows that only those points which actually fall inside the reflector rim will be included in the surface field calculation.

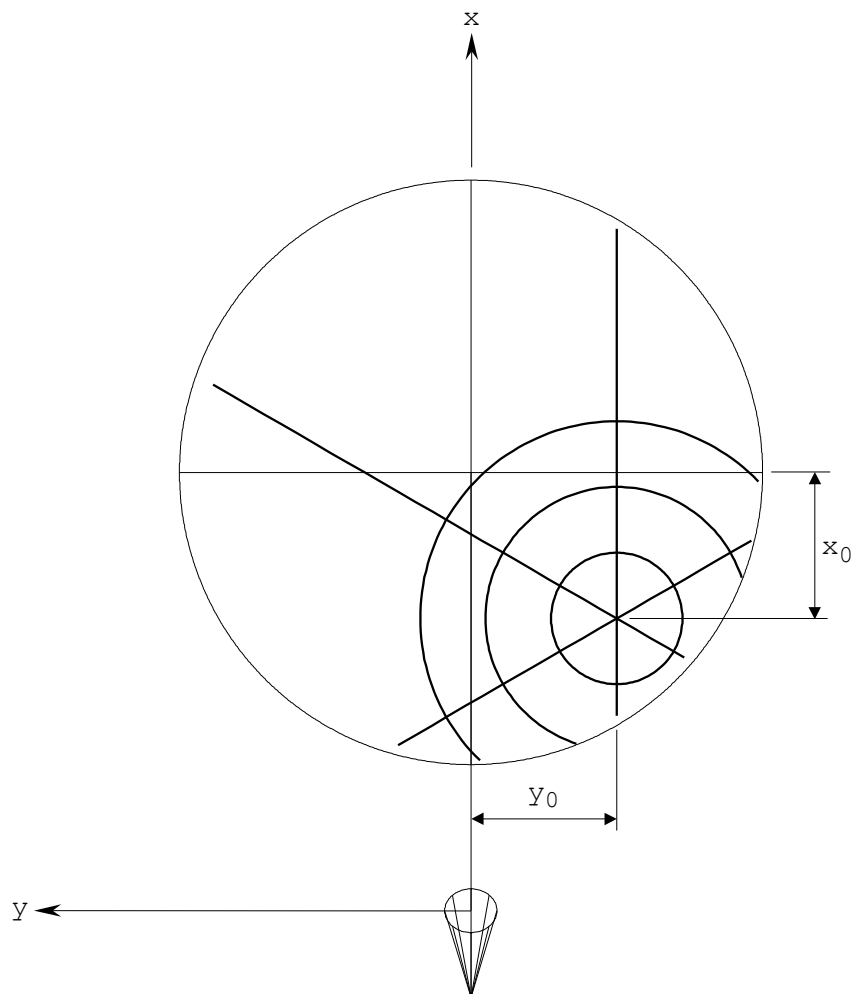


Figure 4.2-6 Radial and circular surface cuts for an offset reflector.

4.2.4.2 Two-dimensional surface grids

The surface points can be specified as a two-dimensional grid in x and y of the coordinate system of the scatterer. The offset of the centre point for the surface cut option is not available here.

4.2.4.3 Aperture fields

The phase of the surface field may be transformed to a plane such that an aperture field is generated. The principle is illustrated in Figure 4.2-7. For each grid point the phase is modified by the factor e^{-jkd} , where d is the distance from the point to the $x_p y_p$ -plane of the polarisation coordinate system. The aperture field defined in this way is very useful for the investigation of shaped beam antennas or antennas with scanned beams.

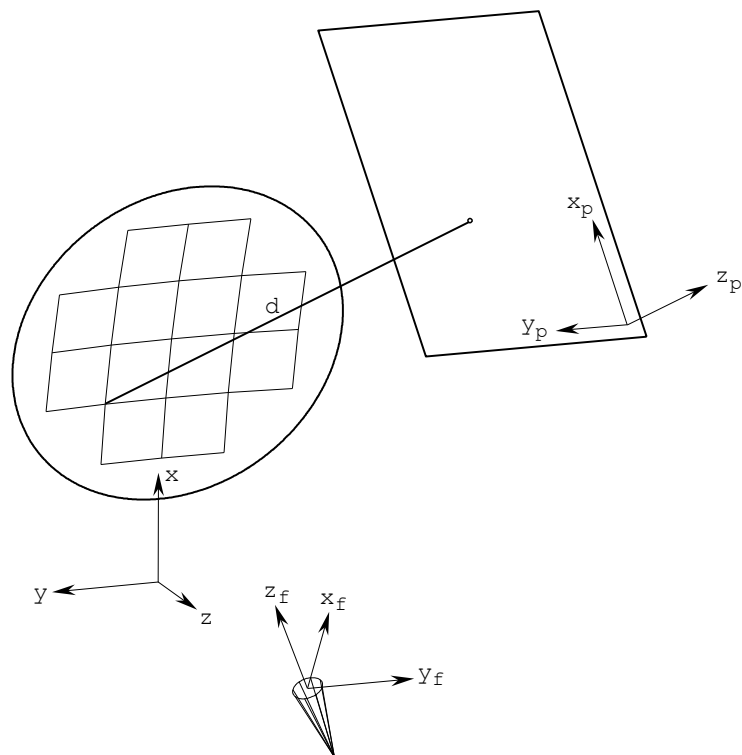


Figure 4.2-7 Offset reflector with two-dimensional surface grid points. The phase is transformed to the $x_p y_p$ -plane of the polarisation coordinate system.

4.3 Interpolation techniques

Two types of interpolation techniques are used in GRASP. Cubic interpolation is used to define a smooth surface between the node points of numerically given reflectors and to expand calculated field patterns in the postprocessor. Whittaker interpolation is an efficient technique to interpolate a field pattern near the main beam region. A survey of these techniques will be given in the following two sections.

4.3.1 Cubic interpolation

The cubic interpolation is a third order interpolation using two second-order Lagrange polynomials and four local sampling

points. The idea of the method is illustrated in Figure 4.3-1, where four equally spaced sample points are shown.

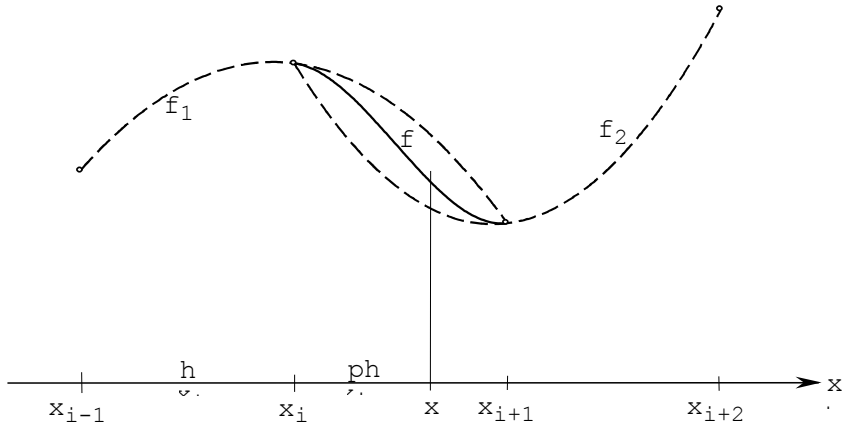


Figure 4.3-1 Cubic interpolation.

The two parabolas $f_1(x)$ and $f_2(x)$ are defined by the first three and by the last three points, respectively, as shown by the dotted lines in the figure. The interpolated value at the point x between x_i and x_{i+1} is given by a linear weighting of the two parabolas, according to the distance to the end points of the interval:

$$f(x_i + ph) = 1 - p f_1(x) + pf_2(x) , \quad (4.3-1)$$

where h is the distance between the input points.

The function f is shown in full line in Figure 4.3-1. In the first and in the last sample intervals only second order interpolation is employed by using the parabolas f_1 and f_2 , respectively.

The cubic interpolation function is identical to the Lagrange third order interpolation formula at $p = 0.5$. The error is near the maximum in the middle of the interval and it is therefore the same as for the Lagrange interpolation, namely proportional to h^4 .

When the cubic interpolation is used for surface representation it is crucial that not only the interpolating function $f(x)$

itself but also the first and second order derivatives are continuous across a node point. A continuous first order derivative is required for the PO currents to be continuous, and to ensure that GO ray tracing can be carried out properly. The second order derivatives must be continuous to avoid discontinuities in the GO and GTD field levels. However, (4.3-1) has discontinuous second order derivatives at the node points, for which reason it is approximated by $g(p)$ given by

$$g(p) = s_i(1-p) + s_{i+1}p \quad (4.3-2)$$

where

$$s_k = \frac{1}{h} \left[\frac{f(x_{k+1}) - f(x_k)}{h} - \frac{f(x_k) - f(x_{k-1})}{h} \right]. \quad (4.3-3)$$

Cubic interpolation in a double grid is illustrated in Figure 4.3-2. First, four interpolated values are determined by interpolation in the y -direction along the four grid lines x_{i-1} , x_i , x_{i+1} and x_{i+2} . Then, the final result is obtained by interpolation between these four values in the x -direction. It may be shown that the procedure is symmetrical in x and y such that the same result would be obtained if the interpolation directions were reversed.

Cubic interpolation in the postprocessor should only be applied to complex field patterns when the distance between the input points is smaller than $0.25\lambda/D$, where λ is the wavelength and D is the size of the scatterer, for example the diameter of a reflector antenna.

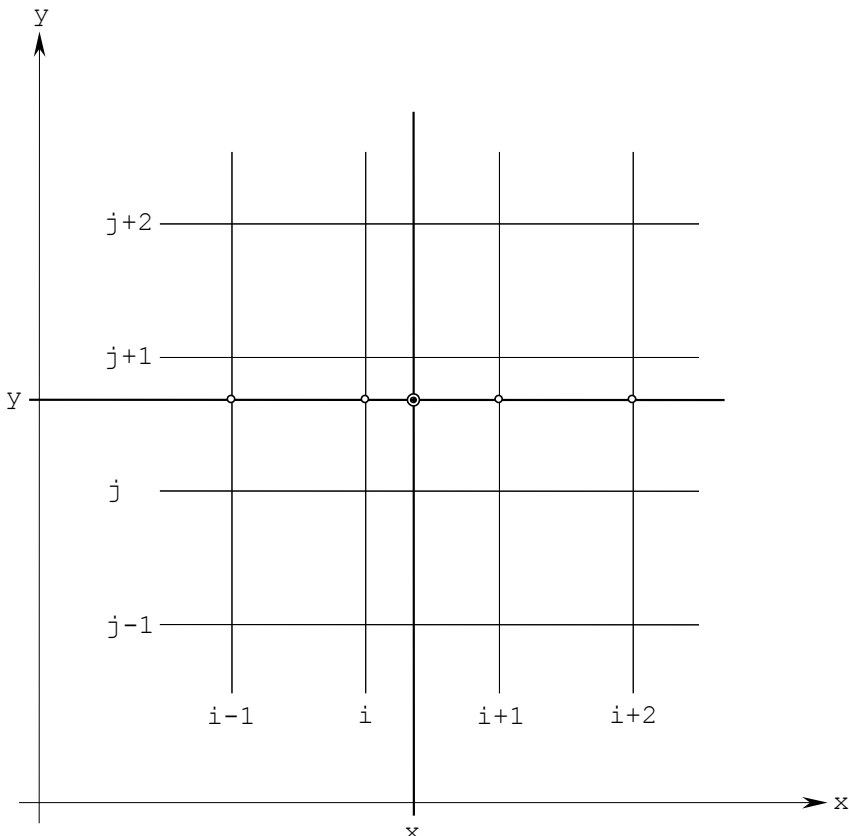


Figure 4.3-2 Cubic interpolation in double grid.

4.3.2 Whittaker interpolation

The Whittaker interpolation should only be used in expansion of calculated far-field patterns as is the case in the postprocessor. It minimises the amount of sampled data required by taking advantage of the fact that the radiation pattern from a finite planar aperture is a band-limited function by virtue of the Fourier-transform relationship between aperture field and far field, (Drabowitch, 1978).

The interpolation procedure may be expressed as

$$f(x) = \sum_{n=-\infty}^{\infty} f(x_n) \frac{\sin \pi \frac{x}{h} - n}{\pi \frac{x}{h} - n} \quad (4.3-4)$$

where h is the sampling rate and x_n are the sampling points.

The sampling rate, h , is defined by the reflector diameter D and the wavelength λ , $h = \lambda/D$ (see Drabowitch, 1978), commonly called the Nyquist rate. In practice, the relationship between the aperture field and the far field of a reflector antenna is not an exact Fourier transform, as the field in the aperture plane is not completely confined to a finite region (Bucci et al., 1980). For this reason an oversampling must take place by selecting the spacing, h , slightly less than the Nyquist rate. The necessary amount of oversampling is varying for different antenna systems. As a rule-of-thumb the number of samples should be equal to the number of lobes plus two (Bucci et al., 1980) or $h \approx 0.85 \lambda/D$.

The interpolation theory is based on an infinite number of samples, but in practice only a finite number of samples can be used, which will result in a truncation error. The interpolation procedure can be expressed by

$$f(x) = \frac{\sin \pi \frac{x}{h}}{\pi} \sum_{n=-N}^N \frac{f(nh)}{\frac{x}{h} - n} + E_N(x) \quad (4.3-5)$$

where $E_N(x)$ is the truncation error which is then given by

$$E_N(x) = \frac{\sin \pi \frac{x}{h}}{\pi} \sum_{n=N+1}^{\infty} (-1)^n \left(\frac{f(nh)}{\frac{x}{h} - n} + \frac{f(-nh)}{\frac{x}{h} + n} \right) . \quad (4.3-6)$$

The maximum truncation error will occur approximately at the middle of an interval

$$x = \left(m + \frac{1}{2} \right) h, \quad -N \leq m \leq N-1 \quad (4.3-7)$$

giving an error for a symmetrical pattern of

$$E_N \cdot m = \frac{2m+1}{\pi} \sum_{n=N+1}^{\infty} \frac{-1^n f(nh)}{(m+1/2)^2 - n^2} . \quad (4.3-8)$$

This indicates that the truncation error is increasing with increasing observation angle. The maximum error will occur at $m = N - 1$ and the magnitude will be in the order of $f(hN)/10$.

The Whittaker interpolation procedure is extended to include sampling for band-limited functions of two variables by (Stearns, 1975)

$$f(u, v) = \frac{1}{\pi^2} \sin \frac{\pi}{\Delta u} \frac{u - u_s}{\Delta u} \sin \frac{\pi}{\Delta v} \frac{v - v_s}{\Delta v} \sum_{n=1}^{N_U} \sum_{m=1}^{N_V} \frac{-1^{n+m} f_{nm}}{u - u_s / \Delta u - n \quad v - v_s / \Delta v - m} \quad (4.3-9)$$

where Δu and Δv are the spacings of u and v , and u_s and v_s the start direction in the uv -grid.

If the field values are to be expanded to a new and more dense grid a faster computation is obtained by separating the interpolation routine into

$$f(u, v) = \frac{1}{\pi^2} \sin \frac{\pi}{\Delta u} \frac{u - u_s}{\Delta u} \sum_{n=1}^{N_U} f_n \cdot v \frac{-1^n}{u - u_s / \Delta u - n} \quad (4.3-10)$$

where

$$f_n \cdot v = \sin \frac{\pi}{\Delta v} \frac{v - v_s}{\Delta v} \sum_{m=1}^{N_V} f_{nm} \frac{-1^m}{v - v_s / \Delta v - m} \quad (4.3-11)$$

for all interpolated v -values.

4.4 Beam analyses

The computed field pattern in two-dimensional uv -grids can be further processed by the GRASP Post-processor. The principal functions are:

- input of one or more element beam data
- generation of composite beam by superposition of the element beams multiplied by complex excitation coefficients
- field expansion by Whittaker or Cubic interpolation, see Section 4.3.
- change of field components, see Section 4.1.4, after field expansion
- calculation of peak gain, peak direction and beamwidth
- calculation of beam efficiency
- calculation of the area of a given contour curve
- calculation of envelope pattern

4.4.1 Peak gain, peak direction and beamwidth

The peak direction is found by using the cubic interpolation around the grid point with the maximum field level u_m, v_m illustrated in Figure 4.4-1.

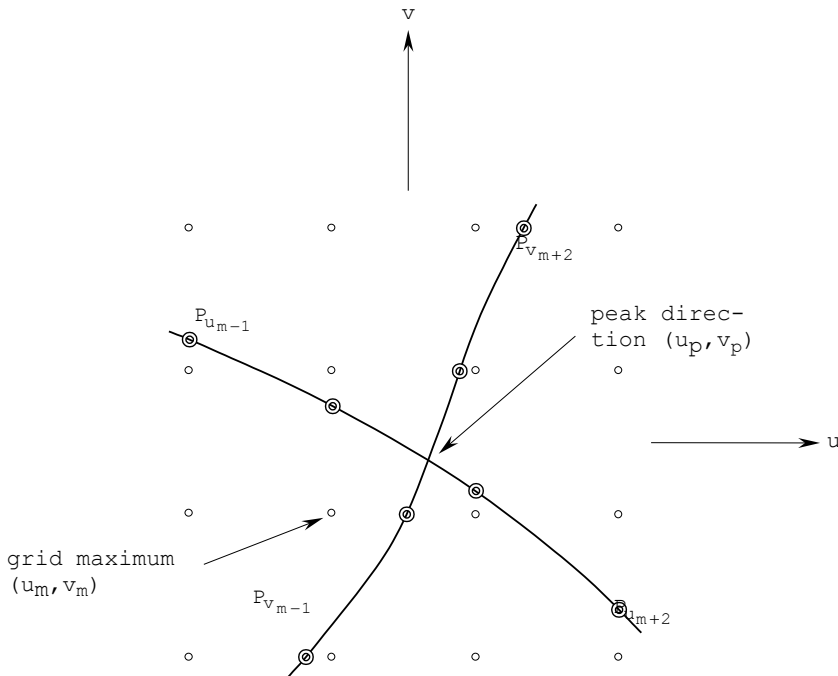


Figure 4.4-1 Interpolation procedure for peak direction determination.

The peak direction in v , v_p , is given by the maximum of the interpolation formula with sample points P_v for $v = v_{m-1}$, v_m , v_{m+1} , v_{m+2} . P_v is the maximum field level in u for the above constant v -values. All maximum points are found by the zero of the first order derivative of the real cubic interpolation with field amplitude as sampling points. The peak in u -direction, u_p , is found by the same method. Having the direction u_p, v_p , the gain is found by complex cubic interpolation.

In order to characterise the beamwidth the angle from the peak centre u_p, v_p to the contour of a specified field level is calculated. The program carries out this calculation in a number of cuts through the peak centre and the maximum and minimum angle are output.

Another way to illustrate the beam shape in the neighbourhood of the peak is to determine the field level on cones around the beam peak direction. For each cone the maximum and minimum field level is output.

4.4.2 Efficiency calculation

The beam efficiency γ is defined by

$$\gamma = \int_{\Omega_o} G(\Omega) d\Omega / W \quad (4.4-1)$$

where

- Ω_o is the solid angular region within which the beam efficiency is evaluated.
- $G(\Omega)$ is the antenna gain function
- W is the input power to the antenna.

The field quantities from GRASP are normalised with respect to isotropic levels, giving

$$\gamma = \frac{1}{4\pi} \int_{\Omega_o} G(\Omega) d\Omega . \quad (4.4-2)$$

The beam efficiencies for each of polarisations A and B are separated into

$$\gamma_A = \frac{1}{4\pi} \int_{\Omega_o} E_A^2(\Omega) d\Omega \quad (4.4-3)$$

$$\gamma_B = \frac{1}{4\pi} \int_{\Omega_o} E_B^2(\Omega) d\Omega . \quad (4.4-4)$$

The region Ω_o may be specified in different ways:

1. the region where the field level is larger than a given specified value
2. an elliptical region in the uv -grid given by the half axes along u and v
3. a rectangular region in the uv -grid given by the half side lengths along u and v
4. the region may be defined as a polygon specified by the user

The centre point for these regions is the direction of the beam peaks described in the previous section. If no peaks are calculated the centre direction is $(u, v) = (0, 0)$.

The numerical evaluation of (4.4-3) and (4.4-4) is obtained by a subdivision of the uv -grid into small patches (see Figure 4.4-2) and can be written as

$$\gamma_A = \frac{1}{4\pi} \sum_{k=1}^2 \sum_{n=1}^{NU-1} \sum_{m=1}^{NV-1} I_A(k, n, m, \omega) \quad (4.4-5)$$

$$\gamma_B = \frac{1}{4\pi} \sum_{k=1}^2 \sum_{n=1}^{NU-1} \sum_{m=1}^{NV-1} I_B(k, n, m, \omega) \quad (4.4-6)$$

where $I(k, n, m, \omega)$ is the efficiency contribution in patch (k, n, m) and NU and NV are the number of u - and v -values, respectively. Each patch is subdivided into two triangles, $k = 1, 2$.

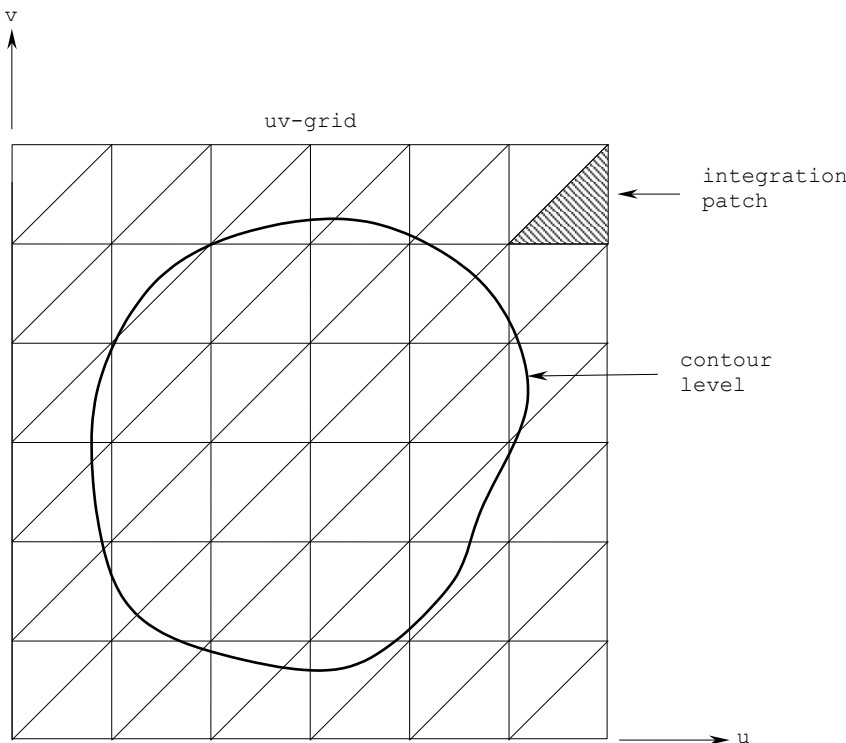


Figure 4.4-2 uv -grid divided into integration patches.

The calculation of $I_{k,n,m,\omega}$ is given by

$$I_{k,n,m,\omega} = \frac{1}{\cos \theta_{k,n,m}} \int_{\omega} F_{k,n,m} u', v' du' dv' \quad (4.4-7)$$

where $\theta_{k,n,m}$ is the centre of the patches defined in Figure 4.4-3, $F_{k,n,m} u', v'$ is a linear approximation of the power of each polarisation inside the patch

$$\begin{aligned} F_{k,n,m} u', v' &= E^2 u, v \\ &+ [E^2 u + \Delta u, v - E^2 u, v] \frac{u' - u}{\Delta u} \\ &+ [E^2 u, v + \Delta v - E^2 u, v] \frac{v' - v}{\Delta v} \end{aligned} \quad (4.4-8)$$

and ω is the part of the patch (k, n, m) where the field level given by (4.4-8) is larger than the specified level, as also illustrated in Figure 4.4-3.

The spacing of the uv -grid is essential for the accuracy of the beam efficiency calculation. A spacing in u and v of $0.1\lambda/D$ will normally give an error level less than 1% and the error is proportional to the square of the spacing.

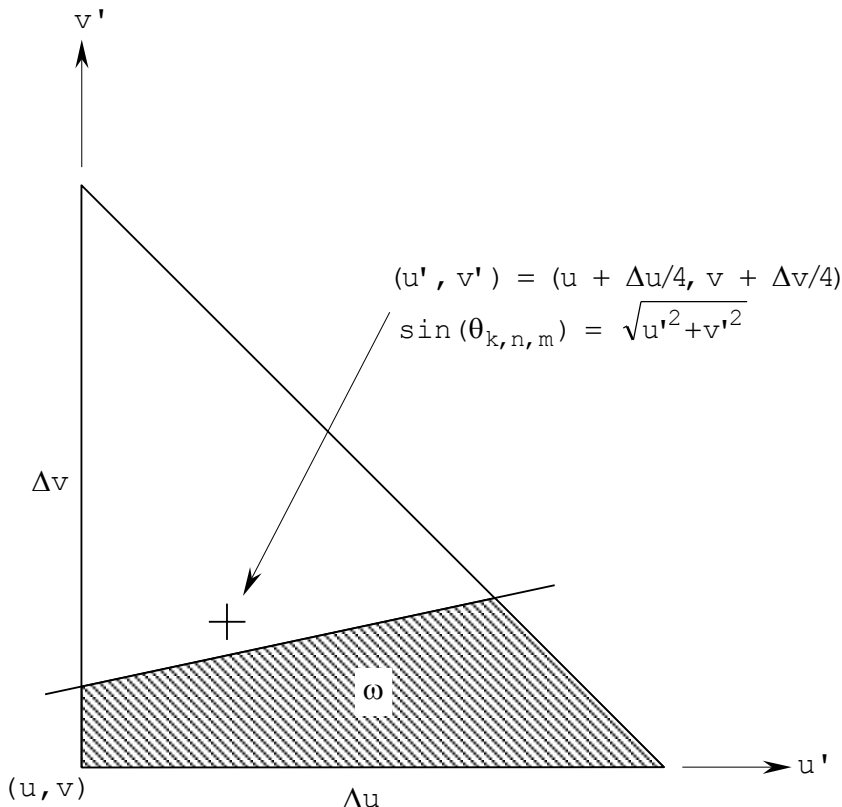


Figure 4.4-3 Integration patch (k, n, m) .

4.4.3 Beam contour area calculation

The coverage area is defined as the solid angle Ω_o where the amplitude of one of the field components is larger than a specified contour level and θ is less than a specified constant angle θ_o . The scenario is illustrated in Figure 4.4-4 showing the contour curves for a main beam and four sidelobes. By means of θ_o only the area of the main beam is calculated. It should be noted that θ_o is here measured from the origin of the uv -grid.

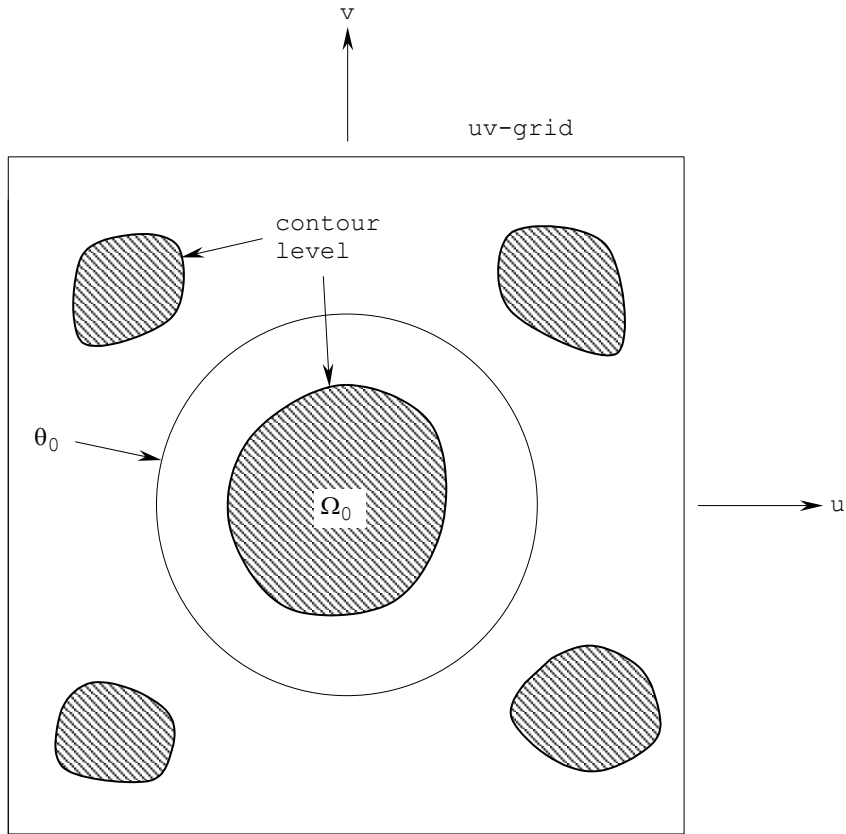


Figure 4.4-4 Definition of coverage area Ω_0 in uv -grid.

The area integral is obtained by a subdivision of the uv -grid into small patches as in Section 4.4.2 (see Figure 4.4-2) and can be written as

$$\Omega_0 = \sum_{k=1}^2 \sum_{n=1}^{NU-1} \sum_{m=1}^{NV-1} A_{k,n,m} , \quad (4.4-9)$$

where $A(k, n, m)$ is the area contribution in patch (k, n, m) . The calculation of $A(k, n, m)$ is separated into two regions

$$A_{k,n,m} = \begin{cases} 0 & \text{for } \theta_{k,n,m} > \theta_0 \\ \frac{1}{\cos \theta_{k,n,m}} \int_{\omega} du' dv' & \text{for } \theta_{k,n,m} \leq \theta_0 \end{cases} . \quad (4.4-10)$$

$\theta_{k,n,m}$ is the centre of the triangular patch (k,n,m) as indicated in Figure 4.4-3 and ω is the area part where the field is above the specified level.

4.4.4 Pattern envelope calculation

The pattern envelope facility is very useful for determining the isolation between contoured beams and for presenting fast oscillating patterns, for example in order to verify that the side-lobe performance meets certain required specifications.

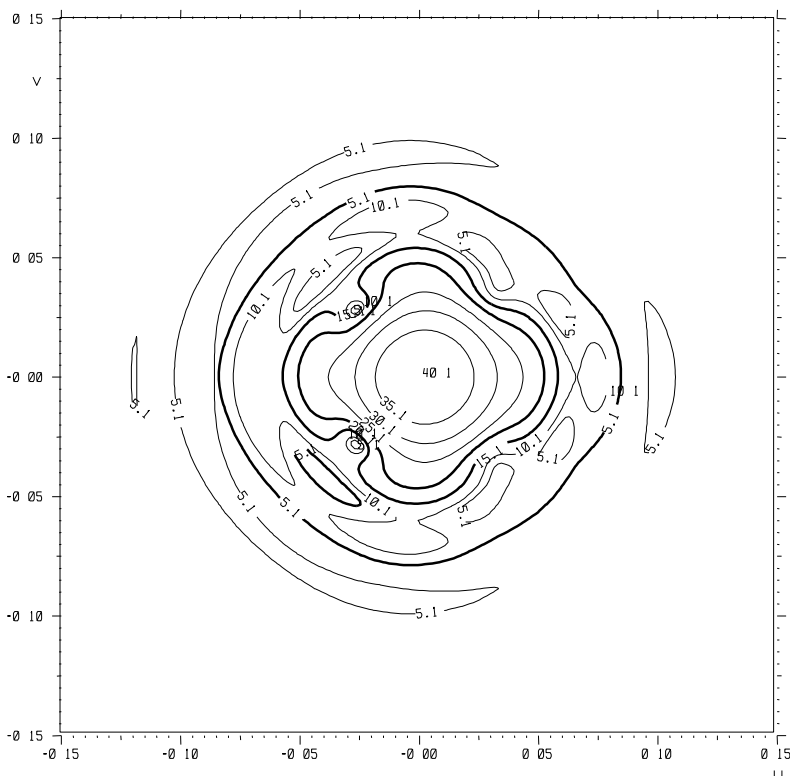


Figure 4.4-5 Contour plot of typical beam, covering the main beam and the first 4-5 sidelobes. The contours shown are 5, 10,..., 35 dB below the beam peak.

The envelope is determined using linear interpolation between the peaks of the lobes in a single cut. The envelope procedure is extended to double grid by calculating the envelope levels in

u for constant v first, as for a single cut, and then in v for constant u . The maximum envelope level in each grid point is then the resulting field envelope level.

Figure 4.4-5 shows a contour plot of a scanned beam including the main beam and the first few sidelobes. The plot clearly shows that the sidelobe behaviour is quite complex and it is difficult to check if possible sidelobe requirements are fulfilled.

The envelope pattern of the field in Figure 4.4-5 is shown in Figure 4.4-6. It is readily seen that this pattern is slowly varying and a comparison to possible sidelobe requirements can easily be accomplished.

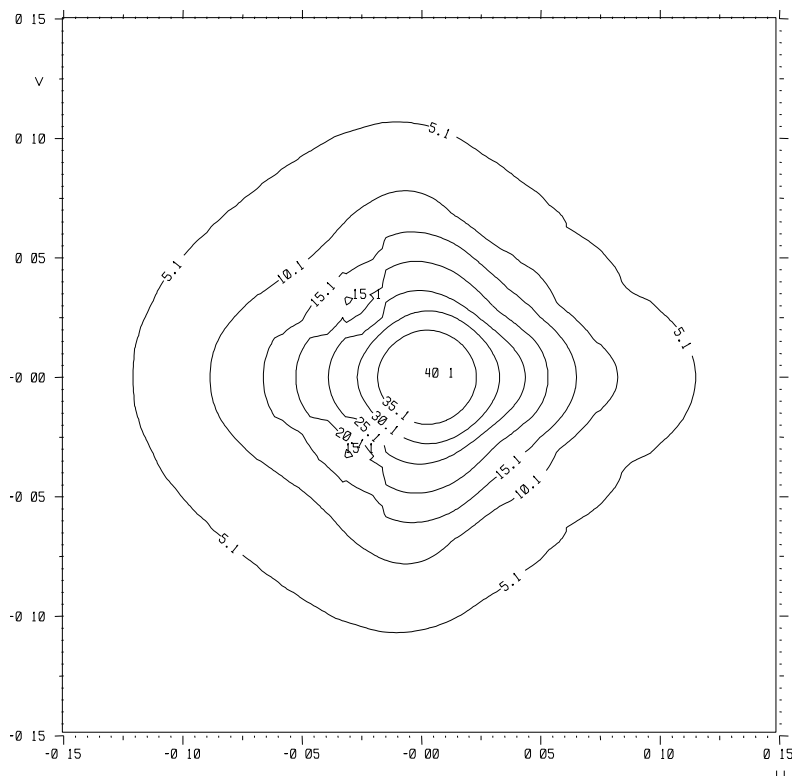


Figure 4.4-6 Contour plot of the envelope pattern corresponding to Figure 4.4-5. The contours shown are 5, 10,..., 35 dB below the beam peak.

5. APPLICATIONAL EXAMPLES

In order to demonstrate the capabilities of GRASP a number of examples are presented in this chapter. The antenna configurations represent cases which are commonly encountered in practice. They are, however, sufficiently advanced to demonstrate numerous complex features.

In this chapter these cases are described from an application point-of-view: the type of antenna configuration to be analysed is described and the results obtained by GRASP are presented.

In the “GRASP User’s Manual” it is shown in detail how to generate input data files for each case and which commands should be submitted in order to obtain the results.

Finally, these files are provided as test case files coming with the installation of GRASP.

5.1 Single reflector with three struts

In this section we will describe the analysis of a single reflector with a circularly symmetric parabolic surface shape, and fed by a feed horn located at the focal point of the paraboloid. The feed is held in place by three struts and the example will show the significance of including the scattering from these supports in the analysis.

5.1.1 Geometry

The antenna is designed to operate in the Ka band at 30 GHz and has the following geometrical characteristics:

Diameter $D = 500$ mm

Focal length $F = 250$ mm

Subtended angle from the focal point $\theta_o = 53.1^\circ$.

The struts are 10 mm in diameter and their position given by three pairs of start and end coordinates relative to the apex of the reflector is:

Strut no.	X _{start} (mm)	Y _{start} (mm)	Z _{start} (mm)	X _{end} (mm)	Y _{end} (mm)	Z _{end} (mm)
1	125.00	0.00	25.625	25.0	0.0	250.0
2	-62.6	108.25	25.625	-12.5	21.651	250.0
3	-62.5	-108.25	25.625	-12.5	21.651	250.0

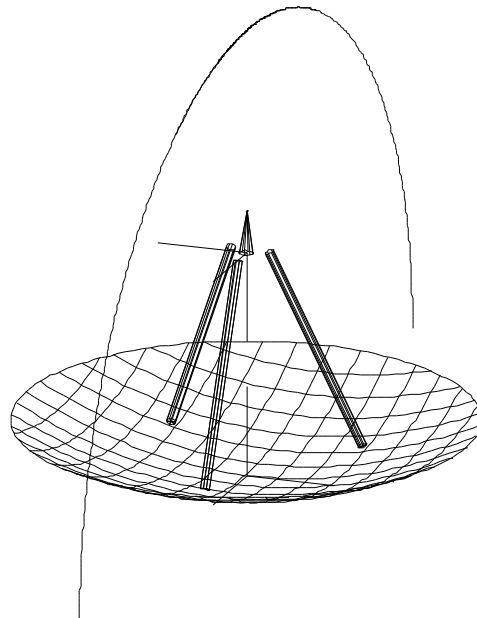


Figure 5.1-1 Geometry plot of single reflector with three struts. The plot also shows a field storage object, a spherical cut ranging from -90° to $+90^\circ$ in θ , for $\phi = 0^\circ$.

A drawing is shown in Figure 5.1-1. The geometry is viewed in a plane projection seen from a view angle given by the spherical coordinates $\theta, \phi = (70.5^\circ, 20.7^\circ)$ in the apex coordinate

system. The view angles can be specified by the user and the above values correspond to a dimetric projection.

Another useful projection is a side view, $\theta, \phi = (90^\circ, 90^\circ)$ as shown in Figure 5.1-2. In this case a ray is launched from the feed in a specified direction and traced forward through the system.

Only one of the three struts is shown and the ray drawing illustrates one of the mechanisms in strut scattering: the feed field is blocked by the strut which creates a shadow on the main reflector in the region between the strut and the reflector rim. This effect will reduce the aperture efficiency and consequently the peak directivity. Furthermore, the field is scattered onto the antenna where it will be reflected in a direction away from boresight. This will usually give rise to an increase in the near-in sidelobe level as we shall see later.

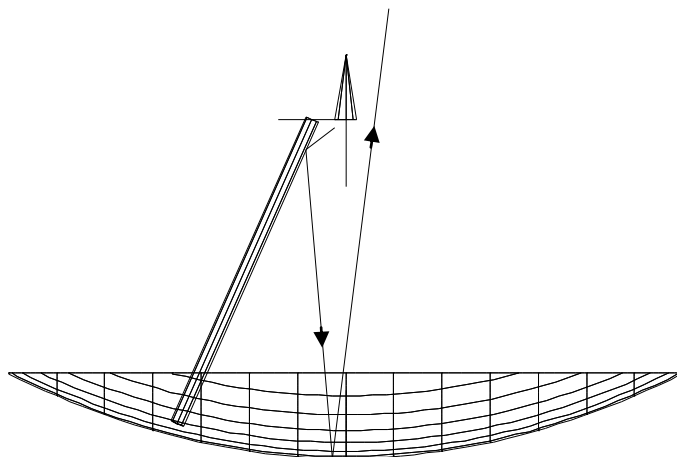


Figure 5.1-2 Side view of geometry with only one strut shown.

Another strut-scattering effect is demonstrated by means of the ray plot in Figure 5.1-3. In this case the strut blocks the field being reflected from the dish, resulting also in a loss of on-axis directivity. The scattered field will cause a sidelobe in-

crease along the so-called Keller cone, a cone with axis along the strut and an opening angle defined by the angle between the strut and the reflector boresight axis. In the present geometry the direction of the reflected ray shown is 48° relative to the boresight axis and an increase in the sidelobe level can be expected here.

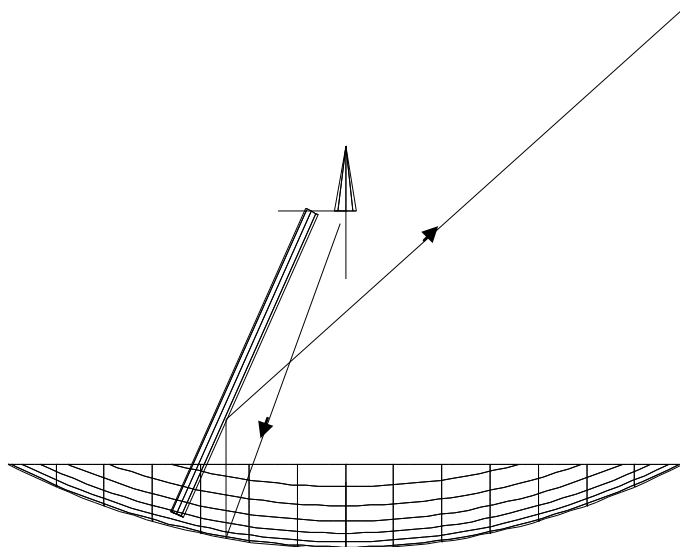


Figure 5.1-3 Side view with a ray reflected first in the reflector and then in the strut.

5.1.2 Nominal pattern analysis

Having accepted the configuration from the drawings it is time to perform the analysis. As the first step the far field from the reflector currents when illuminated by the feed (struts absent) is obtained and this will be the predominant or nominal part of the antenna pattern. The pattern is shown in Figure 5.1-4.

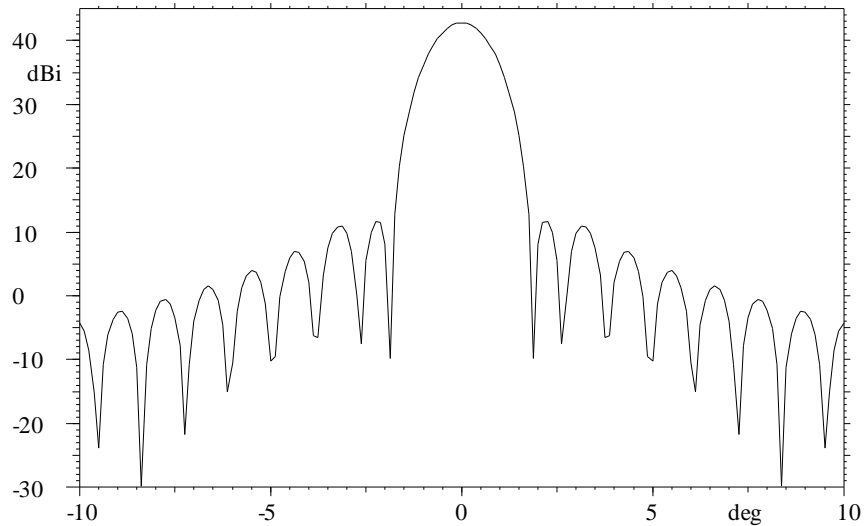


Figure 5.1-4 Nominal radiation pattern for the front-fed paraboloid.

In the pattern shown in Figure 5.1-4 we have only included the radiation from the current distribution. In case also the direct feed radiation had been included in the present example this would have had no visible effect on the pattern since the feed backward radiation is extremely low. However, there are other cases where it is of utmost importance to include this contribution, and in general it should always be done when performing PO calculations in order to ensure a correct result.

5.1.3 Strut scattering of spherical wave

As indicated in Section 5.1.1 the strut will block the field coming from the feed, an effect often referred to as the spherical-wave strut scattering since the field from the feed is approximately a spherical wave. To analyse this effect we will need to calculate induced currents on the struts. In order not to complicate the picture we will first consider only the single strut shown in Figure 5.1-2.

The currents on the strut are calculated using the feed as source. This step is followed by calculating the currents on the main dish with the strut currents as source. Finally the cur-

rents on the reflector are integrated to obtain the far field shown in Figure 5.1-5.

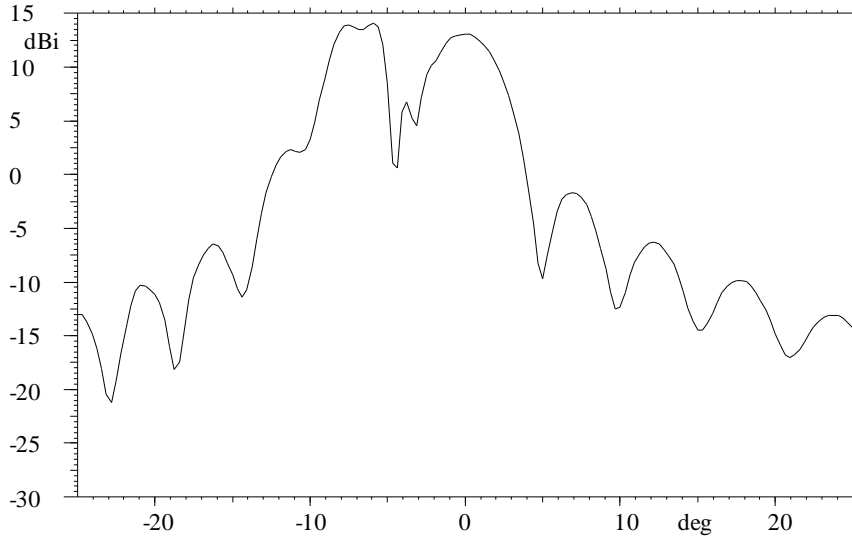


Figure 5.1-5 Scattered field from the main reflector due to the spherical wave strut blockage. Pattern plane is the plane of symmetry.

The figure shows a quite large disturbance field relative to the nominal pattern which had a peak directivity of 42.8 dBi. There are two peaks, one at 0° and one around -7° . The latter is the easiest to explain: this is simply the reflection of the strut-scattered field in the main reflector, as illustrated by the ray in Figure 5.1-2 showing an estimated scan direction of -8.8° , in quite good agreement with the actual pattern.

The peak at 0° requires a more elaborate explanation: due to the strut there will be a shadow region on the main reflector where the incident field is very low. To obtain this incident field it is necessary to add the strut scattered field and the feed field. These will then cancel out (more or less) in a region behind the strut. However, in the present example we are interested in examining the strut effect alone and therefore we have not added the direct feed field when calculating the incident field on the reflector. If this had been done we would have obtained a main lobe pattern similar to the one in Fig-

ure 5.1-4 and with increased sidelobes. Instead we observe here that the scattered field from the strut is quite large in the shadow region, comparable in size and 180° out of phase to the feed field. Consequently the reflection of this portion of the scattered field is a plane wave which peaks in the boresight direction. It can be shown that the lobe in the main beam direction is 180° out of phase with the nominal field and thus will subtract from this when the total field is eventually calculated. The level of the scattered field is around 13 dBi and will then reduce the nominal peak from 42.8 to 42.5 dBi.

5.1.4 Strut scattering of plane wave

The other strut scattering mechanism as shown in Figure 5.1-3 is often referred to as the plane-wave scattering component of the strut blockage since it blocks the predominant field coming from the reflector. The induced currents on the reflector are first calculated and then used to generate currents on the strut.

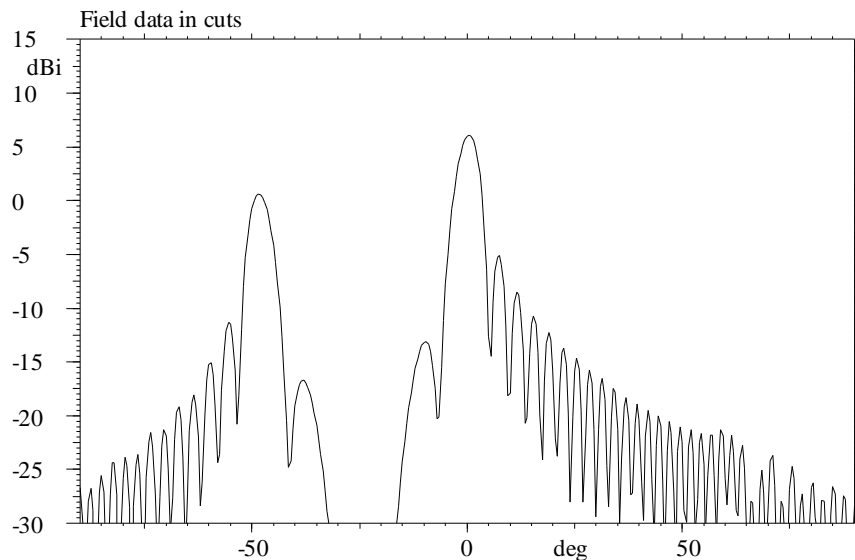


Figure 5.1-6 Scattered field from the strut due to the plane wave from the reflector. Pattern plane is the plane of symmetry.

The pattern is shown in Figure 5.1-6. Two distinct lobes are seen, one in the boresight direction which is 180° out of phase with the nominal field and consequently will reduce the peak directivity, and one at the earlier calculated angle of 48° . Since the lobes are located on a cone with the strut as axis they will also show up in other planes and at other angles from boresight. The peak level is 6 dBi and will thus reduce the antenna directivity further from the 42.5 dBi to 42.4 dBi.

5.1.5 Total pattern

The final step is to take all effects from all three struts into account simultaneously. In this case we first calculate the induced currents on the struts due to the feed. In the following step the reflector currents are calculated with the strut currents and the feed as source. Next, we calculate the currents on all struts when being illuminated by the currents on the main reflector. Finally, we calculate the far field generated by the reflector currents and add the field generated by the strut currents. The final result is shown in Figure 5.1-7.

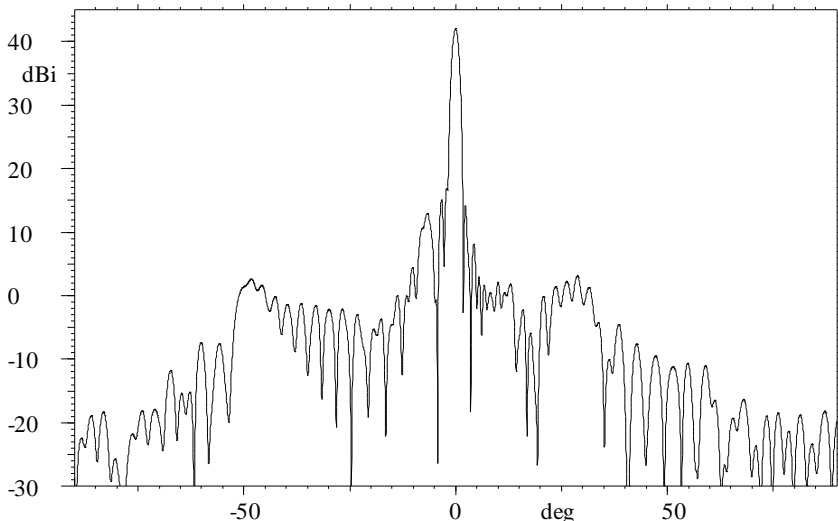


Figure 5.1-7 Total pattern with scattering from all three struts included. Pattern plane is the plane of symmetry.

The strut interference can clearly be identified on the left side of the main beam at $\theta = 10^\circ$ and $\theta = 50^\circ$. There is also a significant sidelobe increase on the right hand side of the main beam. This is the compound effect of all three struts.

5.2 Dual reflector with blockage

The next example concerns a dual reflector antenna system which is rotationally symmetric. In such a case it is important to model the blockage due to the subreflector, since this can have significant influence on the gain and the sidelobes. Also the spillover from the feed must be included in the computations because it can contribute in a dominant way to the off-axis radiation pattern.

While the above effects are present in any symmetric dual reflector system, we have chosen a geometry where they can easily be perceived. First of all the main reflector aperture is only 50 wavelengths, and the feed illumination at the edge of the subreflector is just 12 dB below peak. Such taper provides a good aperture efficiency but in actual systems it is common to use a more directive feed in order to reduce the sidelobes. However, it provides for a better example when the spillover can be clearly seen in the secondary pattern.

A real dual reflector would of course need some sort of support for the subreflector, but this has been neglected in the present example. The reader is referred to the previous section for an example on how to calculate support strut scattering.

5.2.1 Geometry

The antenna is designed for 30 GHz where the wavelength is 0.01 m. Geometrical parameters are:

	Diameter	Focal length	Eccentricity
Main reflector	0.50	0.25	-
Subreflector	0.1142	0.15	3.0

A drawing of the geometry as generated by GRASP is shown in Figure 5.2-1. The feed is modelled as a Gaussian beam with a 12 dB taper at the subreflector edge, thus the feed drawing should in this case only be considered for illustrative purposes, although the parameters are chosen with a realistic feed in mind.

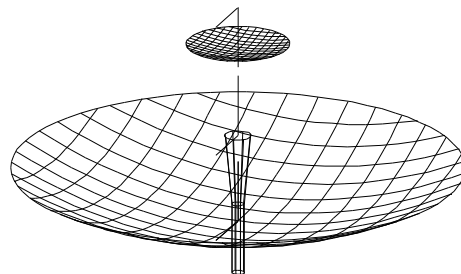


Figure 5.2-1 Geometry of 50λ dual reflector antenna system.

5.2.2 Pattern analysis

One of the significant characteristics of GRASP is that the amount and order of computations is entirely decided by the user. Of course there are certain pre-requisites, for example it will not be possible to calculate the scattered field from the main reflector before the subreflector illumination has been determined. But it enables the user to look at different contributions individually and therefore obtain a better understanding of the various parts that make up the radiation pattern of an antenna. This will be illustrated in the following.

The component of primary interest in the far field from the dual reflector is the reflected field from the main reflector. To

calculate this one has to first calculate the illumination from the subreflector, using one of the available analysis methods PO or GTD. We have chosen PO.

Once the subreflector currents have been calculated they can be used to generate currents on the main reflector. Integrating these provides the above mentioned primary far-field component.

However, a significant contributor to the off-axis sidelobes is the radiation from the feed and the subreflector. We can include this in the analysis by adding the field from the subreflector induced currents and the direct feed radiation to the previously calculated main reflector pattern. The order in which this is done is immaterial but it is important that both the subreflector and the feed contributions are added (for more discussion on this issue, see Section 3.8.3).

A comparison of the results is given in Figure 5.2-2.

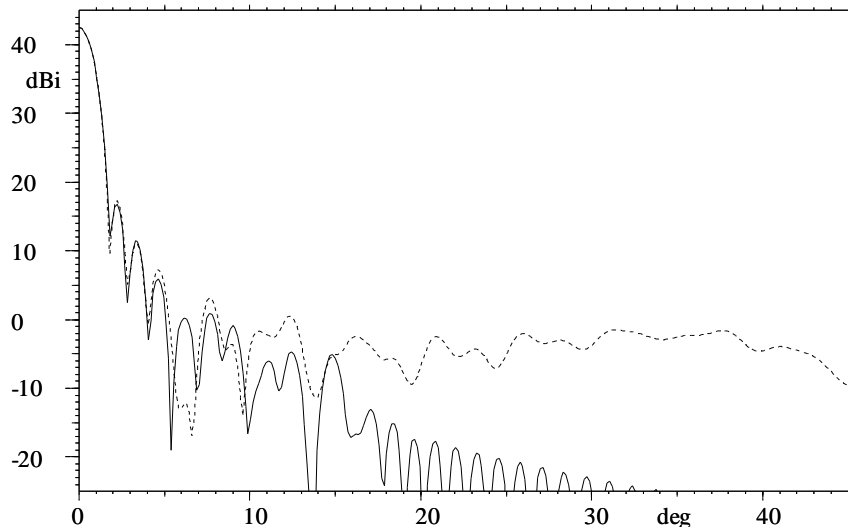


Figure 5.2-2 Radiation pattern from dual reflector without (—) and with (---) spillover included.

The spillover is easy to identify, first as a modulation on the sidelobes from the nominal pattern and then by a large increase in the level at angles where the feed is visible. The dif-

ference in peak gain is not noticeable, but it is obvious that the spillover effects must be considered if the sidelobe predictions are of primary importance.

5.2.3 Blockage considerations

Due to the circular symmetry the subreflector will obstruct the scattered field from the main reflector and give rise to a reduction in the peak gain. There are two approaches in GRASP to model this effect. One is based on the so-called null-field assumption and consists on nulling out those currents on the main reflector which are inside the optical shadow of the sub on the main when seen from the boresight direction. This approach provides a very good estimate of the gain reduction, but it is less accurate when it comes to the effect of the blockage on the sidelobes.

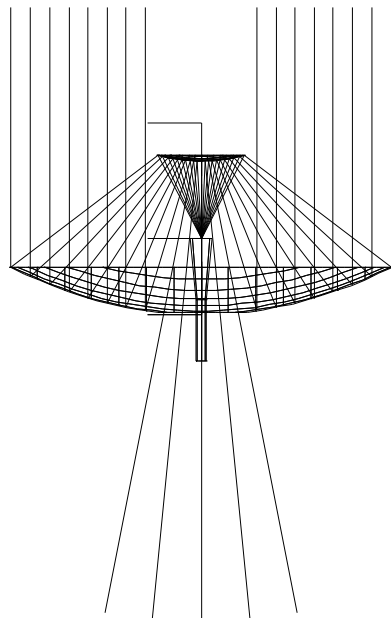


Figure 5.2-3 Rays in a dual reflector system with hole in the centre to model blockage.

Note in Figure 5.2-3 how the rays actually proceed through the central hole when drawn in GRASP.

The influence of the null-field assumption is observed in Figure 5.2-4 where the antenna pattern is shown both when the blockage is neglected and when it is included.

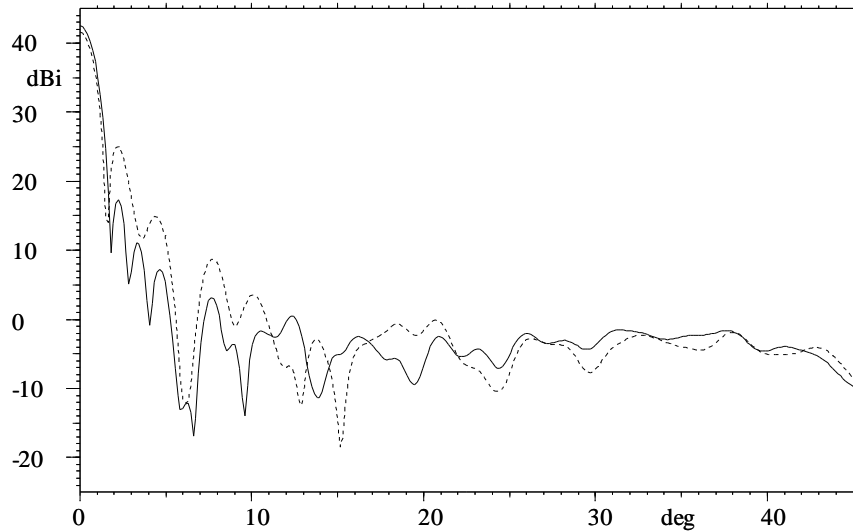


Figure 5.2-4 Blockage effects included by means of the null-field assumption. — no blockage (dashed line in Figure 5.2-2), --- blockage.

The pattern shows a clear reduction in the peak gain as well as an increase in the level of the first few sidelobes.

The other method is much more rigorous and attempts to model the actual scattering rather than introducing any assumptions: the induced currents on the main reflector are used to illuminate the sub and generate a new set of induced currents on this reflector. By adding the field from these currents to the field which was calculated in the previous paragraph we account for the blockage as well as the scattering into the sidelobe region.

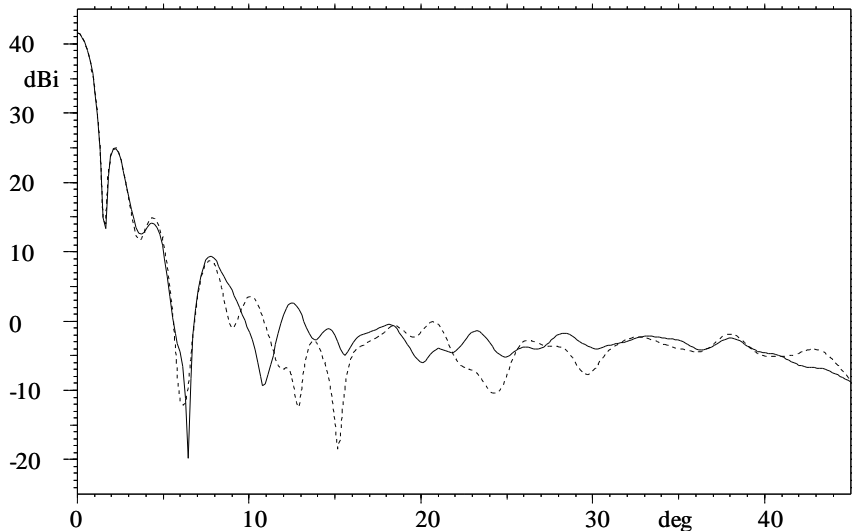


Figure 5.2-5 Comparison of blockage prediction methods.
— rigorous solution, --- null-field assumption
(dashed line in Figure 5.2-4).

Figure 5.2-5 shows a comparison between the two methods. It is seen that they agree very well on the peak gain reduction and the first few sidelobes. Consequently, if this is the only region of interest, then the null-field approach should be selected since this is by far the computationally most efficient method. On the other hand, in case the precise structure of the outer sidelobes is of interest then one is confined to the rigorous method which will give a more accurate prediction of the scattered field in these directions.

5.2.4 A closer look at the hole in the reflector

In some cases the rear radiation from the antenna system is of interest and as it was seen in Section 3.8.3 it is possible to calculate this very accurately. However, it may give rise to some rather confusing results when the null-field assumption is employed. Because the induced currents are set to zero in the central section it will appear as if the antenna indeed has a hole in the middle. Consequently the subreflector will radiate right through this hole - there are no "screening currents" to

cancel the subreflector field behind the main. The result can be observed in Figure 5.2-6, where the rear radiation is calculated both with and without the null-field assumption.

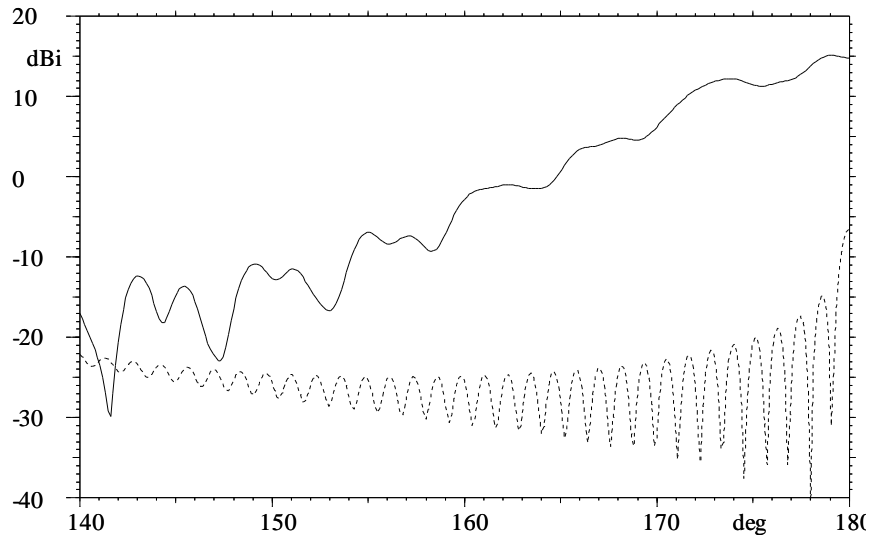


Figure 5.2-6 Rear radiation from dual reflector system when a hole is introduced in the main reflector. — with hole, --- without hole.

The rigorous approach also has its deficit in the rear direction: the secondary set of currents on the subreflector which accounts for the blockage in the forward direction will of course also radiate back towards the main reflector. This means that if we add the field from these currents in the rear direction we will again obtain a pattern level which is too high, because it should in fact have been shadowed by the main reflector.

One could carry the procedure further by calculating a new set of currents on the main reflector due to the secondary currents on the subreflector, but for most practical applications it will suffice to just omit the secondary subreflector current calculation when computing the rear pattern.

5.3 A single shaped reflector with circular polarisation

The previous examples have all dealt with focusing reflectors consisting of conical surfaces which can be described analytically. The ability of GRASP to handle a much wider range of surface shapes was described in Chapter 2 and the following example will show the analysis of a single offset reflector antenna, shaped to produce a highly contoured beam with sidelobe constraints. Because the antenna is operating in circular polarisation it is expected to produce a very high degree of polarisation purity, despite the offset geometry. We will use this example to demonstrate the significance of including the PTD currents in the analysis, by looking carefully at the predicted cross polar performance of the antenna.

5.3.1 Shaped reflector geometry

Since the shaping is not a part of the GRASP program but is carried out with another TICRA software package, we shall not go into detail with that procedure here. Suffice to say that the surface shaping is applied to a conventional offset paraboloid with the following parameters:

$$D = 3.3 \text{ m}, F = 3.3 \text{ m}, \text{clearance} = 0.2 \text{ m}$$

and is given as z -values in a regular xy -grid of points, as specified in Section 2.2.1.1.5. The number of points in the grid is an input parameter to GRASP, which then performs a cubic interpolation to calculate intermediate points. It is assumed that the designer has chosen to output enough points from the shaping program to adequately represent all surface variations, as GRASP otherwise will not be able to predict the radiation pattern accurately. It should be noted that the sampling of the surface has nothing to do with the required density of the PO grid - a slowly varying surface could be represented by very few surface points, but a fine PO integration grid is still needed if the antenna is large in terms of the wavelength.

A plot of the shaped reflector geometry is presented in Figure 5.3-1, where a cone of rays has also been emitted from

the feed. The rays show a behaviour which is typical for these kinds of shaped reflectors: the centre portion forms a nearly parallel beam whereas the edge rays change direction very rapidly. Furthermore it is seen that due to the shaping the rays from the lower section of the reflector will hit the feed although an offset has been introduced which, in a focused system, would ensure a blockage-free condition.

Very often, though, the rays from the edge of the shaped reflector contain only a limited amount of power and may thus not give rise to any significant scattered pattern. But when the ray picture looks as in Figure 5.3-1 it may be wise to perform an analysis of the effect, for example by defining a circular plate of the same size as the feed aperture and place it in front of the feed. The currents induced on this plate by the main reflector currents will approximate the scattered field from the feed.

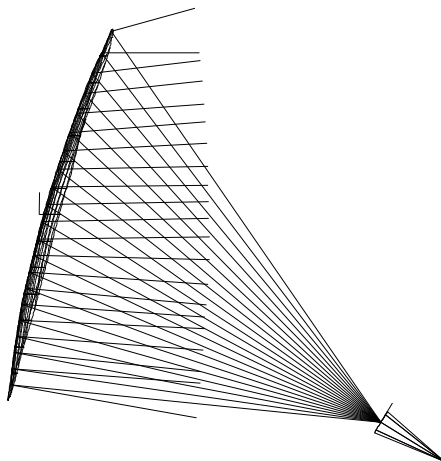


Figure 5.3-1 Shaped reflector generating highly contoured beam.

5.3.2 Coverage requirements

The antenna is designed to operate at a frequency of 4 GHz where the wavelength is 0.075 m. In Figure 5.3-2 below two

polygons of the so-called INTELSAT Hemi-beam type are shown, defining a typical C-band coverage scenario for international telecommunications. The antenna gain must be maximised over the right polygon and minimised over the left coverage such that the spatial isolation is better than 30 dB.

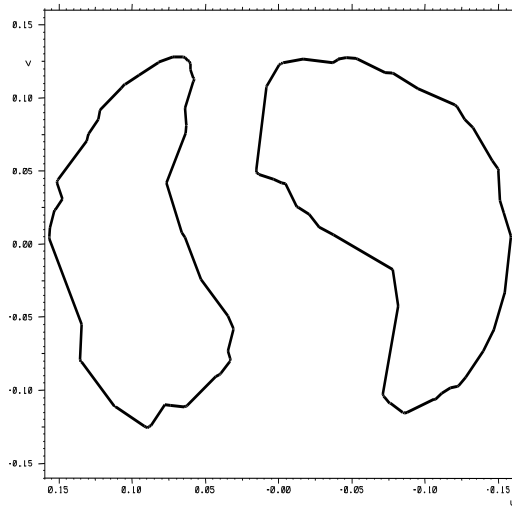


Figure 5.3-2 Coverage polygons defining East and West Hemi beams.

In the design process it is assumed that the antenna can be pointed towards the centre of the east (right) coverage with the coordinates $(u, v) = (-0.08, +0.02)$.

5.3.3 Co-polar pattern analysis

Using PO we predict the pattern shown in Figure 5.3-3.

The 24 dBi contour follows very closely the desired coverage area, whereas the -6 dBi contour just stays clear of the isolation region, an indication that the design goal of 30 dB isolation between the two regions has been achieved. There are a few "holes" inside the west coverage showing that the level at these points is slightly above the specifications, and this is not unusual to see in shaped designs. It is caused by the fact that the shaping operates with a finite number of "stations" inside each coverage at which the field is either maximised or mini-

mised. To save time in the optimisation procedure a limited number of stations is commonly chosen to begin with, and once a reasonable design is obtained the number of stations is increased to perform a final optimisation where the "holes" can be almost eliminated.

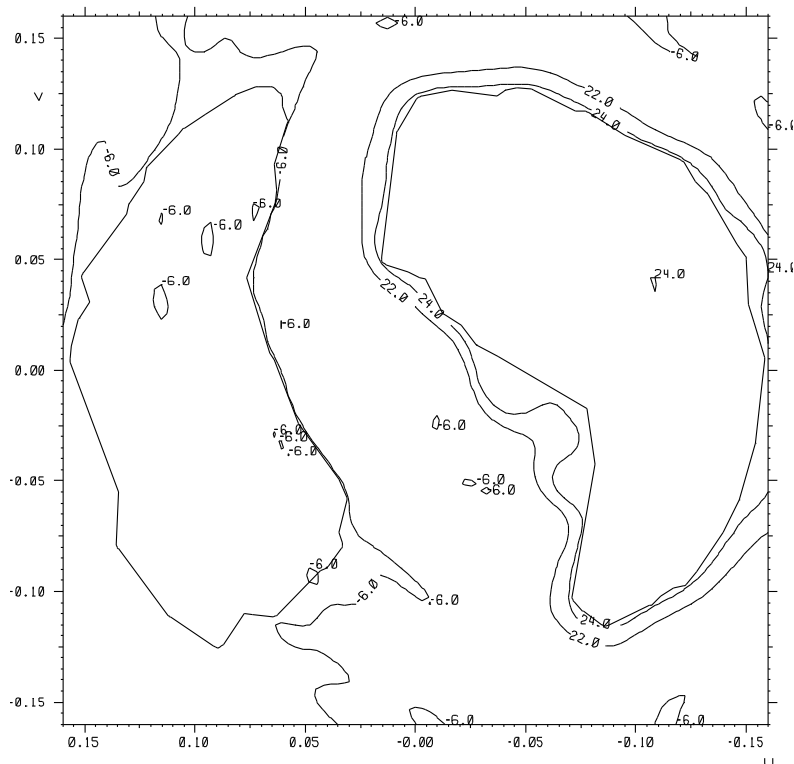


Figure 5.3-3 Co-polar radiation pattern from contoured beam antenna, with the east and west coverage polygons superimposed.

5.3.4 Cross polar pattern analysis

In order to effectively utilise the available frequency spectrum the INTELSAT C-band antennas operate in dual circular polarisation. Therefore the antenna must have good cross-polar isolation, typical in the order of 30-33 dB. There are many factors contributing to the cross polarisation, factors which are not included in the present analysis. Without these effects incorporated it is common to require that the antenna exhibits a

much better performance, perhaps in the order of 40 dB isolation.

In Section 3.8.3 it was shown how inclusion of PTD currents would improve the prediction of the antenna pattern at wide angles and at levels around 60 dB below peak. One may argue the practical relevance of including PTD in such cases; however, in the shaped reflector case it may be more important to include these effects even in the main beam direction. This is especially true for the cross polar predictions, due to the fact that the de-polarisation generated by the offset geometry is very low for circular polarisation and thus the contributing factors come from other parts of the reflector, for example the edge.

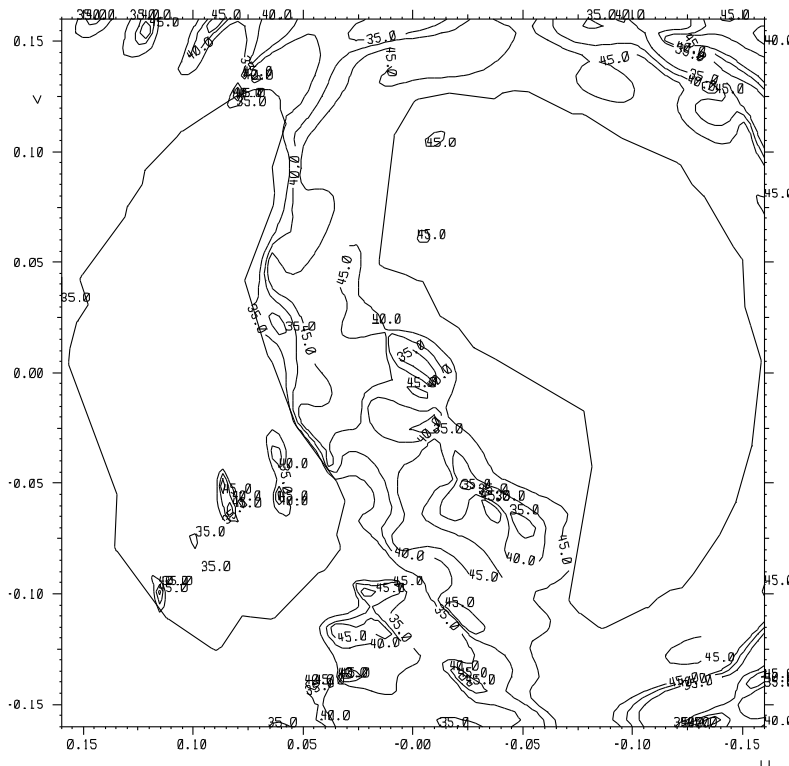


Figure 5.3-4 XPD contours at 35, 40 and 45 dB levels, when PTD is not included in the analysis.

Figure 5.3-4 shows the calculated cross polar discrimination ratio (XPD) for the shaped antenna analysed without PTD. The XPD is simply the ratio between the right-hand and the left-hand circular field components and is often used as an alternative to the cross polar pattern since it provides the local isolation immediately.

The figure shows that the cross polar isolation inside the east coverage is better than 45 dB except for two very small points in the northern part. The same contour plots are now made for the case where PTD is included in the analysis. The results are shown in Figure 5.3-5.

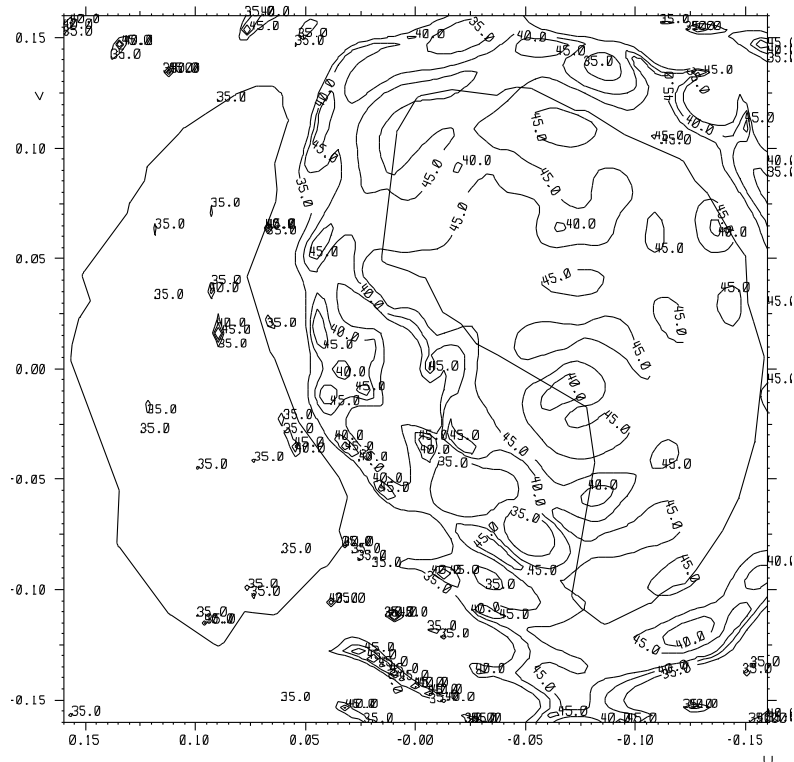


Figure 5.3-5 XPD contours at 35, 40 and 45 dB levels, when PTD is included in the analysis.

Now it is seen that contour levels of both 40 and 45 dB fill the coverage and the isolation is therefore worse than 40 dB.

The disagreements seen in the above figures may very well be the difference between a compliant and non-compliant design. The importance of including PTD can therefore not be over-emphasised in such situations, whereas there are many other examples where it is much less significant. For example, the co-polar pattern of the shaped antenna was also calculated using both methods, and no difference was observable even in the low sidelobe levels over the isolation region.

5.4 Dual gridded reflector

In Section 5.3 the antenna was operating in circular polarisation and it was observed how, in spite of the offset geometry, the cross-polarisation was sufficiently low to allow frequency re-use by means of polarisation discrimination. If linear polarisation is required, the matter is quite different because the offset geometry will imply cross-polarisation levels which are usually in the order of 20-25 dB below the co-polar beam peak level. Consequently other techniques must be employed. Two solutions are dominating: the dual reflector system where the offset surfaces are arranged in such a way as to minimise the geometrically induced de-polarisation, or the gridded reflector where the surface is manufactured from a polarisation sensitive material. Here we shall consider the latter configuration where the polarisation sensitive material consists of a conducting grid.

Systems of the above type are commonly referred to as dual gridded reflectors. The term "dual" is due to the fact that there are most often two reflectors involved, but not in the usual configuration as subreflector and main reflector. Rather, both reflectors are "main reflectors", one for each orientation of linear polarisation. A typical geometry will be explained in the following.

5.4.1 Dual gridded reflector geometry

The antenna is manufactured from two shells, one behind the other, in such a way that they share the same circular output aperture when seen from the boresight direction. The front re-

flector is made from a grid of conducting strips aligned with the desired polarisation orientation of the far field. There is one feed for each reflector as seen in Figure 5.4-1.

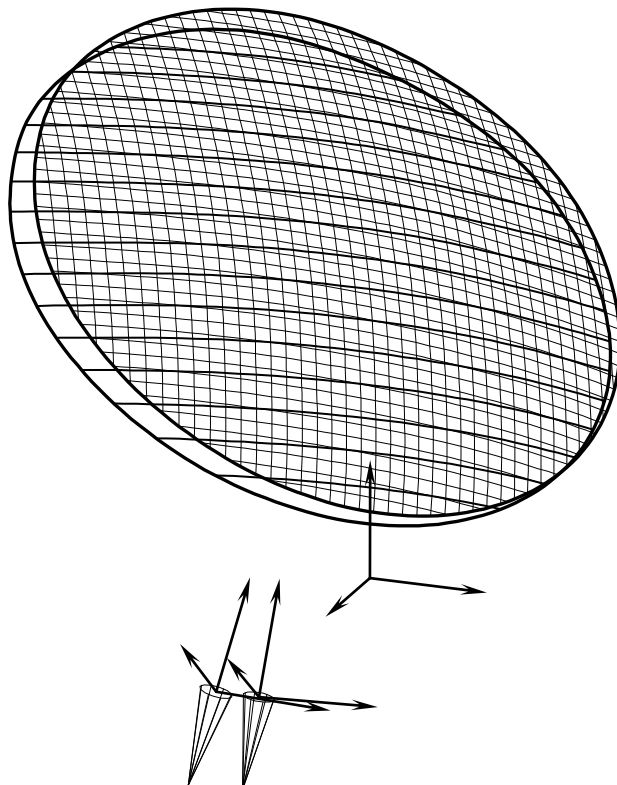


Figure 5.4-1 The dual gridded reflector geometry. The rear reflector is solid and the front reflector is a grid with strips perpendicular to the offset plane.

The function of the system is best described by assuming that the antenna transmits. The ray contributions are shown in the sketch in Figure 5.4-2. One of the feeds, the front feed, is oriented such that its linearly polarised field is aligned with the grid on the front reflector, to the greatest possible extent. Thus the co-polar component will be reflected by the front shell, whereas the feed cross polarisation will be transmitted

through to the rear shell (step 1 in Figure 5.4-2). This is normally made from normal, conducting surface material, and will reflect the feed cross polar field (step 2 in Figure 5.4-2). However, due to the asymmetric arrangement the cross polar field component will be reflected in a direction which can be significantly different from the boresight direction of the front reflector, and will thus appear at locations in the far field where it has no impact on the performance of the antenna. Furthermore, the field reflected in the rear shell is filtered by the grid on the front shell (step 3 in Figure 5.4-2).

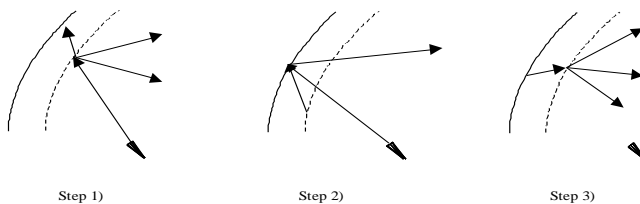


Figure 5.4-2

The three major scattering mechanisms in a dual gridded reflector: 1) scattering of the feed field in the front shell, 2) scattering of the front field and the feed field in the rear shell, 3) scattering of the rear field in the front shell.

The rear feed works in a similar way, except that the primary component of this feed is transmitted through the front shell and reflected by the rear.

To demonstrate the analysis procedure for dual gridded reflector antenna systems we will look at a design made for 12 GHz Ku-band coverage of Australia as shown in Figure 5.4-3.

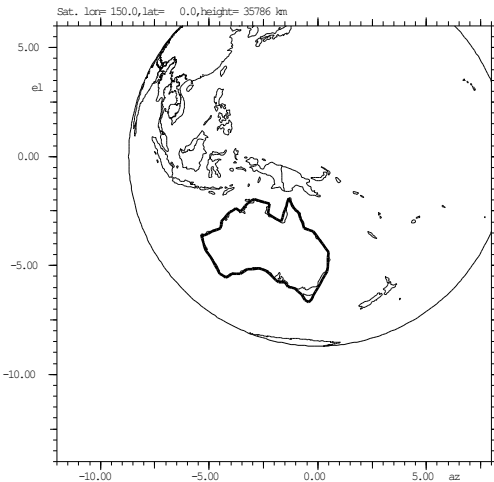


Figure 5.4-3 Coverage requirements for a dual gridded shaped reflector antenna system. Design frequency = 12 GHz, spacecraft location = 150° East. The antenna points 1.81° to the West (Azimuth) and 4.13° to the South (Elevation) relative to the subsatellite point.

The diameter of both shells is 1.0 m and the focal lengths (before shaping) are 0.65 m for the rear and 0.6 m for the front reflector. They are rotated $\pm 3.5^{\circ}$ making it possible to place them behind each other and still have the feeds nearly in the same plane, a desirable feature when integrating the antenna on a spacecraft.

5.4.2 Analysis procedure

We have chosen to demonstrate the steps of the gridded reflector analysis by looking at how the rear feed radiation is scattered in the front and back reflectors. The basic steps are exactly the same for the front feed, but whereas the significant contribution to the scattered field comes from the rear reflector in the example, it would come from the front reflector if the front feed was considered.

The front antenna is made from conducting strips with a width of 0.25 mm and a periodicity of 1.25 mm mounted on a dielectric layer with a thickness of 0.4 mm and a dielectric constant of 2.5. These parameters are such as to ensure good reflection properties for the co-polarised field at 12 GHz whilst transmitting the orthogonal field with limited reflection loss. In GRASP the surface material properties are described in the strip_grid object of the electrical properties class. The strip grid is one of the possible reflector surface materials in GRASP and described in Section 2.2.3.5.

In order to fully appreciate the effect of the polarisation grid we first calculate the field from the rear reflector as if the front reflector was not there. The results are shown as contour plots in Figure 5.4-4 and Figure 5.4-5.

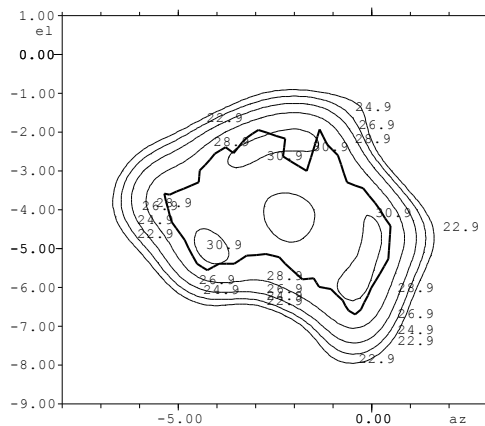


Figure 5.4-4 Co-polar radiation from rear antenna without the front reflector present. Contours are in steps of 2 dB with the highest at 30.9 dBi.

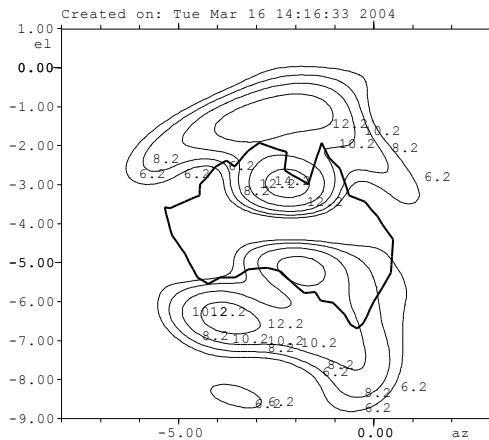


Figure 5.4-5 Cross polar radiation from rear antenna without the front reflector present. Contour levels are in steps of 2 dB with the highest at 14.2 dBi.

It is seen that a normal, solid reflector antenna would give cross polar isolation around 16 dB, usually not commensurate with dual polarisation operation.

When the front reflector is present the three steps of an analysis are (referring to Figure 5.4-2):

1. Calculate the feed field scattering in the front reflector
2. Calculate the transmission of the feed field through the front reflector, and the associated reflection in the rear
3. Calculate the transmission of the rear reflector field through the front

All of the above contributions must be added in order to provide an accurate prediction of the radiated field. We will show each of them individually in the following.

5.4.2.1 *Rear feed reflected in the front reflector*

The rear feed is aligned such as to transmit as much of its co-polar field as possible through the front grid, and consequently it is only the feed cross polar component which gives rise to any considerable scattering in the front. As can be seen in Figure 5.4-6 this component can be quite high, but as it was also stated earlier, it falls outside the coverage region and is therefore of less importance.

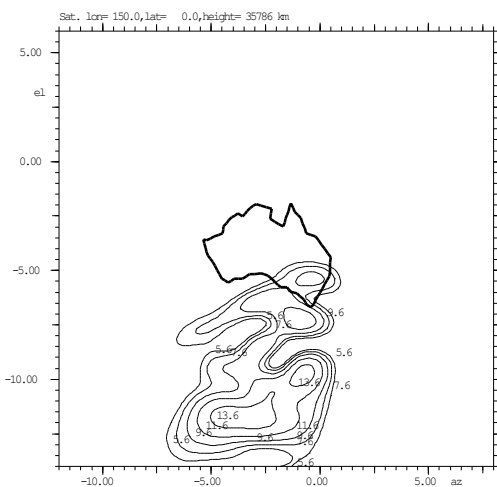


Figure 5.4-6 Cross polar field from rear feed scattered in the front reflector. Highest contour level inside the coverage is 9.6 dBi.

5.4.2.2 *Rear feed through front reflector, scattered in the rear*

The transmission through the front reflector must be calculated in order to determine the induced currents on the rear reflector. This may be done by using either GO or PO on the front reflector. If the reflector can be assumed to be in the far field of the feed (as is very often the case in these systems) GO may be used. The GO analysis in GRASP will trace the direct ray through the front reflector, modify the radiation according

to the surface material properties, and generate the induced currents on the rear.

If on the other hand the reflectors are in the near field of the feed it is necessary to employ PO and first generate induced currents on the front shell and then use these, plus the direct field from the feed, to find the rear reflector currents. In this process it is important to realise that the rear reflector is strongly in the near field of the front reflector and thus a very fine integration grid is necessary on the front.

Once the currents on the rear reflector have been obtained they may be integrated to obtain the scattered far field. The co-polar component is presented in Figure 5.4-7.

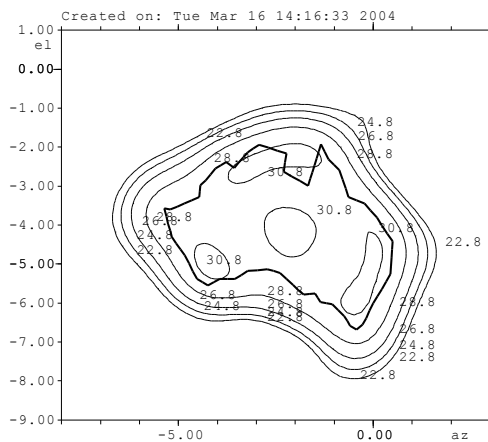


Figure 5.4-7 Co-polar radiation pattern from the rear feed reflected in the rear reflector. The levels are identical to those shown for a solid reflector in Figure 5.4-4.

It is seen that the pattern is for all practical purposes identical to what was obtained with the solid reflector. The cross polar pattern, on the other hand, is much different from that shown in Figure 5.4-5, as can be seen in Figure 5.4-8. However, it is not representative of the final performance of the reflector system, since we have not yet incorporated the effect of the rear reflector field being transmitted through the front reflector and thus passing the polarisation filter once more.

It is important to emphasise that the predicted performance in Figure 5.4-8 is nearly as poor as that in Figure 5.4-5. This has to do with the arrangement of the two reflectors relative to each other, and demonstrates the importance of including all contributing effects into the calculations before a reliable prediction is obtained.

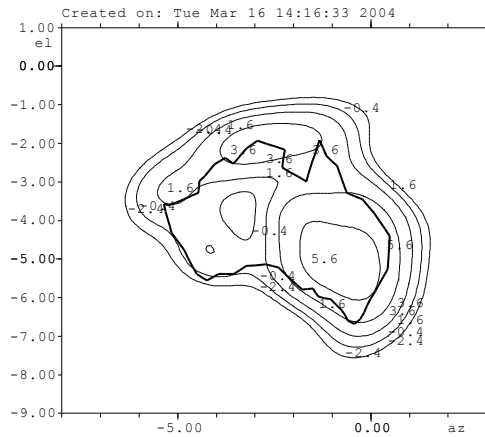


Figure 5.4-8 Cross polar radiation pattern from the rear feed reflected in the rear reflector. The levels are in steps of 2 dB with the highest at 5.6 dBi.

Finally it is mentioned that because we are using a simple far field model for the feed it has no significance if we use GO or PO for the above predictions.

5.4.2.3 Transmission of the rear reflector field through the front reflector

The next step is to calculate the transmission through the front reflector. This is done by calculating induced currents on the front when illuminated from the rear by the rear reflector currents. These currents are the same as those calculated in the previous paragraph, but it should be recognised that whereas we in the previous step would need an integration grid of a certain density in order to obtain convergence in the

far field, it is important with a much more dense grid now due to the proximity of the two reflectors.

The incident field on the front reflector will have a cross polar component caused by depolarisation in the rear reflector. It will be parallel to the grid on the front reflector and hence nearly completely blocked by the grid. Consequently the scattered component from the front shell must be fairly large in order to cancel the far-field component of the incident field, as described in Section 3.8.3.

The incident field will also have a co-polar component, the wanted component, which is orthogonal to the grid and thus largely unaffected by transmission through the grid. The scattered field due to this component will therefore be very small. Figure 5.4-9 and Figure 5.4-10 show these characteristics.

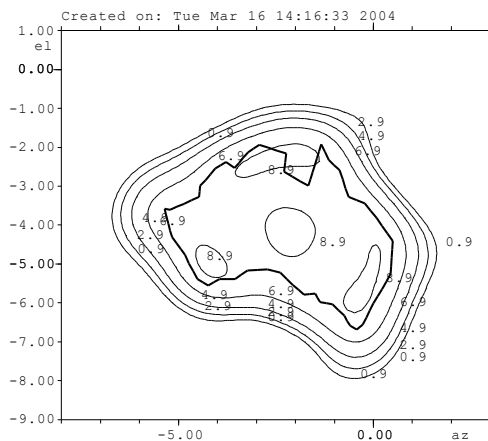


Figure 5.4-9 Co-polar component of scattered field from front reflector when illuminated from the rear by the rear reflector. The highest contour level is 9.0 dBi.

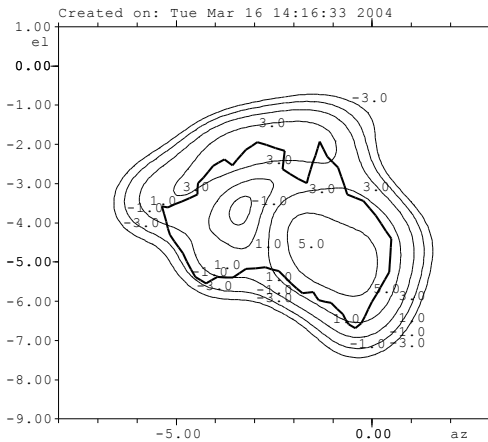


Figure 5.4-10 Cross polar component of scattered field from front reflector when illuminated from the rear by the rear reflector. The highest contour level is 5.3 dBi.

The cross polar pattern closely resembles the pattern from the rear reflector, and if also the phase was plotted we would have seen approximately 180° of phase difference, as there should be for the two components to cancel out.

5.4.2.4 Total field

We can now add each of the contributions in Sections 5.4.2.1 to 5.4.2.3 to obtain the total scattered field from the antenna system, as seen in Figure 5.4-11 and Figure 5.4-12.

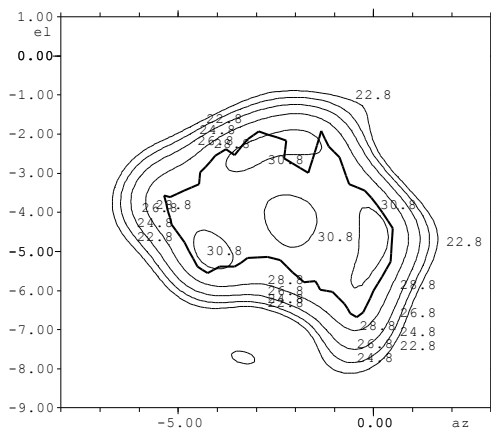


Figure 5.4-11 Total co-polar field from the dual gridded reflector system when using the rear feed. The levels are in steps of 2 dB with the highest at 30.8 dBi.

The co-polar pattern is almost unaffected by the presence of the front reflector in this example (compare Figure 5.4-4 and Figure 5.4-11).

The cross polar pattern is, as expected, widely changed by the polarisation grid. The final pattern shows the lobe which came from the first reflection in the front reflector, whereas the secondary filtering of the field from the rear reflector results in the first contour inside the coverage region being at a level of 7.9 dBi. The cross polar isolation inside the coverage is thus better than 21 dB - indeed it is much better than that over most of the coverage.

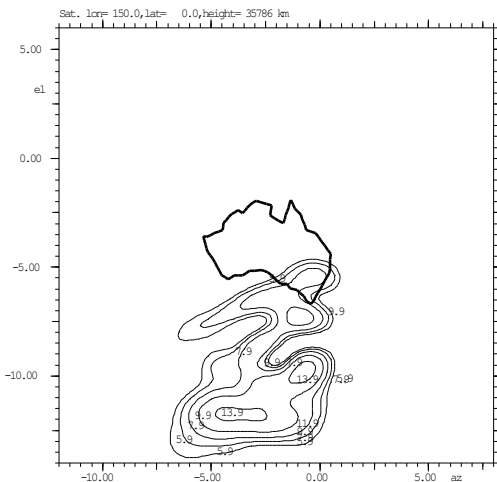


Figure 5.4-12 Total cross polar field from the dual gridded reflector system when using the rear feed. The levels are in steps of 2 dB with the highest at 13.9 dBi.

5.4.3 A closer look at the scattering between the rear and the front reflector

The front reflector is composed of a non-isotropic material and therefore its transmission and reflection characteristics depend on the direction of the incident field. This is not a problem when the illuminating source is the feed, but when the front reflector is illuminated by the rear reflector which is analysed by means of PO it is not obvious how to define this direction, as the source can no longer be characterised as a point source.

As explained in Section 3.4 GRASP provides for various techniques to deal with this problem. In the present example there are two relevant approaches. One is to calculate the incident E- and H-field, determine the real part of Poynting's vector and use its direction. This is achieved by setting the value of the ray_output attribute in the PO object to "none".

The other and more rigorous method consists of treating each current element on the rear surface as a point source when calculating the induced currents on the front. In this case the value of the `ray_output` attribute should be "all". In general this will require much more computer time, but will also provide a more accurate solution to the problem.

In the previous results the simple method was used, but to examine the differences we have also applied the other technique. While there are no visible differences in the co-polar plots, it is possible to observe some differences in the cross polar contours. The cross polar pattern using the last method is shown in Figure 5.4-13

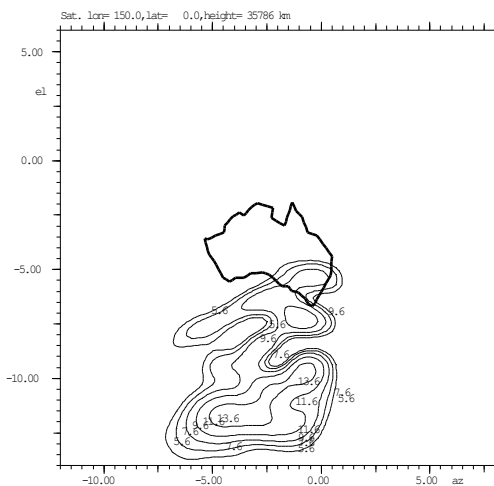


Figure 5.4-13 Cross polar pattern from the shaped dual gridded antenna when using the "`ray_output = all`"-option. The levels are in steps of 2 dB with the highest at 13.6 dBi.

This figure should be compared to Figure 5.4-12 and it is seen that there are very few differences, because the main characteristics are determined by the feed scattering in the front shell and thus not affected by the more detailed analysis. The peak level is altered by 0.3 dB as is the maximum inside the coverage. Even though this difference is very low it may still be important to employ the more accurate of the two models

when the requirements to the isolation are significant, but this has to be considered against the increase in computer time which is inherent with the change of method. Since these types of antennas are normally employed on spacecraft, they are limited in size and do not set insurmountable requirements to the computation speed in general. It may therefore be worthwhile to employ the rigorous method in the final analysis of such systems.

5.5 Feed array

In Section 5.4 a dual gridded antenna with two surfaces shaped for optimum illumination on Australia was analysed.

Shaping the surface of a reflector is one way of generating a contoured beam tailored to a specific coverage – another method is to let an array of feeds illuminate a parabolic reflector. The footprints of the associated beams form a grid covering the region of interest, in this case Australia, and the optimum illumination is obtained by optimising the amplitude and phase of the feeds.

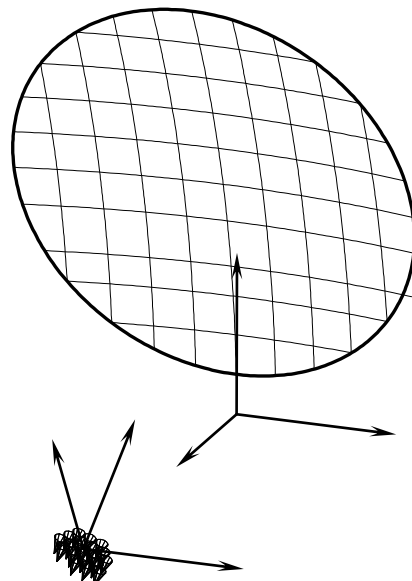


Figure 5.5-1 Multifeed, parabolic reflector

Figure 5.5-1 shows the multifeed, parabolic reflector applied in this example. The diameter of the reflector (projected aperture) is 1000mm and the frequency is 12 GHz, the same as for the dual gridded reflectors in Section 5.4. Hence, the results can be directly compared. The focal length is 1011.76mm and the array consists of 19 feeds, each with a diameter of 29.7mm (1.2λ).

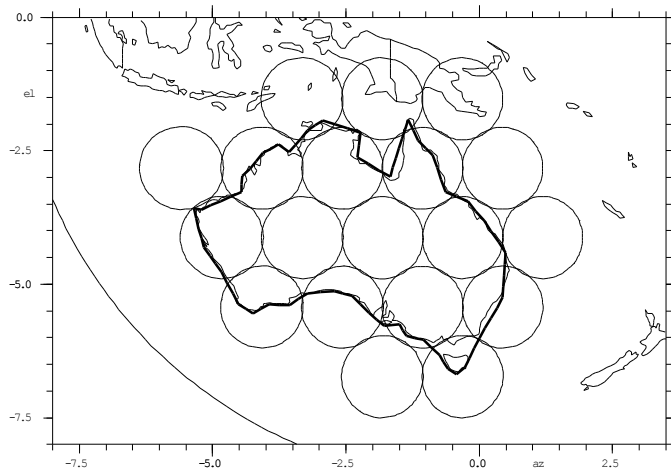


Figure 5.5-2 Footprint of element beams on Australian coverage

In Figure 5.5-2 the footprints (3 dB contours) of the beams from each feed (element beams) are shown on top of the coverage.

By means of the POS4 program the excitation coefficients (i.e. the amplitude and phase values) of the feeds are optimised. The result is the contoured beam shown in Figure 5.5-3.

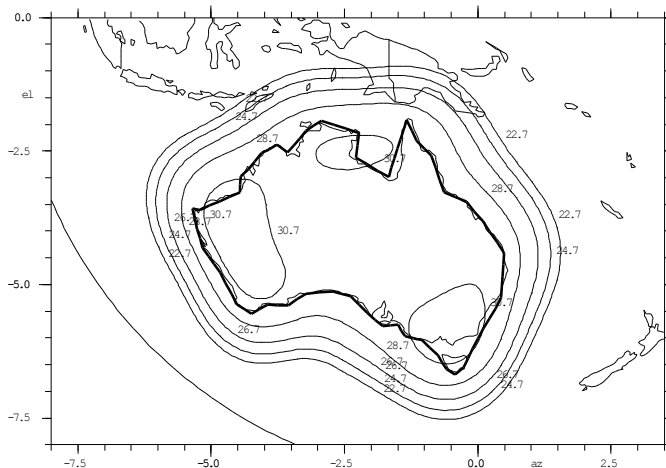


Figure 5.5-3 Optimised contoured beam. Contours at 1, 3, 5, 7 and 9 dB below maximum (31.7 dBi).

This figure should be compared to Figure 5.4-4. With a shaped surface reflector a minimum level of 29.9 dBi was obtained. With the multifeed geometry the optimised minimum level becomes 29.7 dBi. In addition, the beam forming network which is necessary in the multifeed case will introduce losses which reduces the gain of the antenna. The conclusion is that for simple coverages where no reconfigurability is necessary the shaped surface solution is superior in performance.

5.6 Compact antenna test range with serrated edges

The purpose of a compact antenna test range (CATR) is to create a plane wave field in which the antenna under test is placed. This is often achieved by means of a single offset paraboloid, a dual reflector system consisting of parabolic cylinders or a dual reflector system with an ellipsoidal/hyperboloidal subreflector and a parabolic main. In all cases the near field in front of the antenna is nearly a plane wave, with slightly different characteristics depending on the actual configuration. To GRASP, a compact test range is merely a reflector antenna system and can be analysed as such, using the near-field prediction capabilities of the program to as-

sess the quality of the quiet zone. As an example we will consider a CATR of the dual reflector type in the following.

5.6.1 Side-fed offset Cassegrain CATR

A special type of dual reflector antenna geometry which has been successfully employed in CATRs in the past is the side-fed offset Cassegrain, SFOC, as shown in Figure 5.6-1.

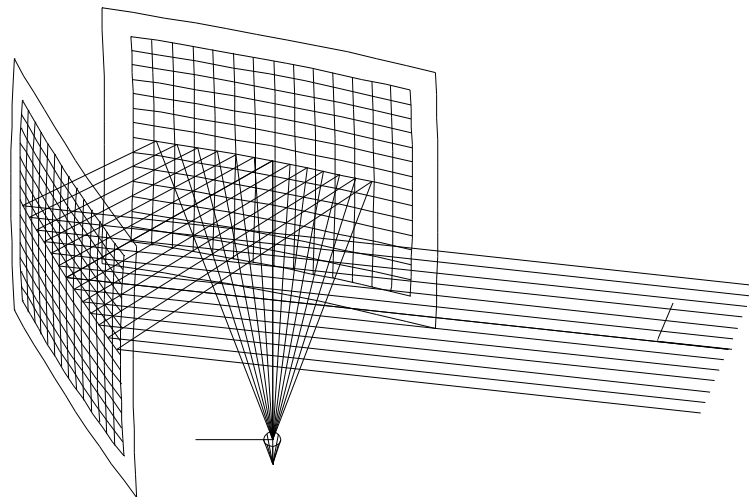


Figure 5.6-1 Example of a compact range with rays shown in the plane of symmetry.

The subreflector is part of a hyperboloid where the branch which is the closest to the feed is chosen (as opposed to regular Cassegrain systems where the most distant branch is used). The main reflector surface is parabolic in shape, and consequently the rays from the point-source feed located at the subreflector focal point will after two reflections form a parallel ray bundle as illustrated in Figure 5.6-1.

The edges of CATR reflectors are serrated in order to reduce diffraction effects which will otherwise create ripples in the plane wave field. A special feature is implemented in GRASP to analyse the influence of such serrations. As explained in Section 2.2.1.4 it is not the actual geometry of the serrations that is modelled. Rather, an inner rim is given inside which

the reflector is solid. An outer rim is also given corresponding to the tips of the serrations.

In the present example the subreflector inner surface is 8.14 m by 6.87 m and the outer boundary is 9.16 m by 7.62 m. The corresponding numbers for the main reflector are 7.30 m by 6.0 m and 8.8 m by 7.5 m and the serrations are assumed to taper off in a linear fashion. The extent of the serrations can be seen in the figure.

5.6.2 Analysis

The specification of a serrated rim has only effect on PO calculations where, as earlier explained, the current distribution is tapered off from where the serrations start to their tip in either a linear or a cosine fashion. The GTD calculations will simply ignore the serrations and generate results for a solid reflector with a boundary conforming to the outer rim. Thus to analyse the SFOC with serrations on both reflectors we will need to employ PO on both reflectors and use a very fine grid because the near field from both antennas shall be evaluated.

Nevertheless, due to the fact that the subreflector is electrically large we will analyse the radiation from this reflector by means of GO, considering only reflected and not diffracted rays. The effect of the serrations is to reduce the diffraction from the rim of the reflectors so this method seems to be adequate. Physical optics will on the other hand be used on the main reflector, and we will perform two sets of calculations, one where the serrations are present and one where they are not. In the latter case it is assumed that the solid reflector occupies the same space as the serrated reflector, in order to provide for a reasonable comparison.

In Figure 5.6-2 we have compared the results in the plane of symmetry or horizontal plane, corresponding to the rays shown in Figure 5.6-1. The benefit of the serrations is obvious as the ripples in the quiet zone are significantly reduced. It is noted that the beam is wider in the non-serrated case, because the main reflector in this case is larger as explained above.

The pattern in the orthogonal plane is shown in Figure 5.6-3 where the same effect can be observed, a dramatic reduction of the ripples in the quiet zone field.

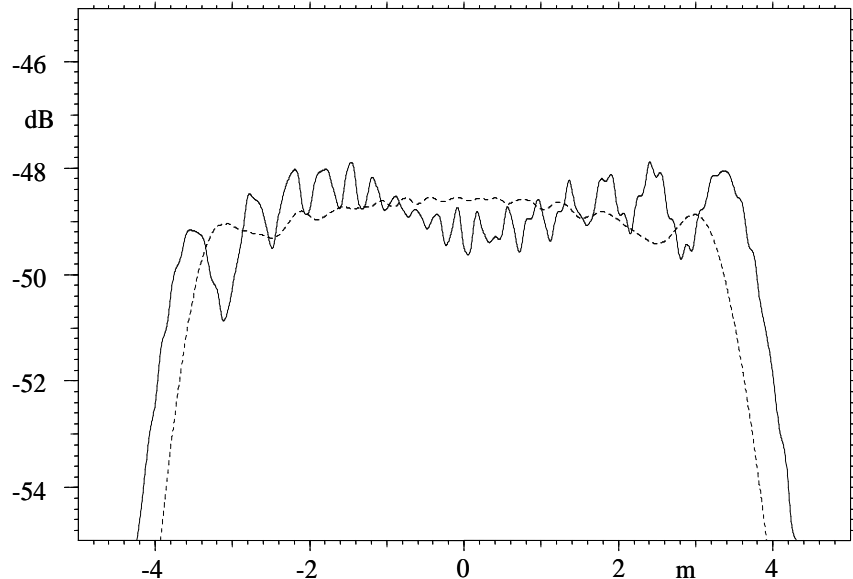


Figure 5.6-2 Near field in front of the main reflector in the plane of symmetry (horizontal plane). Solid line is without serrations, dashed is with.

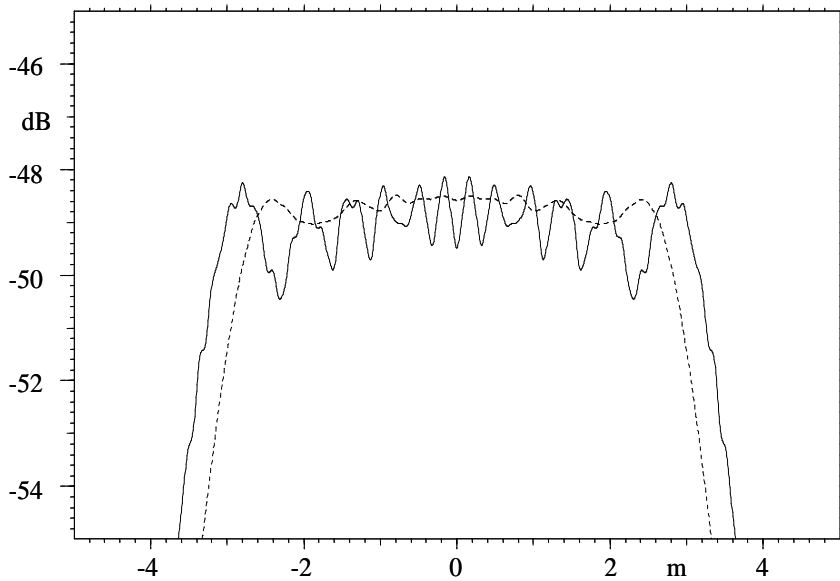


Figure 5.6-3 Near field in front of the main reflector in the plane orthogonal to the plane of symmetry (vertical plane). Solid line is without serrations, dashed is with.

The calculations are made at a frequency of 4 GHz where the size of the main reflector is 117 wavelengths by 100 wavelengths.

In the above calculations only the scattered field from the main reflector is included; however due to the flexibility of GRASP it would be a simple matter to add the field from the feed and the subreflector in order to study the influence of these components.

5.7 Beam waveguide

One of the powerful capabilities of GRASP is the efficient way of analysing a sequence of scatterers. This makes the analysis of a beam waveguide much easier than it was with previous versions of GRASP.

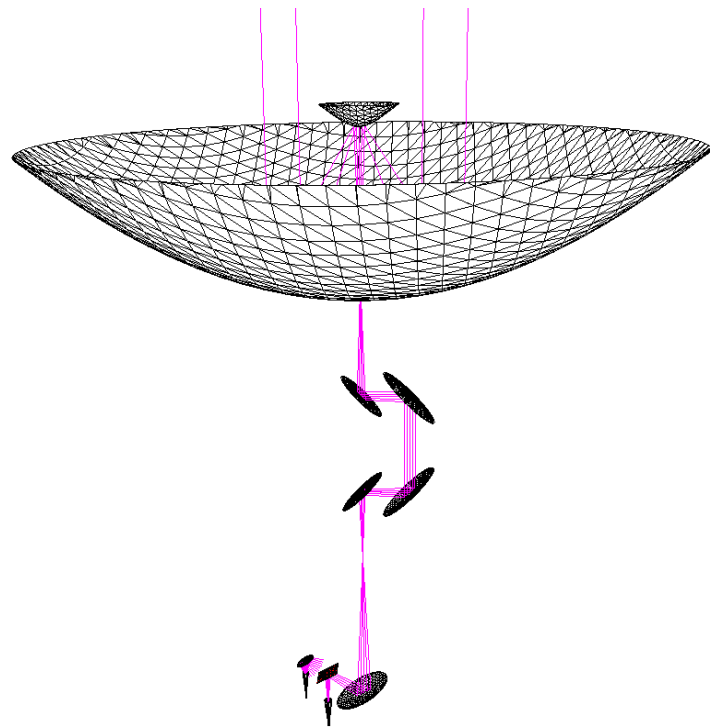


Figure 5.7-1 OpenGL drawing of a beam waveguide antenna (ESA Deep Space Antenna in Perth, Australia)

An example of a beam waveguide antenna is shown in Figure 5.7-1. This is a GRASP visualisation of the ESA Deep Space Antenna located in Perth, Australia, and analysed by Lumholt (1999). The configuration shall work in S-band and in X-band. In Figure 5.7-1 rays are drawn from the position of the S-band feed.

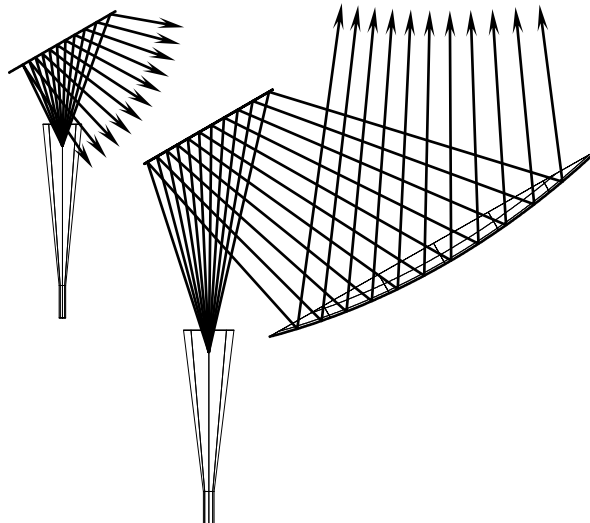


Figure 5.7-2 Close view of feed horns

In Figure 5.7-2 the feed horns and the first scatterers are shown. The rays from the X-band feed are reflected in a mirror (M7) and pass the dichroic mirror M6 before being reflected in the first conical mirror (ellipsoid, M5). The rays from the S-band feed are reflected in M6 and in the ellipsoid. For both feeds the rays are drawn from the best-fit phase centres.

In addition to the first mirror shown in Figure 5.7-2 four more mirrors are included in the ray path, as shown in Figure 5.7-1, before illuminating the sub- and main reflectors.

In the realised instrument the horns radiate circular polarisation and the mirror M6 separating the frequencies is a frequency selective surface (FSS). In this test case the circular polarisation has been replaced by linear polarisation. The S-band feed is polarised in the paper plane in Figure 5.7-2 and the X-band feed is polarised perpendicular to the paper plane. The FSS mirror (M6) has been replaced by a polarisation sensitive grid (ideal grid) with grid lines parallel to the paper plane.

By cascaded Physical Optics calculations the field scattered by one reflector is calculated on the next reflector until the far field from the main reflector is calculated. At S-band the result is the pattern shown in Figure 5.7-3 for the antenna pointing at zenith.

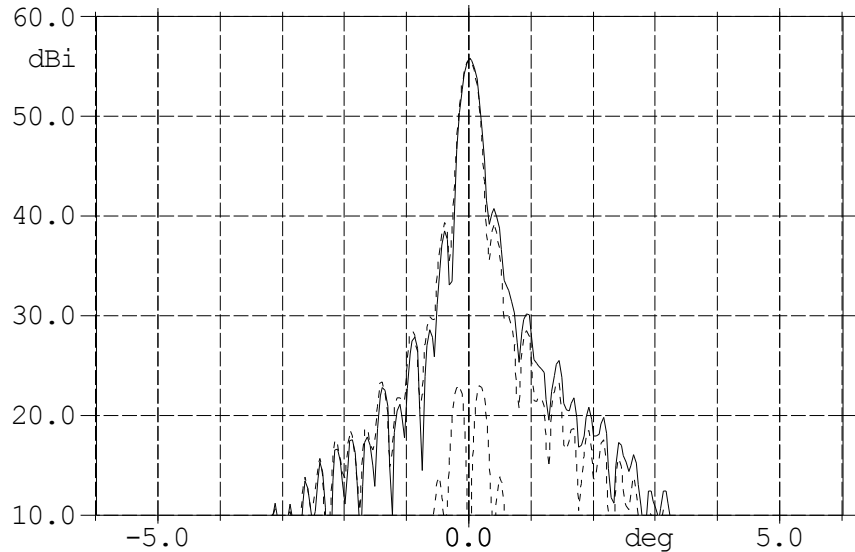


Figure 5.7-3 Far field at S-band. Full line is pattern in symmetry plane – dashed line is pattern in perpendicular plane.

The pattern calculated at X-band is shown in Figure 5.7-4.

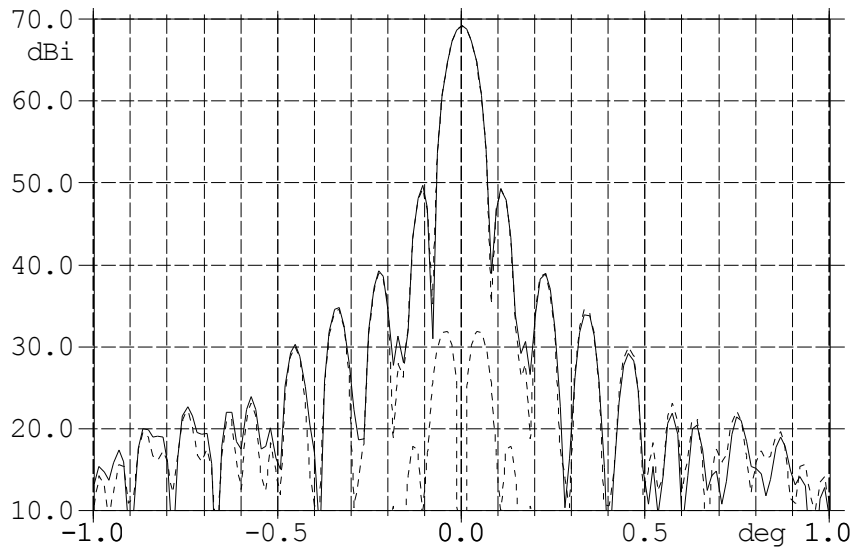


Figure 5.7-4 Far field at X-band. Full line is pattern in symmetry plane – dashed line is pattern in perpendicular plane.

6. USEFUL GEOMETRICAL RELATIONS FOR REFLECTOR ANTENNAS

The surfaces of reflector antennas are often constructed from simple conical surfaces such as paraboloids, hyperboloids and ellipsoids. This chapter describes the most basic and useful geometrical relations for these types of reflector surfaces.

The diffracted rays from the edge of the reflector will often generate caustics in certain directions. The location of these caustics are presented in Section 6.4 for some typical standard antenna designs.

GRASP contains a feature for generating simple, single and dual reflector designs. Section 6.5 describes the input parameters for these designs. For the dual reflector antennas the concept of the equivalent single reflector is introduced and the compensated designs for low cross polarisation are presented.

6.1 Paraboloids

A rotationally symmetric paraboloid with focal length f and focal point F is defined. For a point $P(x, y, z)$ on the paraboloid and with the parameters given in Figure 6.1-1, the following relations hold

$$\rho^2 = x^2 + y^2, \quad (6.1-1)$$

$$\rho^2 = 4fz, \quad (6.1-2)$$

$$r = 2f / \sqrt{1 + \cos 2u} \quad (6.1-3)$$

$$= f + z \quad (6.1-4)$$

$$= f / \cos^2 u, \quad (6.1-5)$$

$$\rho = r \sin 2u \quad (6.1-6)$$

$$= 2f \tan u \quad (6.1-7)$$

$$z = f \tan^2 u \quad (6.1-8)$$

$$u = \arctan \rho / 2f . \quad (6.1-9)$$

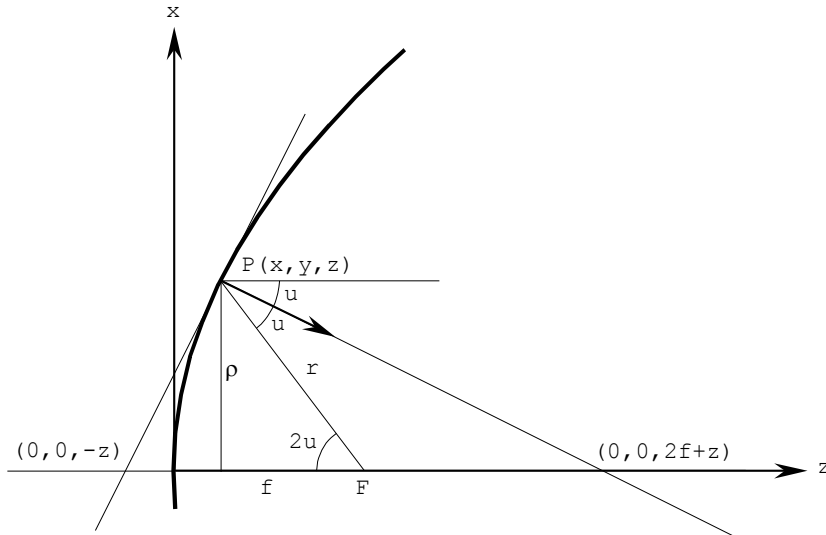


Figure 6.1-1 Geometrical parameters for paraboloid.

The tangent plane at P intersects the z -axis at $(0,0,-z)$. The normal \hat{n} at P intersects the axis at $(0,0,2f+z)$.

The surface curvature in the plane containing the z -axis is

$$\kappa = \frac{\cos^3 u}{2f}, \quad (6.1-10)$$

and the curvature in the orthogonal plane is

$$\kappa_t = \frac{\cos u}{2f}. \quad (6.1-11)$$

An offset paraboloidal reflector may be defined by the aperture diameter D and the clearance D' as indicated in Figure 6.1-2. The reflector rim is also the intersection between the paraboloid and a circular cone tilted the angle

$$\theta_o = \arctan \left\{ \frac{2f D + 2D'}{4f^2 - D' D + D'} \right\} \quad (6.1-12)$$

and with the half cone angle

$$\theta^* = \arctan \left\{ \frac{2fD}{4f^2 + D' D + D'} \right\}. \quad (6.1-13)$$

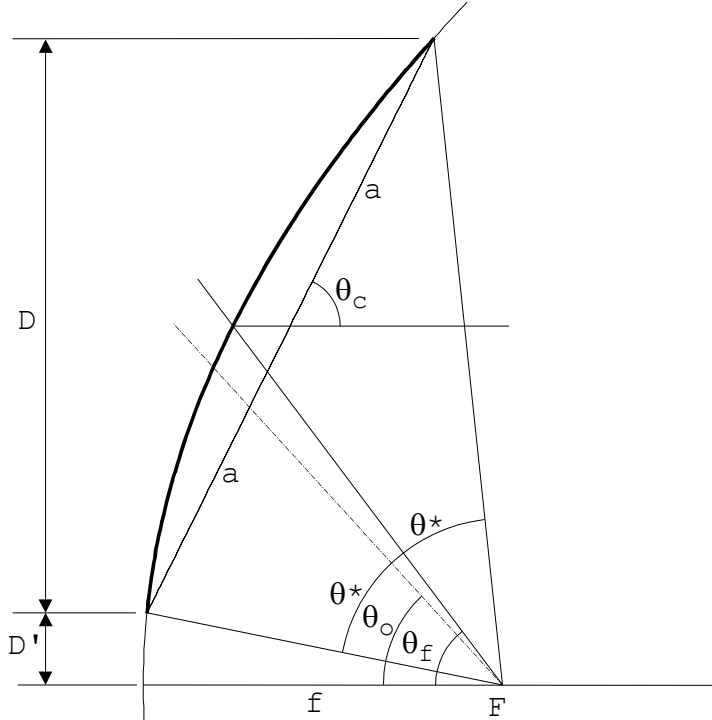


Figure 6.1-2 Offset paraboloidal reflector.

The feed will often be directed towards the centre point on the reflector, i.e. the feed axis is tilted the angle

$$\theta_f = 2 \arctan \left\{ \frac{D' + D/2}{2f} \right\} \quad (6.1-14)$$

The edge of the reflector is contained in a plane which makes the angle

$$\theta_c = \arctan \frac{2f}{D' + D/2} \quad (6.1-15)$$

with the z -axis. The edge curve is an ellipse where the major axis is

$$a = D/2 / \sin \theta_c \quad (6.1-16)$$

and the minor axis is $D/2$.

D and D' expressed by f , θ_o and θ^* become

$$D = 4f \sin \theta^* / \cos \theta_o + \cos \theta^* \quad (6.1-17)$$

and

$$D' = 2f \tan \theta_o - \theta^* / 2 . \quad (6.1-18)$$

6.2 Hyperboloids

A rotationally symmetric hyperboloid is defined by the distance between the focal points, $2c$, and the distance between the vertices, $2a$. With the parameters indicated in Figure 6.2-1 the following relations hold

$$\rho^2 = x^2 + y^2 , \quad (6.2-1)$$

$$z^2/a^2 - \rho^2/b^2 = 1 , \quad (6.2-2)$$

where

$$b^2 = c^2 - a^2 . \quad (6.2-3)$$

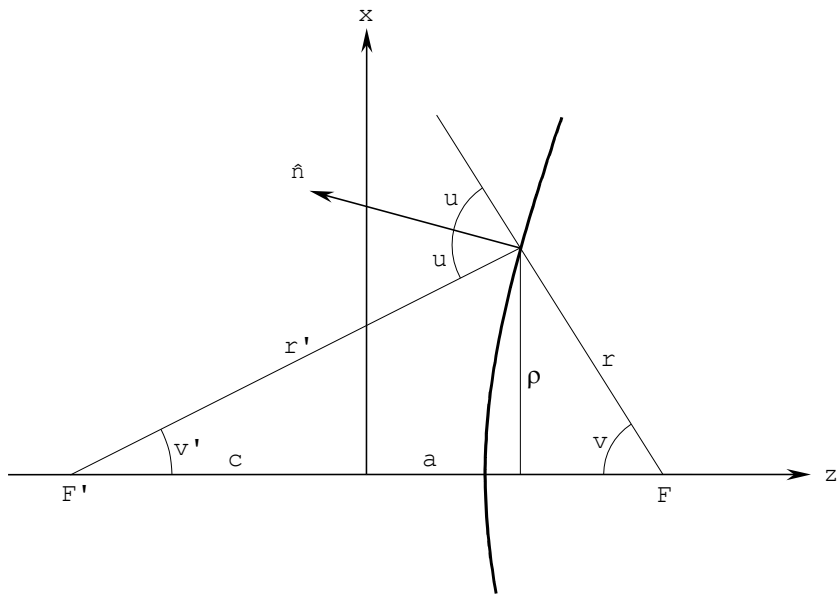


Figure 6.2-1 Geometrical parameters for hyperboloid.

The eccentricity is

$$e = c/a . \quad (6.2-4)$$

$$r = a \sqrt{e^2 - 1} / e \cos v + 1 , \quad (6.2-5)$$

$$r' = a \sqrt{e^2 - 1} / e \cos v' - 1 , \quad (6.2-6)$$

$$\rho = r \sin v \quad (6.2-7)$$

$$= r' \sin v' \quad (6.2-8)$$

$$e = \frac{\sin \frac{v+v'}{2}}{\sin \frac{v-v'}{2}} \quad (6.2-9)$$

$$e + 1 \tan v' / 2 = e - 1 \tan v / 2 , \quad (6.2-10)$$

$$2u = v + v' . \quad (6.2-11)$$

The surface curvature in the plane containing the z -axis is

$$\kappa = a \cos^3 u / b^2 \quad (6.2-12)$$

and the curvature in the orthogonal plane is

$$\kappa_t = a \cos u / b^2 \quad (6.2-13)$$

The rim of a rotationally symmetric hyperboloid is conveniently defined by means of the intersection with a circular cone as illustrated in Figure 6.2-2. The apex of the cone is located at the one focal point, F' , and the cone axis is tilted the angle ψ_o with respect to the hyperboloid axis. The half apex angle is ψ^* . It turns out that the intersection curve between the hyperboloid and the cone is a planar ellipse.

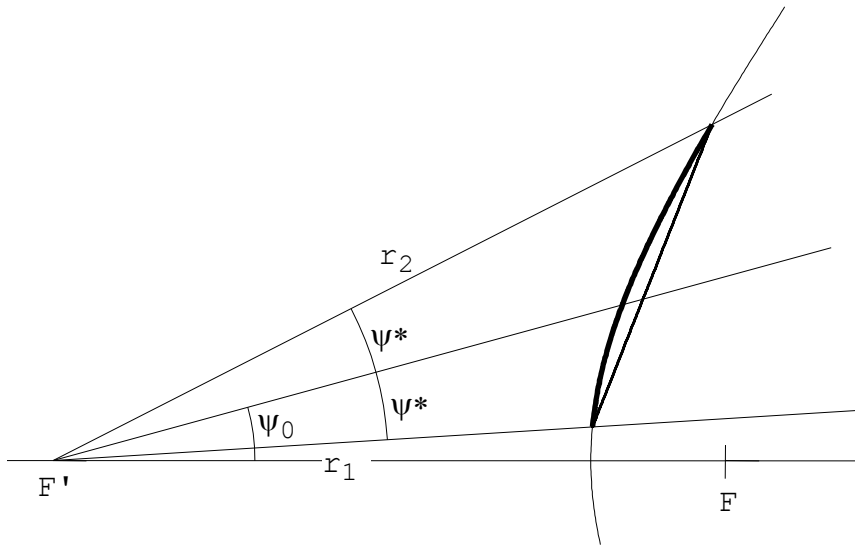


Figure 6.2-2 Determination of the rim of a hyperboloid by a circular cone.

The distances from F' to the top and bottom of the reflector are denoted r_2 and r_1 , respectively, and they may be calculated by expression (6.2-6). The major axis of the rim ellipse is now given by

$$2a_r = \sqrt{r_1^2 + r_2^2 - 2r_1r_2 \cos(2\psi^*)} \quad (6.2-14)$$

and the minor axis is

$$2b_r = \sqrt{(2a_r)^2 - (r_1 - r_2)^2} . \\ = 2\sqrt{r_1 r_2} \sin \psi * \quad (6.2-15)$$

6.3 Ellipsoids

A rotationally symmetric ellipsoid is defined by the focal distance, $2c$, and the major axis, $2a$. With the parameters indicated in Figure 6.3-1 the following relations hold

$$\rho^2 = x^2 + y^2 , \quad (6.3-1)$$

$$z^2/a^2 + \rho^2/b^2 = 1 , \quad (6.3-2)$$

where

$$b^2 = a^2 - c^2 . \quad (6.3-3)$$

The eccentricity is

$$e = c/a . \quad (6.3-4)$$

$$r = a \sqrt{1 - e^2} / \sqrt{1 + e \cos v} , \quad (6.3-5)$$

$$r' = a \sqrt{1 - e^2} / \sqrt{1 - e \cos v'} , \quad (6.3-6)$$

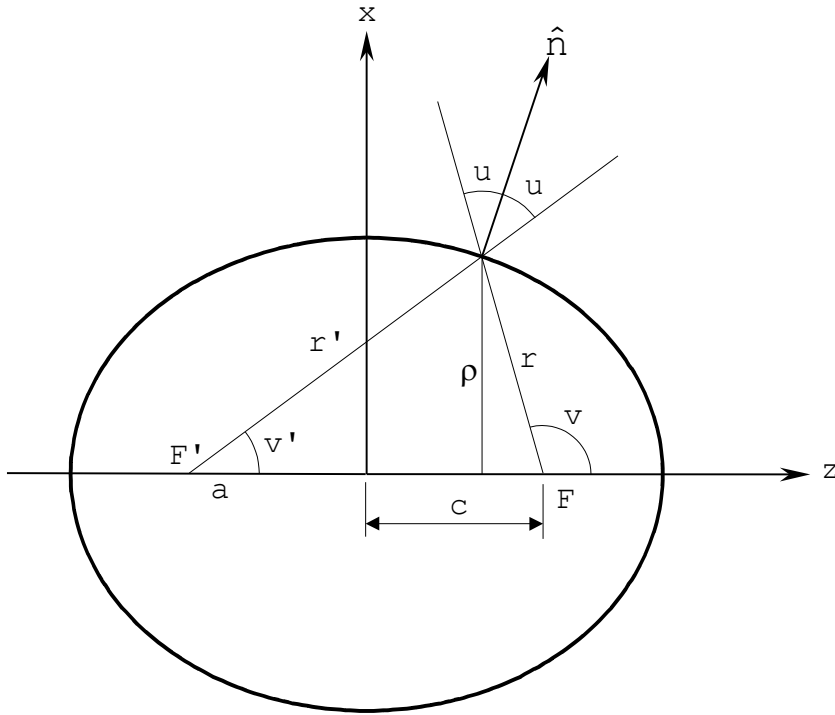


Figure 6.3-1 Geometrical parameters for ellipsoid.

$$\rho = r \sin v \quad (6.3-7)$$

$$= r' \sin v' \quad (6.3-8)$$

$$1 + e \tan v'/2 = 1 - e \tan v/2 , \quad (6.3-9)$$

$$e = \frac{\sin \frac{v-v'}{2}}{\sin \frac{v+v'}{2}} \quad (6.3-10)$$

$$2u = v - v' . \quad (6.3-11)$$

The surface curvature in the plane containing the z -axis is

$$\kappa = a \cos^3 u / b^2 \quad (6.3-12)$$

and the curvature in the orthogonal plane is

$$\kappa_t = a \cos u / b^2 . \quad (6.3-13)$$

Also for the ellipsoid the rim may be specified by the intersection with a circular cone and the expressions for the hyperboloid, (6.2-14) and (6.2-15), are directly applicable.

6.4 Caustic considerations

It has been demonstrated in the previous sections that the rim of a reflector is conveniently described by the intersection with a circular cone with apex at one of the focal points and the shape of the rim curve is a planar ellipse. The configurations are depicted in Figure 6.4-1-3 for the paraboloid, the hyperboloid and the ellipsoid, respectively.

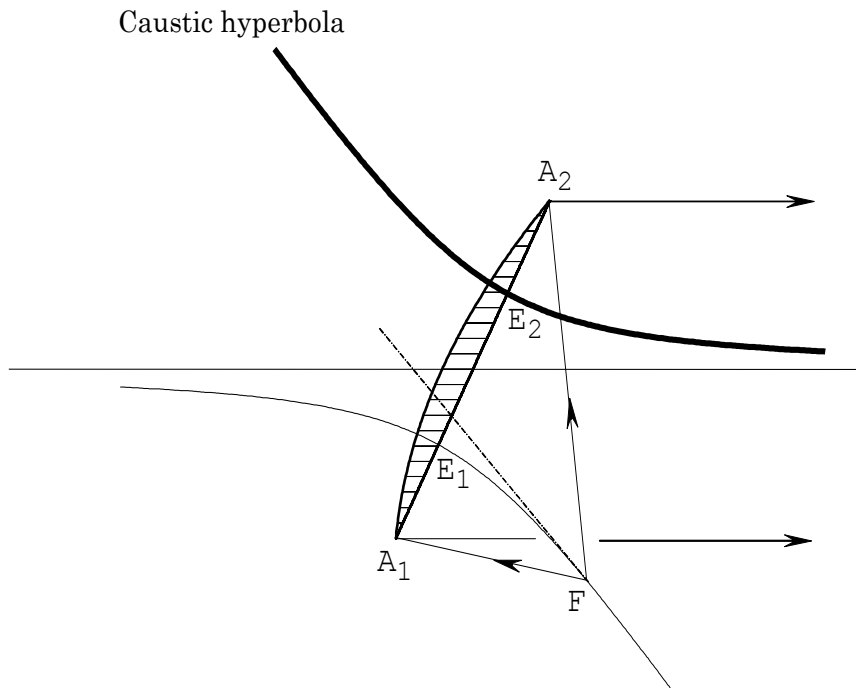


Figure 6.4-1 Caustic hyperbola for paraboloidal reflector with feed at F .

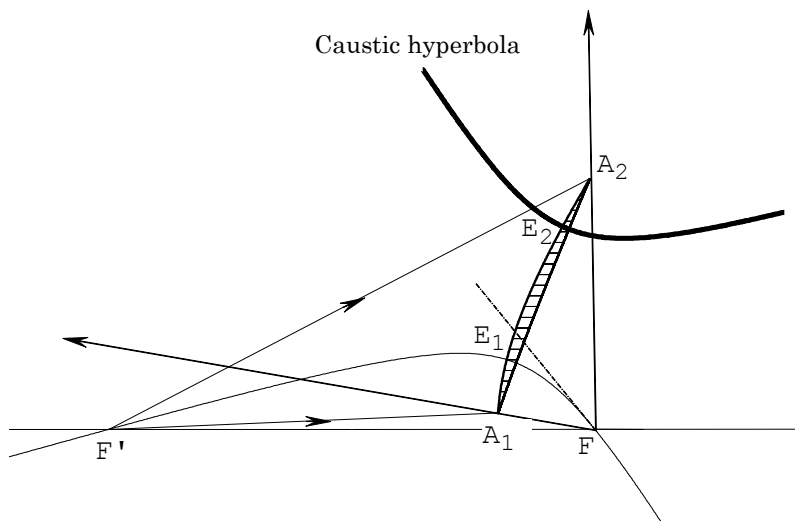


Figure 6.4-2 Caustic hyperbola for hyperboloidal reflector with feed at F' .

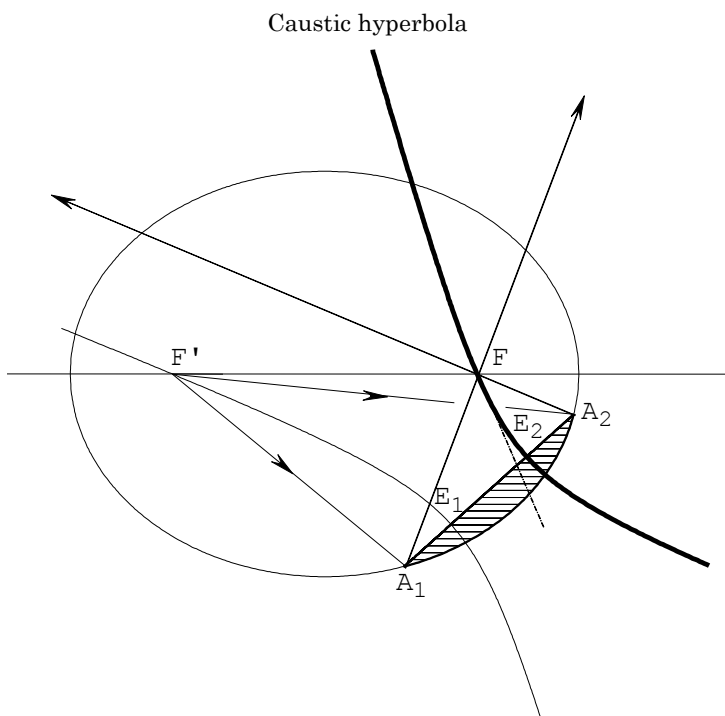


Figure 6.4-3 Caustic hyperbola for ellipsoidal reflector with feed at F' .

The major axis of the rim ellipse is denoted A_1A_2 on the figures and the points E_1 and E_2 are the focal points for the rim. A hyperbola may now be defined by A_1 and A_2 being the focal points and E_1 and E_2 the vertices. From any point on this hyperbola the reflector rim will appear as a circle. The hyperbola passes through the focal points of the reflector, F and F' . The path lengths from a point on the one hyperbola leg via any point on the reflector rim to a point on the other leg are all equal. If a feed is placed at one of the focal points, F or F' , this means that all points on the other hyperbola leg will be caustic points.

For far-field points the caustic directions will be the directions of the asymptotes of the caustic hyperbola. For the paraboloid in Figure 6.4-1 the one caustic direction is the boresight direction of the antenna. The caustic direction behind the antenna will be symmetrical with respect to the plane of the rim ellipse and it therefore appears for $\theta = 2\theta_c$, where θ_c is given by (6.1-15).

For the hyperboloidal reflector in Figure 6.4-2 the one hyperbola leg passes through both of the focal points F and F' . For the ellipsoidal reflector in Figure 6.4-3 each hyperbola leg goes through each separate focal point.

6.5 Basic reflector antenna designs

GRASP has a special feature for generating simple, single and dual reflector antennas. The designs are based on a few geometrical input parameters which must be supplied by the user. Upon the command "generate objects", the program will then automatically set up all the objects necessary for an analysis of the antenna. However, in this process a number of default parameters are selected internally, and if they are not satisfactory they must be modified by the user. The following sections describe the input parameters and the default parameters.

6.5.1 Single reflector design

The single reflector design is a focus-fed symmetrical or offset paraboloidal reflector antenna, as illustrated in Figure 6.5-1.

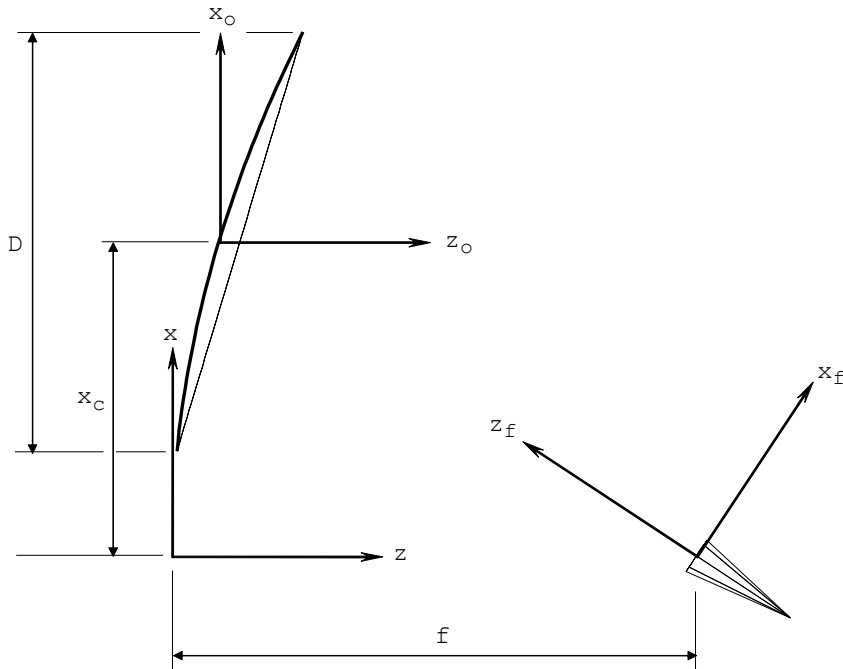


Figure 6.5-1 Single reflector design.

The following parameters are needed to specify the design:

D , aperture diameter of the paraboloidal reflector

f , focal length of the reflector

x_c , the distance from the paraboloid axis to the centre of the aperture

λ , the wavelength of the operating frequency

These parameters are sufficient to define the initial system. After issuing the "generate objects" command the additional default parameter settings are described in the following section.

6.5.1.1 Default parameters

6.5.1.1.1 Coordinate systems

Three coordinate systems are generated:

xyz	the global coordinate system with origin at the vertex of the main reflector paraboloid. The z -axis is parallel to the paraboloid axis and the xz -plane is the plane of symmetry.
$x_fy_fz_f$	the feed coordinate system with origin at the focal point and the z -axis pointing towards the centre of the reflector
$x_oy_oz_o$	the output coordinate system with the origin at the centre point of the reflector surface. The orientation is identical to the global coordinate system

6.5.1.1.2 Feed parameters

The feed is linearly polarised parallel to the plane of symmetry (the xz -plane) and the pattern is a Gaussian feed. The taper is -12 dB at the angle θ^* , where θ^* is the half apex angle of the cone defining the reflector rim, see Figure 6.1-2.

6.5.1.1.3 Output parameters

Two far-field polar cuts in the principal planes are specified. The angular region is symmetrical around the main beam and extends up to about the fourth side lobe. The output components are linear co and cross.

6.5.1.1.4 Computational approach

The antenna is intended to be analysed with PO and an integration grid is generated. The density of the grid is calculated automatically such that convergence is assured at least up to the fourth side lobe.

6.5.2 Dual reflector design

The dual reflector design is illustrated in Figure 6.5-2. It consists of a symmetrical or offset paraboloidal main reflector with focal point F and an ellipsoidal or hyperboloidal subreflector with focal points F and F' . The feed element is located at F' .

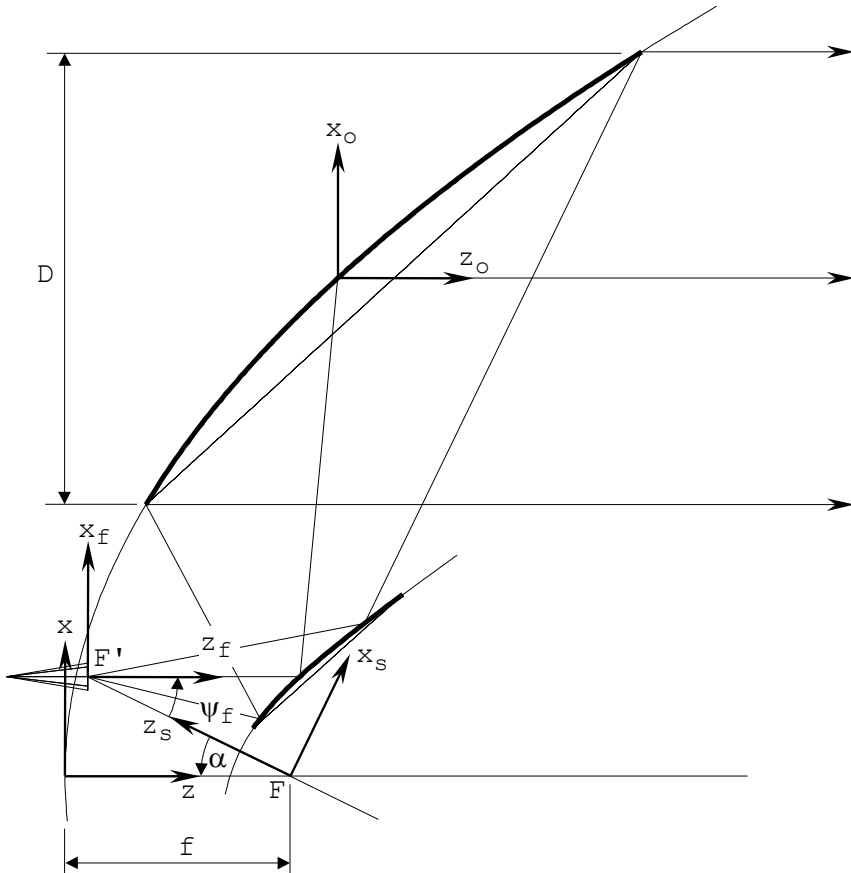


Figure 6.5-2 Dual reflector design parameters.
The parameters on the figure are:
 $f = 50\lambda$, $\alpha = -26^\circ$, $2c = 50\lambda$, $e = 2$,
 $D = 100\lambda$, $\psi_f = 26^\circ$, subreflector size 130%.
Note that for an ellipsoidal subreflector the $x_s y_s z_s$ -coordinate system is selected differently, cf. Section 6.5.2.1.1, such that the $x_s y_s$ -plane becomes parallel to the subreflector rim curve.

The following parameters are needed to specify the design:

- | | |
|-------------|--|
| f , | focal length of the reflector |
| α | angle from the main reflector axis to the subreflector axis, measured positive in the anti-clockwise direction |
| $2c$, | focal distance for the subreflector |
| e , | eccentricity for the subreflector, |
| ψ_f , | angle from the subreflector axis to the feed axis, measured positive in the anti-clockwise direction |
| D , | aperture diameter of the main reflector |
| λ , | the wavelength of the operating frequency |

Based on these parameters the design is constructed in the following way. The central ray from the feed, the direction of which is defined by the angles α and ψ_f , is reflected from the subreflector and hits the main reflector at a point which is selected as the centre for the circular main reflector aperture.

The above parameters may be typed in by the user, but it is also possible to control the position of the feed by means of the mouse. This allows the user to explore a large range of designs in an easy way. The mouse control of the feed only affects the values of the angle α and the focal distance $2c$.

It should be noted that both positive and negative values can be assigned for the angles α and ψ_f . Changing the sign of both angles simultaneously will result in the same antenna system.

The type of subreflector is controlled by the eccentricity e :

- | | |
|---------------|---------------------|
| $e > 1 :$ | convex hyperboloid |
| $0 < e < 1 :$ | ellipsoid |
| $e < -1 :$ | concave hyperboloid |

Before issuing the "generate objects" command it is necessary to specify the size of the subreflector. From Figure 6.5-2 it is seen that the top and bottom rays from the main reflector edge defines the part of the subreflector which is used for the illumination of the main reflector. For various reasons however, it is desirable to be able to change this size of the subreflector. This is explained in connection with Figure 6.5-3. The top and bottom rays define a cone with apex at F' and the cone axis being the bisector of these two rays. This subreflector size corresponds to 100%. Another size of the subreflector is obtained by specifying another half cone angle while keeping the cone axis unchanged. In Figure 6.5-2 and Figure 6.5-3 the subreflector size is selected to 130%.

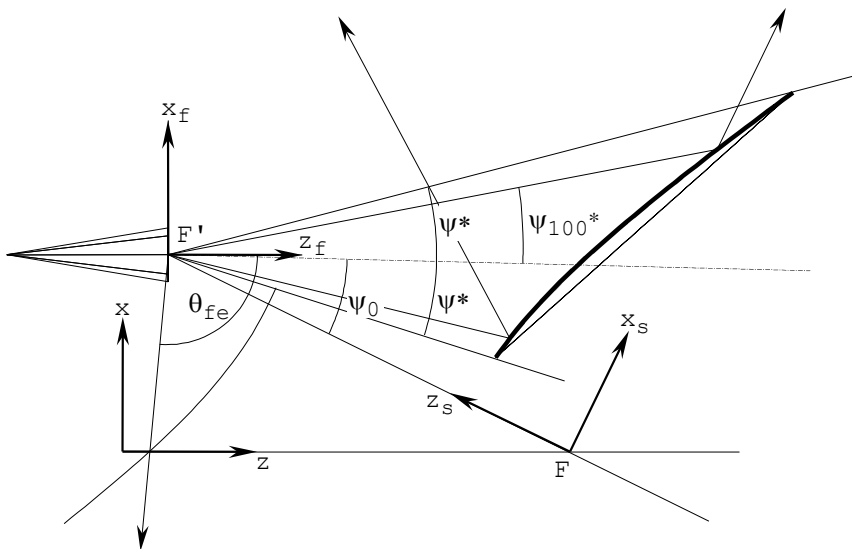


Figure 6.5-3 Details of subreflector. Note that for an ellipsoidal subreflector the $x_s y_s z_s$ -coordinate system is selected differently, cf. Section 6.5.2.1.1, such that the $x_s y_s$ -plane becomes parallel to the subreflector rim curve.

6.5.2.1 Default parameters

The default parameters set up in the objects for the dual reflector antenna system are described in the following subsections.

6.5.2.1.1 Coordinate systems

Four coordinate systems are generated:

- xyz the global coordinate system with origin at the vertex of the main reflector paraboloid. The z -axis is parallel to the paraboloid axis and the xz -plane is the plane of symmetry.
- $x_s y_s z_s$ the subreflector coordinate system with origin at the common focal point for the main and subreflector. For a hyperboloidal subreflector the z_s -axis is pointing along the subreflector axis. For an ellipsoidal subreflector the z_s -axis is orthogonal to the plane of the subreflector rim ellipse. The $x_s z_s$ -plane is the plane of symmetry
- $x_f y_f z_f$ the feed coordinate system with origin at the external focal point of the subreflector and the z_f -axis pointing along the feed centre direction defined above
- $x_o y_o z_o$ the output coordinate system with the origin at the centre point of the reflector surface. The orientation is identical to the global coordinate system

6.5.2.1.2 Feed parameters

The feed is linearly polarised parallel to the plane of symmetry (the xz -plane) and the pattern is a Gaussian feed taking possible near-field effects into account. The taper is -12 dB at the angle ψ_{100}^* , where ψ_{100}^* is the half apex angle of the

cone defining the reflector rim corresponding to a subreflector size of 100%, see Figure 6.5-3.

6.5.2.1.3 *Output parameters*

Two far-field polar cuts in the principal planes are specified. The angular region is symmetrical around the main beam and extends up to about the fourth side lobe. The output components are linear co and cross.

6.5.2.1.4 *Computational approach*

The antenna system is intended to be analysed with PO both for the main reflector and the subreflector. The integration grid density for the main reflector is determined automatically such that convergence is assured at least up to the fourth side lobe. The integration grid for the subreflector is determined automatically such that convergence is assured both for the calculation of the incident field on the main reflector and for the output points.

In many cases it may be preferable to analyse the subreflector by GTD, especially if it is large in terms of the wavelength and it can be assumed that it is the far field from the feed element. In this case the user must define the associated GTD object.

6.5.2.2 *Equivalent single reflector paraboloid*

It may be shown that it is possible to define an equivalent, paraboloidal, single reflector antenna with the same aperture diameter D and illuminated by the same feed. The equivalent reflector antenna for the system in Figure 6.5-2 is shown in Figure 6.5-4.

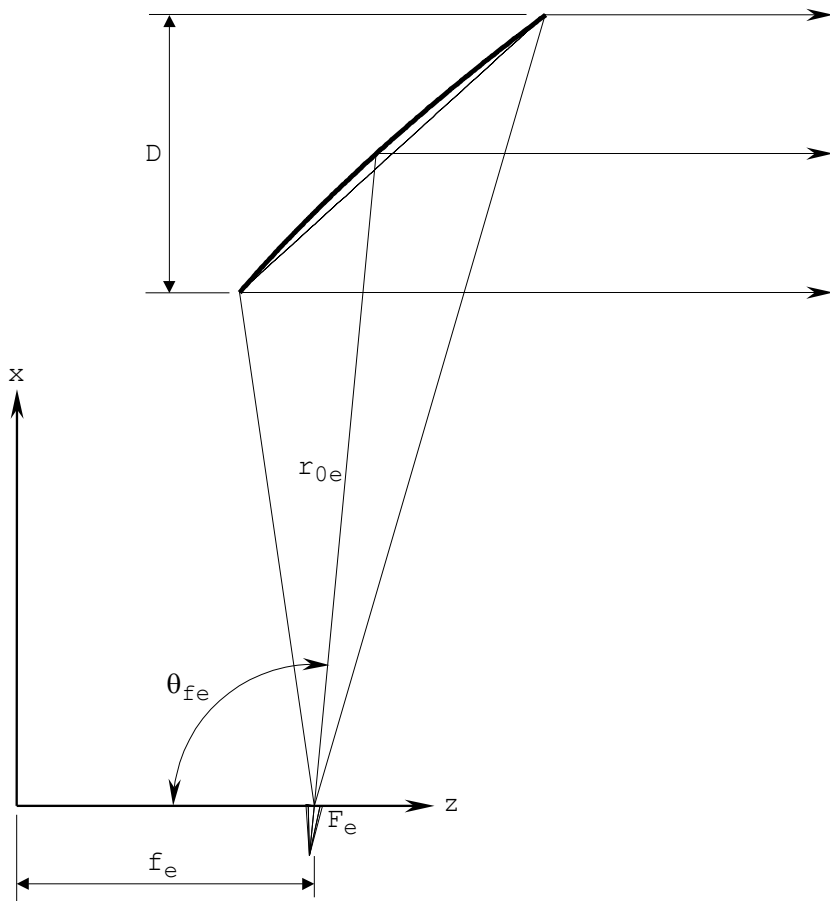


Figure 6.5-4 The equivalent single reflector antenna corresponding to Figure 6.5-2.

The equivalent focal length, f_e , is given by

$$f_e = f M_0 \frac{1 + \tan^2\left(\frac{\alpha}{2}\right)}{1 + M_0^2 \tan^2\left(\frac{\alpha}{2}\right)} \quad (6.5-1)$$

where

$$M_0 = \frac{e+1}{e-1} . \quad (6.5-2)$$

Note, that for an ellipsoidal subreflector M_0 is negative indicating that the rays reflected from the subreflector form a convergent bundle of rays.

The angle, θ_{fe} , to the centre point on the reflector is given by

$$\tan\left(\frac{\theta_{fe}}{2}\right) = \frac{\tan\left(\frac{\psi_f}{2}\right) - M_0 \tan\left(\frac{\alpha}{2}\right)}{1 + M_0 \tan\left(\frac{\alpha}{2}\right) \tan\left(\frac{\psi_f}{2}\right)} \quad (6.5-3)$$

and the distance, r_{oe} , from the focal point, F_e , to the centre point on the reflector is

$$r_{oe} = \frac{2f_e}{1 + \cos\theta_{fe}} \quad . \quad (6.5-4)$$

The offset angle, θ_{fe} , for the equivalent paraboloid can be found on Figure 6.5-3 as the angle between the feed axis z_f and the ray coming from the positive z -direction through the focal point F and reflected in the other leg of the hyperbola specifying the subreflector.

From Figure 6.5-4 it is seen that a beam scan θ will require a lateral displacement of the feed of $r_{oe}\theta$. One of the advantages of the concept of the equivalent system is that the same feed displacement will provide the same beam scan for the equivalent and for the real dual reflector system. The equivalent system can therefore be used for the initial lay-out of the feed array design.

The scan principle is illustrated in Figure 6.5-5 where the pattern for the dual reflector antenna in Figure 6.5-2 is compared to the pattern for the equivalent single reflector antenna in Figure 6.5-4 for two feed elements, one feed at focus and one feed displaced laterally according to a beam scan of 1° . With the dimensions in Figure 6.5-2 one finds $r_{oe} = 235.79\lambda$ and the displacement of the feed is therefore 4.12λ . A feed scan will normally also require a repointing of the feed axis in order to reduce spillover losses. This repointing is not included in Figure 6.5-5 and it cannot be determined from the equivalent reflector system.

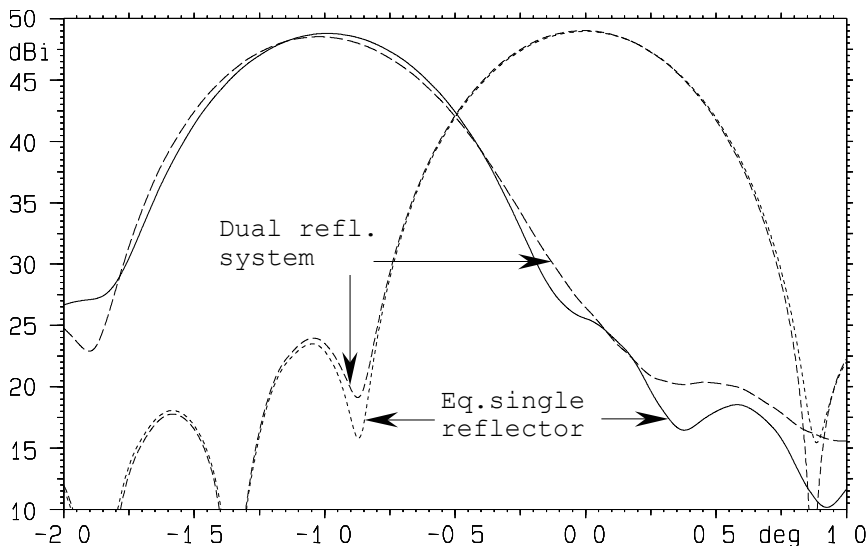


Figure 6.5-5 Far-field patterns for a feed at focus and a feed displaced for 1° scan in the plane of symmetry.

6.5.2.3 Compensated dual reflector systems

Expression (6.5-3) shows that the offset angle for the equivalent paraboloid is zero when

$$\tan\left(\frac{\psi_f}{2}\right) = M_0 \tan\left(\frac{\alpha}{2}\right) . \quad (6.5-5)$$

In this case the equivalent system is therefore a front-fed rotationally symmetric parabolic antenna. This also implies that the cone axis angle, ψ_o in Figure 6.5-3, becomes equal to ψ_f . In other words, the feed axis is also the axis of the cone defining the subreflector edge. The relation (6.5-5) is referred to as the Mizuguchi condition and the reflector antenna is denoted a compensated system.

Compensated reflector antenna systems are normally supplied with a feed with a rotationally symmetric pattern and they then possess very attractive properties:

Due to the offset it is possible to obtain a blockage-free design.

Using Geometrical Optics on the subreflector: the main reflector aperture field is rotationally symmetric.

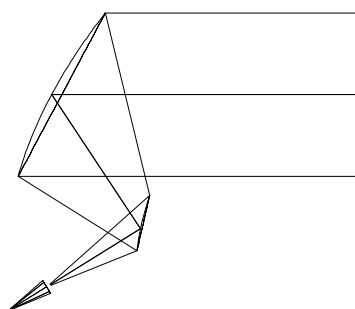
Using Geometrical Optics on the subreflector: for a linearly polarised feed the main reflector surface currents will lie in parallel planes.

The cross polarisation performance, which is generally poor for offset systems, is comparable to similar rotationally symmetric single reflector systems.

The Mizuguchi condition also minimises the scan aberrations.

The Mizuguchi condition may be activated in the simple dual reflector designs in GRASP. In this case the feed direction angle ψ_f is disabled and calculated internally by expression (6.5-5).

Three typical examples of compensated dual reflector antennas are illustrated in Figure 6.5-6. The three antennas have the same aperture diameter $D = 80\lambda$. Also the other input parameters are listed for each design together with the equivalent focal length given by (6.5-1). The top antenna is a Cassegrain design where the subreflector is a convex hyperboloid and the centre antenna is a Gregorian design with an ellipsoidal subreflector. It is noted that for both the Cassegrain and the Gregorian antenna the equivalent focal length is almost three times the focal length of the parent paraboloid. The third antenna in Figure 6.5-6 is called a compact range antenna because the design is typical for a number of compact ranges.

**Cassegrain antenna:**

$$f = 80\lambda$$

$$\alpha = 8^\circ$$

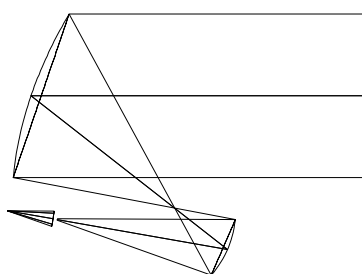
$$2c = 60\lambda$$

$$e = 2$$

$$(\psi_f = 23.70^\circ)$$

$$D = 80\lambda$$

$$f_e = 231.01\lambda$$

**Gregorian antenna:**

$$f = 80\lambda$$

$$\alpha = 5^\circ$$

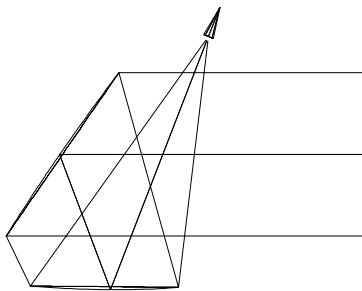
$$2c = 60\lambda$$

$$e = 0.5$$

$$(\psi_f = -14.92^\circ)$$

$$D = 80\lambda$$

$$f_e = -236.40\lambda$$

**Compact range antenna:**

$$f = 300\lambda$$

$$\alpha = 80^\circ$$

$$2c = 480\lambda$$

$$e = -2$$

$$(\psi_f = 31.25^\circ)$$

$$D = 80\lambda$$

$$f_e = 158.04\lambda$$

Figure 6.5-6

Three typical compensated dual reflector antennas

Top: convex hyperboloidal subreflector

Centre: ellipsoidal subreflector

Bottom: concave hyperboloidal subreflector.

7. REFERENCES

- Abramowitz & Stegun (1965),
"Handbook of mathematical functions", Dover Publications Inc., USA.
- Astrakhan, H.I. (1968),
"Reflecting and screening properties of plane wire grids", Radio Engineering, Vol. 23, No. 1, pp. 76-83.
- Bahl, J. & Bhartia, P. (1982),
"Microstrip Antennas", Dedham, MA, Artech House.
- Bauer, L. and Reiss, E.L. (1978),
"Cutoff wavenumbers and modes of hexagonal waveguides", SIAM J. Appl. Math., Vol. 35, pp. 508-514.
- Beeckman, P.A. (1986),
"Prediction of the Fresnel region field of a compact antenna test range with serration edges", Proc. IEE, Vol. 133, Pt. H, No. 2.
- Bergmann, J.R., Hasselmann, F.J.V., Teixeira, F.L. and Rego, C.G. (1994),
"A comparison between techniques for global surface interpolation in shaped reflector analysis", IEEE Trans. Antennas Propagat., Vol. AP-42, No. 1, pp. 47-53.
- Boor, C. (1978),
"A Practical Guide to Splines", Springer Verlag, New York.
- Born, M. and Wolf, E. (1983),
"Principles of Optics", Sixth (corrected) edition, Pergamon Press, Oxford.
- Bucci, O.M., Franceschetti, G. and D'Elia, G. (1980),
"Fast analysis of large antennas - A new computational approach", IEEE Trans. Antennas Propagat., Vol. AP-28, No. 3, pp. 306-310.

Butler, (1982),

"The equivalent radius of a narrow conducting strip",
IEEE Trans. Antennas Propagat., Vol. AP-30, No. 4,
pp. 755-758.

Clarricoats, P.J.B. and Olver, A.D. (1984),

"Corrugated horns for microwave antennas", Peter
Peregrinus Ltd, IEE Electromagnetics Waves Series
18, 1984

Collin, R.E. and Zucker, F.J. (1969),

"Antenna Theory, Part 1", Chapter 1, McGraw-Hill
Book Company, New York.

Compton, R.T. Jr. and Collin, R.E. (1969),

"Open Waveguides and small horns", Chapter 15 in
R.E. Collin and F.J. Zucker, "Antenna theory", Part 1,
McGraw-Hill Book company, New York, 1969.

Cubley, H.D. and Hayre, H.S. (1971),

"Radiation field of spiral antennas employing multi-
mode slow wave techniques", IEEE Trans. Antennas
Propagat., Vol. AP-19, No. 1, pp. 126-128.

Curtis, W.L. (1960),

"Spiral Antennas", IRE Trans. Antennas Propagat.,
Vol. AP-8, pp. 298-306.

Davis, P.J. and Rabinowitz, P. (1984),

"Methods of numerical integration", Second edition,
Academic press, Inc.

Drabowitch, S. (1978),

"Grandes Antennes", Book III in E. Roubine (Ed.),
"Antennes", Paris, Masson, pp. 114-115.

Elliott, R.S. (1981),

"Antenna theory and design", Prentice-Hall Inc., Eng-
lewood Cliffs, NJ, USA.

- Hansen, J.E. (Editor) (1988),
"Spherical near-field measurements", IEE Electromagnetics Wave Series 26, Peter Peregrinus Ltd., UK.
- Ip, H.-P. and Rahmat-Samii, Y. (1998),
"Analysis and characterization of multilayered reflector antennas: Rain/snow accumulation and deployable membrane", IEEE Trans. Antennas Propagat., Vol. 46, No. 11, pp. 1593-1605.
- James, J.R., Hall, P.S. and Wood, C. (1981),
"Microstrip antenna theory and design", Stevenage, Peter Peregrinus Ltd., UK.
- Jensen, F., (1970),
"Electromagnetic near-field far-field correlations", Ph.D. dissertation, LD 15, Laboratory of Electromagnetic Theory, Technical University of Denmark, Lyngby.
- Jensen, F. and Frandsen, A., (2004),
"On the number of modes in spherical wave expansions", Proc. 26th AMTA, Stone Mountain Park, Georgia.
- Johansen, P.M. (1996),
"Uniform Physical Theory of Diffraction Equivalent Edge Currents for Truncated Wedge Strip", IEEE Trans. Antennas Propagat., Vol. 44, No. 7, pp. 989-995.
- Johnson, R.C. and Jasik, H. (1984)
"Antenna Engineering Handbook", McGraw-Hill Book company.
- Keller, J.B. (1957),
"Diffraction by an aperture", J. Appl. Phys., Vol. 28, No. 4, pp. 426-444.

King, H.E. and Wong, J.L. (1980),

"Characteristics of 1 to 8 wavelength uniform helical antennas", IEEE Trans. Antennas Propagat., Vol. AP-28, pp. 291-296. See also Ch. 13 in Johnson, R.C. and Jasik, H. (1984), "Antenna Engineering Handbook", Sec. Ed., McGraw-Hill Book Company, NY, USA.

Kitsuregawa, 1990,

"Advanced technology in satellite communication antennas: electrical and mechanical design", Artech House, Boston, 1990.

Knott, E.F. and Senior, T.B.A. (1974),

"Comparison of three high-frequency diffraction techniques", Proc. IEEE, Vol. 62, No. 11, pp. 1468-1474.

Kouyoumjian, R.G. and Pathak, P.H. (1974),

"A uniform geometrical theory of diffraction for an edge in a perfectly conducting surface", Proc. IEEE, Vol. 62, No. 11, pp. 1448-1461.

Krauss, J.D. (1950),

"Antennas", Ch. 7, McGraw-Hill Book Company, NY, USA.

Larsen, F.H. (1980),

"Probe-corrected spherical near-field antenna measurements", Ph.D. dissertation LD 36, Electromagnetics Institute, Technical University of Denmark, Lyngby.

Laxpati, S.R. and Mittra, R. (1967),

"Boundary value problems associated with source-excited planar-equiangular-spiral antennas", Proc. IEE, Vol. 114, pp. 353-359. See also pp. 372-378 in Collin and Zucker (1969).

Ludwig, A.C. (1973),

"The definition of cross polarisation", IEEE Trans. Antennas Propagat., Vol. AP-21, pp. 116-119.

- Lumholt, M. (1999),
"Supplementary calculations for the Perth Antenna",
TICRA Report S-971-03.
- Nakamura, K. and Ando, M. (1988),
"A full-wave analysis of offset reflector antennas with polarization grids", IEEE Trans. Antennas Propagat., Vol. 36, No. 2, pp. 164-170.
- Pontoppidan, K. (1971),
"Finite-element techniques applied to waveguides of arbitrary cross section", Ph.D. dissertation, Laboratory of Electromagnetic Theory, Technical University of Denmark, Lyngby.
- Pontoppidan, K. (1981),
"Study of offset unfurlable antennas - electrical design aspects", TICRA Report S-144-01.
- Pontoppidan, K. (1986),
"Reflector antennas - An overview of surface distortion effects", Proc. JINA, Nice, pp. 82-93.
- Powell, M.J.D.,
"A hybrid method for non-linear equations", in "Numerical methods for non-linear algebraic equations", ed. P. Rabinowitz, Gordon and Breach, 1970
- Risser, J.R. (1949),
"Waveguide and horn feeds", Ch. 10 in S. Silver (Ed.),
"Microwave Antenna Theory and Design", McGraw-Hill Book Company, NY, USA.
- Savi, P. (1997),
"Analysis of strip gratings (ASG): User guide", CESPA-CNR, Politecnico di Torino, Torino, Italia.
- Schelkunoff, S.A. (1943),
"Electromagnetic waves", D. van Nostrand Co., Inc., Princeton, NJ, USA.

Shore and Yaghjian (1988),

R.A. Shore and A.D. Yaghjian, "Incremental Diffraction Coefficients for Planar Surfaces", IEEE Trans. Antennas Propagat., Vol. AP-36, No. 1, pp. 55-70, Jan. 1988. Correction in Vol. AP-37, No. 10, p. 1342, Oct. 1989.

Shore and Yaghjian (1993),

R.A. Shore and A.D. Yaghjian, "Application of Incremental Length Diffraction Coefficients to Calculate the Pattern Effects of the Rim and Surface Cracks of a Reflector Antenna", IEEE Trans. Antennas Propagat., Vol. AP-41, No. 1, pp. 1-11, Jan. 1993. Correction in Vol. AP-45, No. 5, p. 917, May 1997.

Stearns, S.D. (1975),

"Digital signal analysis", Hayden Book Company, Inc., Rochelle Park, NJ, USA, pp. 61-65.

Stratton, J.A. (1941),

"Electromagnetic theory", McGraw-Hill Book Company, NY, USA.

Sørensen, S.B., Lumholt, M. and Viskum, H.-H. (1999),

"Manual for POS4 - Physical Optics Shaping Program", TICRA Report S-840-004.

Uher, J., Bornemann, J. and Rosenberg, U. (1993),

"Waveguide components for antenna feed systems: Theory and CAD", Artech House Inc., Norwood, MA, USA.

8. SUBJECT INDEX

A

- Array
 - definition of, 151
 - example, 347
 - normalisation, 153, 268
 - power coupling, 268
- Astigmatism, 30

B

- Basic designs
 - dual reflector antenna, 372
 - single reflector antenna, 370
- Beam analyses, 300
 - contour area, 306
 - efficiency, 303
 - pattern envelope, 308
 - peak gain, 301
- Beam waveguide, 353

C

- Cardioid pattern feed, 143
- Cascading material layers, 84
- Caustics, 367
- Central tip, 24
- Circular cone surface, 21
- Circular cylinder surface, 21
- Circular reflector rim, 48
- Coma, 30
- Compact antenna test range, 349
- Compensated antenna systems,
379
- Complex point source, 99
- Conic mirror surface, 18
- Conical horn, 121

Convergence accuracy, 176

Convergence of PO, 173

automatic procedure, 176

Coordinate systems, 11

Euler angles, 13

material definiton, 65, 82

polarisation, 280

Cubic spline surface, 25

D

- Dielectric layer, 79
- Directivity, 266
- Dual gridded reflector, 333
- Dual reflector antenna, 319, 333

E

- Ellipsoids, 16, 365
- Elliptical pattern feed, 111
- Equivalence principle, 147
- Equivalent antenna system, 376

F

- Far field, 265
- Feed elements, 89
 - cardioid pattern, 143
 - conical horn, 121
 - elliptical pattern, 111
 - Gaussian beam, 99
 - halfwave dipole, 141
 - helix, 129
 - Hertzian dipole, 142
 - hexagonal horn, 123
 - Huygens source, 143
 - hybrid mode horn, 144
 - microstrip, 127

normalisation, 266
 Potter horn, 122
 rectangular horn, 117
 simple tapered pattern, 110
 spherical wave expansion, 97
 spiral, 135
 tabulated pattern, 92
 waveguide, 122

Finite conductivity, 69
 Flat plate surface, 21

G

Gaussian beam, 99, 105
 analysis, 252

Geometrical Optics. *See* GO

Geometrical Theory of Diffraction. *See* GTD

GO, 222
 advanced ray tracing, 224
 simple ray tracing, 223

Grating lobes, 44, 47

GTD, 227
 caustic correction, 229
 with material properties, 233

H

Halfwave dipole, 141
 Helix feed, 129
 Hertzian dipole, 142
 Hexagonal horn, 123
 Hinged reflector panels, 57
 Huygens source, 99, 143
 Hybrid mode horn, 144
 Hyperboloids, 17, 362

I

Ideal grid, 70
 Interpolation, 295
 cubic, 295

Whittaker, 298

M

Mesh, 76
 Mesh surface, 42, 45
 Microstrip feed, 127

N

Normalisation, 266, 278

O

Open GL, 3
 Output points
 aperture fields, 294
 cuts, 283
 grids, 285
 cylindrical, 289
 planar, 290
 spherical, 285
 irregularly spaced, 292
 surface points, 292

P

Panel reflector, 54, 57
 Paraboloids, 17, 359
 Perfect absorber, 69
 Perfect conductor, 69
 Physical Optics. *See* PO
 Physical Theory of Diffraction. *See* PTD
 Planar tabulated field, 147
 Plane wave, 151
 Plates, flat, 62
 PO, 155
 convergence of, 173
 with material properties, 215
 PO integration for
 panelled reflectors, 184

- struts, 193, 204
PO integration in
 polar grid, 162
 central blockage, 167
 rectangular grid, 168
 triangular grid, 170
Polarisation, 269
 far fields, 269
 circular, 273
 elevation/azimuth, 272
 linear, 272
 major/minor axes, 273
 power, 274
 theta-phi, 270
 tilt angle, 274
 XPD, 274
near fields, 275
 circular, 276, 277, 278
 linear, 275, 277
 power, 276
 rho-phi, 277
 r-theta-phi, 275
Potter horn, 122
Power flux, 265
Poynting's vector, 265
PTD, 181
 for gaps, 185
 for polygonal struts, 205
 for reflectors, 181
Pyramidal surface, 19
- R**
- Random surface, 33
Rayleigh sphere, 90
Rectangular horn, 117
Rectangular reflector rim, 48
Reflection coefficients, 65
Reflector
 definition of, 14
 distortion, 61
 with hinges, 57
 with hole, 52
 with panels, 54, 57
 with serrations, 58, 349
Reflector material properties, 62
 cascading layers, 84
 definiton of, 65
 dielectric layer, 79
 finite conductivity, 69
 ideal grid, 70
 mesh, 76
 equivalent grid, 77
 perfect absorber, 69
 perfect conductor, 69
 power specified, 68
 strip grid, 72, 84, 333
 tabulated input, 81
 wire grid, 75
Reflector rim
 circular, 48
 definition of, 48
 rectangular, 48
 superelliptical, 49
 tabulated, 50
 triangular, 49
Reflector surface
 central tip, 24
 circular cone, 21
 circular cylinder, 21
 conic mirror, 18
 cubic splines, 25
 definition of, 15
 ellipsoid, 16, 365
 flat plate, 21
 hyperboloid, 17, 362
 irregularly spaced points, 37
 quintic pseudo splines, 37
 triangulation, 38

mesh in triangular grid, 45
mesh with ribs, 42
paraboloid, 17, 359
pyramid, 19
random distortion, 33
regular grid, 21
accuracy of input points, 21
second order polynomial, 20
sphere, 21
tabulated, rotational
symmetric, 24
two foci, 21
Zernike expansion, 28

Rotational symmetric surface, 24

S

Serrated reflector, 58
Shaped reflector antenna, 326
Simple tapered feed, 110
Spherical aberration, 30
Spherical mode sphere, 90
Spherical surface, 21
Spherical wave expansion, 254
ab-modes, 257
number of modes, 256
Q-modes, 260
Spillover, 180
Spiral feed, 135
Strip grid, 72
Struts
calculations, 191

circular, 192
definition of, 87
examples, 208, 311
PO
circular struts, 193
polygonal struts, 204
polygonal, 204
PTD
polygonal struts, 205
typical contributions, 191
Superelliptical reflector rim, 49

T

Tabulated pattern, 92
Tabulated reflector rim, 50
Time factor, 1, 95, 264
Transmission coefficients, 65
Triangular reflector rim, 49
Tricot mesh, 76
Tricot mesh surface, 77

U

Units, 11, 263

W

Wire grid, 75

Z

Zernike mode surface, 28